# Electrothermal Field and Circuit Simulation of Thin Wires and Evaluation of Failure Probabilities

Electrothermal Field and Circuit Simulation of Thin Wires and Evaluation of Failure Probabilities
Elektrothermische Feld- und Schaltungssimulation von dünnen Drähten und Evaluation von
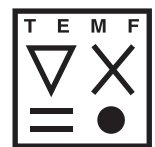Ausfallwahrscheinlichkeiten

To my mother

# Erklärungen laut Promotionsordnung

## §8 Abs. 1 lit. c PromO

Ich versichere hiermit, dass die elektronische Version meiner Dissertation mit der schriftlichen Version übereinstimmt.

## §8 Abs. 1 lit. d PromO

Ich versichere hiermit, dass zu einem vorherigen Zeitpunkt noch keine Promotion versucht wurde. In diesem Fall sind nähere Angaben über Zeitpunkt, Hochschule, Dissertationsthema und Ergebnis dieses Versuchs mitzuteilen.

## §9 Abs. 1 PromO

Ich versichere hiermit, dass die vorliegende Dissertation selbstständig und nur unter Verwendung der angegebenen Quellen verfasst wurde.

## §9 Abs. 2 PromO

Die Arbeit hat bisher noch nicht zu Prüfungszwecken gedient.

Darmstadt, den 30. April 2019

_____

Thorben Casper

# Zusammenfassung

Die vorliegende Dissertation beschäftigt sich mit der elektrothermischen 3D Feld- und Schaltungssimulation für die Berechnung von Ausfallwahrscheinlichkeiten dünner Drähte. Beispielhaft werden Ausfallwahrscheinlichkeiten von Bonddrähten in Chip-Gehäusen aus dem Feld der Mikro- und Nanoelektronik betrachtet. Das in dieser Arbeit verwendete Fehlermodell basiert auf der Temperatur der Bonddrähte unter Verwendung elektrischer Anregung.

Da Bonddrähte im Vergleich zur Größe des umgebenden Chip-Gehäuses sehr dünn sind, stellen die unterschiedlichen geometrischen Skalen eine numerische Herausforderung dar. Anstatt der lokalen Verwendung sehr feiner Gitter wird eine 1D–3D Kopplung eingeführt. Für eine konsistente Diskretisierung werden die singulären Draht-Beiträge durch de Rham-Ströme modelliert. Hierbei liegt ein besonderes Augenmerk auf einer konsistenten 1D–3D Kopplungsbedingung, sodass sich eine physikalische Lösung ergibt. In der gekoppelten Formulierung agieren die Drähte als lösungsabhängige singuläre Linienquellen, was zu verringerten Konvergenzraten des numerischen Lösungsverfahrens führt. In dieser Arbeit wird demonstriert, dass ein abgestuftes 3D Gitter sowie ein Kopplungsradius größer Null in einer Erholung der Konvergenzrate resultiert. Darüber hinaus wird gezeigt, dass diese Art von Problem eng mit der Fluidströmung in porösen 3D-Medien mit 1D-Frakturen verwandt ist.

Neben der Berechnung von elektromagnetischen Feldern werden heutzutage in vielen Workflows auch Schaltungssimulationen erfolgreich eingesetzt. Für einen effizienten Schaltungsentwurf wird ausgehend von diskretisierten Feldmodellen ein Verfahren zur automatisierten Generierung von Netzlisten vorgestellt. Unter Verwendung eines orthogonalen Gitterpaares ergibt sich eine direkte Korrespondenz zwischen Gitterobjekten und Schaltungselementen. Da die resultierende Schaltung mit einem beliebigen Schaltungssimulator simuliert werden kann, werden z.B. die Behandlung von Nichtlinearitäten und die Zeitintegration in den Schaltungslöser verlagert. Darüber hinaus ermöglicht dieser Ansatz eine direkte Art der Feld-Netzwerk Kopplung, indem alle zusätzlichen Schaltungselemente zu der das Feldproblem repräsentierenden Netzliste hinzugefügt werden können. Ein weiterer Vorteil ergibt sich aus den oftmals verfügbaren Schnittstellen von Schaltungssimulatoren zu anderen Software-Paketen, die dank der erhaltenen Schaltungsbeschreibung ebenfalls genutzt werden können. Beispielhaft sei hier die Schnittstelle zwischen XYCE und DAKOTA genannt, die Methoden zur Quantifizierung von Unsicherheiten ermöglicht.

Die vorgestellten Methoden werden anhand von numerischen Testbeispielen verifiziert. Angetrieben von den Zielen des nanoCOPS-Projektes wird für die industrielle Anwendung der Ergebnisse dieser Dissertation beispielhaft die Berechnung der Ausfallwahrscheinlichkeit eines Chip-Gehäuses betrachtet. Die Wahrscheinlichkeit für einen Systemausfall wird exemplarisch anhand der Ausfallwahrscheinlichkeiten einzelner Bonddrähte mit unsicherer Geometrie evaluiert. Für den vorliegenden Fall kleiner Ausfallwahrscheinlichkeiten folgt, dass klassische Methoden wie die Monte-Carlo Simulation eine sehr hohe Anzahl an Samples benötigen. Als Abhilfe wird ein hybrides iteratives Verfahren verwendet, das ein genaues 3D Feldmodell mit einem kostengünstigen polynomiellen Ersatzmodell kombiniert, sodass eine hohe Genauigkeit bei geringen Rechenkosten erreicht wird.

# Abstract

This thesis deals with the electrothermal 3D field and circuit simulation of structures containing thin wires to evaluate their failure probability. Failure probabilities of wires in chip packages from the field of micro- and nanoelectronics are considered as an example. The failure model used in this thesis is based on the temperature of the bond wires under electric operating conditions.

Since bond wires are very thin compared to the size of the surrounding chip package, the different geometric scales rise numerical challenges. Instead of locally applying very fine grids, a 1D–3D coupling approach is introduced. For a consistent discretization, the singular wire contributions are modeled by the powerful framework of de Rham currents. Particular focus lies on a consistent 1D–3D coupling condition to ensure a physical solution. In such a setting, the wires act as solution-dependent singular line sources resulting in a deteriorated convergence rate of the numerical method. It is demonstrated that a graded 3D grid and a non-zero coupling radius result in a recovered convergence rate. Furthermore, it is shown that this kind of problem is closely related to fluid flow in porous 3D media with 1D fractures.

Apart from the calculation of electromagnetic fields, circuit simulation has been successfully integrated into many workflows. To realize circuit designs in an efficient way, a method to automatically generate netlists describing general discretized field problems is presented. Using a pair of orthogonal grids, a one-to-one correspondence between grid objects and circuit elements is obtained. The resulting circuit can then be solved with any state-of-the-art circuit simulator, circumventing the need for handling the nonlinearities or for a custom time integration scheme. Moreover, the approach allows a straightforward field-circuit coupling by adding any additional circuit elements to the generated netlist that represents the field problem. Often, circuit simulators provide interfaces to other useful software packages that may be exploited thanks to the obtained circuit description. One example is given by the interface between Xyce and Dakota to allow for uncertainty quantification methods.

The proposed techniques are verified using numerical test examples. Driven by the goals of the nanoCOPS project, a possible industrial application of the outcomes of this thesis is demonstrated by the computation of the system failure probability of a chip package. The system failure probability is evaluated based on the failure probabilities of the individual bond wires of uncertain geometry. For small failure probabilities, classical Monte Carlo techniques require a very high number of samples. As a remedy, a hybrid iterative sampling scheme combines the accurate 3D field model with a cheap polynomial surrogate model, yielding accurate results at a low computational cost.

# Contents

# List of Figures

# List of Tables

# List of Acronyms

| | |
|---|---|
| 0D | zero-dimensional. |
| 1D | one-dimensional. |
| 2D | two-dimensional. |
| 3D | three-dimensional. |
| ABC | absorbing boundary condition. |
| BC | boundary condition. |
| BDF | backward differentiation formula. |
| BiCG | biconjugate gradient. |
| BiCGSTAB | stabilized biconjugate gradient. |
| CCCS | current-controlled current source. |
| CEM | computational electromagnetics. |
| CG | conjugate gradient. |
| CM | cell method. |
| DAE | differential algebraic equation. |
| DoFs | degrees of freedom. |
| EM | electromagnetic. |
| EQS | electroquasistatic. |
| ET | electrothermal. |
| FD | finite difference. |
| FDTD | finite difference time domain. |
| FE | finite element. |
| FIT | finite integration technique. |
| FV | finite volume. |
| GMRES | generalized minimal residual. |
| KCL | Kirchhoff's current law. |
| MAFIA | Maxwell's equations using the finite integration algorithm. |
| MC | Monte Carlo. |
| MG | multigrid. |
| MGEs | Maxwell grid equations. |
| MNA | modified nodal analysis. |
| MOR | model order reduction. |
| MOSFET | metal oxide semiconductor field effect transistor. |
| MQS | magnetoquasistatic. |
| ODE | ordinary differential equation. |
| PCG | preconditioned conjugate gradient. |
| PDE | partial differential equation. |

PEC     perfect electric conducting.
PEEC    partial element equivalent circuit.
QMR     quasi-minimal residual.
QoI     quantity of interest.
SOR     successive overrelaxation.
SSOR    symmetric successive overrelaxation.
TE      transverse electric.
TM      transverse magnetic.
UQ      uncertainty quantification.
VCCS    voltage-controlled current source.
VCVS    voltage-controlled voltage source.
gPC     generalized polynomial chaos.

# 1 Introduction

In the field of micro- and nanoelectronics, improving the capabilities of electronic devices is always of high interest. During the last decades, this resulted in a continuous downscaling of the feature sizes [158]. Thus, high power densities are an increasing problem and a sophisticated thermal design is required. If an electronic design is not carefully checked for thermal issues, the degeneration of materials, performance restrictions or even system failure may occur. This becomes particularly pronounced when considering power electronics such as power transistors [131, 148], see Figure 1.1a [150]. Hence, today's complexity in the design and fabrication of electronic components leads to a great significance of numerical simulations. In particular, coupled electrothermal (ET) simulations become an indispensable tool for the design of electronic devices. This bi-directional coupling is established by Joule losses on the one hand and by temperature-dependent material parameters on the other hand. In this thesis, we consider the efficient electrothermally coupled field and circuit simulation of thin wires and the evaluation of the corresponding failure probabilities. As an application example, the system failure probability of a microelectronic chip package with bond wires of uncertain geometry is of interest, see Figure 1.1b.

This introductory chapter outlines the ideas of this thesis in the following way. First, Section 1.1 gives an explanation and motivation for computational electromagnetics (CEM) and provides a brief historical overview. The state-of-the-art numerical techniques in CEM are discussed in Section 1.2. Finally, Section 1.3 outlines the goals of this thesis.



(a)

(b)
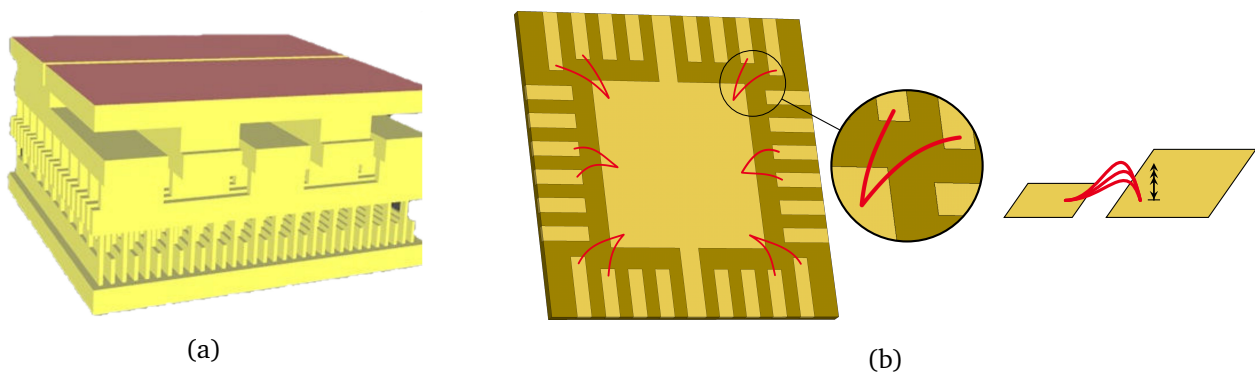
Figure 1.1: (a) Typical layout of a power transistor [150]. (b) Microelectronic chip package with substrate (dark yellow), conducting regions (yellow), and bond wires of uncertain geometry (red) [133].

## 1.1  Computational Electromagnetics and a Historical Overview

Nowadays, engineering products have become very complex, requiring a detailed analysis of the underlying physics. Often, experiments are not possible, since they may be too complicated, expensive, or risky. Additionally, measurements are always subject to uncertainties, introduced for instance by the measurement devices themselves. Instead, *fundamental laws of physics* allow the construction of accurate models and corresponding solution techniques are of interest. Although many analytical methods exist, they are only applicable in the case of very simple geometries. All these reasons underline the relevance of *numerical simulations* for the analysis of engineering problems [181]. In contrast to physical experiments, simulations may be used already at an early design stage at very low cost, which is crucial for an efficient workflow [23]. This point is especially pronounced in the aerospace industry, in which, e.g., Boeing replaced 90 % of the experiments in wing development by simulation [65].

In the field of electromagnetics (EMs), Maxwell's equations provide a precise model for the fields and their interaction with the environment [122]. Solving these equations for complex problems requires computational methods, motivating the field of *computational electromagnetics (CEM)*. Methods in CEM often lead to two-dimensional (2D) or three-dimensional (3D) field simulations, and we must assess their accuracy, a task typically carried out by steps known as *verification* and *validation* [171]. For general problems, different techniques are available. After a simulation tool is developed, a first verification is typically conducted by the construction of simple numerical examples, for which analytical solutions exist. Even if an analytical solution is not directly available, the *method of manufactured solutions* allows to choose the excitation such that the exact solution is known [171, 188]. However, the verification and validation of complex problems relies on the comparison to other codes or to measurements. In CEM, fields of application, especially in micro- and nanoelectronics, include the simulation of high speed silicon electronics, nanophotonic devices, electromagnetic compatibility, wave propagation, and antennas.

Let us consider the field of CEM from a historical perspective. One of the first numerical methods for EM analysis was the *finite difference time domain (FDTD)* scheme as proposed by Yee in the 1960s [254]. Its name dates back to a paper by Taflove in 1980 [214]. This method became popular and is still a standard approach for high-frequency EM simulations [213]. One of its key advantages is its simplicity to implement a full wave solver. About ten years after Yee's article, in the 1970s, Weiland [240] introduced the *finite integration technique (FIT)* as an extension to the FDTD scheme. It preserves basic topological properties of the continuous equations [59] and allows for non-Cartesian and unstructured grids [182]. Furthermore, the FIT is embedded into the mathematical profound framework of differential forms [28] and yields unique, physical solutions [241]. Later developments of FIT led to the usage of integral unknowns to obtain an exact implementation of Maxwell's equations [242]. Compared to FDTD, FIT is more efficient in terms of memory requirements and computing time. Moreover, it allows to conveniently consider semiconductors [191], mainly due to the regular patterns in electronic designs.

After the introduction of the *finite element (FE)* method in the 1950s [62, 230], it became very popular especially in the field of solid and structural mechanics. Therefore, the CEM community was very interested to adapt it also for problems in the field of EMs. Doing so, it appeared natural to consider the nodal elements from mechanics also for EM fields. However, this resulted in *spurious modes*, also known as *spurious solutions*, *ghost modes*, or *unphysical solutions*, which do not satisfy the full set of Maxwell's equations [124, 212]. Despite the presence of spurious modes, the far-field solution remains correct, which is the reason why they remained undiscovered for quite a long time. Spurious modes are attributed to the inability of nodal basis functions to model the null space of the curl-curl operator properly. Another reason for spurious modes lies in the continuity conditions at material boundaries, which cannot be fulfilled by nodal basis functions.
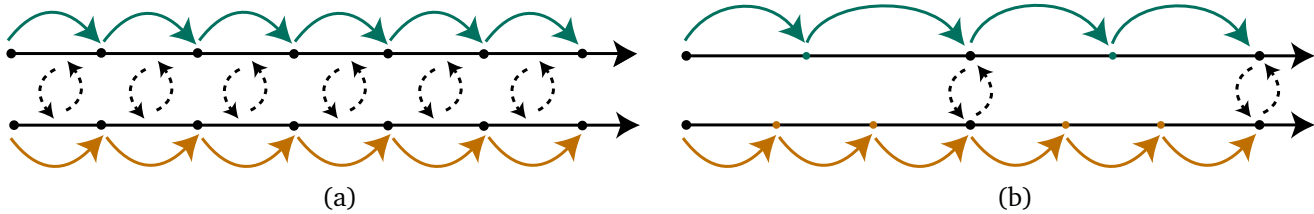
Figure 1.2: Different methods to realize coupling in simulation. (a) Strong (monolithic) coupling, (b) weak (iterative) coupling. This figure is based on [61].

Even if tangential continuity is enforced by an FE approximation, normal continuity is required as well. This dilemma resulted in the introduction of *Nédélec* elements into the field of CEM [166]. Later, the framework of *Whitney* forms was realized to be suitable as well [26, 31, 244]. Using Whitney forms, degrees of freedom are associated with nodes, edges, facets, or volumes of the grid. Therefore, Whitney forms are also known as *node-*, *edge-*, *facet-*, and *volume-elements*.

## 1.2 State of the Art

With the history of CEM outlined in Section 1.1, we now come to the current state and to the currently active research topics in the field of CEM. In general, one is interested in the simulation of complex problems in the most efficient ways. However, many issues arise due to the modern problem sizes in contrast to the finite capabilities of computers. Thus, we need improved numerical methods, supercomputers, high performance clusters, and parallel computations. For the latter, algorithms suited for parallel computer architectures are required [196]. It is interesting to realize that modern software packages such as CST DESIGN STUDIO [67], ANSYS HFSS [4], and EMPRO [130] spend the largest amount of time for geometry manipulations and meshing [23, 121].

With the vision of simulating the world as a whole, we require the coupling of different methods and solvers. Thus, a significant amount of research is currently conducted in the fields of *multi-physics*, *multi-scale*, *multi-rate*, and *multi-domain* techniques [108, 194], terms that are explained in the following. The term *multi-physics* refers to the coupling of different physical phenomena. One example is given by *ET field simulation*, which is important for the design of state-of-the-art nano-electronic devices [192]. *Multi-scale* and *multi-rate* techniques refer to problems that involve spatial and temporal scales of different orders of magnitude [194]. Furthermore, the term *multi-domain* refers to different formulations and discretizations for different parts of the model, motivated by differences in dimension, materials, physical behavior, and numerical challenges. One example is given by *domain decomposition*, which tackles a problem by a divide-and-conquer approach [13, 205]. Multi-domain methods exhibit the advantages of reducing the overall number of degrees of freedom (DoFs), they may reduce the condition number, and they may allow for parallelization. All these coupling approaches result in a currently observed merging of already existing simulation-software companies. Solvers combining electromagnetics, structural dynamics, fluid dynamics, and thermodynamics are already available and indispensable for large classes of engineering problems [108, 151, 192]. However, guarantees on stability and numerical efficiency for these coupled methods do not yet exist and remain an open research topic [61].

Many coupled formulations can be classified into a *strong* (*monolithic*) or a *weak* (*iterative*) approach [61], see Figure 1.2. The former refers to the situation in which both subproblems are combined into one system of

equations that is solved as a whole. In the latter approach, both subproblems are solved independently and the interdependent data is exchanged iteratively. At first sight, a strong coupling might appear more natural. However, due to already available simulation tools, one might prefer a straightforward weak coupling of the individual black-box solvers as an alternative to the integration of one black-box into the other to obtain a monolithic solver. Moreover, if one of the subproblems touches already the limit of the available computational capacity, a monolithic coupling may simply not be possible. On the other hand, an iterative coupling can be done on the implementation level, i.e., by coupling different software packages; on the modeling level, i.e., by coupling different models within one software package; on the simulation level, i.e., by iterating between differently discretized models; or on the algebraic level, i.e., by iterating between the blocks of a coupled linear or nonlinear system of equations. In other words, a weak coupling allows to use different simulation tools, different spatial and temporal discretization schemes, different resolutions, and may allow for parallel computations. However, convergence may be slow or not even guaranteed, a problem especially significant for transient problems. One popular method to increase the convergence of iterative methods is the waveform relaxation (dynamic iteration) [139].

In engineering, circuit models are very popular for a compact description of possibly complex problems. For setting up these models, mostly hand calculations are used, which are not capable of considering nonlinear effects nor non-trivial geometries. Moreover, many circuit models are restricted to a limited operation range, e.g., a constant operating temperature. No generic method for the construction of physical equivalent circuits exists. However, some specific methods are proposed in the literature [12, 88, 225, 246]. Combining circuit solvers with field solvers leads to *field-circuit couplings* [74, 195, 228]. They are a subclass of *hybrid discretizations* [73, 136, 208] and can be classified as multi-domain methods, see above. Realizing such a field-circuit coupling, a field solver can be called from the circuit solver [191] or vice versa [19, 195]. One common approach is the generation of lookup tables by the field solver in an offline step, which then can be used by the circuit solver during simulation. More details about available techniques for circuit generation and simulation are given in Section 6.1.

Another important field of research is the quantification of uncertainties. Any uncertainty may be *aleatoric*, i.e., random, or *epistemic*, i.e., an uncertainty due to incomplete knowledge. The field of *uncertainty quantification (UQ)* uses stochastic models to give quantitative information about the corresponding uncertainty. State-of-the-art techniques include classical *Monte Carlo (MC)* methods [45, 143], *generalized polynomial chaos (gPC)* [250], *stochastic collocation* [10, 251], and *stochastic Galerkin methods* [11, 251]. A comparison between the MC method and gPC is provided, e.g., in [250]. Currently active research is conducted on promising techniques such as *sparse grids* [40], *tensor train decomposition* [174], and *adaptive sparse grid collocation* [93, 146], with a comparison provided, e.g., in [145]. In the field of UQ, repeated evaluations of a field model are often required, motivating the necessity of *multi-fidelity* models [165, 175]. If models of different fidelities are available, the computational efficiency may be improved by their alternating use during repeated evaluations of large field models.

Finally, let us come to the applications of interest in this thesis. For the packaging of micro- and nanoelectronic devices, bond wires are one of the cheapest and mostly used electric connections between the chip and the package. One of the reasons is the fast and fully automated procedure for establishing their connections. Typically, bond wires are made of aluminum, copper, or gold, and their size shrinks along with the general shrinkage of electronic devices [158]. Due to this shrinkage and the resulting increase in power densities, the breakage of bond wires became an important source of failure [155]. The computation of corresponding failure probabilities requires accurate models, giving rise to the requirement of 3D electrothermally coupled field simulation. The main problem when including bond wires into these simulations is their small diameter in relation to the size of the computational domain. Therefore, we require surrogate models for the wires to be coupled to the surrounding domain. One approach is the use of analytical models [82, 167], but they

often do not model all relevant effects. A common approach for general EM problems is to include the wires directly in the field simulation by assigning a perfect conductance to the corresponding edges of the grid. Thus, resolving the diameter of the wires is circumvented. However, when thermal considerations enter the simulation, a perfect thermal conduction would lead to a significant modeling error. Thus, alternative approaches are required.

## 1.3 Research Goals

This thesis deals with the efficient ET field and circuit simulation of thin wires embedded in 3D domains and the evaluation of failure probabilities. The proposed methods are applied to a microelectronic chip package with twelve bond wires of uncertain geometry as shown in Figure 1.1b. In practice, a chip package contains hundreds of bond wires, which further motivates the need for an efficient embedding of thin wires into 3D simulations. Since these bond wires are commonly subject to very high current densities, their steady-state temperatures are of interest. The goals of this thesis are

- to provide a general tool for the ET simulation of micro- and nanoelectronics devices. Due to the regular patterns in electronic devices, FIT is the major discretization scheme considered;

- the computation of bond wire failure probabilities under uncertain manufacturing conditions;

- the development of a thin wire model suitable for the inclusion in the ET simulation of 3D field problems such as a microelectronic chip package. In particular, the temperatures of the individual wires must be determined by numerical simulation;

- to obtain an automated method for the extraction of ET and EM circuits from 3D field problems. With such a model available, model order reduction (MOR) techniques for circuits can be applied to obtain an efficient surrogate model to be used for UQ methods, e.g., together with the available interface between the Xyce simulator [128] and the Dakota package [1].

## 1.4 Summary

This first chapter gave an introduction to the field of computational electromagnetics (CEM) and motivated its relevance for modern engineering problems. To provide the background of this thesis, we summarized the state-of-the-art of the relevant topics. Namely, different kinds of couplings, the construction of circuit models, the quantification of uncertainties, and the use of bond wires were discussed. Moreover, currently active research topics were pointed out. To further define the relevance of this work, the research goals were outlined in the final section of this chapter.

# 2 Field and Circuit Modeling

This chapter introduces the field and circuit descriptions of the electromagnetic (EM) and thermal models used throughout this thesis. While using the modern vector analysis as the calculus in this thesis, we shall not forget the historical background of this powerful mathematical tool [66, 209]. Mainly in the nineteenth century, there was a long search for a convenient system to describe physical laws conveniently. For the description of a system in a high dimensional space, an algebra for multiple variables is required. At that time, the double algebra of complex numbers was already established and served as the starting point to extend its 2D description to the third dimension. Three major systems, the Hamilton, the Graßmann, and the Gibbs-Heaviside system evolved during that period. The first significant success was contributed to Hamilton who published the quadruple algebra of quaternions in 1843. The idea of quaternions is based on one number describing the magnitude and three numbers describing the rotation of a vector. However, its main drawback was the missing property of commutativity of vector multiplication. In 1844, Graßmann published the first full exposition of his system which also included the nowadays well-known inner and outer products. Although many mathematicians struggled with the abstract writings of Graßmann, his system used already many principles from modern vector analysis. In the period between 1840 and 1900, the Hamiltonian and the Graßmannian system existed alongside each other, with the quaternionic system receiving much greater attention. While the former was mainly popular in Great Britain and the United States, the latter was dominant in the German community. In 1884, the triple algebra of modern vector analysis was published independently by Gibbs and Heaviside. Along with many other useful concepts, it introduced two different products of vectors, the well known scalar (dot) and vector (cross) products. The main reasons for the breakthrough of vector analysis include the beneficial algebraic properties and the reasonable intellectual effort required to learn its concept [209]. While Maxwell wrote parts of his "Treatise on Electricity and Magnetism", published in 1873, still in Hamilton's quaternionic system, the Gibbs-Heaviside system of modern vector analysis evolved to be the dominant one by 1910. Thus, it is an evident choice to exploit the latter in this thesis. However, for metric-independent formulations, we also introduce concepts from the field of differential geometry and algebraic topology.

This chapter is organized as follows. In Section 2.1, Maxwell's equations and the constitutive laws are introduced. Section 2.2 presents different low frequency approximations. The thermal description is covered in Section 2.3, establishing the fundamental principles of heat transport. Bringing EMs and thermal effects together, Section 2.4 provides the electrothermal (ET) model of interest in this thesis. For a physically correct solution of the considered ET model, we require initial and boundary conditions (BCs) as discussed in Section 2.5. Section 2.6 presents the fundamentals of circuit theory and introduces the modified nodal analysis (MNA), which is the underlying technique upon which any modern circuit simulator is based. Finally, the treatment of thin wires, as considered in this thesis, requires to discuss distributed current sources in Section 2.7 and we give an introduction to differential forms in Section 2.8.

## 2.1 Maxwell's Equations

Let us consider the *position* $\vec{x} \in \mathcal{D} \subset \mathbb{R}^3$ within the domain $\mathcal{D}$ and its boundary $\Gamma := \partial\mathcal{D}$, and the *time* $t \in I \subset \mathbb{R}$ with the time interval $I = (t_0, t_1]$. The spatial domain $\mathcal{D}$ is visualized in Figure 2.1. Any EM field in $\mathcal{D}$ underlies the set of Maxwell's equations [122]. For a facet $S$ and a volume $V$, they read

$$-\int_{\partial S} \vec{E}(\vec{x}, t) \cdot \mathrm{d}\vec{L} = \int_S \frac{\partial}{\partial t} \vec{B}(\vec{x}, t) \cdot \mathrm{d}\vec{S}, \tag{2.1a}$$

$$\int_{\partial S} \vec{H}(\vec{x}, t) \cdot \mathrm{d}\vec{L} = \int_S \left( \frac{\partial}{\partial t} \vec{D}(\vec{x}, t) + \vec{J}(\vec{x}, t) \right) \cdot \mathrm{d}\vec{S}, \tag{2.1b}$$

$$\int_{\partial V} \vec{D}(\vec{x}, t) \cdot \mathrm{d}\vec{S} = \int_V \varrho(\vec{x}, t) \, \mathrm{d}V, \tag{2.1c}$$

$$\int_{\partial V} \vec{B}(\vec{x}, t) \cdot \mathrm{d}\vec{S} = 0, \tag{2.1d}$$

with suitable initial and boundary conditions (BCs) on $\Gamma$, see Section 2.5. Here, the used quantities are the *electric field* $\vec{E}$, the *magnetic field* $\vec{H}$, the *electric flux density* $\vec{D}$, the *magnetic flux density* $\vec{B}$, the *electric current density* $\vec{J}$, and the *electric charge density* $\varrho$, which all depend on position $\vec{x}$ and time $t$. In general, the electric current density $\vec{J}$ is composed of the conductive, convective, and impressed current densities $\vec{J}_\mathrm{c}$, $\vec{J}_\mathrm{cv}$, and $\vec{J}_\mathrm{i}$, respectively, such that

$$\vec{J}(\vec{x}, t) = \vec{J}_\mathrm{c}(\vec{x}, t) + \vec{J}_\mathrm{cv}(\vec{x}, t) + \vec{J}_\mathrm{i}(\vec{x}, t). \tag{2.2}$$

First, the conductive current density is driven by the electric field and will be defined in the following. Secondly, the convective current density $\vec{J}_\mathrm{cv} = \varrho\vec{v}$ results from the movement of free charges, with their *velocity* $\vec{v}$. Thirdly, the impressed current density acts as a source and is specified independently. To guarantee the uniqueness of the solution, Maxwell's equations are supplemented with the constitutive relations

$$\vec{D}(\vec{x}, t) = \varepsilon_0 \vec{E}(\vec{x}, t) + \vec{P}(\vec{x}, t), \qquad \vec{B}(\vec{x}, t) = \mu_0 \Big( \vec{H}(\vec{x}, t) + \vec{M}(\vec{x}, t) \Big), \qquad \vec{J}_\mathrm{c}(\vec{x}, t) = \sigma(\vec{x}, t) \vec{E}(\vec{x}, t),$$

where $\varepsilon_0$ and $\mu_0$ are the *permittivity* and the *permeability* of vacuum, respectively, and $\sigma$ is the *electric conductivity*. For the physical background and exact definition of $\sigma$, the reader is referred to [109, Section 7.1]. Instead, we focus on the polarizations given by the *electric polarization* $\vec{P}$ and the *magnetic polarization* or *magnetization* $\vec{M}$. These polarizations represent the electric and magnetic dipoles on a molecular level and generally exhibit a nonlinear dependence on the fields. As long as the fields are not too strong, the polarizations are given by

$$\vec{P}(\vec{x}, t) = \varepsilon_0 \chi_\mathrm{e}(\vec{x}) \vec{E}(\vec{x}, t), \qquad\qquad \vec{M}(\vec{x}, t) = \chi_\mathrm{m}(\vec{x}) \vec{H}(\vec{x}, t),$$

where $\chi_\mathrm{e}$ and $\chi_\mathrm{m}$ are the electric and magnetic *susceptibilities* [99, 138], which we assume to be time independent. The susceptibilities describe a change of the field strength and lead to the introduction of the *relative* permittivity and the *relative* permeability defined as

$$\varepsilon_\mathrm{r}(\vec{x}) := 1 + \chi_\mathrm{e}(\vec{x}), \qquad\qquad \mu_\mathrm{r}(\vec{x}) := 1 + \chi_\mathrm{m}(\vec{x}),$$

respectively. Magnetic materials are divided into *diamagnetic*, *paramagnetic*, and *ferromagnetic* materials, for which $\mu_\mathrm{r} < 1$, $\mu_\mathrm{r} > 1$, and $\mu_\mathrm{r} \gg 1$, respectively. Values of $\sigma$, $\varepsilon_\mathrm{r}$, and $\mu_\mathrm{r}$ for certain materials are listed,
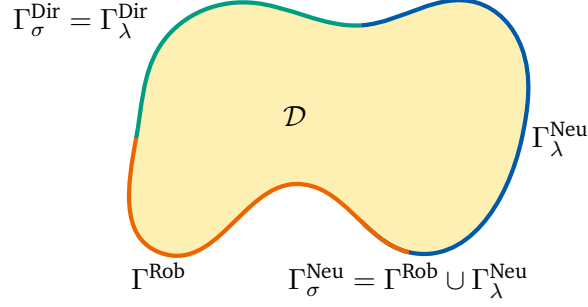
Figure 2.1: Spatial domain $\mathcal{D}$ with boundary $\Gamma$. The boundary is subdivided according to the corresponding BCs. In this illustration, the electric Dirichlet boundary $\Gamma_\sigma^{\text{Dir}}$ coincides with the thermal Dirichlet boundary $\Gamma_\lambda^{\text{Dir}}$, while the electric Neumann boundary $\Gamma_\sigma^{\text{Neu}}$ is the union of the thermal Neumann boundary $\Gamma_\lambda^{\text{Neu}}$ and the Robin boundary $\Gamma^{\text{Rob}}$.

e.g., in [109]. In general, materials can be anisotropic and dispersive, which results in tensor-valued and frequency-dependent values for $\varepsilon_{\text{r}}$ and $\mu_{\text{r}}$, respectively. In this thesis, due to the applications of interest and without loss of generality, we consider isotropic materials that do not depend on frequency nor the strength or direction of the EM field. However, as we will see in Section 2.3, we allow a possible temperature dependence of the materials. This gives us the simplified relations

$$\vec{D}(\vec{x},t) = \varepsilon(\vec{x})\vec{E}(\vec{x},t), \qquad \vec{B}(\vec{x},t) = \mu(\vec{x})\vec{H}(\vec{x},t), \qquad \vec{J}_{\text{c}}(\vec{x},t) = \sigma(\vec{x})\vec{E}(\vec{x},t), \qquad (2.3)$$

where we refer to $\varepsilon := \varepsilon_0\varepsilon_{\text{r}}$ and $\mu := \mu_0\mu_{\text{r}}$ simply as the permittivity and the permeability of a material, respectively.

## 2.2 Low Frequency Approximation

In many applications, it is not required to consider the full set of Maxwell's equations but to use appropriate approximations instead. Often, the propagation of waves and radiative effects can be neglected due to the size of the considered geometry. If the geometry is small compared to the wavelength, the fields propagate instantaneously and a quasi-stationary approximation becomes valid. For homogeneous materials, the corresponding condition is stated by [79, 109]

$$\Delta \ll \frac{v}{f} = \frac{1}{f\sqrt{\varepsilon\mu}}, \qquad (2.4)$$

where $f$ is the *frequency*, $\Delta := \text{diam}(\mathcal{D})$ is the diameter of the domain, and $v$ is the speed of propagation. If an inhomogeneous permittivity or permeability is involved, appropriate modifications of (2.4) are discussed in [79]. To formulate a quasi-stationary approximation, we apply the Helmholtz theorem [99] which allows us to decompose the fields into irrotational and solenoidal parts with subscripts $_0$ and $_s$, respectively. With the time derivative $\partial_t$, the Helmholtz decomposition for the electric field reads

$$\vec{E}(\vec{x},t) = \vec{E}_0(\vec{x},t) + \vec{E}_{\text{s}}(\vec{x},t), \qquad \nabla \times \vec{E}_0(\vec{x},t) = 0, \qquad \nabla \cdot \vec{E}_{\text{s}}(\vec{x},t) = 0, \qquad (2.5)$$

$$\vec{E}_0(\vec{x},t) = -\nabla\varphi(\vec{x},t), \qquad \vec{E}_{\text{s}}(\vec{x},t) = -\partial_t\vec{A}(\vec{x},t), \qquad (2.6)$$

| Approximation | Validity range | Ampère's law |
|---|---|---|
| Full Maxwell | No restriction | $\nabla \times \vec{H} = \partial_t \vec{D} + \sigma \vec{E} + \vec{J_\mathrm{i}}$ |
| Quasi-stationary (Darwin) | $\Delta \ll \frac{v}{f}$ | $\nabla \times \vec{H} = \partial_t \vec{D}_0 + \sigma \vec{E} + \vec{J_\mathrm{i}}$ |
| Quasi-static | $\Delta \ll \frac{v}{f}$ and $\sigma \ll f\varepsilon$ | $\nabla \times \vec{H} = \partial_t \vec{D}_0 + \vec{J_\mathrm{i}}$ |
| Displacement-current-free (MQS) | $\Delta \ll \frac{v}{f}$ and $\sigma \gg f\varepsilon$ | $\nabla \times \vec{H} = \sigma \vec{E} + \vec{J_\mathrm{i}}$ |
| Eddy-current-free (EQS) | $\Delta \ll \frac{v}{f}$ and $\Delta \ll \delta$ | $\nabla \times \vec{H} = \partial_t \vec{D}_0 + \sigma \vec{E}_0 + \vec{J_\mathrm{i}}$ |

Table 2.1: Overview of the most popular cases of low frequency approximations compared to the full Maxwell case. The required condition and the corresponding form of Ampère's law are given for each case.

where the *electric scalar potential* $\varphi$ and the *magnetic vector potential* $\vec{A}$ are introduced. Being able to write $\vec{E}_0$ in terms of a scalar potential results from the Poincaré lemma [31] together with the choice of the Coulomb gauge $\nabla \cdot \vec{A} = 0$. We realize at this point that the formulation of any quasi-stationary approximation requires a choice of the gauging while the formulation of Maxwell's equations is gauge independent. The most general quasi-stationary approximation consists of neglecting the solenoidal part of the electric displacement current $\vec{D}_\mathrm{s}$ in Ampère's law by assuming $\|\partial_t \vec{D}_\mathrm{s}\| \ll \|\vec{J} + \partial_t \vec{D}_0\|$ [79]. We recall that we neglect convective currents and obtain the quasi-stationary form of Ampère's law given by

$$\nabla \times \vec{H}(\vec{x},t) = \partial_t \vec{D}_0(\vec{x},t) + \sigma(\vec{x})\vec{E}_0(\vec{x},t) + \sigma(\vec{x})\vec{E}_\mathrm{s}(\vec{x},t) + \vec{J_\mathrm{i}}(\vec{x},t). \tag{2.7}$$

Together with (2.1a), (2.1c), (2.1d), and (2.3), the relations (2.6) and (2.7) constitute what is also known as the Darwin model which is valid under the condition (2.4) [79, 137].

Starting from (2.6) and (2.7), many applications allow to specify additional approximations. The most popular cases are [79]

1. the quasi-static field for poor conductors $\sigma \ll f\varepsilon$ giving $\|\sigma \vec{E}_0\| \ll \|\partial_t \vec{D}_0\|$ and $\|\sigma \vec{E}_\mathrm{s}\| \ll \|\partial_t \vec{D}_\mathrm{s}\|$,

2. the displacement-current-free field for good conductors $\sigma \gg f\varepsilon$ giving $\|\partial_t \vec{D}_0\| \ll \|\sigma \vec{E}_0\|$, and

3. the eddy-current-free field valid if $\Delta \ll \delta$ giving $\|\sigma \vec{E}_\mathrm{s}\| \ll \|\partial_t \vec{D}_0 + \sigma \vec{E}_0 + \vec{J_\mathrm{i}}\|$,

where $\delta$ is the skin depth and the second case being the reverse of the first. In addition to the names given above, case 2 is commonly known as the magnetoquasistatic (MQS) approximation, and case 3 is known as the electroquasistatic (EQS) approximation. To summarize all considered low frequency approximations, Table 2.1 gives an overview including the required condition and the corresponding form of Ampère's law. Apart from the formal conditions listed in Table 2.1, a feeling of the appropriate approximation can also be gained from the limit case of zero operating frequency. In this case and under the assumption of perfect conductors and perfect insulators, any system behaves as a static system. If this limit case results in vanishing magnetic fields, the system is EQS; if this limit case results in vanishing electric fields, the system is MQS. Practical examples of EQS and MQS models can be found, e.g., in [109].

In this thesis, we are mainly concerned with applications from the field of micro- and nanoelectronics. For most electronic devices, inductive and wave propagation effects are negligible [79]. On the other hand, capacitive currents for instance in metal oxide semiconductor field effect transistors (MOSFETs) are very relevant. Thus, the displacement current cannot be ignored. This leaves us with the EQS approximation of

Maxwell's equations, see Table 2.1, which reads

$$\nabla \times \vec{E}(\vec{x}, t) = 0, \tag{2.8a}$$

$$\nabla \times \vec{H}(\vec{x}, t) = \partial_t \vec{D}(\vec{x}, t) + \sigma(\vec{x}) \vec{E}(\vec{x}, t) + \vec{J_i}(\vec{x}, t), \tag{2.8b}$$

$$\nabla \cdot \vec{D}(\vec{x}, t) = \varrho(\vec{x}, t), \tag{2.8c}$$

$$\nabla \cdot \vec{B}(\vec{x}, t) = 0, \tag{2.8d}$$

using differential operators instead of the integral form. Note that, by abuse of notation, we denote the irrotational fields $\vec{D}_0$ and $\vec{E}_0$ in the EQS case simply by $\vec{D}$ and $\vec{E}$. Applying the divergence operator to (2.8b), using the constitutive laws (2.3), and the electric scalar potential as introduced in (2.6), we obtain the governing equation of EQS given by

$$\nabla \cdot (\varepsilon(\vec{x}) \nabla \dot{\varphi}(\vec{x}, t)) + \nabla \cdot (\sigma(\vec{x}) \nabla \varphi(\vec{x}, t)) = \nabla \cdot \vec{J_i}(\vec{x}, t), \tag{2.9}$$

where $\dot{\varphi}$ denotes the time derivative of $\varphi$. Throughout this thesis, we use three equivalent notations for a time derivative: $\frac{\partial}{\partial t}$, $\partial_t$, and the above dot notation. For most practical problems, a closed form solution to (2.9) is not available and a numerical discretization scheme becomes necessary. One possible choice is the finite integration technique (FIT) for which Section 3.3 provides all the required details.

The stationary limit of the EQS case is of particular importance in this thesis and is referred to as the electrokinetic problem. In addition to the assumptions as required for the EQS approximation, the stationary case is established by allowing only constant charge transport. Thus, Ampère's law simplifies to

$$\nabla \times \vec{H}(\vec{x}, t) = \sigma(\vec{x}) \vec{E}(\vec{x}, t) + \vec{J_i}(\vec{x}, t),$$

and (2.9) becomes

$$\nabla \cdot (\sigma(\vec{x}) \nabla \varphi(\vec{x}, t)) = \nabla \cdot \vec{J_i}(\vec{x}, t), \tag{2.10}$$

and we refer to (2.10) as the governing equation of electrokinetics. Its left-hand side can be decomposed into balance, constitutive, and kinematic part given by [152]

$$\nabla \cdot \vec{J_c}(\vec{x}, t) = 0, \qquad \vec{J_c}(\vec{x}, t) = \sigma(\vec{x}) \vec{E}(\vec{x}, t), \qquad \vec{E}(\vec{x}, t) = -\nabla \varphi(\vec{x}, t), \tag{2.11}$$

respectively, which becomes important when considering the approximative properties of spatial discretization schemes as discussed in Chapter 3.

## 2.3 Principles of Heat Transport

Any EM problem with at least a partly conducting domain raises *Joule losses* resulting in the generation of heat. Let us here recall the fundamental principles of heat transfer [20, 142]. In general, the term heat describes the energy that is stored within a domain or transported across the boundaries of a domain. Greater amounts of heat yield a higher temperature. Typically, the direction of heat transfer is determined by temperature gradients and is always oriented towards decreasing temperatures.

There are three dominating heat transfer principles: *conduction*, *convection*, and *radiation*. First, conduction is driven by the interaction of neighboring molecules that possess a certain kinetic energy according to the temperature of the molecules. While there is no molecular motion at zero temperature, temperatures greater than zero lead to a random motion yielding collisions of neighboring molecules. Due to these collisions, the

kinetic energy is transferred from one molecule to another. Thus, conduction is based on interactions on a molecular scale without any macroscopic motion involved. Secondly, convection is based on the physical mass transport mostly due to the heating of gases or liquids. It is classified into forced convection that causes motion of a fluid by outer forces; and natural convection, which is driven by a spatially nonuniform distribution of density. The latter can be due to an inhomogeneous temperature distribution or due to a nonuniform concentration of a fluid mixture. In this thesis, we focus only on natural convection caused by an inhomogeneous temperature distribution. In a gravitational field, due to buoyancy effects, this results in an upward motion of heated fluids and a downward motion of cooled fluids. Apart from conductive and convective effects, every body emits radiation in form of EM waves. Since waves also propagate in vacuum, see Section 2.1, radiative heat transfer does not require any transport medium.

Let us now introduce the mathematical description of heat transfer. We do not delve into molecular processes; instead, we use the macroscopic model of the heat equation. First, with the *temperature $T$*, we define the *thermal power density* as

$$Q_{\rho c}(\vec{x}, t) := \rho(\vec{x}) c(\vec{x}) \dot{T}(\vec{x}, t),$$

where the *volumetric mass density $\rho$* and the *specific heat capacity $c$* make up the *volumetric heat capacity $\rho c$*. The constitutive Fourier's law defines the *heat flux* as

$$\vec{q}(\vec{x}, t) := -\lambda(\vec{x}) \nabla T(\vec{x}, t), \tag{2.12}$$

where $\lambda$ is the thermal conductivity, which is highest for solid bodies, followed by liquids, and gases. Values of $\rho$, $c$, and $\lambda$ for certain materials are listed in, e.g., [234]. With these definitions, we can write the transient heat equation in integral form as

$$\int_V \left[ \rho(\vec{x}) c(\vec{x}) \dot{T}(\vec{x}, t) - Q_{\mathrm{i}}(\vec{x}, t) \right] \mathrm{d}V = \int_{\partial V} [\lambda(\vec{x}) \nabla T(\vec{x}, t) - \vec{q}_{\mathrm{i}}(\vec{x}, t)] \cdot \mathrm{d}\vec{S}, \tag{2.13}$$

where $Q_{\mathrm{i}}$ and $\vec{q}_{\mathrm{i}}$ represent any *impressed* volumetric thermal flow and thermal flux density, respectively. In this thesis, we neglect impressed thermal fluxes and treat impressed volumetric thermal sources to result exclusively from Joule losses given by

$$Q_{\mathrm{i}}(\vec{x}, t) = Q_{\mathrm{J}}(\sigma(\vec{x}, t), \varphi(\vec{x}, t)) = \sigma(\vec{x})(\nabla \varphi(\vec{x}, t) \cdot \nabla \varphi(\vec{x}, t)). \tag{2.14}$$

In general, when thermal effects are considered, all constitutive parameters become a function of the temperature. However, for most problems considered in this thesis, the temperature dependence of the electric conductivity is dominant and we neglect the dependence of all other constitutive parameters.

## 2.4 Coupled Electrothermal Problem

With the Joule losses as defined by (2.14), heat is generated by EM problems whenever conducting materials are involved. Then, the electric conductivity $\sigma$ becomes a function of the temperature and a link between (2.1) and the transient heat equation (2.13) is established. In this thesis, as described in Section 2.2, we focus on the EQS case and consider the ET coupling of (2.9) and (2.13) given by

$$\nabla \cdot (\varepsilon(\vec{x}) \nabla \dot{\varphi}(\vec{x}, t, T)) + \nabla \cdot (\sigma(\vec{x}, T) \nabla \varphi(\vec{x}, t, T)) = \nabla \cdot \vec{J}_{\mathrm{i}}(\vec{x}, t), \tag{2.15a}$$

$$-\rho(\vec{x}) c(\vec{x}) \dot{T}(\vec{x}, t) + \nabla \cdot (\lambda(\vec{x}) T(\vec{x}, t)) = \nabla \cdot \vec{q}_{\mathrm{i}}(\vec{x}, t) - Q_{\mathrm{J}}(\sigma, \varphi), \tag{2.15b}$$

where $\sigma$ and $\varphi$ are now functions of the temperature $T$.
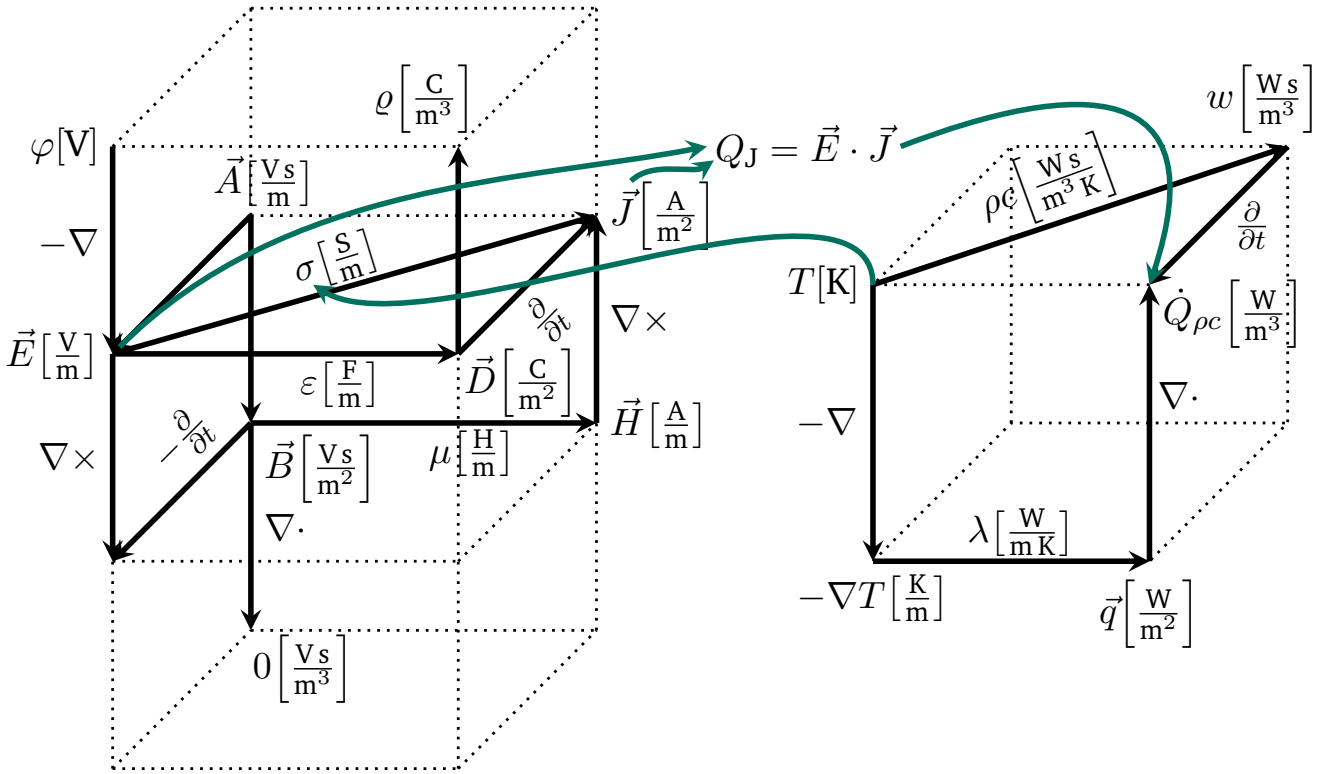
Figure 2.2: Maxwell and thermal houses linked by the Joule losses and the temperature-dependent electric conductivity to form the ET house inspired by [77, 224]. The diagonal links represent the time derivative, the vertical links represent differential operators, and the horizontal links represent the constitutive laws.

Considering the coupled ET problem given by (2.15), Figure 2.2 shows its illustration based on the Tonti diagrams [77, 224]. We refer to this illustration as the continuous ET house which shows all quantities involved in (2.15) and their individual relations. The figure consists of two parts showing the Maxwell house on the left-hand side and the thermal house on the right-hand side. Each part comprises diagonal, vertical, and horizontal links. The diagonal links represent the time derivative, the vertical links represent the differential operators, and the horizontal links represent the constitutive laws. From a differential form perspective, see Section 2.8, the vertical links correspond to applying the exterior derivative and the horizontal links correspond to applying the Hodge operator. Thus, the quantities on the left of each diagram represent straight forms, while the quantities on the right represent twisted forms. The ET coupling given by (2.15) links the two houses by the Joule losses $Q_J$ and the temperature-dependent electric conductivity $\sigma$. In contrast to other illustrations of the thermal part [3, 91], we choose the negative temperature gradient as the primal 1-form in analogy to the definition of the electric 1-form.

## 2.5 Initial and Boundary Conditions

Due to the finite computational capabilities of a computer, any computational domain must be truncated, giving rise to the requirement of initial conditions and BCs. The specification of initial conditions requires to impress a valid field distribution at $t = t_0$ that complies with the specified BCs. Since the subprob-

|                  | Homogeneous Dirichlet | Homogeneous Neumann |
| ---------------- | --------------------- | ------------------- |
| EM field         | $\vec{n}_\mathcal{D} \times \vec{E} = 0$ | $\vec{n}_\mathcal{D} \times \vec{H} = 0$ |
| Electric current | $\vec{n}_\mathcal{D} \cdot \vec{J} \neq 0$ | $\vec{n}_\mathcal{D} \cdot \vec{J} = 0$ |
| Magnetic flux    | $\vec{n}_\mathcal{D} \cdot \vec{B} = 0$ | $\vec{n}_\mathcal{D} \cdot \vec{B} \neq 0$ |

Table 2.2: Homogeneous Dirichlet and Neumann BCs for the scalar potential formulation given by (2.15a) and their implications on the tangential and normal components of the EM field. The vector $\vec{n}_\mathcal{D}$ is the outer unit normal of $\mathcal{D}$. In EMs, Dirichlet and Neumann BCs are also termed *electric* and *magnetic* BCs, respectively.

lems (2.15a) and (2.15b) can be treated separately, we discuss the BCs for both subproblems one after another.

For the electric subproblem, setting the tangential electric field at the boundary $\Gamma$ to zero is known as an electric BC and is equivalent to a wall for the magnetic flux. Due to $\vec{E} = -\nabla\varphi$, a prescribed electric potential on the boundary corresponds to electric BCs as well. On the other hand, setting the tangential magnetic field at the boundary $\Gamma$ to zero is known as a magnetic BC and is equivalent to a wall for the electric current. For the electric potential formulation as used in (2.15a), the electric and magnetic cases correspond mathematically to Dirichlet and Neumann conditions, respectively. They read

$$\varphi(\vec{x}, t) = \varphi_{\mathrm{Dir}}(\vec{x}, t), \qquad \vec{x} \in \Gamma_\sigma^{\mathrm{Dir}}, \quad t \in I,$$
$$-\vec{n}_\mathcal{D} \cdot (\sigma(\vec{x}) \nabla \varphi(\vec{x}, t)) = \vec{J}_{\mathrm{Neu}}(\vec{x}, t), \qquad \vec{x} \in \Gamma_\sigma^{\mathrm{Neu}}, \quad t \in I,$$

where $\vec{n}_\mathcal{D}$ is the outer unit normal of $\mathcal{D}$, $\Gamma_\sigma^{\mathrm{Dir}}$ is the electric Dirichlet part of the boundary, and $\Gamma_\sigma^{\mathrm{Neu}}$ is the electric Neumann part of the boundary, see Figure 2.1. Additionally, $\varphi_{\mathrm{Dir}}$ describes a prescribed electric potential, and $\vec{J}_{\mathrm{Neu}}$ is a prescribed electric current through the boundary. Table 2.2 shows a summary of the BCs discussed here.

For the thermal subproblem, the BCs are classified into first, second, and third kind, also termed Dirichlet, Neumann, and Robin type, respectively [142]. Dirichlet conditions prescribe temperature values on the boundary, Neumann conditions prescribe the thermal flux through the boundary, and Robin conditions describe a temperature-dependent flux passing through the boundary. Dirichlet and Neumann conditions are expressed as

$$T(\vec{x}, t) = T_{\mathrm{Dir}}(\vec{x}, t), \qquad \vec{x} \in \Gamma_\lambda^{\mathrm{Dir}}, \quad t \in I,$$
$$-\vec{n}_\mathcal{D} \cdot (\lambda(\vec{x}) \nabla T(\vec{x}, t)) = \vec{q}_{\mathrm{Neu}}(\vec{x}, t), \qquad \vec{x} \in \Gamma_\lambda^{\mathrm{Neu}}, \quad t \in I,$$

where $\Gamma_\lambda^{\mathrm{Dir}}$ is the thermal Dirichlet part of the boundary, and $\Gamma_\lambda^{\mathrm{Neu}}$ is the thermal Neumann part of the boundary, see Figure 2.1. Additionally, $T_{\mathrm{Dir}}$ describes a prescribed boundary temperature, and $\vec{q}_{\mathrm{Neu}}$ is a prescribed heat flux through the boundary. Convective and radiative boundaries are both described by Robin conditions, which read

$$-\vec{n}_\mathcal{D} \cdot (\lambda(\vec{x}) \nabla T(\vec{x}, t)) = r(T(\vec{x}, t)) - r(T_\infty), \qquad \vec{x} \in \Gamma^{\mathrm{Rob}}, \quad t \in I,$$

where $r(T) = h_{\mathrm{cv}} T + \varepsilon_{\mathrm{R}} \sigma_{\mathrm{R}} T^4$ for combined convective and radiative BCs. Here, $h_{\mathrm{cv}}$ is the *heat transfer coefficient* which typically depends on the fluid properties, the properties of the convection process, and the geometrical configuration. Furthermore, $\sigma_{\mathrm{R}}$ is the *radiation coefficient* or *Stefan-Boltzmann constant*, and $\varepsilon_{\mathrm{R}}$

is the emissivity. The amount of radiative emission depends on the body's surface temperature, with the maximum reached by ideal black bodies, thus termed black body radiation. For any real body, its radiation is correctly described by introducing the emissivity $\varepsilon_R \in [0, 1]$, which models the deviation of the real body from a black body. Typical values for $\varepsilon_R$ are found in [234].

## 2.6 Circuit Theory and Modified Nodal Analysis

Nowadays, the majority of electronic designs is based on circuit simulation. This became possible thanks to the introduction of standard tools such as ORCAD PSPICE [173], XYCE [128], and CADENCE SPECTRE [44] that revolutionized the electronics industry. Most modern circuit simulators are based on the *modified nodal analysis (MNA)* [104, 117], which is an extension of the standard nodal analysis. In addition to the standard nodal analysis, the MNA simplifies the processing of voltage sources and current-dependent circuit elements in an efficient manner. In this section, we follow [47] and briefly review some fundamentals of circuit theory and the MNA. Kirchhoff's current and voltage laws are derived and form the basics for circuit analysis.

Any circuit can be understood as a directed graph consisting of interconnected nodes and branches. Let $v_i$ be one of the $N_n$ nodal potentials in a circuit and $b_n$ one of $N_b$ directed branches. With the incidence matrix $\mathbf{A} \in \{-1, 0, 1\}^{N_n \times N_b}$ linking nodes and branches, the voltage-potential relation is given by

$$\mathbf{V} = \mathbf{A}^\top \mathbf{v}.$$

The entries of $\mathbf{A}$ are given by

$$a_{in} := \begin{cases} 1, & \text{if the branch } b_n \text{ is directed away from node } n_i, \\ -1, & \text{if the branch } b_n \text{ is directed towards node } n_i, \\ 0, & \text{if the node } n_i \text{ is neither starting nor ending point of } b_n. \end{cases}$$

With this definition, the exemplary voltage $V_n$ on the branch $b_n$ directed from $n_i$ to $n_j$ reads $V_n = v_i - v_j$.

For time invariant geometries, the current continuity equation reads

$$\int_{\partial V} \vec{J} \cdot \mathrm{d}\vec{S} + \int_V \dot{\varrho} \, \mathrm{d}V = 0, \tag{2.16}$$

for an arbitrary volume $V$. By considering a volume $\widetilde{V}_i$ around an arbitrary circuit node $n_i$ and assuming that capacitive charges are located either fully inside or outside of $\widetilde{V}_i$, the total charge and also the charge's change rate in $\widetilde{V}_i$ is zero. Therefore, (2.16) becomes

$$\int_{\partial \widetilde{V}_i} \vec{J} \cdot \mathrm{d}\vec{S} = 0.$$

If $\partial \widetilde{V}_i$ is composed by a finite number $s$ of conductors with cross-sectional areas $\widetilde{A}_n$, Kirchhoff's current law (KCL) is obtained as

$$\sum_{n=1}^{s} I_n = \sum_{n=1}^{s} \int_{\widetilde{A}_n} \vec{J} \cdot \mathrm{d}\vec{S} = 0, \tag{2.17}$$

Figure 2.3: KCL example for (a) a single node and (b) multiple nodes. The net current flow into a node must be zero. These figures are taken from [47].

where $I_n$ is the total current through the facet $\widetilde{A}_n$, see Figure 2.3a. To express (2.17) for all nodes in the circuit, see Figure 2.3b, the incidence matrix $\mathbf{A}$ can be used such that

$$\mathbf{AI} = \mathbf{0}, \tag{2.18}$$

where $\mathbf{I} \in \mathbb{R}^{N_b}$ is a vector of all currents allocated to the branches.

In a circuit, the basic branch elements are conductors, capacitors, inductors, as well as voltage and current sources. As these elements are allocated to branches, sets of $N_G$, $N_C$, $N_L$, $N_V$ and $N_I$ branches are defined, respectively. Hence, $\mathbf{A}$ can be arranged into a block matrix with sub-blocks for these elements [104], reading

$$\mathbf{A} = \begin{bmatrix} \mathbf{A}_G & \mathbf{A}_C & \mathbf{A}_L & \mathbf{A}_V & \mathbf{A}_I \end{bmatrix}.$$

An exemplary circuit consisting of a current source, two resistors and two capacitors together with the corresponding block structure of $\mathbf{A}$ is shown in Figure 2.4. A similar subdivision is done for the current and voltage vectors, giving

$$\mathbf{I}^\top = \begin{bmatrix} \mathbf{I}_G^\top & \mathbf{I}_C^\top & \mathbf{I}_L^\top & \mathbf{I}_V^\top & \mathbf{I}_I^\top \end{bmatrix},$$
$$\mathbf{V}^\top = \begin{bmatrix} \mathbf{V}_G^\top & \mathbf{V}_C^\top & \mathbf{V}_L^\top & \mathbf{V}_V^\top & \mathbf{V}_I^\top \end{bmatrix}.$$

With these definitions, the branch voltages read

$$\mathbf{V}_G = \mathbf{A}_G^\top \mathbf{v}, \qquad \mathbf{V}_C = \mathbf{A}_C^\top \mathbf{v}, \qquad \mathbf{V}_L = \mathbf{A}_L^\top \mathbf{v}, \tag{2.19a}$$
$$\mathbf{V}_V = \mathbf{A}_V^\top \mathbf{v}, \qquad \mathbf{V}_I = \mathbf{A}_I^\top \mathbf{v}, \tag{2.19b}$$

and (2.18) becomes

$$\mathbf{A}_G \mathbf{I}_G + \mathbf{A}_C \mathbf{I}_C + \mathbf{A}_L \mathbf{I}_L + \mathbf{A}_V \mathbf{I}_V + \mathbf{A}_I \mathbf{I}_I = \mathbf{0}. \tag{2.20}$$

The relation between voltages and currents for the different branches is established by constitutive diagonal matrices that contain the element-wise material parameters. These are the conductance, capacitance, and inductance matrices $\mathbf{G}$, $\mathbf{C}$, and $\mathbf{L}$, respectively. Expressing the corresponding source branches by means of the source voltages $\mathbf{V}_s$ and source currents $\mathbf{I}_s$, this relation becomes

$$\mathbf{I}_G = \mathbf{G}\mathbf{V}_G, \qquad \mathbf{I}_C = \mathbf{C}\dot{\mathbf{V}}_C, \qquad \mathbf{I}_L = \mathbf{L}^{-1} \int \mathbf{V}_L \, \mathrm{d}t, \tag{2.21a}$$

$$\mathbf{V}_V = \mathbf{V}_s, \qquad \mathbf{I}_I = \mathbf{I}_s. \tag{2.21b}$$
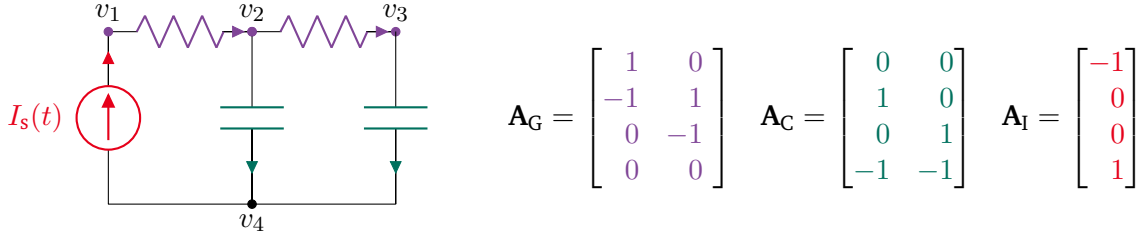
Figure 2.4: Circuit example and its branch matrices. This figure is taken from [47].

Combining (2.19), (2.20), and (2.21), we obtain the MNA formulation

$$\mathbf{A}_C \mathbf{C} \mathbf{A}_C^\top \dot{\mathbf{v}} + \mathbf{A}_G \mathbf{G} \mathbf{A}_G^\top \mathbf{v} + \mathbf{A}_L \mathbf{I}_L = -\mathbf{A}_I \mathbf{I}_s - \mathbf{A}_V \mathbf{I}_V, \tag{2.22a}$$

$$\mathbf{L} \dot{\mathbf{I}}_L = \mathbf{A}_L^\top \mathbf{v}, \tag{2.22b}$$

$$\mathbf{A}_V^\top \mathbf{v} = \mathbf{V}_s. \tag{2.22c}$$

Note that in contrast to the standard MNA theory, (2.22) still requires regularization, typically done by the introduction of a reference node, typically called the *ground* node. Furthermore, solving (2.22) requires a time stepping scheme, see Section 3.4 for a general overview. For time stepping schemes as specifically used in circuit simulation, see, e.g., [190]. In practice, most circuit simulators use the trapezoidal rule or backward differentiation formula (BDF) schemes, which both are multi-step methods. If largely different time scales are involved, multi-rate methods enable an efficient circuit simulation as reported on for instance in [103, 176, 183].

## 2.7 Distributed Current Sources

EM sources are often concentrated in a very small region. This allows point and line sources to be reasonable models for small circular electrodes or for thin wires, respectively. With *thin* we refer to any wire with a radius that is much smaller than the diameter of the domain, a condition stated by $\bar{r} \ll \Delta$.

We now follow [109, Chapter 7] to define distributed current sources. The notion of *distributions* originates from the book by Schwartz entitled "Theory of Distributions" [200]. In the electrokinetic problem (2.10), the right-hand side can also be expressed by a *volume distribution of current sources* denoted by $s$ with units A/m$^3$ such that

$$\nabla \cdot (\sigma \nabla \varphi) = \nabla \cdot \vec{J}_i = -s, \tag{2.23}$$

which is understood in a weak sense. This distribution $s$ allows to formally introduce *point*, *line*, and *surface current sources* given by

$$I_p := \lim_{\substack{s \to \infty \\ |V| \to 0}} \int_V s \, \mathrm{d}V, \qquad K_1 := \lim_{\substack{s \to \infty \\ |S| \to 0}} \int_S s \, \mathrm{d}S, \qquad J_s := \lim_{\substack{s \to \infty \\ |L| \to 0}} \int_L s \, \mathrm{d}L,$$

respectively. Here, $V$ denotes an arbitrary volume, $S$ denotes an arbitrary facet, and $L$ denotes an arbitrary edge. Based on [109], Figure 2.5 shows an illustration of these three types of distributed current sources.
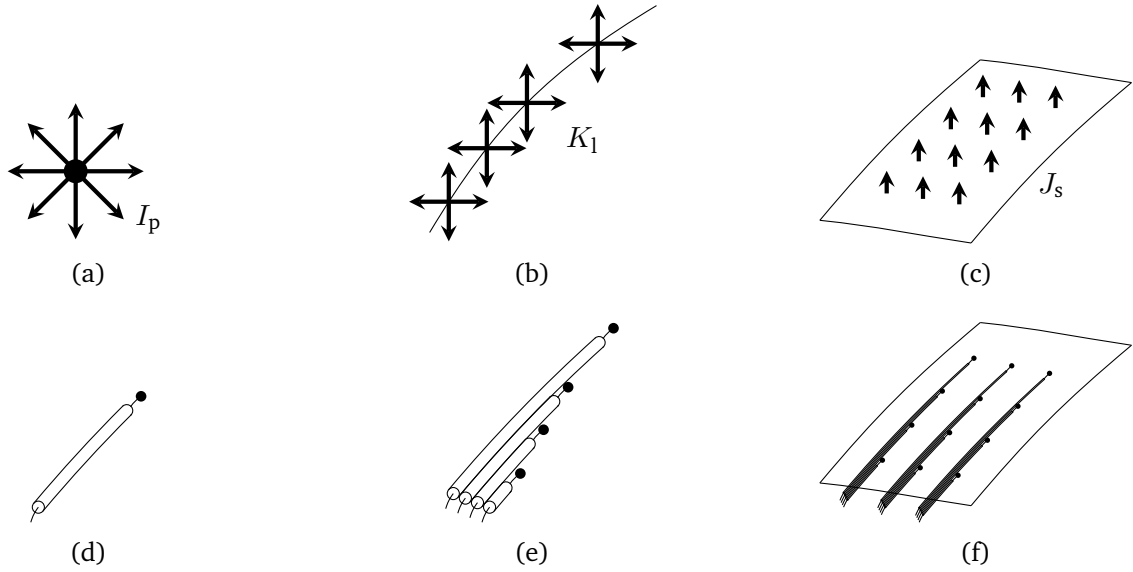
Figure 2.5: Distributed current sources for (a) a point current source $I_p$, (b) a line current source $K_l$, and (c) a surface current source $J_s$. In (d), (e), and (f), possible physical realizations using insulated wire feeds are shown for the three cases. This figure is based on [109].

Physical realizations of such current sources can be implemented by using insulated wire feeds as shown in the lower part of Figure 2.5. Using these definitions, (2.23) in integral form reads

$$\int_{\partial V} \sigma \nabla \varphi \cdot \mathrm{d}\vec{S} = -I_p, \qquad \int_{\partial V} \sigma \nabla \varphi \cdot \mathrm{d}\vec{S} = -\int_{L_K} K_l \, \mathrm{d}L, \qquad \int_{\partial V} \sigma \nabla \varphi \cdot \mathrm{d}\vec{S} = -\int_{S_J} J_s \, \mathrm{d}S, \qquad (2.24)$$

for a point, line, and surface current source, respectively. Here, $L_K$ refers to the line on which $K_l$ is defined, and $S_J$ denotes the surface on which $J_s$ is defined. For a homogeneous domain $\mathcal{D}$ filled with a material of conductivity $\sigma$, the solution to the point and line current case of (2.24) is obtained by evaluating concentric integrals around the corresponding source. Then, the electric potential and the field are obtained in spherical coordinates with the radial distance $r$ and the unit vector $\vec{e}_r$ as

$$\varphi = \frac{I_p}{4\pi\sigma}\frac{1}{r} + C, \qquad\qquad \vec{E} = \frac{I_p}{4\pi\sigma}\frac{1}{r^2}\vec{e}_r,$$

for the point current case and with an arbitrary constant $C \in \mathbb{R}$. Similarly, for line current sources using cylindrical coordinates with the radial distance $r$, we obtain

$$\varphi = -\frac{I_l}{2\pi\sigma}\ln\left(\frac{r}{r_0}\right), \qquad\qquad \vec{E} = \frac{I_l}{2\pi\sigma}\frac{1}{r}\vec{e}_r,$$

for an arbitrary reference radius $r_0 > 0$ and $I_l := \int_{L_K} K_l \, \mathrm{d}L$.

## 2.8 Introduction to Differential Forms and de Rham Currents

Although the vector field representation in (2.1) is the most commonly known version of Maxwell's equations, more general descriptions exist. In particular, vector analysis notations require a notion of metric and a screw-sense of the underlying coordinate system. A more general concept originates from the mathematical field

of *differential geometry* and is known as the concept of *differential forms* [41, 89, 123], which are defined as fields of multilinear mappings from $\mathbb{R}^p$ to $\mathbb{R}$, where $p$ is the *degree* of the form [31]. Differential forms are defined on *manifolds*, which can be seen as a generalization of the Euclidean space $\mathbb{R}^3$. Differential forms are expressions on which integrals operate [77]. The great benefit of their usage is the elimination of any metrical notion from Maxwell's equations yielding a unified formalism for the concepts of electromagnetism. However, a metric enters once constitutional relations are considered, requiring the introduction of the Hodge operator, see below. Apart from electromagnetism, differential forms are also used in disciplines like classical mechanics, optics, and quantum mechanics.

In general, let us refer to a differential form of degree $p$ concisely as $p$-form and denote the space of $p$-forms on the domain $\mathcal{D}$ by $\mathscr{D}^p(\mathcal{D})$. The familiar concept of gradient, curl and divergence generalizes in the framework of differential forms to the concept of the *exterior derivative* or *exterior differential* d. Thus, the well-known vector identities $\nabla \times (\nabla \psi) \equiv 0$ and $\nabla \cdot (\nabla \times \vec{F}) \equiv 0$ generalize to $d(d\omega) \equiv 0$ for any scalar field $\psi$, any vector field $\vec{F}$, and any differential form $\omega$. Defining operations on differential forms introduces the field of *exterior calculus*. Apart from the degree, differential forms classify into *straight* and *twisted* forms. In the literature, straight forms are often referred to as even or ordinary forms while twisted forms may be referred to as odd or impair forms. The connection between straight and twisted forms is introduced by the *Hodge operator* denoted by $\star$ that maps straight $p$-forms into twisted $q$-forms, where $q := (n - p)$, and $n$ is the dimension of the domain $\mathcal{D}$. These connections are also illustrated in Figure 2.2, which was introduced in Section 2.4.

Let us now apply the concept of differential forms to EMs and the transient heat equation in 3D space. We follow [30, 41, 77] to write down Maxwell's equations using differential forms, giving

$$\mathrm{d}e = -\partial_t b, \tag{2.25a}$$

$$\mathrm{d}\tilde{h} = \partial_t \tilde{d} + \tilde{j}, \tag{2.25b}$$

$$\mathrm{d}\tilde{d} = \tilde{\varrho}, \tag{2.25c}$$

$$\mathrm{d}b = 0, \tag{2.25d}$$

with the straight 1-form $e$ representing the electric field and the straight 2-form $b$ representing the magnetic flux density. Furthermore, $\tilde{h}$ is a twisted 1-form representing the magnetic field, $\tilde{d}$ is a twisted 2-form representing the electric flux density, $\tilde{j}$ is a twisted 2-form representing the electric current density and $\tilde{\varrho}$ is a twisted 3-form representing the electric charge density. We recall that this form of Maxwell's equations does not require any metric at all. The transient heat equation using differential forms reads

$$\partial_t \tilde{Q} = \mathrm{d}\tilde{q} + \tilde{Q}_{\mathrm{s}},$$

with the twisted 2-form $\tilde{q}$ representing the heat flux density and the twisted 3-form $\tilde{Q}$ and $\tilde{Q}_{\mathrm{s}}$ describing the thermal power density and the thermal source term, respectively. The Hodge operator establishes the link between straight and twisted forms and thus links (2.25a)–(2.25d) by introducing the constitutive laws

$$b = \star_\mu \tilde{h}, \qquad \tilde{d} = \star_\varepsilon e, \qquad \tilde{j} = \star_\sigma e, \qquad \tilde{q} = \star_\lambda t,$$

with the straight 1-form $t = -\mathrm{d}T$, where $T$ is a straight 0-form representing the temperature. At last, let us introduce a notion of energy and power in this framework. Energy and power quantities are represented by twisted forms and result from the *wedge product* or *exterior product* of a straight form with a twisted form. For instance, the power density of a field is described by a twisted form given by the wedge product $e \wedge \tilde{j}$ [27]. Table 2.3 gives an overview of physical quantities in the framework of differential forms. Some of

| | Straight forms | Twisted forms |
|---|---|---|
| 0-forms | temperature, electric scalar potential | – |
| 1-forms | thermal tension, electric field, magnetic vector potential | magnetic field |
| 2-forms | magnetic flux density | thermal heat flux, electric flux density, electric current density |
| 3-forms | – | power density, charge density |

Table 2.3: Straight and twisted differential forms and examples of physical quantities.

these quantities have already been introduced here, others are mentioned additionally, and this list does not claim to be complete.

We further introduce continuous de Rham currents that represent distributions on differential forms and thus, a generalization to differential forms and chains [75]. Originally, the term *current* was motivated by the nature of a current being 1D in 3D space. In EMs, de Rham currents are important to appropriately represent singular sources, such as line and surface currents as well as point and surface charges. In this thesis, this framework is important for the inclusion of line currents arising from thin wires. A $q$-current maps from $n-q$-forms with compact support in $\mathcal{D}$ to real numbers and is independent of any metric. We largely avoid the formalism of exterior calculus and instead, identify differential forms with their vector proxies. In particular, we can identify $\mathscr{D}^0(\mathcal{D})$ with $C_0^\infty(\mathcal{D})$ and $\mathscr{D}^1(\mathcal{D})$ with $(C_0^\infty(\mathcal{D}))^3$.

Quantities such as energy or power densities are represented by 0-currents, see [229]. More precisely, using a test function $v$, a power density $Q$ gives rise to a 0-current

$$\mathcal{Q}(v) := \int_{\mathcal{D}} Q v \, \mathrm{d}V, \quad v \in C_0^\infty(\mathcal{D}). \tag{2.26}$$

On the other hand, physical currents such as the electric current density and the thermal heat flux as well as surface and line currents give rise to 1-currents. For convenience, we use $\vec{J}_\alpha$ with $\alpha \in \{\varepsilon, \sigma, \lambda\}$ to have at hand a general notation for the electric displacement current $\partial_t \vec{D}$, the electric conductive current $\vec{J}_c$, and the thermal heat flux $\vec{q}$, respectively. Using this notation, $\vec{J}_\alpha$ gives rise to a 1-current

$$\mathcal{J}_\alpha(\vec{v}) := \int_{\mathcal{D}} \vec{J}_\alpha \cdot \vec{v} \, \mathrm{d}V, \quad \vec{v} \in (C_0^\infty(\mathcal{D}))^3.$$

Now, we illustrate how (2.15) can be reformulated in the setting of de Rham currents. We start with the electrokinetic part given by (2.10), neglect any impressed field, multiply (2.10) with the test function $v \in C_0^\infty(\mathcal{D})$, integrate over $\mathcal{D}$, and integrate by parts such that

$$\int_{\mathcal{D}} \nabla \cdot \vec{J}_\sigma v \, \mathrm{d}V = - \int_{\mathcal{D}} \vec{J}_\sigma \cdot \nabla v \, \mathrm{d}V = \boldsymbol{div} \mathcal{J}_\sigma(v) = 0, \tag{2.27}$$

in the sense of distributions, where the electric current reads $\vec{J}_\sigma := -\sigma \nabla \varphi$. Here, we used the general relation [8]

$$\boldsymbol{div} \mathcal{K}(v) = -\mathcal{K}(\nabla v), \quad \forall v \in C_0^\infty(\mathcal{D}), \tag{2.28}$$

for any 1-current $\mathcal{K}$. Similarly, (2.27) holds also for $\vec{J}_\alpha$, representing additionally the displacement current and the thermal heat flux. Moreover, by the definition of (2.26), the de Rham 0-currents associated to $\rho c \dot{T}$ and $Q_J$ are given by

$$\mathcal{Q}_{\rho c}(v) = \int_{\mathcal{D}} \rho c \dot{T} v \, \mathrm{d}V, \qquad\qquad \mathcal{Q}_{J}(v) = \int_{\mathcal{D}} Q_J v \, \mathrm{d}V,$$

for all $v \in C_0^\infty(\mathcal{D})$, respectively. Hence, the de Rham current reformulation of (2.15) without impressed fields reads

$$\boldsymbol{div}(\mathcal{J}_\varepsilon + \mathcal{J}_\sigma)(v) = 0, \tag{2.29}$$
$$\mathcal{Q}_{\rho c}(v) + \boldsymbol{div}\mathcal{J}_\lambda(v) = \mathcal{Q}_{J}(v), \tag{2.30}$$

for all $v \in C_0^\infty(\mathcal{D})$. Using this formulation, we will see in Section 3.3 that the concept of de Rham currents is a mathematical tool that aids the construction of a discrete representation of a field description [216].

## 2.9 Summary

For the simulation of an engineering problem, the first step consists of finding a suitable model. Starting from Maxwell's equations, we realized that a low frequency formulation is sufficient for the electric description of the relevant applications in this thesis. Due to the increasing necessity of thermal analysis in the design of electronic devices, we discussed the fundamental principles of heat transport to arrive at the coupled electrothermal (ET) formulation as the governing model in this thesis. Since we are also interested in circuit simulation, we recalled the generally applied method for circuit simulation, known as the modified nodal analysis (MNA). To prepare for the thin wire model to be presented in Chapter 5, we closed this chapter by the discussion of distributed current sources and we gave an introduction to differential forms and de Rham currents.

# 3  Discretization

Most relevant problems exhibit complex geometries or nonlinearities such that closed form solutions of the underlying partial differential equations (PDEs) are not available. This motivates the need for numerical techniques to obtain an approximate solution. During the last century, several techniques have been developed. The most prominent examples include finite elements, finite volumes, finite differences, finite integration, cell method, boundary element method, isogeometric methods, and hybrid methods, where the latter uses a combination of at least two other methods. Any of these methods allows to solve PDEs up to a certain error. In the best case, this error is known or at least can be estimated. To increase the accuracy of any method, the most common approaches are $h$- and $p$-refinement, referring to a refinement of the spatial mesh and to an increase of the approximation order, respectively. Other approaches include, e.g., defect correction, which is used to estimate a part of the numerical error and subtract it from the obtained solution [24]. Over the years, several commercial tools established themselves on the market. Some examples for electromagnetic (EM) field simulation include CST DESIGN STUDIO [67], ANSYS HFSS [4], and EMPRO [130]. Well-known circuit simulation tools are for instance ORCAD PSPICE [173], XYCE [128], and CADENCE SPECTRE [44].

The purpose of this chapter is the introduction of the numerical techniques that are used throughout this thesis. We start very generically with some useful concepts from algebraic topology in Section 3.1 and the definitions of chains, cochains, and discrete de Rham currents in Section 3.2. Section 3.3 describes the finite integration technique (FIT), which is the principal spatial discretization technique used in this thesis and fits elegantly in the framework of differential forms [28]. Therein, we introduce the topological notions and the material approximation that constitute the Maxwell grid equations (MGEs). Furthermore, we discuss the discrete Joule losses, the inclusion of boundary conditions (BCs), notions about the computational grid and a graded grid in particular, and distinguish FIT from other schemes. Section 3.4 explains the idea of time integration by referencing some known schemes and by applying a particular choice to the problem at hand. Methods to solve the underlying linear system of equations are discussed in Section 3.5. Finally, to quantify the accuracy of a scheme, precise error definitions are required and given in Section 3.6.

## 3.1  Some Useful Concepts from Algebraic Topology

In this section, let us recall a few concepts from algebraic topology. Following Tonti [221, 223, 224], we introduce the notions of global variables, cell complexes, and orientation. Covering these topics enhances the understanding of discretization schemes and the choice and description of the computational mesh. While we only touch the surface of these concepts, a more detailed and more formal description of algebraic topology in the context of computational electromagnetics (CEM) is available for instance in [100].
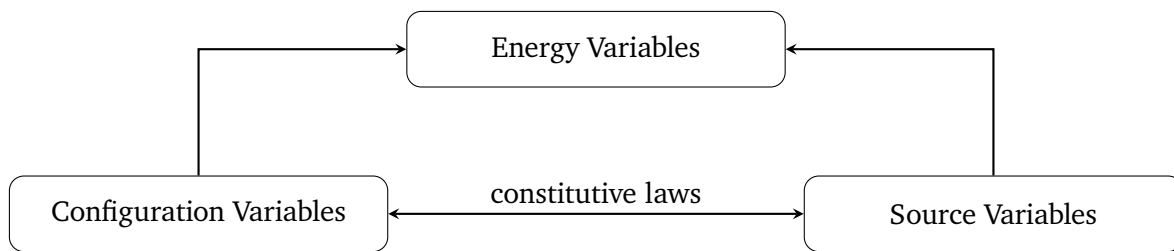
Figure 3.1: Physical variables can be classified into configuration, source, and energy variables [223]. Configuration and source variables are linked by the constitutive laws and their product gives energy variables.

Physical variables can be classified into *configuration*, *source*, and *energy variables*, see [221, 223]. Figure 3.1 shows the relation between these variables. While constitutive laws link configuration and source variables, energy variables are obtained by the multiplication of configuration and source variables. One might argue that the true value of any of these variables is given by measurements, corresponding to the evaluation of a field function on a finite region of space. This is the motivation and the definition of a *global variable*: the integrated value of a field function on a finite region of space that can be obtained by measurements. Some examples for global variables in the field of EMs are the electric charge content, the electric current, the electric voltage, the magnetic flux, and the electric flux. They correspond in vector field formulation to the electric charge density, the electric current density, the electric field, the magnetic flux density, and the electric flux density, see Section 2.1. In contrast to the vector field formulation, global variables are continuous through the separation surface of two materials.

Let us now define the notion of a *cell complex* which generalizes the concept of a computational mesh [223]. In the case of a 3D space, there are $p$-cells with $p = 0, 1, 2, 3$, which represent points, lines, facets, and elements, respectively. It is important to distinguish the terms *face*, *coface*, and *facet*. The $q$-cells with $q < p$ that are part of the boundary of a $p$-cell are called the $q$-*faces* of the $p$-cell. Reversely, those $q$-cells with $q > p$ that share a common $p$-cell are called $q$-*cofaces* of the $p$-cell. On the other hand, the term *facet* is reserved to explicitly refer to a 2-cell in general. While a face of a $p$-cell belongs to the *boundary* of the $p$-cell, a coface of a $p$-cell belongs to its *coboundary*. Here, we omit the precise definitions of the above terms and refer to Figure 3.2 to get an intuition for the 3D space involving points, edges, facets, and elements.

To work with cell complexes in physical sciences, the association of physical variables to their cells was introduced in [36]. The correct association of quantities with the appropriate type of cell is very important; otherwise, the problem of *spurious modes* may occur [124, 212]. For a correct allocation, due to the separation into configuration and source variables, it is convenient to introduce a secondary cell complex in addition to the primal one. Configuration variables are allocated to cells of the primal complex, while source variables are allocated to cells of the secondary complex that is typically chosen to be geometrically dual to the primal one, see Section 3.3.6. Another important property of a pair of the primal and dual cell complexes is the adjointness of the resulting gradient on the primal complex and the negative divergence on the dual complex, which is shown for the coboundary operator in [152]. The coboundary operator is a discrete generalization of the commonly known gradient, divergence, and curl operators, see Section 3.2. For properly formed complexes, the adjointness of the discrete gradient and the negative divergence operators is fulfilled [224].

The use of a dual cell complex is further motivated by the existence of two types of *orientations* [152, 223], a concept which is entirely ignored when vector analysis formulations are used. In general, we distinguish between *internal* and *external* orientation, also known as *inner* and *outer* orientation. For example, the
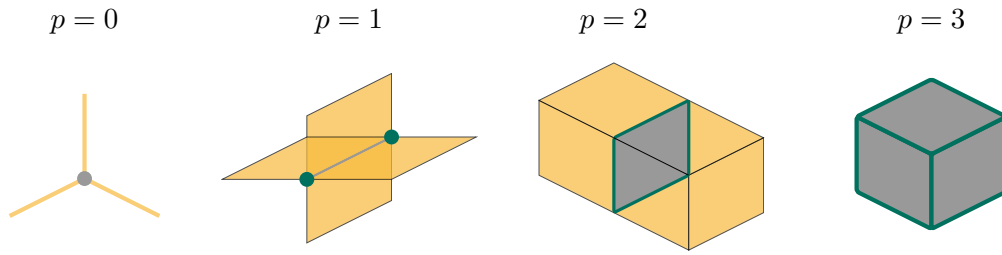
Figure 3.2: Faces, cofaces, boundary, and coboundary of $p$-cells in the case of a 3D rectilinear grid. The cases $p = 0, 1, 2, 3$ are shown and represent points, edges, facets, and elements, respectively. While a $p$-cell is shown in gray, its faces are shown in green making up its boundary. Similarly, its cofaces are shown in orange and make up its coboundary.
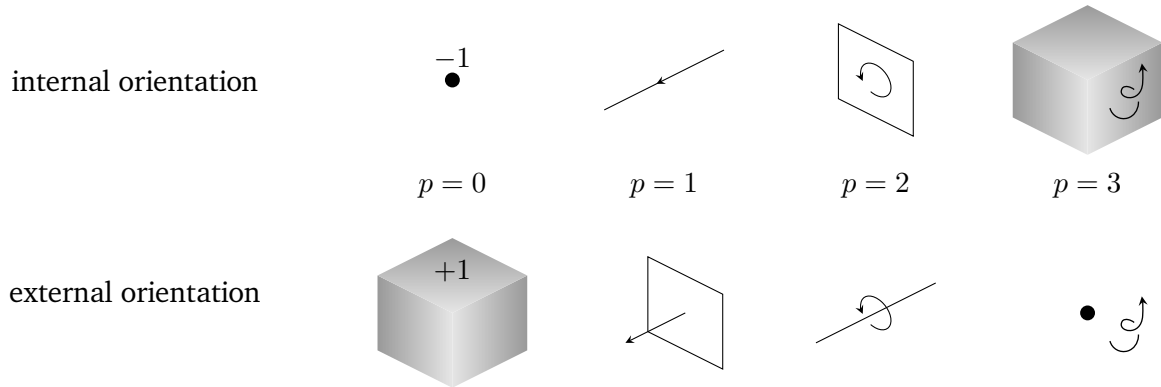


Figure 3.3: Illustration of internal and external orientation in 3D space. The internal orientation of a $p$-cell determines the external orientation of an $(n - p)$-cell. This figure is inspired by [223].

internal orientation of an edge is a sense of direction when moving along the edge. On the other hand, the external orientation of an edge is a sense of turning around the edge. A special case is the internal orientation of a point, which can be oriented as a source or as a sink. Due to the typical convention to orient a point as a sink and the contradicted convention to orient elements as a source (i.e., to orient their boundary by their outgoing normal), the characteristic minus sign in front of the gradient term such as in (2.6) and (2.12) is required for compensation. Figure 3.3 illustrates the concept of internal and external orientations for points, edges, facets, and elements in 3D space, and we refer to [223] for a more detailed explanation. While internal orientation is an independent notion, external orientation depends on the orientation (and thus, also on the dimension) of the surrounding space, which is typically defined by a screw sense. As stated by Veblen and Whitehead [235], when a dual cell complex is considered, the internal orientation of a primal $p$-cell induces the external orientation of a dual $(n - p)$-cell, where $n$ is the dimension of the surrounding space. Let us remark that the role of primal and dual complexes can easily be interchanged; however, we choose to follow the common convention that all cells of a primal complex exhibit internal orientation while all cells of the dual complex exhibit external orientation. This is also depicted in Figure 3.3, where $p$-cells and $(n - p)$-cells are organized on top of each other. To bring orientation and allocation of physical variables into context, Table 3.1 shows the type of orientation of thermal and EM quantities and their allocation to the different cells.

| Object | Cell type | Internal orientation | External orientation |
|---|---|---|---|
| Points | 0-cell | temperature, electric scalar potential | – |
| Edges | 1-cell | thermal tension, electric field, magnetic vector potential | magnetic field |
| Facets | 2-cell | magnetic flux density | thermal heat flux, electric flux density, electric current density |
| Elements | 3-cell | – | power density, charge density |

Table 3.1: Allocation of thermal and EM quantities to different geometric objects and corresponding types of cells. Additionally, the type of orientation associated with the different quantities is given.

## 3.2 (Co-)Chains, Discrete de Rham Currents, Discrete Hodge Operators

Let us introduce chains, cochains, discrete de Rham currents, and the discrete Hodge operator. These notions form the discrete counterpart to differential forms, which were introduced in Section 2.8. We require only some basic notions and refer to [100, 115] and references therein for further details.

A *p-chain* for $p$-cells as introduced in Section 3.1 is defined as

$$C_p := \sum_i n_i c_p^i,$$

where $c_p^i$ is a $p$-cell with multiplicity $n_i$. The concept of *multiplicity* corresponds to an integer number assigned to each cell and can be seen as a weighting. A negative multiplicity corresponds to a negative orientation. The notion of chains allows algebraic manipulations of domains and enables the representation of an entire discretized geometry. The boundary $\partial c_p$ of an oriented $p$-cell is the $(p-1)$-chain composed by the linear combination of those $(p-1)$-cells that have a nonempty intersection with $c_p$. The individual orientations and multiplicities follow from the incidences of the $(p-1)$-cells with the $p$-cell and are thus induced by $c_p$. It is interesting to note that the boundary of a $p$-cell has no boundary. As an example, the boundary of a surface is given by a closed loop and thus, does not have a boundary itself. Having defined the boundary of a cell, we may now define the boundary of a $p$-chain as

$$\partial C_p := \sum_i n_i \partial c_p^i.$$

Therefore, the boundary of a $p$-chain is given by the linear combination of the boundaries of the cells $c_p^i$, taking into account their multiplicities.

A *p-cochain* is a linear mapping of a $p$-chain into the real numbers. It can be identified with coefficient vectors of the same dimensions as the respective chains [8]. Typically, cochains are used for the representation of fields since they are the proper description of physical variables on a cell-complex. An example is given by the charge density $\rho^{(3)}$, which is a 3-cochain that leads to the total charge $Q^C$ for a 3-chain $C_3$ by

$$\langle C_3, \rho^{(3)} \rangle = Q^C,$$

where the bracket-notation is commonly used to denote the evaluation of a cochain on a chain. Note that we choose a chain as the first argument and a cochain as the second argument in the bracket notation, which

might be in conflict with the notation of other authors. Using this concept, it allows to write, e.g., the balance and kinematic equations of thermostatics using chains and cochains as

$$\langle C_3, Q^{(3)} \rangle = \langle \partial C_3, \vec{q}^{(2)} \rangle, \qquad\qquad \langle C_1, \vec{G}^{(1)} \rangle = \langle \partial C_1, T^{(0)} \rangle,$$

respectively. Here, $Q^{(3)}$ is a 3-cochain evaluated on a 3-chain $C_3$ to yield the heat associated to $C_3$. This heat equals the heat flux described by the pairing of a 2-cochain $\vec{q}^{(2)}$ leaving the 2-chain $\partial C_3$. Similarly, the temperature difference is described by the pairing of a 1-cochain $\vec{G}^{(1)}$ evaluated on a 1-chain $C_1$. This temperature difference equals the pairing of a 0-cochain of the temperature $T^{(0)}$ evaluated on $\partial C_1$.

Let us now give a more precise definition of the *boundary operator* $\partial$ and the *coboundary operator* $\delta$. The former establishes a connection between chains of different degrees on the same cell-complex, while the latter establishes a connection between cochains of different degrees on the same cell-complex. The boundary operator $\partial$ is formally defined as a map from a $p$-chain to a $(p-1)$-chain. Since a $p$-cell is a special case of a $p$-chain, this definition carries over to cells. However, the boundary of a $p$-cell usually consists of multiple $(p-1)$-cells, i.e., it is given by a $(p-1)$-chain. As mentioned in Section 3.1, the boundary of a cell does not have a boundary. The same concept applies to chains, resulting in the property $\partial\partial \equiv 0$. On the other hand, the coboundary operator $\delta$ maps $p$-cochains to $(p+1)$-cochains. From a vector analysis perspective, the coboundary operator acts as the discrete generalization of the commonly known differential operators $\nabla$, $\nabla\cdot$, and $\nabla\times$. Thus, similar as for the exterior derivative in the framework of differential forms, see Section 2.8, $\delta\delta \equiv 0$ holds true.

In analogy to the continuous de Rham currents as introduced in Section 2.8, we introduce their discrete counterpart here. A *discrete de Rham current* of dimension $p$ and degree $n-p$ is a functional that maps from $p$-cochains to the real numbers. Similar to the continuous case, a discrete $p$-current can be identified with a $p$-chain and hence, represented by coefficient vectors. Therefore, $p$-chains as well as $(n-p)$-cochains both qualify as de Rham currents [8]. The entries of their coefficient vectors can be computed in a particular basis. In the context of a discretization based on a cell complex, the canonical basis is given by the cells of the complex. For example, the canonical basis for the electric current represented by the discrete de Rham current $\mathcal{J}$ would be given by the set of 2-cells in the cell complex. In other words, these 2-cells correspond to facets in a computational mesh.

Lastly, we introduce the *discrete Hodge operator* as a mapping from $p$-cochains on the primal complex to $(n-p)$-cochains on the dual complex. With the knowledge of de Rham currents, an equivalent definition applies [8]. Since $(n-p)$-cochains can also be seen as currents, the discrete Hodge operator maps from cochains to currents. We denote the discrete Hodge operator by $\bigstar_\alpha$, where $\alpha$ is a material coefficient, representing the finite-dimensional approximation of $\star_\alpha$, see Section 2.8. Depending on the explicit implementation of a Hodge operator, a specific numerical scheme is obtained, see Section 3.3.7. With the definition of a discrete Hodge operator at hand, the notion of *discrete energy* becomes possible. Let $\mathbf{e}$ and $\tilde{\mathbf{h}}$ denote coefficient vectors describing the discrete electric and magnetic fields on the primal and dual cell complexes, respectively. Then, for linear materials, $1/2\langle\bigstar_\varepsilon\mathbf{e}, \mathbf{e}\rangle$ describes the discrete electric energy and $1/2\langle\bigstar_\mu\tilde{\mathbf{h}}, \tilde{\mathbf{h}}\rangle$ describes the discrete magnetic energy, where $\langle\cdot,\cdot\rangle$ represents the dot product [27]. For a consistent formulation and an appropriate refinement strategy, these discrete energies are expected to converge to their continuous counterparts.

## 3.3 Finite Integration Technique for Electrothermal Coupling

After the finite integration technique (FIT) was first introduced in 1976 to solve Maxwell's equations [240], it received great popularity in the community of CEM. Originally, the theory was developed for frequency domain applications [242]. Nowadays however, FIT is mainly used for high frequency problems in the time domain. Particular attention was attributed to FIT due to the software package *Maxwell's equations using the finite integration algorithm (MAFIA)* [217] that was the first distributed 3D code for radio-frequency field simulation. The applicability of FIT covers the range from statics over harmonics up to time-dependent fields. Its main features are low memory requirements and its consistent formulation such that analytical properties of EM fields in the discretized space are maintained. In particular, the solenoidality of the discrete fields is fulfilled, circumventing the problem of spurious modes and parasitic charges, a topic discussed in [124, 212]. Furthermore, the integral formulation does not require any knowledge of the weak form or concepts from functional analysis, enabling even undergraduate students to understand and apply the basic principles. In case of an orthogonal dual grid structure, diagonal material matrices are obtained, see Section 3.3.2. This diagonality property allows to use an explicit time integration scheme, making up for the efficiency of the time domain leap-frog scheme [223, 242]. Another advantage of the leap-frog scheme constitutes in its discrete energy conservation [198]. In this thesis, the FIT receives particular attention due to its convenient consideration of semiconductors [191].

The drawbacks of FIT are mainly related to the restrictions of the typically employed rectilinear grid, see Section 3.3.6. It results in a staircase approximation that can result in very poor accuracy even for simple geometries [119, 170]. To overcome the staircase error, several techniques are available. The most popular ones are the usage of conformal mesh techniques [60], partially filled cells [189], triangular filling techniques [199], tetrahedral filling technique [160], subgridding [218], cell methods [64], and the well-known perfect boundary approximation [132]. Some of these techniques involve non-regular and non-orthogonal grids, for which corresponding theory is available as well [182, 197]. Approaches for non-orthogonal meshes date back to the first methods for finite difference time domain (FDTD) in 1983 [118], resulting in non-diagonal but still symmetric material matrices. Even tetrahedral meshes together with FIT may allow for diagonal material matrices if an appropriate lumping technique is used [32].

The goal of this section is the precise formulation of the classical FIT for a thermal coupling to Maxwell's equations. First, Section 3.3.1 introduces topological notions such as the grid topology, incidence matrices, and the allocation of physical quantities to the grid objects. A great advantage of FIT is the diagonal structure of the material matrices as it will be presented in Section 3.3.2. Putting all ingredients together, Section 3.3.3 provides the corresponding semi-discrete Maxwell's equations obtained by FIT, also known as MGEs. Taking thermal losses into account, Section 3.3.4 defines the discrete representative of the Joule losses. Before the semi-discrete equations can be solved, BCs must be applied, a topic discussed in Section 3.3.5. The quality of a solution depends also on the employed computational grid and may require a grading if singularities are involved, see Section 3.3.6. Lastly, the relation of FIT to other discretization schemes is discussed in Section 3.3.7.

### 3.3.1 Topological Notions

The FIT requires a domain $\mathcal{D}$ to be discretized by a grid pair given by the primal grid $\mathcal{G}$ and its dual $\widetilde{\mathcal{G}}$. Such a dual grid pair can be seen as a special choice of a dual cell complex, see Section 3.1. For more details about the properties and the construction of a grid, see Section 3.3.6. For $p = 0, 1, 2, 3$, the $p$-cells in the

| Description | Normal | Index |
|:---:|:---:|:---:|
| $i$-th primal point | $P_i$ | $i$ |
| $i$-th dual point | $\widetilde{P}_i$ | $\tilde{i}$ |
| $n$-th primal edge | $L_n$ | $n$ |
| $n$-th dual edge | $\widetilde{L}_n$ | $\tilde{n}$ |
| $n$-th primal facet | $A_n$ | $n$ |
| $n$-th dual facet | $\widetilde{A}_n$ | $\tilde{n}$ |
| $i$-th primal element | $V_i$ | $i$ |
| $i$-th dual element | $\widetilde{V}_i$ | $\tilde{i}$ |

Table 3.2: Normal and index notation format for different grid objects. This table is taken from [47].

grid $\mathcal{G}$ are given by primal points $P_i$, $i = 1, \ldots, N_\text{P}$, primal edges (links) $L_n$, $n = 1, \ldots, N_\text{E}$, primal facets (areas) $A_n$, $n = 1, \ldots, N_\text{F}$, and non-overlapping primal elements (volumes) $V_i$, $i = 1, \ldots, N_\text{V}$, respectively. Similarly, the grid $\widetilde{\mathcal{G}}$ consists of dual points $\widetilde{P}_i$, $i = 1, \ldots, \widetilde{N}_\text{P}$, dual edges $\widetilde{L}_n$, $n = 1, \ldots, \widetilde{N}_\text{E}$, dual facets $\widetilde{A}_n$, $n = 1, \ldots, \widetilde{N}_\text{F}$, and dual elements $\widetilde{V}_i$, $i = 1, \ldots, \widetilde{N}_\text{V}$. The grids $\mathcal{G}$ and $\widetilde{\mathcal{G}}$ are dual to each other in the sense that a primal edge $L_n$ intersects a dual facet $\widetilde{A}_n$ and a primal point $P_i$ is located inside a dual element $\widetilde{V}_i$ and vice versa. For a rectilinear grid, the grid staggering is depicted in Figure 3.4. Due to this duality, the number of primal and dual grid objects fulfills

$$N_\text{E} = \widetilde{N}_\text{F}, \quad N_\text{F} = \widetilde{N}_\text{E}, \quad N_\text{V} = \widetilde{N}_\text{P}, \quad N_\text{P} = \widetilde{N}_\text{V}.$$

As mentioned above, we write $L_n$ for the $n$-th edge of the primal grid and we emphasize the duality of edges and facets by using the same index. Thus, $\widetilde{A}_n$ is the dual facet corresponding to the primal edge $L_n$ and $\widetilde{L}_n$ is the dual edge corresponding to the primal facet $A_n$. Let us further introduce a short (index) notation for geometric objects. If $L_n$ or $A_n$ are used as an index, we simply write $n$ instead. Whether $n$ refers to an edge or a facet should become clear from the context. For the dual objects, we use $\tilde{n}$ instead of $\widetilde{L}_n$ or $\widetilde{A}_n$. The notation for points and elements and their duals is realized accordingly. In Table 3.2, we summarize this notation.

The grid counterparts of the continuous field quantities, which have been introduced in Chapter 2, are allocated to points, edges, facets, or elements and are collected in column vectors. For a consistent allocation, the degree of the underlying differential form, or rather of the corresponding cochain, dictates the dimension of the corresponding geometric object, see Sections 2.8 and 3.2. Due to this convention, the discrete fields fulfill all required continuity conditions by construction. Typical examples from EMs are the discrete electric potentials $\boldsymbol{\varphi} \in \mathbb{R}^{N_\text{P}}$, voltages $\widehat{\mathbf{e}} \in \mathbb{R}^{N_\text{E}}$, currents $\widehat{\widehat{\mathbf{j}}} \in \mathbb{R}^{N_\text{F}}$ and charges $\widehat{\widehat{\widehat{\mathbf{q}}}} \in \mathbb{R}^{N_\text{V}}$ that are allocated to primal points, edges, facets and elements, respectively. The number of bows indicates the dimension of the corresponding geometric object. Nevertheless, we typically write $\mathbf{q}$ instead of $\widehat{\widehat{\widehat{\mathbf{q}}}}$ for conciseness. Defining all other grid quantities accordingly, their allocation is shown in Figure 3.4. If we want to indicate a grid quantity, e.g., an electric field, to be allocated to an edge $L_n$ that is part of the boundary of a facet $A_k$, i.e., $L_n \cap \partial A_k = L_n$, we use the indexed notation $\widehat{e}_{k;n}$. Recalling the concept of internal and external orientation as introduced in Section 3.1, the visualization in Figure 3.4 suggests an external orientation of $\widehat{\widehat{\mathbf{b}}}$ on the primal grid and an internal orientation of $\widehat{\mathbf{h}}$ on the dual grid, contradicting the convention of internal orientations on the primal grid and external orientation on the dual grid [224]. However, in the FIT community, this type of visualization is a common choice and does not influence the calculation of the fields.

The FIT uses discretized field quantities represented by vectors whose entries are defined by means of inte-
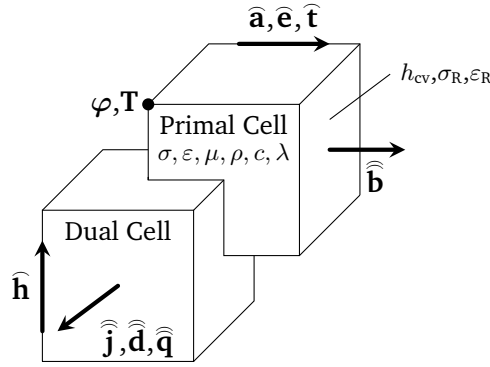
Figure 3.4: Staggered pair of primal and dual element for a rectilinear grid with the allocation of the discrete electric, magnetic and thermal quantities. This figure is taken from [47].

gration with respect to the corresponding geometrical object, such that

$$\varphi_i^{\mathrm{e}} := \varphi(P_i), \qquad \widehat{e}_n^{\mathrm{e}} := \int_{L_n} \vec{E} \cdot \mathrm{d}\vec{L}, \qquad \widehat{\widehat{b}}_n^{\mathrm{e}} := \int_{A_n} \vec{B} \cdot \mathrm{d}\vec{S}, \qquad q_i^{\mathrm{e}} := \int_{\widetilde{V}_i} \varrho \, \mathrm{d}V,$$

where an analogous definition applies for the remaining field quantities of interest. The superscript $^{\mathrm{e}}$ indicates that these quantities are exact values, representing the value of the integrated field. The degrees of freedom (DoFs) computed with FIT are approximations of these exact quantities and given by, e.g.,

$$\varphi \approx \varphi^{\mathrm{e}}, \qquad \widehat{e} \approx \widehat{e}^{\mathrm{e}}, \qquad \widehat{\widehat{b}} \approx \widehat{\widehat{b}}^{\mathrm{e}}, \qquad \mathbf{q} \approx \mathbf{q}^{\mathrm{e}}.$$

Due to the integration, these terms are called grid voltages instead of discrete fields, grid currents (fluxes) instead of discrete current (flux) densities and grid charges instead of discrete charge densities.

To relate grid quantities on different entities of each grid to each other, topological matrices, representing the continuous differential operators, are used. In particular, relations between

- points and edges,
- edges and facets, and
- facets and elements

are established. First, the incidence between grid points and edges is given by the discrete gradient matrix $\mathbf{G} \in \{-1, 0, 1\}^{N_{\mathrm{E}} \times N_{\mathrm{P}}}$ with the entries

$$G_{ni} := \begin{cases} 1, & \text{if } P_i \in \partial L_n \text{ and } P_i \text{ is the end point of } L_n, \\ -1, & \text{if } P_i \in \partial L_n \text{ and } P_i \text{ is the start point of } L_n, \\ 0, & \text{if } P_i \notin \partial L_n. \end{cases}$$

Secondly, the discrete curl matrix $\mathbf{C} \in \{-1, 0, 1\}^{N_{\mathrm{F}} \times N_{\mathrm{E}}}$ denotes the incidence between grid edges and facets given by the entries

$$C_{kn} := \begin{cases} 1, & \text{if } L_n \in \partial A_k \text{ and } L_n \text{ is oriented the same way as } \partial A_k, \\ -1, & \text{if } L_n \in \partial A_k \text{ and } L_n \text{ is oriented the opposite way than } \partial A_k, \\ 0, & \text{if } L_n \notin \partial A_k. \end{cases}$$

Finally, the discrete divergence matrix $\mathbf{S} \in \{-1, 0, 1\}^{N_V \times N_F}$ denotes the incidence between grid facets and elements giving the entries

$$S_{ik} := \begin{cases} 1, & \text{if } A_k \in \partial V_i \text{ and } L_k \text{ is oriented the same way as } \partial V_i, \\ -1, & \text{if } A_k \in \partial V_i \text{ and } L_k \text{ is oriented the opposite way than } \partial V_i, \\ 0, & \text{if } A_k \notin \partial V_i. \end{cases}$$

The dual gradient matrix $\widetilde{\mathbf{G}} \in \{-1, 0, 1\}^{\widetilde{N}_E \times \widetilde{N}_F}$, the dual curl matrix $\widetilde{\mathbf{C}} \in \{-1, 0, 1\}^{\widetilde{N}_F \times \widetilde{N}_E}$, and the dual divergence matrix $\widetilde{\mathbf{S}} \in \{-1, 0, 1\}^{\widetilde{N}_V \times \widetilde{N}_P}$ are defined in analogy. Thanks to the duality of the grids, we obtain the relations $\mathbf{G} = -\widetilde{\mathbf{S}}^\top$, $\widetilde{\mathbf{G}} = -\mathbf{S}^\top$ and $\mathbf{C} = \widetilde{\mathbf{C}}^\top$ [59]. Since the topological matrices are metric-independent, they are closer to an implementation of the coboundary operator $\delta$ than to the differential operators $\nabla$, $\nabla\cdot$, and $\nabla\times$, see Section 3.2. Therefore, in analogy to $\delta\delta \equiv 0$, these matrices fulfill the important topological properties $\mathbf{CG} = \mathbf{0}$, $\mathbf{SC} = 0$ and, equivalently, $\widetilde{\mathbf{C}}\widetilde{\mathbf{G}} = \mathbf{0}$, $\widetilde{\mathbf{S}}\widetilde{\mathbf{C}} = 0$, respectively. Here, $\mathbf{0}$ is a vector of zeros of suitable dimension. Note that all the relations in this paragraph also hold for unstructured finite element (FE) meshes at least as long as a Delaunay-Voronoi grid pair is given, see Section 3.3.6.

## 3.3.2 Material Approximation

This section deals with the approximation of the material distribution in the domain $\mathcal{D}$. As mentioned in Section 2.1, we focus only on standard isotropic and non-dispersive materials, and refer to [135] for gyrotropic and anisotropic materials, and to [105, 207] for dispersive materials. We follow [59, 242], allocate the material coefficients to the primal elements, and derive the material relations that link quantities on the primal grid to quantities on the dual grid and vice versa. In particular, for the problems considered in this thesis, material matrices are introduced to relate

- quantities allocated to primal edges to quantities allocated to dual facets,

- quantities allocated to primal facets to quantities allocated to dual edges, and

- quantities allocated to primal points to quantities allocated to dual elements.

Since the introduction of material matrices requires a metric, it is time to define geometric matrices that contain the measures of edges, facets, and elements for both primal and dual mesh. The geometric matrices are denoted by $\mathbf{D}_S$, $\mathbf{D}_A$, and $\mathbf{D}_V$ for the lengths of the primal edges, the areas of the primal facets and the volumes of the primal elements, respectively. Accordingly, $\widetilde{\mathbf{D}}_S$, $\widetilde{\mathbf{D}}_A$, and $\widetilde{\mathbf{D}}_V$ contain the measures for the dual objects. These matrices are diagonal matrices with the corresponding measures on the diagonal. As an example, we define the matrix of primal edge lengths as

$$\mathbf{D}_S := \mathrm{diag}(L_1, \ldots, L_{N_E}),$$

while the other geometric matrices are defined equivalently. For a convenient numbering scheme, implementations of these matrices often include zero values on the diagonal corresponding to so-called *ghost* cells that are not part of the computational domain. However, throughout this thesis, we assume that these ghost entries have been eliminated.

Let us now provide the precise definition of the material matrices. First, we define the matrix $\mathbf{M}_\alpha \in \mathbb{R}^{\widetilde{N}_F \times N_E}$ relating quantities on primal edges to quantities on dual facets as

$$\mathbf{M}_\alpha(\,\cdot\,) := \widetilde{\mathbf{D}}_A \boldsymbol{\alpha}^{\mathrm{avg}}(\,\cdot\,) \mathbf{D}_S^{-1} := \mathrm{diag}\left( \frac{\alpha_1^{\mathrm{avg}}(\,\cdot\,)|\widetilde{A}_1|}{|L_1|}, \frac{\alpha_2^{\mathrm{avg}}(\,\cdot\,)|\widetilde{A}_2|}{|L_2|}, \ldots, \frac{\alpha_{\widetilde{N}_F}^{\mathrm{avg}}(\,\cdot\,)|\widetilde{A}_{\widetilde{N}_F}|}{|L_{N_E}|} \right), \tag{3.1}$$

where $\alpha \in \{\sigma, \varepsilon, \lambda\}$ and the $\alpha_n^{\mathrm{avg}}$ are averaged material values defined on dual facets and obtained by a suitable averaging scheme [59]. Additionally, it is indicated that possible dependencies of the materials, such as the temperature dependence of $\sigma$, propagate to a dependency of the matrix itself. Perfect electric conducting (PEC) regions are handled apart from the material matrices by forcing the corresponding electric grid voltages to zero. Secondly, we define the matrix $\mathbf{M}_\nu \in \mathbb{R}^{\widetilde{N}_{\mathrm{E}} \times N_{\mathrm{F}}}$ relating quantities on primal facets to quantities on dual edges as

$$\mathbf{M}_\nu := \widetilde{\mathbf{D}}_{\mathrm{S}} \boldsymbol{\nu}^{\mathrm{avg}} \mathbf{D}_{\mathrm{A}}^{-1} := \mathrm{diag}\left( \frac{\nu_1^{\mathrm{avg}}|\widetilde{L}_1|}{|A_1|}, \frac{\nu_2^{\mathrm{avg}}|\widetilde{L}_2|}{|A_2|}, \ldots, \frac{\nu_{\widetilde{N}_{\mathrm{E}}}^{\mathrm{avg}}|\widetilde{L}_{\widetilde{N}_{\mathrm{E}}}|}{|A_{N_{\mathrm{F}}}|} \right), \tag{3.2}$$

where the $\nu_n^{\mathrm{avg}}$ are averaged reluctivity values defined on dual edges and obtained by a suitable averaging scheme [18, 242]. Lastly, we define the matrix $\mathbf{M}_{\rho c} \in \mathbb{R}^{\widetilde{N}_{\mathrm{V}} \times N_{\mathrm{P}}}$ relating quantities on primal points to quantities on dual elements as

$$\mathbf{M}_{\rho c} := \widetilde{\mathbf{D}}_{\mathrm{V}} \boldsymbol{\rho} \boldsymbol{c}^{\mathrm{avg}} := \mathrm{diag}\left( \rho c_1^{\mathrm{avg}}|\widetilde{V}_1|, \rho c_2^{\mathrm{avg}}|\widetilde{V}_2|, \ldots, \rho c_{\widetilde{N}_{\mathrm{V}}}^{\mathrm{avg}}|\widetilde{V}_{\widetilde{N}_{\mathrm{V}}}| \right), \tag{3.3}$$

where the $\rho c_i^{\mathrm{avg}}$ are averaged volumetric heat capacities defined on dual elements and obtained by a suitable averaging scheme [52]. In the case of an orthogonal grid pair together with the case of isotropic materials or anisotropic materials for which the principal axes of anisotropy coincide with the coordinate axes, $\mathbf{M}_\alpha$, $\mathbf{M}_\nu$, and $\mathbf{M}_{\rho c}$ are diagonal matrices with non-negative entries. The diagonal entries of $\mathbf{M}_\varepsilon$, $\mathbf{M}_\lambda$, $\mathbf{M}_\nu$, and $\mathbf{M}_{\rho c}$, as well as the entries of $\mathbf{M}_\sigma$ for $\sigma > 0$, are even strictly positive.

With the above definition of the material matrices, the discrete constitutive relations read

$$\widehat{\widehat{\mathbf{j}}}_{\mathrm{c}} = \mathbf{M}_\sigma \widehat{\mathbf{e}}, \qquad \widehat{\widehat{\mathbf{d}}} = \mathbf{M}_\varepsilon \widehat{\mathbf{e}}, \qquad \widehat{\mathbf{h}} = \mathbf{M}_\nu \widehat{\widehat{\mathbf{b}}}, \qquad \widehat{\widehat{\mathbf{q}}} = \mathbf{M}_\lambda \widehat{\mathbf{t}}, \qquad \mathbf{Q}_{\rho c} = \mathbf{M}_{\rho c} \dot{\mathbf{T}}, \tag{3.4}$$

and we call $\mathbf{M}_\sigma$ the *electric conductance matrix*, $\mathbf{M}_\varepsilon$ the *electric capacitance matrix*, $\mathbf{M}_\nu$ the *magnetic reluctance matrix*, $\mathbf{M}_\lambda$ the *thermal conductance matrix*, and $\mathbf{M}_{\rho c}$ the *thermal capacitance matrix*. Due to the involved material approximation, it is important to note that the relations (3.4) are in general not valid for the exact integral quantities with superscript $^{\mathrm{e}}$. The here obtained material matrices can be interpreted as the FIT implementations of the discrete Hodge operator, which was introduced in Section 3.2. Since the choice of the Hodge implementation determines whether a scheme is *consistent*, it is of major importance for any numerical method [33]. We recall that consistency along with stability are the key properties for a convergent scheme.

To illustrate the involved material approximation, we consider the electric conductivity as an example. The exact electric grid current for facet $\widetilde{A}_n$ is approximated by

$$\widehat{\widehat{\jmath}}_n^{\mathrm{e}} = \int_{\widetilde{A}_n} \vec{J} \cdot \mathrm{d}\vec{S} = -\int_{\widetilde{A}_n} (\sigma \nabla \varphi) \cdot \mathrm{d}\vec{S} \approx -\frac{\sigma_n^{\mathrm{avg}}|\widetilde{A}_n|}{|L_n|} \int_{L_n} \nabla \varphi \cdot \mathrm{d}\vec{L} = (\mathbf{M}_\sigma)_{nn} \widehat{e}_n^{\mathrm{e}},$$

and for quasi-uniform grids, see Section 3.3.6, it is well known that

$$\widehat{e}_n^{\mathrm{e}} = \widehat{\widehat{\jmath}}_n^{\mathrm{e}} \frac{|L_n|}{\sigma_n^{\mathrm{avg}}|\widetilde{A}_n|} + \mathcal{O}(\Delta^\gamma), \quad \text{with} \quad \Delta := \max_{n=1,\ldots,N_{\mathrm{E}}} |L_n|. \tag{3.5}$$

Here, $\gamma = 3$ for equidistant grids and a homogeneous material distribution, and $\gamma = 2$ otherwise. In other words, the FIT material approximation is at least second-order convergent in space. However, to derive the convergence rate of the solution from the material approximation, we require further analysis as shown in the following.

For electrostatics, it can be shown that the error in computing the electric grid voltage is bounded by the error in the material approximation [216, 242], viz.

$$\|\widehat{\mathbf{e}}^{\mathrm{e}} - \widehat{\mathbf{e}}\|_{\varepsilon} \leq \|\widehat{\mathbf{e}}^{\mathrm{e}} - \mathbf{M}_{\varepsilon}^{-1}\widehat{\widehat{\mathbf{d}}}^{\mathrm{e}}\|_{\varepsilon},$$

which results for quasi-uniform grids in a final error of

$$\|\widehat{\mathbf{e}}^{\mathrm{e}} - \widehat{\mathbf{e}}\|_{\varepsilon} = \mathcal{O}(\Delta^{\gamma}),$$

where $\gamma = 2$ for equidistant grids and a homogeneous material distribution, and $\gamma = 1$ otherwise. For high frequency problems in the frequency domain, there holds

$$\|\widehat{\mathbf{h}}^{\mathrm{e}} - \widehat{\mathbf{h}}\|_{\mu} + \|\widehat{\mathbf{e}}^{\mathrm{e}} - \widehat{\mathbf{e}}\|_{\varepsilon} = \mathcal{O}(\Delta^{\gamma}),$$

where $\gamma = 2$ for equidistant grids and a homogeneous material distribution, and $\gamma = 1$ otherwise. The norms as used above are defined as

$$\|\widehat{\mathbf{e}}^{\mathrm{e}} - \widehat{\mathbf{e}}\|_{\varepsilon} := \|\widehat{\mathbf{e}}^{\mathrm{e}} - \widehat{\mathbf{e}}\|^{\top}\mathbf{M}_{\varepsilon}\|\widehat{\mathbf{e}}^{\mathrm{e}} - \widehat{\mathbf{e}}\|, \qquad \|\widehat{\mathbf{h}}^{\mathrm{e}} - \widehat{\mathbf{h}}\|_{\mu} := \|\widehat{\mathbf{h}}^{\mathrm{e}} - \widehat{\mathbf{h}}\|^{\top}\mathbf{M}_{\nu}^{-1}\|\widehat{\mathbf{h}}^{\mathrm{e}} - \widehat{\mathbf{h}}\|.$$

However, it was shown in [157] that the Yee scheme is globally second-order convergent even on a nonuniform grid, an effect known as supraconvergence. This observation carries over to the FIT as well.

### 3.3.3 Grid Equations

Having established the notion of primary grid $\mathcal{G}$ and dual grid $\widetilde{\mathcal{G}}$ together with the corresponding topological and material matrices, Maxwell's equations (2.1) upon such a grid pair read [242]

$$-\mathbf{C}\widehat{\mathbf{e}} = \mathbf{M}_{\nu}^{-1}\frac{\mathrm{d}\widehat{\mathbf{h}}}{\mathrm{d}t}, \tag{3.6a}$$

$$\widetilde{\mathbf{C}}\widehat{\mathbf{h}} = \mathbf{M}_{\varepsilon}\frac{\mathrm{d}\widehat{\mathbf{e}}}{\mathrm{d}t} + \widehat{\widehat{\mathbf{j}}}, \tag{3.6b}$$

$$\widetilde{\mathbf{S}}\widehat{\widehat{\mathbf{d}}} = \mathbf{q}, \tag{3.6c}$$

$$\mathbf{S}\widehat{\widehat{\mathbf{b}}} = \mathbf{0}, \tag{3.6d}$$

and are commonly referred to as the *Maxwell grid equations (MGEs)*. Casting also the heat equation (2.13) into a spatially discrete form [3, 58], we obtain

$$\mathbf{M}_{\rho c}\dot{\mathbf{T}} - \widetilde{\mathbf{S}}\mathbf{M}_{\lambda}\mathbf{G}\mathbf{T} = \mathbf{Q}_{\mathrm{J}} - \widetilde{\mathbf{S}}\widehat{\widehat{\mathbf{q}}}_{\mathrm{i}}, \tag{3.7}$$

where $\mathbf{Q}_{\mathrm{J}}$ is defined on dual elements and represents the discrete vector of the Joule losses. For details on the computation of $\mathbf{Q}_{\mathrm{J}}$, see Section 3.3.4. The impressed thermal fluxes are given by their discrete representative $\widehat{\widehat{\mathbf{q}}}_{\mathrm{i}}$. Restricting (3.6) to the electroquasistatic (EQS) case, see Section 2.2, and carrying out the coupling to (3.7), the discretization of (2.15) is obtained and reads

$$\widetilde{\mathbf{S}}\mathbf{M}_{\varepsilon}\mathbf{G}\dot{\boldsymbol{\varphi}} + \widetilde{\mathbf{S}}\mathbf{M}_{\sigma}(\mathbf{T})\mathbf{G}\boldsymbol{\varphi} = -\widetilde{\mathbf{S}}\widehat{\widehat{\mathbf{j}}}_{\mathrm{i}},$$
$$\mathbf{M}_{\rho c}\dot{\mathbf{T}} - \widetilde{\mathbf{S}}\mathbf{M}_{\lambda}\mathbf{G}\mathbf{T} = \mathbf{Q}_{\mathrm{J}} - \widetilde{\mathbf{S}}\widehat{\widehat{\mathbf{q}}}_{\mathrm{i}}.$$

To lighten the notation, we introduce $\mathbf{K}_\alpha := -\widetilde{\mathbf{S}}^\top \mathbf{M}_\alpha \mathbf{G}$ giving

$$\mathbf{K}_\varepsilon \dot{\boldsymbol{\varphi}} + \mathbf{K}_\sigma(\mathbf{T})\boldsymbol{\varphi} = -\widetilde{\mathbf{S}}\widehat{\widehat{\mathbf{j}}}_{\mathrm{i}}, \tag{3.8a}$$

$$\mathbf{M}_{\rho c}\dot{\mathbf{T}} + \mathbf{K}_\lambda \mathbf{T} = \mathbf{Q}_{\mathrm{J}} - \widetilde{\mathbf{S}}\widehat{\widehat{\mathbf{q}}}_{\mathrm{i}}. \tag{3.8b}$$

Alternatively, let us sketch the idea of obtaining (3.8) when starting from the de Rham current formulation given by (2.30). Discretizing (2.30) can be carried out by choosing standard lowest order nodal functions on a rectilinear grid, also referred to as *nodal Whitney functions*. Whitney functions are the discrete counterpart of differential forms; hence, discrete currents are defined as maps from the space of Whitney functions into the real numbers. In this way, by denoting discrete de Rham currents with the same symbols as their continuous counterparts, we obtain the discrete counterpart of (2.30) as

$$\boldsymbol{div}\mathcal{J}_\sigma(\mathcal{N}_k) = 0, \tag{3.9a}$$

$$\mathcal{Q}_{\rho c}(\mathcal{N}_k) + \boldsymbol{div}\mathcal{J}_\lambda(\mathcal{N}_k) = \mathcal{Q}^{\mathrm{w}}(\mathcal{N}_k), \tag{3.9b}$$

where $\mathcal{N}_k$ refers to the nodal Whitney function associated with node $P_k$. Next, we require the discrete counterpart of (2.28) at the grid level, which reads

$$\boldsymbol{div}\mathcal{K}(\mathcal{N}_k) = -\mathcal{K}(\nabla\mathcal{N}_k) + BC, \tag{3.10}$$

for any discrete 1-current $\mathcal{K}$ and possible boundary contributions $BC$, see [8]. This boundary contribution is omitted for the time being and is further discussed in Section 3.3.5. By applying (3.10) to the current $\mathcal{J}_\alpha$ and evaluating the Whitney functions on the grid, we obtain

$$\boldsymbol{div}\mathcal{J}_\alpha(\mathcal{N}_k) = -\mathbf{j}_\alpha^\top \mathbf{G}\mathbf{e}_k = -(\mathbf{G}^\top \mathbf{j}_\alpha)_k, \tag{3.11}$$

with the coefficient vector $\mathbf{j}_\alpha$ of the current $\vec{J}_\alpha$, and the unit basis vector $\mathbf{e}_k$, see again [8]. Applying (3.11) to (3.9), we obtain the discrete system

$$-\mathbf{G}^\top \mathbf{j}_\sigma(\boldsymbol{\varphi}) = \mathbf{0}, \tag{3.12a}$$

$$\mathbf{M}_{\rho c}\dot{\mathbf{T}} - \mathbf{G}^\top \mathbf{j}_\lambda(\mathbf{T}) = \mathbf{0}, \tag{3.12b}$$

which is equivalent to (3.8) as long as impressed sources are neglected.

After carrying out the discretization of all relevant electrothermal (ET) quantities, we can introduce the discrete ET house as shown in Figure 3.5. The topology and the different links that make up the house are explained in detail in Section 2.4. Due to the integral nature of FIT as a discretization scheme, all units are free of metrical notions. Nevertheless, metric enters through the implementation and construction of the material matrices. We stress that approximations are only introduced when following one of the horizontal links, representing the constitutive laws realized by the material matrices. In practice however, one may be interested in field values at arbitrary positions $\vec{x}$ or in integral quantities evaluated on $p$-cells that are not part of the grid, giving rise to additional interpolation errors. In contrast to other illustrations of the thermal part [3, 91], we choose the negative temperature gradient as the primal 1-form in analogy to the definition of the electric 1-form.
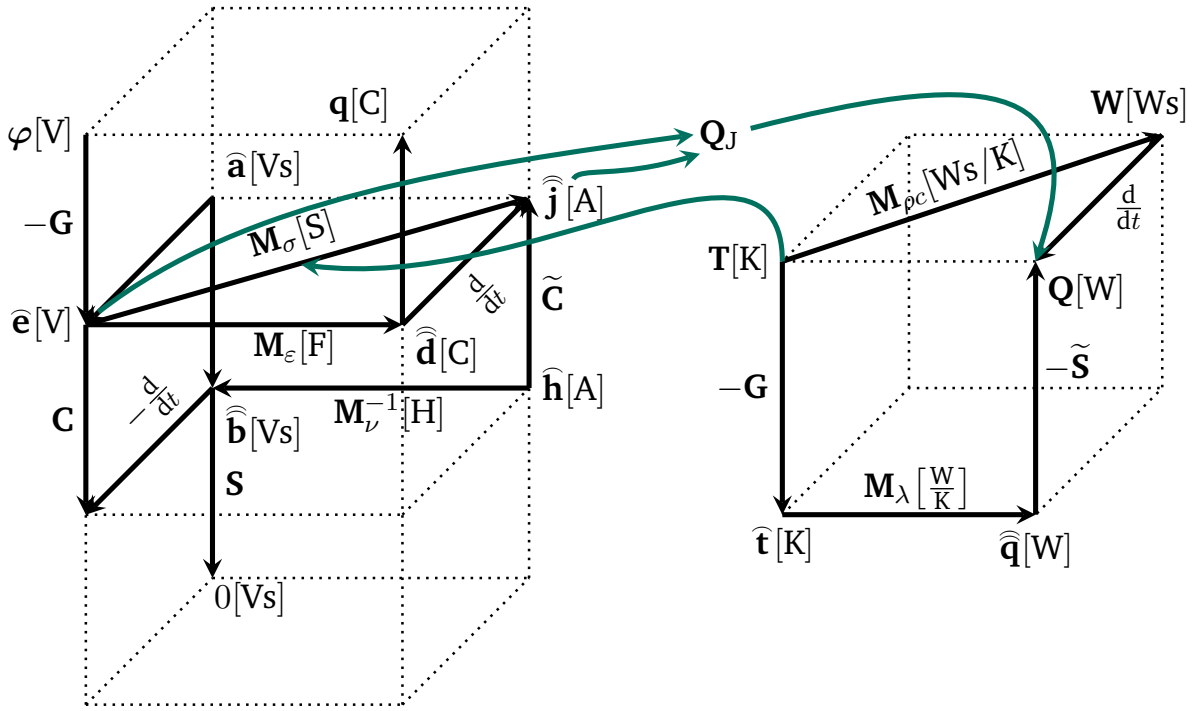
Figure 3.5: Discrete Maxwell and thermal house linked by the Joule losses and the temperature-dependent conductance matrix to form the discrete ET house inspired by [77, 224].

### 3.3.4 Discrete Joule Losses

The heat powers generated by the Joule losses are calculated by [3]

$$\widehat{\mathbf{Q}}_{\mathrm{J}} = \mathrm{diag}(\widehat{\mathbf{e}})\mathbf{M}_\sigma\widehat{\mathbf{e}},$$

with the vector $\widehat{\mathbf{Q}}_{\mathrm{J}} \in \mathbb{R}^{\widetilde{N}_{\mathrm{F}}}$ that allocates the thermal losses to the *control elements* $\widehat{V}_n$ with the volume $|\widehat{V}_n| = |\widetilde{A}_n||L_n|$. The control element $\widehat{V}_n$ is located along the edge $L_n$ with a transverse extension of $|\widetilde{A}_n|$. Figure 3.6 shows such an element for a pair of primal edge $L_n$ and dual facet $\widetilde{A}_n$. To include all calculated heat contributions as sources in the heat equation, they need to be distributed from the control elements $\widehat{V}_n$ to the corresponding neighboring dual elements. For the case of a rectilinear grid, half of each control element contributes to a dual element such that

$$(\mathbf{Q}_{\mathrm{J}})_i = \sum_{n=1}^{6} \frac{1}{2}\left(\widehat{\mathbf{Q}}_{\mathrm{J}}\right)_n,$$

where $n$ is a local counter that loops over all control elements that intersect the dual element $\widetilde{V}_i$. From a topological perspective as introduced in Section 3.1, $n$ iterates over all 2-faces corresponding to the 3-cell $\widetilde{V}_i$; or equivalently, $n$ iterates over all 1-cofaces corresponding to the 0-cell $P_i$. For all dual elements, the Joule losses are collected in a vector given by

$$\mathbf{Q}_{\mathrm{J}} = \frac{1}{2}|\widetilde{\mathbf{S}}|\widehat{\mathbf{Q}}_{\mathrm{J}},$$

where we exploit the dual divergence matrix $\widetilde{\mathbf{S}}$.
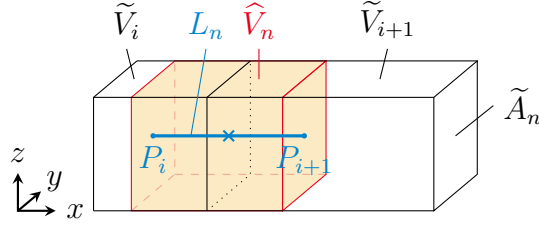
Figure 3.6: Visualization of the control element $\widehat{V}_n$ for a pair of primal edge $L_n$ and dual facet $\widetilde{A}_n$ for the case of a rectilinear grid. This figure is taken from [46].

### 3.3.5 Implementation of Boundary Conditions

Due to the finite computational capabilities of a computer, any computational domain must be truncated, giving rise to the requirement of BCs. For the continuous field problem, we discussed BCs already in Section 2.5. Here, we follow [48] and discuss BCs for the numerical implementation and focus on the discrete ET approximation given by (3.8). The discussion of BCs for the electric and thermal subproblems is independent; thus, we discuss one after another. Since both subproblems use scalar nodal degrees of freedom, Dirichlet conditions refer to prescribed values at the nodes, and Neumann conditions refer to prescribed values of the flux through the boundary. For the electric part using scalar nodal degrees of freedom, Dirichlet conditions are often referred to as electric BCs, while Neumann conditions are referred to as magnetic BCs, see Table 2.2.

To impose Dirichlet BCs for the electric part, we follow [114] and introduce the notion of active nodes, see Figure 3.7a. More precisely, the $N_P^a$ active nodes associated with $\Gamma^{\mathrm{Dir}}$ are obtained by removing all nodes that are contained in the closure of $\Gamma^{\mathrm{Dir}}$. Then, with the restriction operators $\mathbf{R}_P^a \in \{0,1\}^{N_P^a \times N_P}$ and $\mathbf{R}_P^{\mathrm{Dir}} \in \{0,1\}^{N_P^{\mathrm{Dir}} \times N_P}$ (denoted as trace operator $\mathbf{T}$ in [114]), we decompose the electric potential into active nodal potentials $\boldsymbol{\varphi}^a = \mathbf{R}_P^a \boldsymbol{\varphi}$ and prescribed nodal potentials contained in the closure of $\Gamma^{\mathrm{Dir}}$ given by $\boldsymbol{\varphi}^{\mathrm{Dir}} = \mathbf{R}_P^{\mathrm{Dir}} \boldsymbol{\varphi}$. An alternative is to nullify the boundary entries in the corresponding material matrix [193, Section A.1.3]. Based on these definitions, we can reduce (3.8) as

$$\mathbf{R}_P^a \mathbf{K}_\varepsilon (\mathbf{R}_P^a)^\top \dot{\boldsymbol{\varphi}}^a + \mathbf{R}_P^a \mathbf{K}_\sigma (\mathbf{T}) (\mathbf{R}_P^a)^\top \boldsymbol{\varphi}^a = -\mathbf{R}_P^a \mathbf{K}_\varepsilon (\mathbf{R}_P^{\mathrm{Dir}})^\top \dot{\boldsymbol{\varphi}}^{\mathrm{Dir}} - \mathbf{R}_P^a \mathbf{K}_\sigma (\mathbf{T}) (\mathbf{R}_P^{\mathrm{Dir}})^\top \boldsymbol{\varphi}^{\mathrm{Dir}}$$

by incorporating Dirichlet conditions and neglecting impressed sources. To further shorten notation, we introduce

$$\mathbf{K}_\alpha^a (\mathbf{T}) := \mathbf{R}_P^a \mathbf{K}_\alpha (\mathbf{T}) (\mathbf{R}_P^a)^\top,$$
$$\mathbf{K}_\alpha^{\mathrm{Dir}} (\mathbf{T}) := \mathbf{R}_P^a \mathbf{K}_\alpha (\mathbf{T}) (\mathbf{R}_P^{\mathrm{Dir}})^\top,$$

and we obtain the electrical part with BCs given by

$$\mathbf{K}_\varepsilon^a \dot{\boldsymbol{\varphi}}^a + \mathbf{K}_\sigma^a (\mathbf{T}) \boldsymbol{\varphi}^a = -\mathbf{K}_\sigma^{\mathrm{Dir}} (\mathbf{T}) \boldsymbol{\varphi}^{\mathrm{Dir}} - \mathbf{K}_\varepsilon^{\mathrm{Dir}} \dot{\boldsymbol{\varphi}}^{\mathrm{Dir}}.$$

Due to the typical choice of the dual grid at the boundaries, see Section 3.3.6, homogeneous Neumann conditions are automatically fulfilled.

Thanks to the similar mathematical structure of the thermal part, Dirichlet and Neumann conditions are imposed exactly as done for the electric part. Additionally, thermal problems may require convective and radiative BCs, which are identified as Robin type. It is important to realize that this kind of BC is naturally
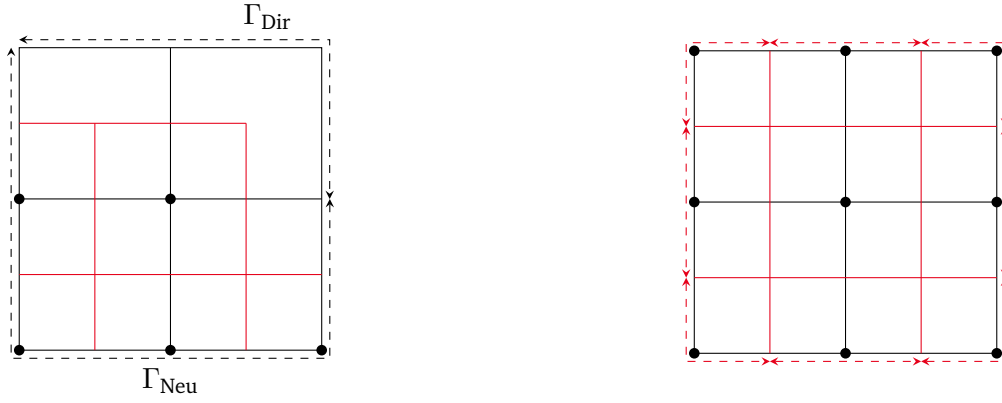
(a) Electrical grid with mixed boundaries      (b) Thermal grid augmented for Robin boundaries

Figure 3.7: (a) Active nodes for Dirichlet and Neumann boundaries, and (b) augmented grid. The primal grid is shown in black, whereas the dual grid is shown in red. Dirichlet and Neumann boundaries are indicated by $\Gamma^{\mathrm{Dir}}$ and $\Gamma^{\mathrm{Neu}}$, respectively. Active nodes are shown by the bullets while active boundary facets are indicated by the (red) arrows in (b). These figures are based on [114] and taken from [48].

associated with boundary elements, and not with boundary nodes [152]. For incorporating Robin BCs, it is convenient to consider the augmented dual grid [114], where $N_{\mathrm{P}}^{\Gamma} = \widetilde{N}_{\mathrm{F}}^{\Gamma}$ dual facets (primal points) on the boundary are introduced that complete the boundaries of the dual elements, see Figure 3.7b. For the augmented dual grid, the boundary contribution $BC$ in (3.10) does not vanish. Following [114], the additional term is quantified as

$$BC = (\mathbf{R}_{\mathrm{P}}^{\Gamma})^{\top}\widetilde{\mathbf{R}}_{\mathrm{F}}^{\Gamma}\mathbf{j}_{\lambda}(\mathbf{T}),$$

arises, where $\mathbf{R}_{\mathrm{P}}^{\Gamma} \in \{0,1\}^{N_{\mathrm{P}}^{\Gamma} \times N_{\mathrm{P}}}$ and $\widetilde{\mathbf{R}}_{\mathrm{F}}^{\Gamma} \in \{-1,0,1\}^{\widetilde{N}_{\mathrm{F}}^{\Gamma} \times \widetilde{N}_{\mathrm{F}}}$ denote the restriction operators to the primal boundary nodes and to the boundary dual facets of the augmented dual grid, respectively. Furthermore, $\mathbf{j}_{\lambda}$ denotes the coefficient vector corresponding to the thermal flow through the boundary. Note that the signs in $\widetilde{\mathbf{R}}_{\mathrm{F}}^{\Gamma}$ are chosen in such a way that the orientation of the restricted fluxes with respect to the outer normal is taken into account. For convective boundaries, let $\mathbf{M}_{h}^{\Gamma} := \mathrm{diag}(h_{k_i}|\widetilde{A}_{k_i}^{\Gamma}|) \in \mathbb{R}^{N_{\mathrm{P}}^{\Gamma} \times N_{\mathrm{P}}^{\Gamma}}$, where $k_i$ refers to the index of the $i$-th boundary node, $i = 1, \ldots, N_{\mathrm{P}}^{\Gamma}$, and $\widetilde{A}_{k_i}^{\Gamma} := \partial\widetilde{V}_{k_i} \cap \Gamma$ is the part of the element $\widetilde{V}_{k_i}$ that touches the boundary $\Gamma$. Let $\mathbf{T}_{\infty} \in \mathbb{R}^{N_{\mathrm{P}}}$ be a constant vector containing the entries $T_{\infty}$. Then, by using the discrete Robin BC

$$\widetilde{\mathbf{R}}_{\mathrm{F}}^{\Gamma}\mathbf{j}_{\lambda}(\mathbf{T}) = \mathbf{M}_{h}^{\Gamma}\mathbf{R}_{\mathrm{P}}^{\Gamma}(\mathbf{T} - \mathbf{T}_{\infty}), \tag{3.13}$$

and the notation $\mathbf{M}^{\Gamma} := (\mathbf{R}_{\mathrm{P}}^{\Gamma})^{\top}\mathbf{M}_{h}^{\Gamma}\mathbf{R}_{\mathrm{P}}^{\Gamma}$, we obtain the thermal problem with Robin BCs which reads

$$\mathbf{M}_{\rho c}\dot{\mathbf{T}} + \left(\mathbf{K}_{\lambda}(\mathbf{T}) + \mathbf{M}^{\Gamma}\right)\mathbf{T} = \mathbf{Q}_{\mathrm{J}} + \mathbf{M}^{\Gamma}\mathbf{T}_{\infty}. \tag{3.14}$$

By the usage of $\mathbf{M}_{h}^{\Gamma}$, which can be thought of as a material matrix, it is understood that Robin BCs can be treated by constitutive equations at the boundary [152]. Similarly, radiative BCs would result in an equivalent equation as (3.13), but with a fourth-order temperature term. To also add Dirichlet BCs to (3.14),

we introduce the abbreviations

$$\mathbf{M}_{\rho c}^{\mathrm{a}} := \mathbf{R}_{\mathrm{P}}^{\mathrm{a}} \mathbf{M}_{\rho c} (\mathbf{R}_{\mathrm{P}}^{\mathrm{a}})^{\top},$$
$$\mathbf{M}_{\rho c}^{\mathrm{Dir}} := \mathbf{R}_{\mathrm{P}}^{\mathrm{a}} \mathbf{M}_{\rho c} (\mathbf{R}_{\mathrm{P}}^{\mathrm{Dir}})^{\top},$$
$$\mathbf{K}_{\lambda}^{\Gamma,\mathrm{a}} := \mathbf{R}_{\mathrm{P}}^{\mathrm{a}} (\mathbf{K}_{\lambda} + \mathbf{M}^{\Gamma}) (\mathbf{R}_{\mathrm{P}}^{\mathrm{a}})^{\top},$$
$$\mathbf{K}_{\lambda}^{\Gamma,\mathrm{Dir}} := \mathbf{R}_{\mathrm{P}}^{\mathrm{a}} (\mathbf{K}_{\lambda} + \mathbf{M}^{\Gamma}) (\mathbf{R}_{\mathrm{P}}^{\mathrm{Dir}})^{\top},$$

such that the discrete ET system including BCs reads

$$\mathbf{K}_{\varepsilon}^{\mathrm{a}} \dot{\boldsymbol{\varphi}}^{\mathrm{a}} + \mathbf{K}_{\sigma}^{\mathrm{a}}(\mathbf{T}) \boldsymbol{\varphi}^{\mathrm{a}} = -\mathbf{K}_{\sigma}^{\mathrm{Dir}}(\mathbf{T}) \boldsymbol{\varphi}^{\mathrm{Dir}} - \mathbf{K}_{\varepsilon}^{\mathrm{Dir}} \dot{\boldsymbol{\varphi}}^{\mathrm{Dir}}, \tag{3.15a}$$

$$\mathbf{M}_{\rho c}^{\mathrm{a}} \dot{\mathbf{T}}^{\mathrm{a}} + \mathbf{K}_{\lambda}^{\Gamma,\mathrm{a}}(\mathbf{T}) \mathbf{T}^{\mathrm{a}} = \mathbf{R}_{\mathrm{P}}^{\mathrm{a}} \mathbf{Q}_{\mathrm{J}} + \mathbf{R}_{\mathrm{P}}^{\mathrm{a}} \mathbf{M}^{\Gamma} \mathbf{T}_{\infty} - \mathbf{M}_{\rho c}^{\mathrm{Dir}} \dot{\mathbf{T}}^{\mathrm{Dir}} - \mathbf{K}_{\lambda}^{\Gamma,\mathrm{Dir}} \mathbf{T}^{\mathrm{Dir}}. \tag{3.15b}$$

Note that instead of (3.14), we can also write

$$\mathbf{M}_{\rho c} \dot{\mathbf{T}} + \mathbf{K}_{\lambda}(\mathbf{T}) \mathbf{T} = \mathbf{Q}_{\mathrm{J}} - \underbrace{\left(\mathbf{R}_{\mathrm{P}}^{\Gamma}\right)^{\top} \widetilde{\mathbf{R}}_{\mathrm{F}}^{\Gamma} \mathbf{j}_{\lambda}(\mathbf{T})}_{=:\mathbf{Q}^{\Gamma}(\mathbf{T})}, \tag{3.16}$$

and hence, the Robin thermal BC, describing a heat exchange with the environment by, e.g., convection or radiation, can also be expressed by a source heat power density $\mathbf{Q}^{\Gamma}$.

### 3.3.6 Computational Grid and Grading

Most numerical techniques require a mesh to discretize the computational domain. We use the term *mesh* as a general term for a domain's tessellation of arbitrary dimension. However, we restrict ourselves to the practical one-, two-, and three-dimensional cases and refer to the corresponding meshes as 1D, 2D, and 3D meshes, respectively. In general, we distinguish between *structured* in contrast to *unstructured* meshes and *equidistant*, *uniform*, or *homogeneous* meshes in contrast to *non-equidistant*, *non-uniform*, or *inhomogeneous* meshes. Structured meshes exhibit regular connectivity of their elements such that it is not required to store the individual incidence relationships. On the other hand, unstructured meshes exhibit irregular connectivity and thus, require additional memory, but allow for a more accurate approximation of curved geometries. In this thesis, we denote any structured mesh by the term *grid* and use the term *Cartesian grid* for a grid consisting of edges of unit length only. In a mesh termed equidistant, uniform, or homogeneous, every edge has the same length. If at least one edge has a different length, the mesh is called non-equidistant, non-uniform or inhomogeneous. Let us also introduce the notion of a *simplex element* in $n$-dimensional space [203]. It is defined by the minimal possible nontrivial element in that space and thus, it is spanned by $n + 1$ vertices. With this definition, the simplex element in 1D is a line, in 2D it is a triangle, and in 3D it is a tetrahedron.

We begin with the definition of a 1D grid $\overline{\mathcal{G}}$ being a discretization of a possibly bent line. Any 1D grid is a structured grid and can be either homogeneous or inhomogeneous. Figure 3.8a and 3.8b show a homogeneous and an inhomogeneous 1D grid for a bent line, respectively. To quantify the *resolution* of a 1D grid, we use the average length of its edges and denote it by $\overline{h}$. Note that for homogeneous grids, all edges have the same length given by $\overline{h}$.

In 2D, a simplex element is identified as a triangle and to this end, we consider a 2D mesh to be assembled by triangles, also called a *triangulation*. A triangle is termed *right-angled* if one of its interior angles equals 90° and is termed *oblique* otherwise. An oblique triangle is further classified into *acute* if all interior angles

(a)                                                                    (b)
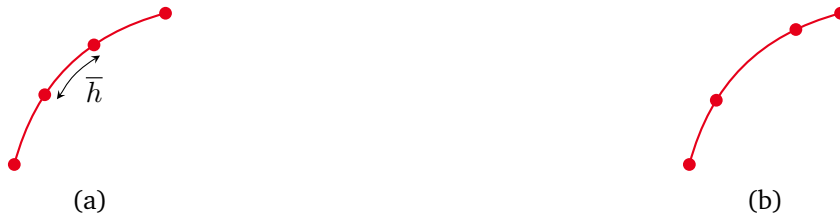
Figure 3.8: (a) Homogeneous and (b) inhomogeneous 1D grid $\overline{\mathcal{G}}$. The resolution of both grids is quantified by using the average edge length $\overline{h}$.



(a)                                      (b)                                      (c)
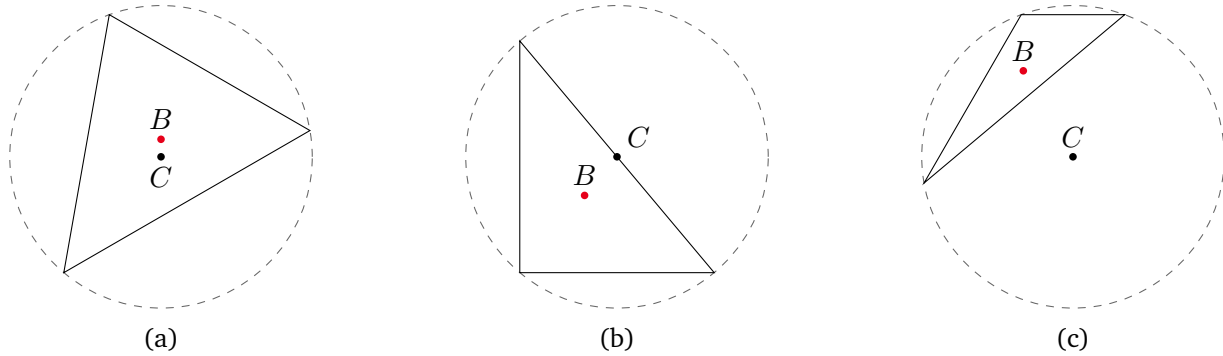
Figure 3.9: (a) An acute, (b) a right-angled, and (c) an obtuse triangle with the notation of their circumcenters $C$ and barycenters $B$. Note that the circumcenter of an obtuse triangle lies outside of the triangle whereas the barycenter lies always in the triangle. For equal-sided triangles, the circumcenter and the barycenter fall together.

are smaller than 90°, and *obtuse* if any angle is larger than 90°. This classification is depicted in Figure 3.9 and becomes relevant when the *circumcenter $C$* of a triangle is considered. The circumcenter exists for any triangle; however, as shown in the figure, it may lie inside or outside of the triangle. Additionally, the figure shows the barycenter $B$ of each triangle, which always lies inside of a triangle. For an equilateral triangle, the circumcenter and barycenter coincide. When constructing a dual mesh, a one-to-one relation of primal elements and dual points is important. Therefore, a dual point must always lie inside of a primal element. This gives rise to certain restrictions for the shape of a triangle. A well-known choice is the *Delaunay triangulation* [76], which starts with an arbitrary number of points and constructs a triangular mesh with these points as its vertices. Its main prerequisite is that the circumcircle of each triangle must not contain any other point. This procedure results in maximizing the smallest angle over all triangles and thus avoids narrow triangles, which are known as *sliver triangles*. Algorithms to generate a Delaunay triangulation from $N$ initial points exhibit at best the complexity $\mathcal{O}(N \log N)$ [210]. As an example, Figures 3.10a and 3.10b show a Delaunay triangulation for a given set of points. In 3D, triangles become tetrahedra, and the circumcircle used to determine a Delaunay triangulation becomes a circumsphere.

To construct a dual mesh, two major approaches are commonly followed [223]. The first approach uses the barycenters of the triangles as the dual points while the second approach uses the circumcenters as the dual points. While the former approach exhibits the advantage that the barycenter always lies inside of a triangle, the latter approach yields a dual mesh that is orthogonal to the primal mesh. Since the orthogonality condition is important to obtain diagonal material matrices, see Section 3.3.2, choosing the circumcenters is much more common. This choice falls together with what is known as a *Voronoi tessellation* [238, 239], which is uniquely determined by a given set of points. Each region of this tessellation contains one of these points,
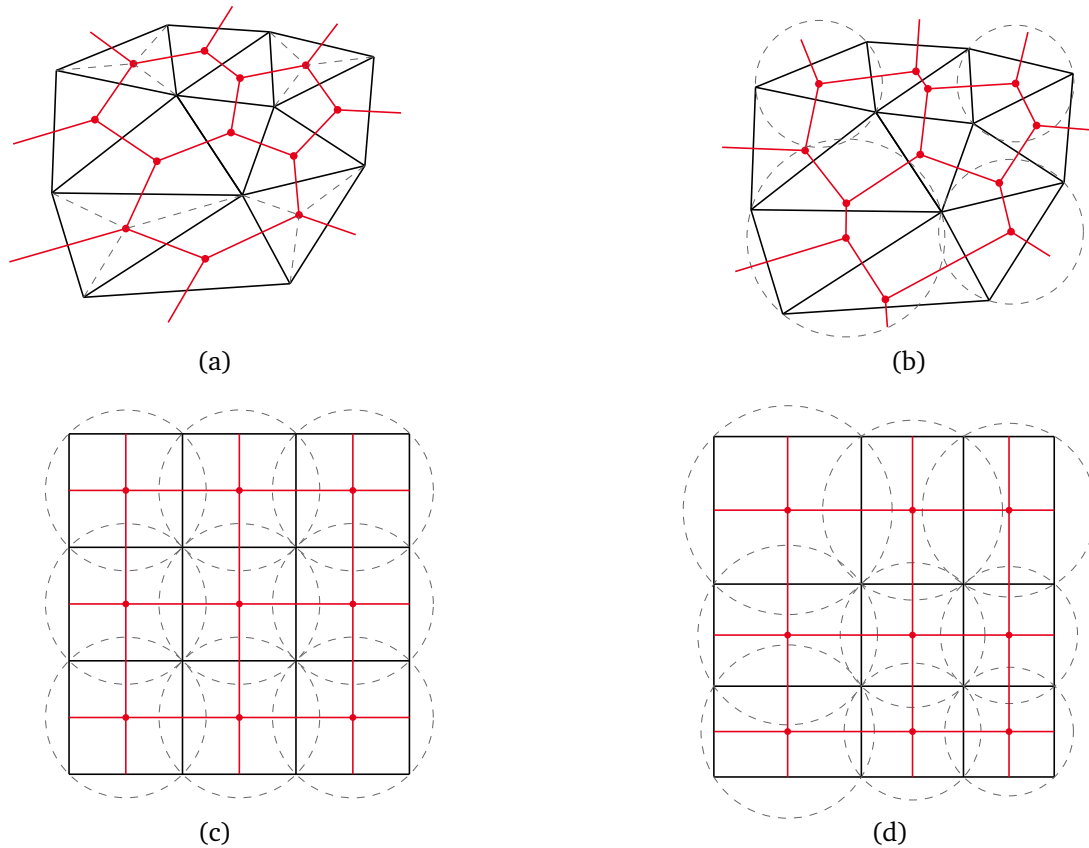
Figure 3.10: (a) Delaunay triangulation in black with barycentric dual mesh in red. Some median lines that define the barycenters are shown. (b) Delaunay triangulation in black with Voronoi dual mesh in red making up a Delaunay-Voronoi tessellation. Some circumcircles that define the circumcenters used for the Voronoi dual are shown. (c) Homogeneous Cartesian grid consisting of unit squares with a Voronoi dual grid for which all circumcircles are shown. (d) Inhomogeneous rectilinear grid with a Voronoi dual grid for which all circumcircles are shown. Note that for any rectilinear grid, barycenters and circumcenters fall together.

called the *seed* or *site* of the region and falls together with a primal point in our case. The main property of a Voronoi tessellation is that any point in a region is closer to its seed than to any other point in the set of points. This premise determines a unique segmentation for a given set of points in a space of any dimension. The most efficient algorithms to generate the Voronoi tessellation from a given set of $N$ points exhibit the complexity $\mathcal{O}(N \log N)$. Once a Voronoi tessellation is constructed, the primal Delaunay triangulation follows directly as its dual. For an exemplary Delaunay triangulation, the corresponding barycentric and Voronoi duals are shown in Figures 3.10a and 3.10b, respectively. Additionally, some medians and circumcircles to determine the barycenters and circumcenters, respectively, are shown. The concepts explained here for the dual 2D mesh extend in a straightforward manner also to the 3D case.

For a *rectilinear grid* as commonly used together with FIT, homogeneous and inhomogeneous examples are shown in Figures 3.10c and 3.10d, respectively. If a rectilinear grid is homogeneous and composed of unit squares in 2D or unit cubes in 3D, it is termed *Cartesian grid*. In 2D, an element is given by a rectangle for which its barycenter and circumcenter lie always inside of the rectangle. Moreover, in the case of a rectangle,
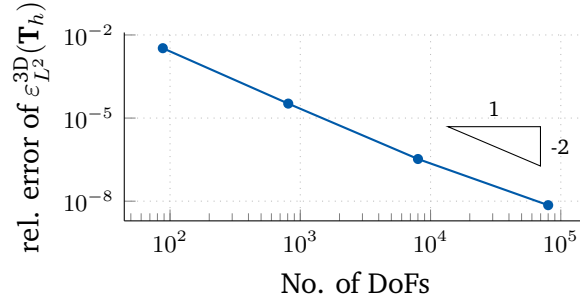
Figure 3.11: Convergence of a standard stationary ET model problem.

these points fall together which unifies the concept of barycentric and Voronoi dual grids. At the boundary of a regular grid, it is a common choice to cut off the dual edges when they touch the primal boundary. Such a dual grid is referred to as one with degenerated dual edges at the primal boundary. Due to their ease of implementation and due to the mostly rectangular structures in electronic devices, the most general mesh used for any implementation in the context of this thesis is a 3D inhomogeneous rectilinear grid. However, if no further restrictions are mentioned, the theory holds also for unstructured meshes, as long as a Delaunay-Voronoi pair is given. Another commonly used term is a regular grid, which compared to rectilinear grids additionally demands congruent elements and includes curvilinear grids that are not considered in this thesis. The construction of a rectilinear grid in 2D can be carried out by applying the Cartesian product to two straight 1D grids. Furthermore, following the same procedure, a rectilinear 3D grid is constructed by the Cartesian product of three 1D grids yielding hexahedrals for the primal and also for the dual elements. Any 3D primal grid constructed by this approach is denoted by $\mathcal{G}$ and consists of non-overlapping elements composed of points, edges, and planar facets. Any 3D dual grid that is constructed as a Voronoi dual to $\mathcal{G}$ with degenerated edges at the primal boundary is denoted by $\widetilde{\mathcal{G}}$. For all grids $\mathcal{G}$, the step sizes $h$ and $\widetilde{h}$ for primary and dual grid, respectively, are defined as the average edge lengths given by

$$h := \frac{1}{N_{\mathrm{E}}} \sum_{n=1}^{N_{\mathrm{E}}} |L_n|, \qquad \widetilde{h} := \frac{1}{\widetilde{N}_{\mathrm{E}}} \sum_{n=1}^{\widetilde{N}_{\mathrm{E}}} |\widetilde{L}_n|,$$

with a notation as introduced in Section 3.3.1. Any grid $\mathcal{G}$ is called quasi-uniform if

$$\min_{n=1,\dots,N_{\mathrm{E}}} |L_n| \geq C \mathrm{diam}(\mathcal{D}) \max_{n=1,\dots,N_{\mathrm{E}}} |L_n|,$$

with an arbitrary constant $C$. The property of quasi-uniformity is relevant, e.g., to determine the expected convergence rates of FIT, see Section 3.3.2.

As discussed in Section 3.3.2, the error of any solution obtained by FIT is dominated by the material approximation and is expected to converge with an order between one and two. To confirm this theoretical argument numerically, we consider a 1D stationary electrothermal model problem with a material jump at the center of the domain. Note that a 1D problem in FIT is realized by a 3D geometry with only one cell in $y$- and $z$-direction to mimic a 1D behavior. The excitation is applied in terms of Dirichlet BCs and the stationary electric and thermal subproblems are solved one after another. For this problem, an analytical solution is available and it is used to study the convergence rate of the relative error $\varepsilon_{L^2}^{3D}(\mathbf{T}_h)$, see Section 3.6 for the exact definition of the error. Figure 3.11 shows that the solution exhibits optimal second-order accuracy which is in accordance with the theory. However, if the solution exhibits any singularity, the standard theory is not valid any more and the convergence rate deteriorates [163, 232]. For elliptic boundary value problems, a possible remedy to recover the optimal convergence rate is the employment of a graded grid [7].
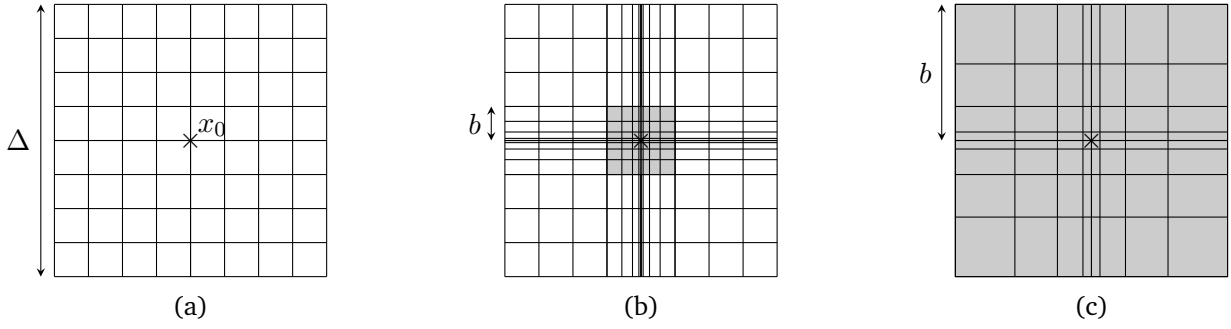
Figure 3.12: Cross-sectional view of (a) an equidistant 3D grid $\mathcal{G}_1$, (b) a locally graded grid $\mathcal{G}_{0.5,4}^{\Delta/8}$, and (c) a globally graded grid $\mathcal{G}_{0.5}$, where the grading region $\mathcal{D}_g$ is shown in gray. Annotated are the domain size $\Delta$ and the grading radius $b$. These figures are taken from [48].

We follow [7, 48] to provide the definition of a graded grid. In this context, we use the term *refinement* to denote that additional grid lines are inserted to an already existing grid. On the other hand, if the total number of grid lines remains constant, the process of shifting the position of the grid lines towards a singularity is denoted as *grading*. However, a grading may also include a refinement if graded grid lines are inserted into an already existing grid. This is the strategy followed here and it is explained in the following. Let us consider a 3D domain $\mathcal{D}$ with a line on which the solution is singular. We assume that an initial, equidistant grid $\mathcal{G}_1$ is given, see Figure 3.12a. As the 3D grid is constructed by the Cartesian product of individual 1D grids, it is sufficient to describe the grading strategy for a 1D grid. Based on [7], the 1D grading around a singular point $x_0$ is applied using the layers

$$r_i = b\left(\frac{i}{\mathcal{N}}\right)^{\frac{1}{\mu}}, \quad \text{with} \quad i = 0, \dots, \mathcal{N}, \tag{3.17}$$

where $\mathcal{N} \in \mathbb{N}$ is the number of grading layers, $\mu \in (0,1] \subset \mathbb{R}$ is the grading strength and $b > 0$ is the radius of the inserted grading. Note that $\mu = 1$ results in an equidistant refinement whereas $\mu \to 0$ yields a grading towards the singularity. Furthermore, $b$ is chosen such that no grid points of $\mathcal{G}_1$ fall in the grading region $\mathcal{D}_g \subset \mathcal{D}$. The only exception to this rule is a possible grid point at $x_0$. After applying the Cartesian product to the individually graded 1D grids, a locally graded 3D grid is obtained and denoted by $\mathcal{G}_{\mu,\mathcal{N}}^b$, see Figure 3.12b. For a grading with $\mathcal{N}$ grading layers with the assumption that $x_0$ was part of $\mathcal{G}_1$, $2\mathcal{N}$ 1D points are added. Due to the regular 3D grid, this results in a propagation of the grading along the coordinate directions. Thus, $2\mathcal{N}$ additional 1D points result in $(2\mathcal{N}+1)^2 - 1$ additional points for a 2D grading and $(2\mathcal{N}+1)^3 - 1$ additional points for a 3D grading. For line sources which are the main source of singularities in this thesis, a 2D grading is required.

With the local grading as introduced above, a global grid grading can be defined as a specific choice of the local grading. Let an initial grid contain the singular point only. Then, by choosing the grading radius $b = \Delta/2$, the grading given by (3.17) results in a grading on the entire computational domain $\mathcal{D}$ such that $\mathcal{D}_g = \mathcal{D}$. A grid obtained by this special choice is denoted by $\mathcal{G}_\mu$, see Figure 3.12c. Note that an additional choice of $\mu = 1$ results in an equidistant grid $\mathcal{G}_1$ without any refinement nor grading. To investigate the influence of a graded grid on problems with singular solutions, two test cases were set up. The first test case is a point source centered in a unit cube and subject to the Laplace problem, for which the BCs are set in accordance with the exact solution. The relative error $\varepsilon_{L^2}^{3D}(\varphi_h)$ for three grids of different gradings is plotted in Figure 3.13a. Although the problem is simpler than the one analyzed in Figure 3.11, the convergence rate is deteriorated significantly. However, if the grading is intensified for $\mu \to 0$, the convergence rate recovers and is expected
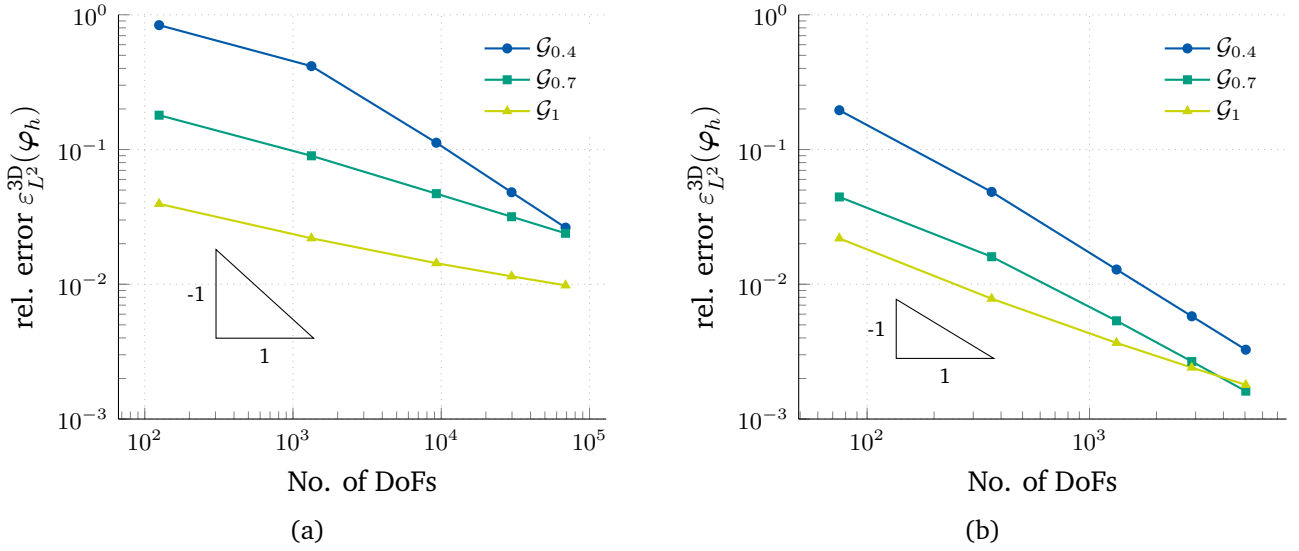
Figure 3.13: Convergence of (a) the point source test case and (b) the line source test case for different globally graded grids.

to reach the optimal convergence rate in the limit case. The second test case is a line source and is set up in analogy to the point source case. Figure 3.13b shows the corresponding results again for three different grid gradings. Similar to the point source case, the convergence rate is deteriorated and recovers for stronger gradings. For this test case, the theory predicts first order convergence at least for an FE discretization [201]. Comparing both test cases, the point source case suffers from a much higher deterioration than the line source case. In general, if a point source is seen as a 0D source in 3D, and the line source as a 1D source in 3D, a high discrepancy between surrounding space and the dimensionality of the singular source results in a strong deterioration of the convergence rate.

### 3.3.7 Relation to Other Discretization Schemes

The main advantage of FIT is the straightforward derivation of diagonal, symmetric, and positive definite material matrices given by (3.1), (3.2), and (3.3). When other discretization schemes are considered, this is not always the case. In this section, we want to shed some light on other techniques and their relation to FIT, which is employed in this thesis. For instance, the difference between the FE method and FIT boils down to the choice of implementing the Hodge operator [114, 216], which constitutes in the definition of the material matrices. First, we briefly put finite difference (FD), finite difference time domain (FDTD) and finite volume (FV) methods into perspective. Then, we give more details about the FE method and the cell method (CM) in comparison to FIT.

While FIT carries out the approximation by the definition of the material matrices, see Section 3.3.2, FD methods solve PDEs by approximating the derivatives by FDs. However, there are strong relations to FD schemes such as mimetic FD schemes [38, 233] and the FDTD method [215]. The former allows for an enhanced grid variety and the latter provides a very efficient explicit solver for high frequent wave propagation problems. Seen from this perspective, the FIT contains FDTD as a subset by the definition of the leap-frog scheme [223, 242]. While FD and also FE schemes use the discretization of field functions, FV

schemes resemble the FIT in the sense that global variables, see Section 3.1, are used for the formulation.

When comparing FIT to the FE method for EM problems [203], a well-known complementarity can be formulated, see [33]. While the FE method uses only one explicit grid, an underlying dual grid is implicitly defined by the basis functions that define a spread element around each node [152]. Using a Galerkin approach, sparse, but non-diagonal positive definite matrices given by

$$\left(\mathbf{M}_\alpha^{\mathrm{FE}}\right)_{ij} := \int_{\mathcal{D}} \alpha \vec{w}_i \cdot \vec{w}_j \, \mathrm{d}\vec{x}, \tag{3.18a}$$

$$\left(\mathbf{M}_\nu^{\mathrm{FE}}\right)_{ij} := \int_{\mathcal{D}} \nu \vec{W}_i \cdot \vec{W}_j \, \mathrm{d}\vec{x}, \tag{3.18b}$$

$$\left(\mathbf{M}_{\rho c}^{\mathrm{FE}}\right)_{ij} := \int_{\mathcal{D}} \rho c \mathcal{N}_i \mathcal{N}_j \, \mathrm{d}\vec{x}, \tag{3.18c}$$

are obtained, where $\alpha \in \{\varepsilon, \sigma, \lambda\}$. Here, $\mathcal{N}$, $\vec{w}$, and $\vec{W}$ are nodal, edge, and facet basis functions, respectively [29, 166]. To obtain diagonal matrices for a tetrahedral mesh, linear basis functions together with an appropriate mass lumping for the material matrices can be used [25, 32]. An equivalent approach consists of approximating the integrals in (3.18) by the midpoint rule. In both cases, the resulting matrices coincide with those constructed by FIT [25].

The last method to consider here is the CM [221]. Instead of a mesh or a grid, the CM is based on the more general concept of a cell complex, see Section 3.1. In practice however, such a cell complex boils down to a mesh-based discretization. Since the CM is also applied to unstructured meshes, a Voronoi dual is not always possible to be built in three dimensions; thus, a barycentric dual mesh is typically used [2], see Section 3.3.6. Due to the barycentric dual mesh, the two meshes are not mutually orthogonal, resulting in non-diagonal material matrices, see Section 3.3.2. The matrices obtained by the CM when using linear interpolation coincide with those obtained by the FE method with linear basis functions [221]. On the other hand, if quadratic interpolation is used, non-symmetric matrices are obtained. In contrast to all other numerical methods which use a vector analysis formulation as the starting point, the CM starts directly from a discrete formulation using global variables, as introduced in Section 3.1. Due to all properties discussed here, the CM may also be seen as a FIT-like technique on structured or unstructured meshes [222].

## 3.4 Time Integration Methods

For the numerical solution of PDEs, discretization schemes are required. By applying a spatial discretization to a time-dependent PDE, it is reduced to an ordinary differential equation (ODE). In this context, methods for solving the resulting ODE are often referred to as a *method of lines*, *temporal discretization* or *time integration*. The available theory for the numerical solution of ODEs is vast, including some excellent textbooks [42, 98, 106]. Here, we give only an overview of the most common approaches in the context of the topics covered in this thesis. Typically, if higher order time derivatives are present in an ODE, it can be rewritten as a first order ODE. Thus, the treatment of first order ODEs suffices for any practical problem. The available approaches can be classified into *one-step* in contrast to *multi-step* schemes. A one-step method is characterized by the fact that it requires only the most recent time step to compute the solution for the new time step. Conversely, multi-step methods require a combination of multiple already computed time steps to advance in time. For the purposes of this thesis, we focus mainly on one-step methods and briefly discuss the leap-frog method as one example of a multi-step method. Furthermore, any time integration method can be an *explicit* or an

*implicit* scheme. Explicit schemes offer the advantage that an explicit formula is obtained to compute the solution for the next time step. However, the stability region for explicit schemes is limited and a stability criterion that provides the maximal allowed time step must be fulfilled [107]. On the other hand, implicit schemes are often unconditionally stable, but require to solve a possibly nonlinear system of equations in each time step. Apart from solving a ODE in the time domain, it can also be solved in the frequency domain by exploiting the Fourier transform [34]. Nevertheless, if a broad band solution is of interest, time domain methods are commonly more efficient.

Let us consider a general ODE with right-hand side $g$ and initial condition $y(t_0) = y_0$ given by

$$\frac{\mathrm{d}y}{\mathrm{d}t}(t) = g(t, y(t)).$$

To solve (3.4), simple time integration schemes are described by the class of $\theta$-methods [179], which read for time step $(i + 1)$

$$\frac{1}{\Delta t}\left(y^{(i+1)} - y^{(i)}\right) = \theta g\left(t^{(i+1)}, y^{(i+1)}\right) + (1 - \theta)g\left(t^{(i)}, y^{(i)}\right),$$

for $0 \leq \theta \leq 1$ and the step width $\Delta t$. The case $\theta = 0$ refers to the *explicit* or *forward Euler* method, $\theta = 1$ refers to the *implicit* or *backward Euler* method, both being first order convergent in time. Furthermore, the case $\theta = 1/2$ refers to the *implicit Crank-Nicolson* scheme, also known as *implicit midpoint rule*, being at best second order convergent in time. Apart from the $\theta$-method, another important class of one-step methods is given by *Runge-Kutta schemes*, of which explicit and implicit variants exist [42, 98, 106]. Formally, this class also includes the explicit and implicit Euler methods, but is mostly important due to its higher order schemes. The most popular higher order scheme from this class is the *classical* Runge-Kutta method, which is an explicit scheme of fourth order.

When coupled problems are considered, very different time scales may appear, leading to the necessity of *multi-rate* methods [94]. However, in this thesis, we assume comparable time scales and focus on the treatment of thin wires, circuit extraction, and the evaluation of failure probabilities instead. One particularly suited time integration method for coupled problems is the method of *fractional steps*, often also referred to as *method of splitting* or *operator-splitting* [179, 252]. Its idea is to split the spatial differential operator, or the corresponding matrix in the semi-discrete case, into a sum of components of simpler structure. To apply the method of fractional steps to the semi-discretized electrothermal problem given by (3.8), we first neglect impressed sources and rewrite (3.8) formally as

$$\begin{pmatrix} \dot{\boldsymbol{\varphi}} \\ \dot{\mathbf{T}} \end{pmatrix} + \begin{pmatrix} \mathbf{K}_\varepsilon^{-1}\mathbf{K}_\sigma(\mathbf{T}) & \mathbf{0} \\ \mathbf{0} & \mathbf{M}_{\rho c}^{-1}\mathbf{K}_\lambda \end{pmatrix}\begin{pmatrix} \boldsymbol{\varphi} \\ \mathbf{T} \end{pmatrix} = \begin{pmatrix} \mathbf{0} \\ \mathbf{M}_{\rho c}^{-1}\mathbf{Q}_J \end{pmatrix}. \tag{3.19}$$

Then, following [179], (3.19) can be split into

$$\frac{\boldsymbol{\varphi}^{(i+1/2)} - \boldsymbol{\varphi}^{(i)}}{\Delta t} + \mathbf{K}_\varepsilon^{-1}\mathbf{K}_\sigma^{(i)}\boldsymbol{\varphi}^{(i+1/2)} = \mathbf{0},$$

$$\frac{\mathbf{T}^{(i+1)} - \mathbf{T}^{(i+1/2)}}{\Delta t} + \mathbf{M}_{\rho c}^{-1}\mathbf{K}_\lambda\mathbf{T}^{(i+1)} = \mathbf{M}_{\rho c}^{-1}\mathbf{Q}_J^{(i+1/2)}.$$

This splitting allows to successively solve the electric and thermal subproblems for each time step, and circumvents the necessity of solving a large coupled system at once. The method of fractional steps exhibits the desired property that it retains the first order convergence of the implicit Euler method [179]. Moreover,
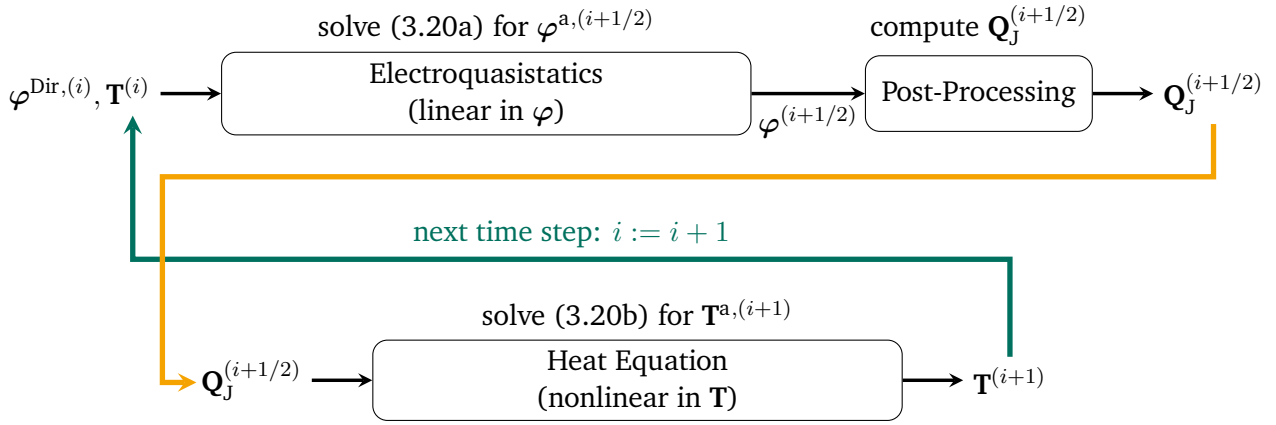
Figure 3.14: Solution procedure for time step $i$ of the fractional step method applied to the electrothermally coupled problem (3.15). Note that the inflation of $\boldsymbol{\varphi}^{\mathrm{a},(i+1/2)}$ and $\mathbf{T}^{\mathrm{a},(i+1)}$ in terms of the corresponding Dirichlet values is not shown explicitly. The inflated vectors are given as $\boldsymbol{\varphi}^{(i+1/2)}$ and $\mathbf{T}^{(i+1)}$, respectively.

for an at least positive semi-definite matrix in (3.19), it is unconditionally stable [147]. Thanks to the positive semi-definiteness of the material matrices, see Section 3.3.2, this condition is guaranteed. Applying this method to (3.15), in which BCs are considered as well, we obtain

$$\mathbf{K}_\varepsilon^{\mathrm{a}} \frac{\boldsymbol{\varphi}^{\mathrm{a},(i+1/2)} - \boldsymbol{\varphi}^{\mathrm{a},(i)}}{\Delta t} + \mathbf{K}_\sigma^{\mathrm{a},(i)} \boldsymbol{\varphi}^{\mathrm{a},(i+1/2)} = -\mathbf{K}_\sigma^{\mathrm{Dir},(i)} \boldsymbol{\varphi}^{\mathrm{Dir},(i)} - \mathbf{K}_\varepsilon^{\mathrm{Dir}} \dot{\boldsymbol{\varphi}}^{\mathrm{Dir},(i)}, \tag{3.20a}$$

$$\mathbf{M}_{\rho c}^{\mathrm{a}} \frac{\mathbf{T}^{\mathrm{a},(i+1)} - \mathbf{T}^{\mathrm{a},(i+1/2)}}{\Delta t} + \mathbf{K}_\lambda^{\Gamma,\mathrm{a}} \mathbf{T}^{\mathrm{a},(i+1)} = \mathbf{R}_{\mathrm{P}}^{\mathrm{a}} \mathbf{Q}_{\mathrm{J}}^{(i+1/2)} + \mathbf{R}_{\mathrm{P}}^{\mathrm{a}} \mathbf{M}^\Gamma \mathbf{T}_\infty - \mathbf{M}_{\rho c}^{\mathrm{Dir}} \dot{\mathbf{T}}^{\mathrm{Dir},(i)} - \mathbf{K}_\lambda^{\Gamma,\mathrm{Dir}} \mathbf{T}^{\mathrm{Dir},(i)}. \tag{3.20b}$$

Figure 3.14 visualizes the principle of the fractional step method. For time step $i$, the Dirichlet potentials and the currently computed temperature distribution are used to solve (3.20a) for $\boldsymbol{\varphi}^{\mathrm{a},(i+1/2)}$. Then, from $\boldsymbol{\varphi}^{(i+1/2)}$, obtained by inflating $\boldsymbol{\varphi}^{\mathrm{a},(i+1/2)}$ with the Dirichlet potentials, the Joule losses $\mathbf{Q}_{\mathrm{J}}^{(i+1/2)}$ are computed to solve (3.20b) for $\mathbf{T}^{\mathrm{a},(i+1)}$. The last step for time step $i$ involves inflating $\mathbf{T}^{\mathrm{a},(i+1)}$ by the Dirichlet temperatures such that $\mathbf{T}^{(i+1)}$ is used for the next time step.

Another scheme of major importance in CEMs is the multi-step *leap-frog* algorithm, which is second order accurate [223, 242]. It is very efficient for high frequency time domain problems and for non-conducting domains reads

$$\widehat{\mathbf{h}}^{(i+1)} = \widehat{\mathbf{h}}^{(i)} - \Delta t \mathbf{M}_\nu \mathbf{C} \widehat{\mathbf{e}}^{(i+1/2)},$$

$$\widehat{\mathbf{e}}^{(i+3/2)} = \widehat{\mathbf{e}}^{(i+1/2)} + \Delta t \mathbf{M}_\varepsilon^{-1} \left( \widetilde{\mathbf{C}} \widehat{\mathbf{h}}^{(i+1)} - \widehat{\widetilde{\mathbf{j}}}^{(i+1)} \right).$$

Its efficiency results from the explicit scheme enabled by the diagonality of the material matrices, see Section 3.3.2. Moreover, due to the high frequent nature of the considered problems, the time step required for a reasonably accurate solution typically fulfills the stability criterion of the explicit scheme.

Apart from choosing a suitable time integration method, the choice of the time steps is at least as crucial. The total number of time steps determines the computational burden since at each time step, a possibly nonlinear system of equations must be solved. While a small time step results in an accurate solution but a long computation, a large time scale results in higher errors or even instabilities. For a flexible compromise of

both, adaptive time stepping schemes are available, which can be seen as a problem of optimal control [85, 98, 206]. One straightforward implementation of an adaptive time stepping is based on the Richardson extrapolation [106]. Its idea is to use a method of order $p$ to compute the solution for two steps of size $h$ and one step of size $2h$. Then, the combination of the results yields an approximation of the order $p + 1$, which can be used to assess the necessity for further refinement.

## 3.5  Solving Systems of Equations

Most numerical techniques require at some stage the solution to a possibly large system of equations. Typically, due to the local interactions of the differential operator on a computational mesh, the system matrix is *sparse*. This sparsity enables to use efficient techniques for storing a matrix in a computer's memory. An overview of the most common techniques can be found for instance in [14, 187]. Moreover, a sparse system allows for efficient solvers that will be discussed in this section.

If the original problem is nonlinear, a linear system is obtained by first applying, e.g., a *fixed point iteration* scheme or *Newton's method*. While the latter exhibits a convergence rate of second order, it requires the computation of the Jacobi matrix which may lead to a non-diagonal differential material matrix [81], see Section 3.3.2. On the other hand, a fixed point iteration scheme may only achieve an acceptable convergence rate when *relaxation* is used. A relaxation scheme is given by $\mathbf{x}^{(i+1)} = \mathbf{x}^{(i)} + \alpha \Delta \mathbf{x}^{(i)}$ with $\alpha \in (0, 1]$ and is typically used either to achieve convergence or to improve the convergence speed of an iterative scheme. For time domain methods, it has been observed that Newton's method may be especially useful when large time steps are used [81].

Let us now come to the problem of solving a linear system in the context of CEM. We consider a general linear system given by

$$\mathbf{A}\mathbf{x} = \mathbf{b}, \tag{3.21}$$

where $\mathbf{A} \in \mathbb{C}^{N \times N}$ is a matrix of size $N$, and $\mathbf{x} \in \mathbb{C}^N$, $\mathbf{b} \in \mathbb{C}^N$ are vectors of size $N$. Here, $\mathbb{C}$ is the set of complex numbers. In CEM, typical values of $N$ range from a few thousand to several millions, depending on the individual problem. The required effort to solve (3.21) for $\mathbf{x}$ depends mainly on the system's size $N$ and the condition number of $\mathbf{A}$. The condition number for an *Euclidean* and a *normal* matrix $\mathbf{A}$ reads [110, 226]

$$\kappa(\mathbf{A}) = \frac{\lambda_{\max}(\mathbf{A})}{\lambda_{\min}(\mathbf{A})},$$

where $\lambda_{\min}$ and $\lambda_{\max}$ are the smallest and largest eigenvalue of $\mathbf{A}$, respectively. A higher value of $N$ and/or $\kappa$ results in an increased effort to solve (3.21). In the field of CEM and other computational sciences, high condition numbers may result for instance from computational meshes with degenerated elements or from a high difference in the coefficients of different materials. To solve (3.21), many techniques are known; an extensive description, a historical overview, and a list of freely available implementations is given in [110]. These methods can be classified in *direct* and *iterative* so-called *relaxation* or *splitting* methods [97, 126, 187, 226]. Especially when using iterative methods, the exact solution of (3.21) is typically not available; instead, an approximate solution $\tilde{\mathbf{x}}$ is computed. To assess the quality of $\tilde{\mathbf{x}}$ without having the exact solution at hand, the error bound

$$\varepsilon_{\mathrm{LS}} = \frac{\|\tilde{\mathbf{x}} - \mathbf{x}\|}{\|\tilde{\mathbf{x}}\|} \leq \mathrm{cond}(\mathbf{A}) \frac{\|\mathbf{r}\|}{\|\mathbf{A}\| \cdot \|\tilde{\mathbf{x}}\|} \tag{3.22}$$

is available, where $\varepsilon_{\mathrm{LS}}$ is the relative error attributed to the linear system solve and $\mathbf{r} = \mathbf{A}\tilde{\mathbf{x}} - \mathbf{b}$ is the *residual* associated to the approximate solution [110]. For more details about the error components of any solution obtained in the field of CEM, see Section 3.6

Direct methods use dedicated algorithms to construct an inverse of $\mathbf{A}$ by factorization such that an exact solution of (3.21) up to machine precision is obtained in a finite number of arithmetic steps. Often, the efficiency of direct methods depends strongly on the ordering of the equations and the unknowns. Therefore, heuristic reordering methods as the minimum degree algorithm are used to achieve further speedup [187]. Furthermore, compared to iterative methods, direct methods are less sensitive to a bad condition of $\mathbf{A}$. Popular algorithms to solve (3.21) by direct methods include Gaußian elimination, LU decomposition, and Cholesky factorization [97, 126, 226]. The latter works only for symmetric and positive definite matrices, but requires half as many operations when compared to LU decomposition. In general, solving (3.21) with direct methods requires $\mathcal{O}(N)$ steps, each requiring $\mathcal{O}(N^2)$ iterations, resulting in a total complexity of $\mathcal{O}(N^3)$. Thanks to the obtained factorization, a set of problems with constant matrix $\mathbf{A}$ but a varying right-hand side $\mathbf{b}$ can be solved with low additional cost. However, if $\mathbf{A}$ reaches a certain size, the inverse construction becomes unfeasible mainly due to memory limitations. For really large systems as they appear in complex 3D examples in CEM, iterative methods have to be used.

Iterative methods start with an initial guess of the solution and successively improve it until a desired accuracy is reached. In the worst case, these methods require $\mathcal{O}(N^2)$ operations for each of the $\mathcal{O}(N)$ steps, but in many cases, an improved complexity is achieved. In the ideal case however, a total complexity of $\mathcal{O}(N)$ is possible, but in practice, complexities of less than $\mathcal{O}(N^2)$ are already quite satisfying. Details on iterative solvers and a comparison between the individual methods are, e.g., available in [14, 126, 187, 226]. This class of methods is further divided into *stationary* and *non-stationary* methods. Stationary methods are typically easy to implement but are not guaranteed to converge. Popular examples listed in order of ascending convergence rate are the Jacobi method, the Gauß-Seidel method, and the successive overrelaxation (SOR) method. A variant of the latter is the symmetric successive overrelaxation (SSOR), which is seldom faster than SOR, but may be useful as a preconditioner, a topic discussed in Section 3.5.1. All of these methods guarantee convergence only under specific conditions; however, these are often satisfied for practical problems. In contrast, non-stationary methods are harder to apply, but very effective when a good preconditioner is used. The most important type is the class of *Krylov subspace methods* that generate the increment directions based on the residual. Well-known examples are the generalized minimal residual (GMRES) method and the conjugate gradient (CG) method [126, 187, 226]. The former also works for non-symmetric matrices, features a monotonically decreasing error but requires to store all incremental directions. Thus, it is typically restarted after a certain number of iterations. On the other hand, the CG method is based on the Lanczos algorithm and is only applicable to the solution of symmetric, positive definite systems. Anyhow, it is often successfully used also for symmetric indefinite systems [125]. The CG method is known to converge after $N$ iterations and only requires to store the two last incremental directions. However, to obtain a desired accuracy, the required number of iterations may be much less than $N$ but it is proportional to the square root of the condition number. Extensions of the CG method for non-symmetric matrices are, e.g., the biconjugate gradient (BiCG) method based on a Petrov-Galerkin approach, the quasi-minimal residual (QMR) method, and the stabilized biconjugate gradient (BiCGSTAB) method [126, 187, 226].

A comparison of different methods to solve linear systems of equations by iterative methods is shown in Table 3.3 [110, Chapter 11]. The methods subject to comparison are the Cholesky method for dense and sparse matrices, the Jacobi method, the Gauß-Seidel method, the optimal SOR method, the standard CG method, the preconditioned conjugate gradient (PCG) method, and the multigrid (MG) method. The data is based on the application of a FD method discretizing an elliptic boundary value problem on an equidistant rectilinear grid of $N$ points in each direction. For each method, ignoring the proportionality constants, the

| Method | 2D | 3D |
|---|---|---|
| Dense Cholesky | $N^6$ | $N^9$ |
| Jacobi | $N^4 \log N$ | $N^5 \log N$ |
| Gauß-Seidel | $N^4 \log N$ | $N^5 \log N$ |
| Band Cholesky | $N^4$ | $N^7$ |
| Optimal SOR | $N^3 \log N$ | $N^4 \log N$ |
| CG | $N^3$ | $N^4$ |
| PCG | $N^{2.5}$ | $N^{3.5}$ |
| Full MG | $N^2$ | $N^3$ |

Table 3.3: Computational cost of solving elliptic boundary value problems using FD combined with iterative methods as a function of the number of points $N$ along each dimension of an equidistant rectilinear 2D or 3D grid. The estimates were taken from [110, Chapter 11].

computational cost is shown for the 2D and 3D cases and represents the optimally achieved value for each individual method. Despite the fact that one method may be cheaper than another, Table 3.3 does not contain any information about reliability, robustness, or ease of implementation of a method. Thus, the presented data is very problem-dependent and gives only a rough indication of the capability of the individual methods. For more details on this subject, see [110].

### 3.5.1 Preconditioners

To improve the convergence properties of a non-stationary method, *preconditioners* are commonly applied. Their idea is to reduce the condition number of a linear system such as (3.21) by the multiplication with an approximate inverse of **A** yielding a modified system for which the iterative solver converges much faster, see Section 3.5. Using a suitable preconditioner, iterative methods become robust even for non-gauged systems that exhibit a singular system matrix **A**. The most popular method to solve large problems with symmetric and positive definite system matrix is the PCG method featuring low memory requirements and a super-linear convergence behavior. The choice of the preconditioner is often more crucial than the choice of the iterative method itself. It must be inexpensive to compute and at the same time a good approximation of the inverse of **A**. Well-known and effective candidates are the (block) Jacobi preconditioner, the symmetric Gauß-Seidel preconditioner, the incomplete LU decomposition, the incomplete Cholesky factorization and the use of SSOR [14, 126, 226]. At the time of writing, the most efficient methods for preconditioning are domain decomposition methods [205], and the usage of MG techniques that date back to the works of Brandt [35].

In the field of CEM, *multigrid (MG)* techniques are used for over twenty years [116]. Often, people also use the term *multilevel* which is a slightly more general term not requiring the notion of a grid. While there is an extensive amount of literature on MG methods as for instance [39, 243], the reader may be referred to an excellent paper that gives a compact explanation and a historical overview of the subject [80]. The idea of MG techniques is to combine results obtained from a hierarchy of grids. In particular, the solutions on a fine grid are enriched by correction terms obtained from the solution on coarser grids. Thus, MG techniques require the matrix and the right-hand side for different levels of refinement. This results in a more involved implementation than for a single grid iterative method, but provides the benefit of efficiency and high convergence rates. For a large class of problems, MG techniques promise a complexity of $\mathcal{O}(N)$,

where $N$ is the size of the system matrix $\mathbf{A}$; however, in general, at least a complexity of $\mathcal{O}(N \log N)$ is achieved [243]. Moreover, while the convergence rate of basic iterative methods may deteriorate for large systems, MG methods provide a grid independent rate of convergence [243]. MG methods can further be classified as *geometric* and *algebraic* MG methods. In contrast to the geometric MG method, algebraic MG methods exhibit the advantage to qualify as black box solvers since they solely rely on algebraic properties of the linear system. As an example, for a nonlinear magnetostatic problem, it has been shown that the computation of the FE solution is reduced by a factor of 6 when using the algebraic MG method instead of an SSOR-CG solver [154].

## 3.6 Error Definitions

In this section, we introduce error measures to quantify the error of a numerical result. First of all, let us distinguish between the different types of errors that are typically committed when running a simulation for a real world problem. Before any equation is established, the modeling step is subject to the modeling error $\epsilon_\mathrm{M}$. Then, a PDE is obtained and one requires a spatial and temporal discretization for its solution, see Sections 3.3 and 3.4, described by the errors $\epsilon_\mathrm{SD}$ and $\epsilon_\mathrm{TD}$, respectively. Once all these steps are completed, a possibly nonlinear system of equations needs to be solved, see Section 3.5. The nonlinearity is typically handled by, e.g., a fixed point iteration or Newton's method, committing an error $\epsilon_\mathrm{NL}$ attributed to the linearization. Solving the resulting linear system may introduce an additional error, denoted as $\epsilon_\mathrm{LS}$. Finally, all these steps are subject to a machine's precision, giving rise to the machine error $\epsilon_\mathrm{PC}$. The total error $\epsilon$ is given by the sum of the individual errors, thus,

$$\epsilon = \epsilon_\mathrm{M} + \epsilon_\mathrm{SD} + \epsilon_\mathrm{TD} + \epsilon_\mathrm{NL} + \epsilon_\mathrm{LS} + \epsilon_\mathrm{PC}.$$

As we are mainly interested in the error committed by a specific numerical method, we focus on the error $\epsilon_\mathrm{SD}$, for which error definitions based on [48] are given in the following. Due to the 1D–3D coupling as discussed in Chapter 5, we require error definitions for 1D and 3D quantities. For a general definition, let $\mathbf{u}$ and $\overline{\mathbf{u}}$ denote any 3D and 1D discrete solution vectors on a grid $\mathcal{G}$, respectively, and let $u$ and $\overline{u}$ denote any exact continuous solution in 3D and 1D, respectively. To define an error measure, we first need to define the norms in which these measures are to be defined. Typically, an approximation to the continuous $L^2$ norms

$$\|\overline{u}\|_{L^2}^{\mathrm{1D}} := \left( \int_{\overline{\Lambda}} \overline{u}^2 \, \mathrm{d}s \right)^{1/2}, \quad \|u\|_{L^2}^{\mathrm{3D}} := \left( \int_{\Omega} u^2 \, \mathrm{d}V \right)^{1/2}, \tag{3.23}$$

for the 1D and 3D cases, respectively, is desired. Here, $\overline{\Lambda}$ and $\Omega$ refer to the 1D and 3D domains in which the errors are evaluated, respectively. A discrete approximation of (3.23) is given by

$$\|\overline{\mathbf{u}}\|_{L^2,h}^{\mathrm{1D}} := \left( \overline{\mathbf{u}}^\top \overline{\mathbf{D}}_{\widetilde{\mathsf{S}}} \overline{\mathbf{u}} \right)^{1/2}, \quad \|\mathbf{u}\|_{L^2,h}^{\mathrm{3D}} := \left( \mathbf{u}^\top \widetilde{\mathbf{D}}_{\mathsf{V}} \mathbf{u} \right)_{\Omega}^{1/2}, \tag{3.24}$$

where $\overline{\mathbf{D}}_{\widetilde{\mathsf{S}}}$ is a diagonal matrix with the 1D dual lengths on the diagonal and is defined in analogy to the geometric matrices in 3D, see Section 3.3.2. Furthermore, the notation $(\,\cdot\,)_{\Omega}$ restricts the discrete vectors or matrices to the evaluation domain $\Omega$.

Now, we have all the prerequisites to define the relative error norms of interest. First, we define

$$\varepsilon_{L^2}^{\mathrm{1D}}(\overline{\mathbf{u}}_h) := \frac{\|\overline{\mathbf{u}}_h - \overline{\mathbf{u}}\|_{L^2,h}^{\mathrm{1D}}}{\|\overline{\mathbf{u}}\|_{L^2,h}^{\mathrm{1D}}}, \quad \varepsilon_{L^2}^{\mathrm{3D}}(\mathbf{u}_h) := \frac{\|\mathbf{u}_h - \mathbf{u}\|_{L^2,h}^{\mathrm{3D}}}{\|\mathbf{u}\|_{L^2,h}^{\mathrm{3D}}}, \tag{3.25}$$

where $\mathbf{u}_h$ and $\overline{\mathbf{u}}_h$ refer to the approximate FIT solutions on a grid $\mathcal{G}$. Secondly,

$$\delta_{L^2}^{1\mathrm{D}}(\overline{\mathbf{u}}_h) := \frac{\left| \|\overline{\mathbf{u}}_h\|_{L^2,h}^{1\mathrm{D}} - \|\overline{u}\|_{L^2}^{1\mathrm{D}} \right|}{\|\overline{u}\|_{L^2}^{1\mathrm{D}}}, \quad \delta_{L^2}^{3\mathrm{D}}(\mathbf{u}_h) := \frac{\left| \|\mathbf{u}_h\|_{L^2,h}^{3\mathrm{D}} - \|u\|_{L^2}^{3\mathrm{D}} \right|}{\|u\|_{L^2}^{3\mathrm{D}}}, \tag{3.26}$$

where the norm of the analytical solution is compared to the norm of the FIT solution. Lastly, if the exact solution is not available, we use

$$\Delta_{L^2}^{1\mathrm{D}}(\overline{\mathbf{u}}_h) := \frac{\left| \|\overline{\mathbf{u}}_h\|_{L^2,h}^{1\mathrm{D}} - \|\overline{\mathbf{u}}\|_{L^2,h}^{1\mathrm{D}} \right|}{\|\overline{\mathbf{u}}\|_{L^2,h}^{1\mathrm{D}}}, \quad \Delta_{L^2}^{3\mathrm{D}}(\mathbf{u}_h) := \frac{\left| \|\mathbf{u}_h\|_{L^2,h}^{3\mathrm{D}} - \|\mathbf{u}\|_{L^2,h}^{3\mathrm{D}} \right|}{\|\mathbf{u}\|_{L^2,h}^{3\mathrm{D}}}, \tag{3.27}$$

where $\mathbf{u}$ and $\overline{\mathbf{u}}$ are FIT solutions computed on a very fine grid.

## 3.7 Summary

This chapter provided a detailed explanation of the different steps to obtain an approximate solution of a continuous 3D field problem. We started the discussion with some useful concepts from algebraic topology and the notions of chains, cochains, discrete de Rham currents, and Hodge operators. Then, we introduced the finite integration technique (FIT) to spatially discretize the governing electrothermal (ET) coupled problem. Among other ingredients, FIT requires a material approximation, a computational grid, and the implementation of boundary conditions (BCs). To not restrict ourselves to one specific discretization scheme, we also discussed the relation of FIT to other schemes, such as the finite element (FE) method. After we obtained the semi-discretized formulation, the next steps involved the temporal discretization and the step of solving the resulting (non-)linear system of equations. Finally, we provided some useful error definitions to be used in subsequent chapters for the assessment of numerical errors and the corresponding convergence rates.

# 4 Evaluation of Failure Probabilities

In this chapter, the efficient computation of failure probabilities of electric devices is discussed. Uncertainties in material and geometrical properties stemming from tolerances in the manufacturing process may result in unexpected behavior. These manufacturing tolerances often result in small failure probabilities, which are particularly challenging to compute. Nowadays, in electronics, thermal designers use empirical knowledge in the form of guidelines or other inefficient and heuristic methods to avoid thermal problems in their designs. However, this may lead to inaccurate modeling and overdesign, asking for more sophisticated methods.

For an accurate prediction of the manufactured functionality, numerical simulations are becoming increasingly popular. Using relevant uncertain parameters as inputs, uncertainty quantification (UQ) techniques help to understand the influence of manufacturing tolerances on the performance of a device. The evaluation of failure probabilities becomes possible, yet the computation of small failure probabilities is numerically challenging. These small probabilities inevitably occur in the context of a six sigma design goal. With predicted failure probabilities at hand, a yield analysis before the manufacturing step is possible.

One approach to compute small failure probabilities was first presented by Li and Xiu in [141] and uses combined Monte Carlo (MC) sampling of the original computational model with a polynomial approximation. Such a hybrid approach uses the computationally cheaper but less accurate polynomial model as long as a sample far away from the failure region is considered. Once a sample falls within the vicinity of the failure region, the original expensive model is used to ensure accurate results. The threshold deciding which model needs to be evaluated, is determined iteratively as outlined in [141]. This iterative procedure minimizes the number of full model evaluations, yielding accurate results at a low cost. Thanks to the non-intrusive idea of this method, it can be readily embedded in the context of this thesis. A possible extension to additionally compute rare failure probabilities, i.e., below $1 \times 10^{-5}$, can be realized by, e.g., the usage of importance sampling as presented in [140].

Parts of this chapter closely follow [50] and it is organized as follows. We start with Section 4.1 to provide some fundamentals of probability theory and to introduce the most important concepts and notations. Then, Section 4.2 defines the failure probability with the help of a performance function. To compute failure probabilities efficiently, we use a sampling scheme based on MC together with a surrogate model, see Section 4.3. Finally, Section 4.4 presents a hybrid iterative algorithm which circumvents the problem that even an accurate surrogate model may lead to significantly wrong failure probabilities.

## 4.1 Fundamentals of Probability Theory

One concern of this thesis is the quantification of uncertainties that dominate the solution of a problem. Possible sources for uncertainties in a device are, e.g., tolerances in the manufacturing process or the variability

of involved parameters. The goal of uncertainty quantification is to quantify the impact of any uncertain input parameter on a quantity of interest obtained from the output. Once such a quantification is achieved, costly and time-consuming over-engineering of a product can be avoided. For this purpose, we require some basic notions from probability theory that are the topic of this section.

We closely follow [250] to introduce the probabilistic terms as required in this thesis. To this end, we define the objects that make up a *probability space* given by the triplet $(\Omega, \mathcal{A}, P)$, with the *outcome space* $\Omega$, the *$\sigma$-algebra* $\mathcal{A}$ and the *probability* $P$. First, we define the outcome space $\Omega$ by taking as an example the experiment of throwing a coin with the possible outcomes heads or tails. In this case, the outcome space $\Omega = \{\text{heads}, \text{tails}\}$ contains two elements. For an ideal coin, the outcome is not predictable and thus referred to as random. This motivates the introduction of a *random variable* $Y = Y(\hat{\omega}) \in \{0, 1\}$, where $\hat{\omega} \in \Omega$ is a possible outcome of an experiment. Each numerical value of a random variable is assigned to one element of the outcome space. Here, we choose 1 to represent heads and 0 to represent tails. In general, a problem may require to use multiple (continuous or discrete) random variables, giving $\mathbf{Y} = (Y_1, Y_2, \ldots, Y_N)$ with $N$ elements. An $N$-dimensional random variable is a function defined on $\Omega$, reading $\mathbf{Y} : \Omega \to \mathbb{R}^N$. We denote a realization of a random variable $\mathbf{Y}$ by $\mathbf{y}$. We further introduce a $\sigma$-algebra $\mathcal{A}$ of $\Omega$ as a collection of subsets that satisfies certain conditions. These conditions include for instance non-emptiness of $\mathcal{A}$ and the inclusion of $\Omega$ in $\mathcal{A}$. For more details on the conditions, the reader is referred to [250]. The third object of a probability space is the probability $P$. It measures the likelihood of an event to occur. For example, the probability of tail is expressed as

$$P(\{\hat{\omega} : Y(\hat{\omega}) = 0\}) = p.$$

According to the law of large numbers, the value of $p$ can be obtained by a very large number of repetitions of an experiment. In our (ideal) coin example, this gives a probability of both possible outcomes in $\Omega$ to equal 0.5 which agrees with our empirical observations. In practice, it is important to distinguish between input and output variables, see Figure 4.1. Typically, the distributions of the input variables are given by measurements and subject to uncertainty. Then, after stochastic modeling and simulation, the output uncertainty can be determined in the quantity of interest (QoI) $\mathcal{Q}$, e.g., the temperature of bond wires. If, reversely, uncertain output quantities are given, solving an inverse problem yields the uncertain input parameters. The output variable is often a QoI $\mathcal{Q}$ that is given as a functional $g$ of the solution. For instance, if $T$ is the temperature field representing the solution, $\mathcal{Q}(\mathbf{Y}) = g(T(\mathbf{Y}))$ describes the quantity of interest being dependent on $\mathbf{Y}$.

To quantify the probability of a continuous random variable falling within a particular range of values, a *probability density function* $f_Y$ is used. It is defined such that

$$F_Y(x) = \int_{-\infty}^{x} f_Y(y) \, \mathrm{d}y,$$

where $F_Y(x) \geq 0$ and $\int_{-\infty}^{\infty} f_Y(y) \, \mathrm{d}y = 1$. Here, $F_Y$ is the *distribution function* of the random variable $Y$ defined as

$$F_Y(x) = P(X \leq x) := P(\{\hat{\omega} : Y(\hat{\omega}) \leq x\}).$$

With the definition of $F_Y$, the probability that $Y$ belongs to an interval $(a, b]$ reads

$$P(\{\hat{\omega} : a < Y(\hat{\omega}) \leq b\}) = F_Y(b) - F_Y(a),$$

for $a < b$. Popular probability density functions include the uniform, Gaußian, and Weibull distributions.

In general, one is interested in characteristic values that quantify the uncertainty of a random variable. Such values are known as statistical moments, with the first two being the mean value or expectation, and the
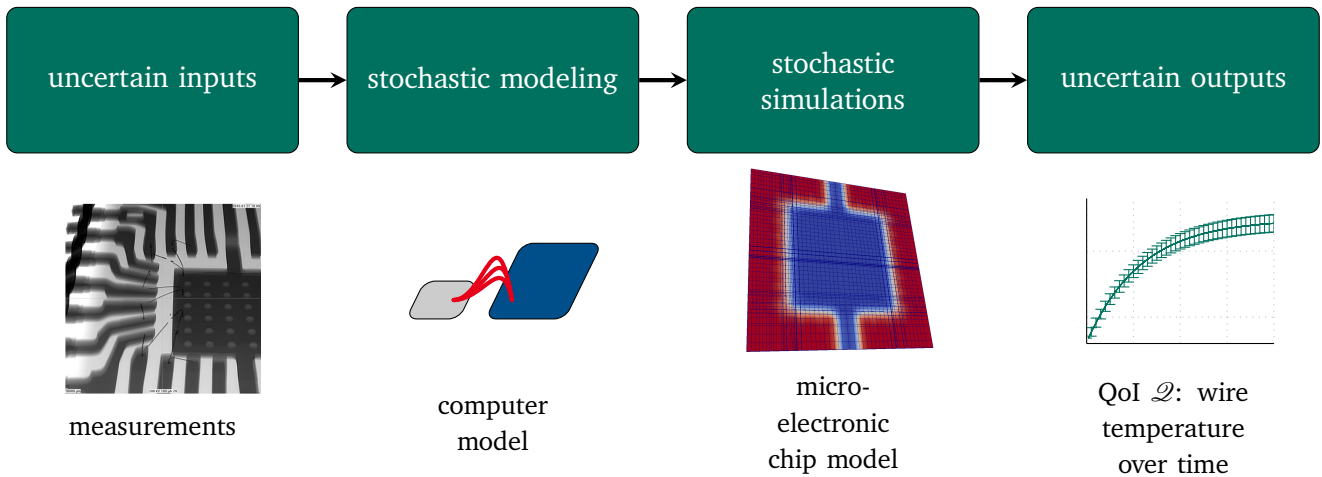
Figure 4.1: Propagation of the uncertainty in the input variables to the QoI at the output of a simulation. If uncertainties are involved, the steps of stochastic modeling and simulation yield uncertainties in the output variable. This output could be characterized by, e.g., the temperature of bond wires.

variance. These two are also the most commonly used ones. The expectation of a random variable $Y$ with density $f_Y$ represents the most likely value of $Y$ and is defined as

$$\mathbb{E}[Y] := \int_{-\infty}^{\infty} x\, f_Y(x)\, \mathrm{d}x.$$

On the other hand, the variance is given by

$$\sigma_Y^2 := \mathrm{var}(Y) := \int_{-\infty}^{\infty} (x - \mathbb{E}[Y])^2 f_Y(x)\, \mathrm{d}x,$$

where $\sigma_Y$ is known as the standard deviation of $Y$.

## 4.2 Failure Probability

Failures occurring in technical applications due to manufacturing tolerances (resulting in, e.g., uncertain geometries) are of stochastical nature. The calculation of failure probabilities is of particular importance to avoid undesired configurations of an engineering device and to prevent the destruction of material or a significant loss of performance.

Following [141], a failure shall be modeled with the help of a *performance function* $g : \mathbb{R}^N \to \mathbb{R}$ that describes a failure when $g < 0$. Those points of the *observation space* $\Gamma \subset \mathbb{R}^N$ that result in a negative performance function constitute the failure region, denoted as $\Gamma_F$. Any uncertainty shall be modeled by the realization $\mathbf{y} : \Omega \to \Gamma$ of a random variable $\mathbf{Y}$ in $\Gamma$. Each of the entries in $\mathbf{Y}$ is distributed according to a probability density function $f_Y$. For the case of two uncertain input variables $y_1$ and $y_2$, Figure 4.2 depicts schematically the rectangular observation space $\Gamma$ and its subspace $\Gamma_F$, separated by the solid line. With the definition of the characteristic function

$$\mathbb{1}_{\Gamma_F}(\mathbf{y}) = \begin{cases} 1, & \mathbf{y} \in \Gamma_F, \\ 0, & \mathbf{y} \notin \Gamma_F, \end{cases} \tag{4.1}$$
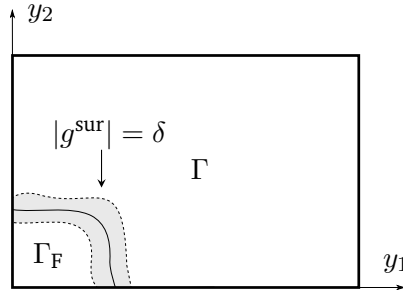
Figure 4.2: Separation of a 2D observation space $\Gamma$ into a safe region and a region of failure. Additionally, the region is decomposed into a gray region where the full model is evaluated, and a white region, where the surrogate model is evaluated. Full model evaluations within the gray region are triggered by $|g^{\text{sur}}| = \delta$ with the threshold $\delta$. This figure is taken from [50].

the failure probability is given by

$$P_{\text{F}} = \int_{\Gamma} \mathbb{1}_{\Gamma_{\text{F}}}(\mathbf{y}) f_Y(\mathbf{y}) \, \mathrm{d}\mathbf{y}. \tag{4.2}$$

## 4.3 Monte Carlo Sampling and Surrogate Model

To compute the failure probability, the integral in (4.2) may be approximated using numerical sampling. This evaluation can become very demanding since the complexity often scales exponentially with the number of considered parameters, an issue commonly known as the *curse of dimensionality* [17]. In this section, we present two examples of sampling schemes, namely the family of MC method and stochastic collocation.

Commonly, failure probabilities are approximated using MC sampling [45, 143]. The MC method is based on the generation of $M$ random input samples according to the probability distribution $f_Y$ of the random variable $\mathbf{Y}$ [250]. For each selected sample, a deterministic problem is obtained, resulting in a set of $M$ solutions for $M$ deterministic problems. These $M$ solutions allow to compute statistical moments such as the expectation value and the variance. Since we are interested in the calculation of failure probabilities, we can use the MC method to approximate the integral in (4.2) by

$$P_{\text{F}} \approx \frac{1}{M} \sum_{j=1}^{M} \mathbb{1}_{\Gamma_{\text{F}}}(\mathbf{y}^j),$$

with a random sample $\mathbf{y}^j$ drawn according to the probability distribution $f_Y$. One advantage of the MC method is that it does not suffer from the curse of dimensionality. However, its complexity highly depends on the cost to evaluate $\mathbb{1}_{\Gamma_{\text{F}}}(\mathbf{y}^j)$ and its convergence speed is relatively slow, given by $\mathcal{O}(1/\sqrt{M})$ [45]. Improvements to MC include the quasi MC method [78] which chooses the samples in a deterministic sequence, or the multilevel MC method [92, 96], which makes use of different fidelities of the model to evaluate.

To reduce the cost required to evaluate $\mathbb{1}_{\Gamma_{\text{F}}}$, let us adapt the non-intrusive *stochastic collocation* procedure presented in [10], also known as *generalized polynomial chaos (gPC)* [250]. Thanks to its non-intrusiveness, this

method is readily applicable to the governing electrothermal (ET) problem of this thesis given by (2.15). In the simplest case of tensor grid collocation, with *collocation points* $\hat{\mathbf{y}}^m$, $m = 1, \ldots, (p+1)^N$ and polynomial degree $p$, we approximate the QoI $\mathscr{Q}$ such that the performance function follows as

$$g(\mathbf{y}) \approx g^{\text{sur}}(\mathbf{y}) = \sum_{m=1}^{(p+1)^N} g(\hat{\mathbf{y}}^m) L_m(\mathbf{y}),$$

where $L_m$ are multivariate Lagrange polynomials. After setting up this surrogate model, only polynomial evaluations are required, reducing the computational cost substantially. However, stochastic collocation is subject to the curse of dimensionality; thus, it becomes prohibitively expensive when the number of parameters is high. Only under very strict assumptions on the regularity of the solution and the randomness of the input, the curse may be surpassed [54]. In all other cases in which a high number of uncertain input parameters is involved, more sophisticated methods such as sparse grids [168] or low-rank tensor approximations [145] can be used to mitigate the curse. In the following, the failure region evaluated with $g^{\text{sur}}$ instead of $g$ is denoted by $\Gamma_{\text{F}}^{\text{sur}}$ and the associated failure probability reads

$$P_{\text{F}}^{\text{sur}} = \int_\Gamma \mathbb{1}_{\Gamma_{\text{F}}^{\text{sur}}}(\mathbf{y}) f_Y(\mathbf{y}) \, d\mathbf{y} \approx \frac{1}{M} \sum_{j=1}^M \mathbb{1}_{\Gamma_{\text{F}}^{\text{sur}}}(\mathbf{y}^j). \tag{4.3}$$

## 4.4 Hybrid Approach to Compute Small Failure Probabilities

Now, we assume that a surrogate model such as the one obtained by stochastic collocation method is available, see Section 4.3. While the evaluation of a surrogate model is more efficient than the evaluation of the corresponding full model, the computed failure probabilities can be inaccurate. It has been shown that this shortcoming may persist even if a very accurate surrogate model is employed together with a large number of samples [141]. As a remedy, a hybrid iterative scheme, combining the accurate partial differential equation (PDE) model with the efficient surrogate model is described here [141].

The idea is to evaluate the surrogate model only when the considered sample lies far away from the failure region, i.e., $|g^{\text{sur}}(\mathbf{y}^j)|$ larger than a certain threshold $\delta$. Once $|g^{\text{sur}}(\mathbf{y}^j)|$ becomes smaller than this threshold and thus close to the failure region, the original model is used to evaluate $\mathbb{1}_{\Gamma_{\text{F}}}$ instead of $\mathbb{1}_{\Gamma_{\text{F}}^{\text{sur}}}$. This idea is illustrated in Figure 4.2 and reduces the problem to the one of finding an adequate value for $\delta$.

One possible approach to determine $\delta$ is an iterative method [141] as outlined in the following. First, the surrogate model is evaluated for the full set of samples to obtain $\{g^{\text{sur}}(\mathbf{y}^j)\}_{j=1}^M$. This allows to evaluate $\mathbb{1}_{\Gamma_{\text{F}}^{\text{sur}}}$ with implicitly given $\Gamma_{\text{F}}^{\text{sur}}$ and hence an initial value of the hybrid failure probability given by

$$P_{\text{F}}^{\text{hyb},(1)} := P_{\text{F}}^{\text{sur}}$$

is obtained. Then, the full model is evaluated for the $\delta M < M$ samples that are the closest to the failure region. For these samples, $\mathbb{1}_{\Gamma_{\text{F}}^{\text{sur}}}$ is replaced with $\mathbb{1}_{\Gamma_{\text{F}}}$ in the failure probability estimate. If the associated change in the failure probability estimate exceeds a certain tolerance $\eta$, the hybrid failure probability for step $(k+1)$ is updated with the $\delta M$ full model evaluations. Then, the next $\delta M$ samples are selected and the procedure is repeated until

$$|P_{\text{F}}^{\text{hyb},(k+1)} - P_{\text{F}}^{\text{hyb},(k)}| \leq \eta.$$

The described procedure is listed in Algorithm 1, where it is understood that $M/\delta M$ is an integer.

---

**Algorithm 1** Iterative algorithm to compute the hybrid failure probability using an expensive computer model $g$ and a cheaper surrogate model $g^{\text{sur}}$. The tolerance $\eta$ determines the termination of the algorithm. This listing is taken from [50].

---

1: **procedure** HYBRID($g$, $g^{\text{sur}}$, $M$, $\delta M$, $\mathbf{y}$, $\eta$)
2:      set $M^{(1)} = 0$                                                                                          ▷ Initialization
3:      evaluate $P_{\text{F}}^{\text{hyb},(1)} = P_{\text{F}}^{\text{sur}}$ using (4.3)
4:      sort $\{\mathbf{y}^j\}_{j=1}^M$ as $\{\mathbf{y}_{\text{asc}}^j\}_{j=1}^M$ s.t. $\{|g^{\text{sur}}(\mathbf{y}_{\text{asc}}^j)|\}_{j=1}^M$ ascends
5:      **for** $k = 1$ **to** $M/\delta M$ **do**                                                                 ▷ Iteration
6:          define $M_1 = M^{(k)} + 1$
7:          define $M_2 = M^{(k)} + \delta M$
8:          evaluate $g(\{\mathbf{y}_{\text{asc}}^j\}_{j=M_1}^{M_2})$ yielding $\mathbb{1}_{\Gamma_{\text{F}}}(\{\mathbf{y}_{\text{asc}}^j\}_{j=M_1}^{M_2})$
9:          set $\Delta P_{\text{F}}^{\text{hyb},(k)} = \frac{1}{M}\sum_{j=M_1}^{M_2}\left(-\mathbb{1}_{\Gamma_{\text{F}}^{\text{sur}}}(\mathbf{y}_{\text{asc}}^j) + \mathbb{1}_{\Gamma_{\text{F}}}(\mathbf{y}_{\text{asc}}^j)\right)$
10:         set $P_{\text{F}}^{\text{hyb},(k+1)} = P_{\text{F}}^{\text{hyb},(k)} + \Delta P_{\text{F}}^{\text{hyb},(k)}$
11:         **if** $|P_{\text{F}}^{\text{hyb},(k+1)} - P_{\text{F}}^{\text{hyb},(k)}| \leq \eta$ **then**
12:             **return** $P_{\text{F}}^{\text{hyb},(k+1)}$
13:         **end if**
14:         update $M^{(k+1)} = M^{(k)} + \delta M$
15:     **end for**
16:     **return** $P_{\text{F}}^{\text{hyb},(k+1)}$
17: **end procedure**

---

Algorithm 1 ensures that the error in the computed failure probability decreases as the accuracy of the surrogate model increases, in contrast to sampling the surrogate model alone [141]. However, the result might depend on the choice of the step size $\delta M$ and the tolerance $\eta$, which have to be determined empirically. As an alternative to this iterative approach, if an error estimator is available, the value of the threshold $\delta$ may be estimated a posteriori yielding full control on the accuracy of the failure probability.

Mathematically [141], the resulting hybrid failure probability is given by

$$P_{\text{F}}^{\text{hyb}} = \int_\Gamma \mathbb{1}_{\Gamma_{\text{F}}^{\text{hyb}}}(\mathbf{y}) f_Y(\mathbf{y})\,\mathrm{d}\mathbf{y} \approx \frac{1}{M}\sum_{j=0}^M \mathbb{1}_{\Gamma_{\text{F}}}^{hyb},$$

with

$$\mathbb{1}_{\Gamma_{\text{F}}^{\text{hyb}}} = \mathbb{1}_{\{g^{\text{sur}} < -\delta\}} + \mathbb{1}_{\{|g^{\text{sur}}| < \delta\} \cap \{g < 0\}}.$$

Here, the compact notation of, e.g., $\{g < 0\}$ is short for $\{\mathbf{y} \mid g(\mathbf{y}) < 0\}$.

## 4.5 Summary

The major purpose of this chapter was to introduce the evaluation of failure probabilities. We started off with some fundamentals of probability theory. Important terms such as probability space, outcome space, $\sigma$-algebra, probability, and random variable were defined. We provided the precise definition of a failure probability and used a performance function to decide whether a failure occurs. For the computation of

failure probabilities, we motivated the necessity of a sampling scheme such as the classical Monte Carlo (MC) sampling. However, for small failure probabilities, pure MC becomes prohibitively expensive and the use of a polynomial surrogate model was discussed. To overcome the problem of inaccurate failure probabilities even when using an accurate surrogate model, we introduced a hybrid scheme as first presented in [141]. This hybrid scheme allows for a compromise between accuracy and low computational cost. To determine the threshold parameter $\delta$ that decides whether to use the full or the surrogate model, we proposed an iterative algorithm. The drawback of this algorithm lies in the parameters $\delta M$ and $\eta$ that require an empirical choice. For a more sophisticated method to obtain the threshold $\delta$ a posteriori, an error estimator would give full control on the accuracy of the failure probability estimate.

# 5 Numerical Approach for the Simulation of Thin Wires in a 3D Setting

In micro- and nanoelectronic applications, bond wires are used to connect the chip to its surrounding package. Compared to the sizes of the other components in a chip package, the radius of the wires is typically very small. Due to this fact, we speak of a *thin wire* and we are interested to include thin wires in the package-level simulation of electronic devices. The problem is challenging due to the different spatial scales of the wires and the surrounding package, requiring locally very fine meshes, which results in a high computational cost. The approach adapted here, which is not restricted to electronic applications, consists of modeling wires as 1D structures and of computing the solution using an additional 1D equation. Originally, this study was motivated by problems in the scope of the EU FP-7 project *nanoCOPS* [149].

In computational electromagnetics (CEM), different approaches circumventing the problem of resolving the thin wires using locally refined meshes have been developed. From analytical models to complex numerical models, approaches of different fidelities are available. While analytical models allow a fast characterization of a thin wire, sophisticated numerical models enable a more detailed analysis at the cost of a high computational effort. Most commonly however, the influence of a wire is modeled by an infinitely thin, perfect electric conducting (PEC) wire together with the modification of the material properties in its neighborhood. This approach has been verified in numerous publications by comparison to other solvers or measurements; however, convergence analyses of this type of methods are not available. Moreover, the PEC approach is very specific to electric problems, for which conductors exhibit conductivities that are several orders of magnitude higher than those of insulators. When considering other disciplines, such as thermal conduction, the values for the different materials show a much lower discrepancy. Therefore, the absolute material values have to be taken into account and a different wire model is required.

This chapter closely follows [48] to address an alternative numerical approach for the simulation of 3D problems involving thin wires. It is based on modeling a thin wire as a 1D line $\Lambda$ as shown in Figure 5.1. In this case, the necessity of very fine grids is relaxed and substantial computational savings are obtained. By embedding the 1D wire model into the surrounding 3D geometry, the bent geometry of a wire can be incorporated without suffering from a staircase approximation within the rectilinear grid. Staircase approximations are very common for thin wire approximations in CEM and the associated drawbacks are discussed in Section 3.3.2. Due to the dimensional gap, a 1D wire embedded in 3D space represents a singular substructure. Such singular substructures are frequently encountered and dealt with in CEM [169, 231, 248]. An appropriate tool to model singularities in CEM is the framework of de Rham currents [75] and their discrete counterparts [8]. We employ these concepts and present a detailed mathematical model both on the continuous as well as on the discrete level. Furthermore, we show that the problem at hand is closely related to fluid flow in porous 3D media with 1D fractures as studied, e.g., in [53, 70, 71]. Hence, mathematical tools for elliptic problems with Dirac measures [72] can be applied. The approach followed here is also similar to that of immersed boundary methods, in which singular source terms are used to represent the structural parts of fluid-structure interactions [112]. A careful formulation of the 1D–3D coupling condition is essential to obtain a stable scheme
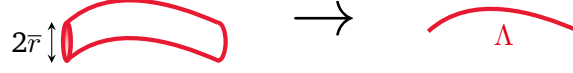
Figure 5.1: 1D wire model on line $\Lambda$ as an approximation to the real wire of radius $\overline{r}$.

yielding a physical solution. We provide elliptic model problems that are used to investigate the numerical errors and the corresponding convergence rates. The transient electrothermal (ET) simulation of a simplified microelectronic chip package as used in industrial applications is presented in Section 7.2. Although we employ the finite integration technique (FIT) for this problem, generalizations to other schemes are straightforward and follow from their close relation to FIT, see Section 3.3.7.

This chapter is structured as follows. In Section 5.1, we present the 1D–3D ET coupled problem including de Rham currents, specific details concerning the 1D–3D coupling, and the corresponding discretization. In Section 5.3, we relate our approach to a finite element (FE) method for flow problems with 1D fissures [53, 70, 71]. Finally, numerical convergence rate studies for a simplified elliptic model problem are presented in Section 5.4. In particular, a simplified 0D–2D coupling, and the straight and bent wire case for the 1D–3D case are investigated.

## 5.1 Continuous Formulation of the 1D−3D Coupling

First, we consider the ET formulation for a single wire embedded in a 3D domain $\mathcal{D}$. Due to the typically very small radius of a wire compared to the domain size $\Delta$, we model a wire as a line $\Lambda$ with zero radius embedded in $\mathcal{D}$, see Figure 5.1. Furthermore, we establish a 1D domain $\overline{\Lambda}$ and connect it to the 3D domain by using a wire parameterization $\Lambda = \{\vec{x}_\Lambda(s), s \in \overline{\Lambda} = (0,1)\}$ defined by $\vec{x}_\Lambda$ that maps from $\overline{\Lambda}$ to $\Lambda$. To distinguish quantities associated to the 3D domain $\mathcal{D}$ from those associated to the 1D domain $\overline{\Lambda}$, we denote the latter by an overline. In the following, a formulation for this coupling is presented for the continuous and for the discrete setting.

We consider capacitive effects only for the thermal 3D part and examine the coupling of an electrokinetic problem with the transient heat equation. Due to the small wire radius, we assume that the resistive losses in the wires are dominating and we neglect the losses in the 3D domain. Here, we use the Dirac distribution $\delta_\Lambda$ to formulate the coupled 1D–3D ET problem as

$$-\nabla \cdot (\sigma(\vec{x}, T)\nabla\varphi(\vec{x}, t)) = q_\sigma(\vec{x}, \overline{\varphi})\delta_\Lambda, \qquad \vec{x} \in \mathcal{D}, t \in I, \tag{5.1a}$$

$$-\frac{\partial}{\partial s}\left(\overline{\sigma}(s, \overline{T})\frac{\partial}{\partial s}\overline{\varphi}(s, t)\right) = \overline{q}_\sigma(s, \varphi), \qquad s \in \overline{\Lambda}, t \in I, \tag{5.1b}$$

$$\rho(\vec{x})c(\vec{x})\partial_t T(\vec{x}, t) - \nabla \cdot (\lambda(\vec{x})\nabla T(\vec{x}, t)) = q_\lambda(\vec{x}, \overline{T})\delta_\Lambda, \qquad \vec{x} \in \mathcal{D}, t \in I, \tag{5.1c}$$

$$-\frac{\partial}{\partial s}\left(\overline{\lambda}(s)\frac{\partial}{\partial s}\overline{T}(s, t)\right) = \overline{q}_\lambda(s, T) + \overline{Q}^{\mathrm{w}}(\overline{\varphi}), \quad s \in \overline{\Lambda}, t \in I, \tag{5.1d}$$

which is understood in a weak sense, and the quantities on the 3D domain have been defined in Sections 2.1, 2.2, and 2.3. In addition, the quantities on the 1D domain are the electric potential $\overline{\varphi}$, the temperature $\overline{T}$, the 1D wire material coefficients given by $\overline{\sigma} = |\overline{A}|\sigma^{\mathrm{w}}/|\frac{\mathrm{d}\vec{x}_\Lambda}{\mathrm{d}s}|$ and $\overline{\lambda} = |\overline{A}|\lambda^{\mathrm{w}}/|\frac{\mathrm{d}\vec{x}_\Lambda}{\mathrm{d}s}|$, where $|\overline{A}|$ is the wire's cross-sectional area, and $\sigma^{\mathrm{w}}$ and $\lambda^{\mathrm{w}}$ are the electric and thermal conductivities of the wire's material. The bidirectional ET coupling is established by the temperature-dependent materials and the 1D resistive losses $\overline{Q}^{\mathrm{w}}$. As mentioned in Section 2.3, the temperature dependence of $\lambda$, $\rho$, and $c$ is neglected. In addition to (2.15),

the 1D–3D formulation requires a coupling for the electric currents (thermal flows) and for the electric potentials (temperatures), manifested on the right-hand sides of (5.1a)–(5.1d). The former is reflected by the contributions $q_\sigma$ ($q_\lambda$) from the 1D to the 3D domain, and by $\overline{q}_\sigma$ ($\overline{q}_\lambda$) from the 3D to the 1D domain. With finite contact conductivities $\beta_\sigma$ ($\beta_\lambda$) between the 1D and the 3D domain, the coupling is similar to [70, 72] and it reads

$$\overline{q}_\sigma = \overline{\beta}_\sigma((\Pi\varphi) \circ \vec{x}_\Lambda - \overline{\varphi}),$$
$$\overline{q}_\lambda = \overline{\beta}_\lambda((\Pi T) \circ \vec{x}_\Lambda - \overline{T}),$$

where $\overline{\beta}_\sigma = |\frac{\mathrm{d}}{\mathrm{d}s}\vec{x}_\Lambda|\beta_\sigma \circ \vec{x}_\Lambda$ and $\overline{\beta}_\lambda = |\frac{\mathrm{d}}{\mathrm{d}s}\vec{x}_\Lambda|\beta_\lambda \circ \vec{x}_\Lambda$. In our setting, we neglect the contact resistance ($\beta \to \infty$), resulting in $q_\sigma$ and $\overline{q}_\sigma$ (as well as $q_\lambda$ and $\overline{q}_\lambda$) canceling each other. This yields the coupling conditions

$$\left|\frac{\mathrm{d}}{\mathrm{d}s}\vec{x}_\Lambda\right|q_\sigma(\vec{x}_\Lambda(s),\overline{\varphi}) = \overline{q}_\sigma(s,\varphi), \qquad s \in \overline{\Lambda}, \tag{5.1e}$$

$$\left|\frac{\mathrm{d}}{\mathrm{d}s}\vec{x}_\Lambda\right|q_\lambda(\vec{x}_\Lambda(s),\overline{T}) = \overline{q}_\lambda(s,T), \qquad s \in \overline{\Lambda}, \tag{5.1f}$$

$$\overline{\varphi}(s,t) = \Pi\varphi(\vec{x}_\Lambda(s),t), \quad s \in \overline{\Lambda}, t \in I, \tag{5.1g}$$

$$\overline{T}(s,t) = \Pi T(\vec{x}_\Lambda(s),t), \quad s \in \overline{\Lambda}, t \in I. \tag{5.1h}$$

Here, the coupling of the electric potential (temperature) is established by the coupling operator $\Pi$ that will be defined in Section 5.1.2. Note that no explicit boundary conditions (BCs) for the 1D case are required due to the strong coupling by $\Pi$. On the other hand, the initial conditions and the BCs for the 3D case have been introduced in Section 2.5.

## 5.1.1 de Rham Currents

After a general introduction of de Rham currents was given in Section 2.8, we now apply the concept to the additional wire contribution. Since de Rham currents are a mathematical tool applicable to any physical discipline, the term *current* applies to electric and thermal quantities equally well. With $\alpha \in \{\sigma, \lambda\}$, the 1-current on the oriented wire curve $\Lambda$ reads

$$\mathcal{I}^\alpha(\vec{v}) := \int_\Lambda I^\alpha(\vec{x})\vec{t} \cdot \vec{v}\, \mathrm{d}\vec{x} \quad \vec{v} \in (C_0^\infty(\mathcal{D}))^3,$$

with a line current $I^\alpha, \vec{x} \in \Lambda$, and the unit tangent vector $\vec{t}$. The space $C_0^k$ contains $k$-times differentiable functions on the computational domain $\mathcal{D}$ (without wires) with homogeneous Dirichlet conditions at the boundary. Note that the current $I^\alpha$ may vary along the line $\Lambda$ since we allow a current exchange between $\Lambda$ and its surrounding.

We recall the de Rham current reformulation of the ET problem given by (2.30) and rewrite it while neglecting electric displacement currents,

$$\boldsymbol{div}\mathcal{J}_\sigma(v) = 0, \tag{5.2a}$$

$$\mathcal{Q}_{\rho c}(v) + \boldsymbol{div}\mathcal{J}_\lambda(v) = \mathcal{Q}_\mathrm{J}(v). \tag{5.2b}$$

From now on, we account for the presence of $\overline{N}$ wires by an additional index $i$ resulting in $\vec{x}_\Lambda^i$ now mapping from $\overline{\Lambda}^i$ to $\Lambda^i$. The embedding into the 3D domain is achieved by considering the 1D current $\overline{I}_\alpha^i := -\overline{\alpha}^i\partial_s\overline{u}_\alpha^i$

and the associated de Rham current $\overline{\mathcal{I}}^{\,i}_\alpha$ [75] and mapping them to the 3D domain by applying a coordinate transformation. Here, $\overline{\alpha} \in \{\overline{\sigma}, \overline{\lambda}\}$, and $\overline{u}_\alpha$ represents $\overline{u}_\sigma := \overline{\varphi}$ and $\overline{u}_\lambda := \overline{T}$. More precisely, we set

$$
\begin{aligned}
\mathcal{I}^i_\alpha(\vec{v}) = \overline{\mathcal{I}}^{\,i}_\alpha((\vec{x}^i_\Lambda)^*\vec{v}) &= \int_\Lambda I^i_\alpha \vec{t}^{\,i} \cdot \vec{v} \, \mathrm{d}\vec{x} \\
&= \int_{\overline{\Lambda}} I^i_\alpha \circ \vec{x}^i_\Lambda \left(\vec{t}^{\,i} \circ \vec{x}^i_\Lambda\right) \cdot \left(\vec{v} \circ \vec{x}^i_\Lambda\right) \left|\frac{\mathrm{d}\vec{x}^i_\Lambda}{\mathrm{d}s}\right| \mathrm{d}s \\
&= \int_{\overline{\Lambda}} \overline{I}^{\,i}_\alpha \left(\vec{t}^{\,i} \circ \vec{x}^i_\Lambda\right) \cdot \left(\vec{v} \circ \vec{x}^i_\Lambda\right) \left|\frac{\mathrm{d}\vec{x}^i_\Lambda}{\mathrm{d}s}\right| \mathrm{d}s,
\end{aligned}
\tag{5.3}
$$

for all $\vec{v} \in (C_0^\infty(\mathcal{D}))^3$. Here, $(\vec{x}^i_\Lambda)^*$ denotes the pullback by $\vec{x}^i_\Lambda$ and we used the substitution $\vec{x} = \vec{x}^i_\Lambda$ and the relation $\overline{I}^{\,i}_\alpha = I^i_\alpha \circ \vec{x}^i_\Lambda$. After applying (2.28) to (5.3), we obtain

$$
\boldsymbol{div}(\mathcal{I}^i_\alpha)(v) = -\int_{\overline{\Lambda}} \overline{I}^{\,i}_\alpha \left(\vec{t}^{\,i} \circ \vec{x}^i_\Lambda\right) \cdot \left(\nabla v \circ \vec{x}^i_\Lambda\right) \mathrm{d}s, \quad \forall v \in C_0^\infty(\mathcal{D}),
\tag{5.4}
$$

and the de Rham current for $\overline{N}$ wires is obtained from the single wire 1-currents as $\mathcal{I}_\alpha := \sum_{i=1}^{\overline{N}} \mathcal{I}^i_\alpha$. What remains is the de Rham current representation of the Joule losses $\mathcal{Q}_\mathrm{J} := \mathcal{Q}^\mathrm{w}$, where $\mathcal{Q}^\mathrm{w}$ describes the 1D Joule losses and the 3D losses are neglected. Using (2.26), these losses are expressed by

$$
\mathcal{Q}^{\mathrm{w},i}(v) = \overline{\mathcal{Q}}^{\mathrm{w},i}((\vec{x}^i_\Lambda)^*v) = \int_{\overline{\Lambda}} \overline{Q}^{\mathrm{w},i} v \circ \vec{x}^i_\Lambda \, \mathrm{d}s, \quad \forall v \in C_0^\infty(\mathcal{D}),
\tag{5.5}
$$

where $\overline{Q}^{\mathrm{w},i} := \overline{\sigma}^i |\partial_s \overline{\varphi}^i|^2$. Again, the contribution for $\overline{N}$ wires is given by $\overline{Q}^\mathrm{w} := \sum_{i=1}^{\overline{N}} \overline{Q}^{\mathrm{w},i}$.

With these definitions at hand, adding (5.4) and (5.5) to (5.2) yields the 1D–3D ET coupled problem in terms of de Rham currents given by

$$
\boldsymbol{div}(\mathcal{J}_\sigma + \mathcal{I}_\sigma)(v) = 0,
\tag{5.6a}
$$

$$
\mathcal{Q}_{\rho c}(v) + \boldsymbol{div}(\mathcal{J}_\lambda + \mathcal{I}_\lambda)(v) = \mathcal{Q}^\mathrm{w}(v),
\tag{5.6b}
$$

for all $v \in C_0^\infty(\mathcal{D})$.

### 5.1.2 Coupling Operator

In this section, we come to the definition of the *coupling operator* $\Pi$ as used in the coupling conditions (5.1g) and (5.1h). Due to the singularity of the 3D solution at $\Lambda$, a direct coupling of the 1D and the 3D solution at $\Lambda$ is not possible. Instead, following the 1D–3D coupling as applied to blood flow through human tissues [72], we use an averaging scheme given by

$$
\Pi u_\alpha := \gamma \frac{1}{2\pi} \int_0^{2\pi} u_\alpha(\vec{x}(s, r_\mathrm{cpl}, \vartheta)) \, \mathrm{d}\vartheta,
\tag{5.7}
$$

where $u_\alpha$ represents $u_\sigma := \varphi$ and $u_\lambda := T$, and $\gamma$ is a scaling coefficient. Note that $(s, r_\mathrm{cpl}, \vartheta)$ refer to cylindrical coordinates around $\Lambda$, where $r_\mathrm{cpl}$ is the coupling radius, see Figure 5.2. Typically, we choose $r_\mathrm{cpl} \gg \overline{r}$, to circumvent resolving the *wire radius* $\overline{r}$ by the mesh.
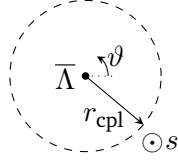
Figure 5.2: Cross-section of a wire with its radius confined to a line $\overline{\Lambda}$ in $s$-direction. Further denoted are the coupling radius $r_{\mathrm{cpl}}$ and the angle $\vartheta$ around the wire. This figure is taken from [48].

For a 3D Laplace problem with Dirac right-hand side as given by (5.1a) and (5.1c), cylindrical coordinates, a domain $\mathcal{D}$ of infinite extension, and an electrically perfectly conducting $\Lambda$ being a *straight line* that coincides with the $z$-axis, the solution has the form

$$u_\alpha(\vec{x}(s,r,\cdot)) = -\frac{q_\alpha(\vec{x}(s,0,\cdot),\overline{u}_\alpha)}{2\pi\alpha} \log\left(\frac{r}{r_0}\right),\tag{5.8}$$

where $r_0$ is a reference radius. Taking this logarithmic dependence into account, a consistent coupling scheme requires the scaling coefficient to be given by

$$\gamma = \log(\overline{r}/r_0)/\log(r_{\mathrm{cpl}}/r_0)$$

such that it scales from the averaged value at the coupling radius $r_{\mathrm{cpl}}$ to the physical value of the line source solution at the wire radius $\overline{r}$. With this definition of $\gamma$, applying (5.7) to (5.8) yields the corresponding 1D solution given by

$$\overline{u}(s) = -\frac{q_\alpha(\vec{x}(s,0,\cdot),\overline{u})}{2\pi\alpha} \log\left(\frac{\overline{r}}{r_0}\right).\tag{5.9}$$

Note that this choice of $\gamma$ is motivated by $\Lambda$ to be electrically perfectly conducting. However, we employ this coefficient $\gamma$ also in the more general case of a finite conductivity. The consistency of the 1D–3D coupling is observed since the usage of (5.9) as source term in (5.1a) and (5.1c) results again in the 3D solution given by (5.8). Finally, for arbitrary curves $\Lambda$, the above solutions are valid in a sufficiently small neighborhood of $\Lambda$.

## 5.2  Discrete Formulation of the 1D−3D Coupling

The discretization of the 1D–3D ET coupled problem is carried out using the FIT [58, 240, 242], mainly motivated by its natural relation to discrete differential forms [33]. We emphasize that no conceptual difficulty would arise when a comparable discretization scheme as, e.g., Whitney FE, would be used instead [29]. A more detailed discussion of this aspect and the numerical discretization errors is given in Sections 3.3.7 and 5.3. In this section, we focus on the discretization of the wire contribution based on the de Rham current formulation (5.6). In particular, we extend (3.9) with the wire contribution such that we obtain

$$\boldsymbol{div}(\mathcal{J}_\sigma + \mathcal{I}_\sigma)(\mathscr{N}_k) = 0,\tag{5.10a}$$

$$\mathcal{Q}_{\rho c}(\mathscr{N}_k) + \boldsymbol{div}(\mathcal{J}_\lambda + \mathcal{I}_\lambda)(\mathscr{N}_k) = \mathcal{Q}^{\mathrm{w}}(\mathscr{N}_k),\tag{5.10b}$$

with BCs to be applied as presented in Section 3.3.5. Here, $\mathscr{N}_k$ refers to the nodal Whitney function associated with node $P_k$, see Section 3.3.7. Notice that continuous de Rham currents are typically defined
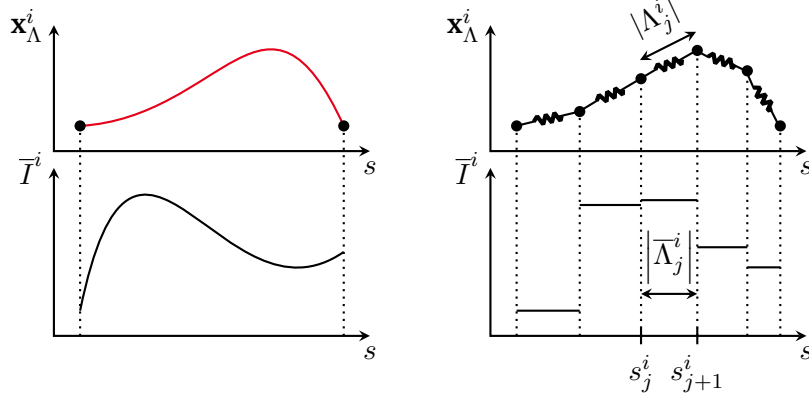
Figure 5.3: 1D discretization of wire $i$ visualized using lumped elements for the example of $N^{1D,i} = 6$ points. The wire's current $\overline{I}^i$ is discretized using piecewise constant basis functions. This figure is taken from [48].

on $C_0^\infty$ while the discrete counterpart is given by discrete de Rham currents defined on functions that are not necessarily zero on the boundary [8]. In the following, we will derive the algebraic expressions for $\mathcal{J}_\alpha$ and $\mathcal{Q}^{\mathrm{w}}$ that are required for the implementation of (5.10). This procedure results in a system of differential algebraic equations (DAEs), which can be implemented and solved for with standard algorithms.

We model each wire part as a 1D element giving a series connection of $N^{1D,i} - 1$ elements for wire $i$. Then, the FIT-discretization of $\overline{I}_\alpha$ results in a piecewise constant discretization on every wire part (curved element) $\Lambda_j^i$ for wire $i = 1, \dots, \overline{N}$ and $j = 1, \dots, N^{1D,i}$ with $|\Lambda_{N^{1D,i}}^i| = 0$, cf. Figure 5.3. In the 1D domain, the partitioning of $\Lambda^i$ results in a partitioning of $\overline{\Lambda}^i$ by dividing $[0,1]$ using the points $\{s_j^i\}$, $j = 1, \dots, N^{1D,i}$. Let $\overline{\mathbf{P}}_s^i \in \{-1, 0, 1\}^{(N^{1D,i}-1) \times N^{1D,i}}$ denote the partial derivative operator of wire $i$, defined as

$$\left(\overline{\mathbf{P}}_s^i\right)_{kj} := \begin{cases} 1, & \text{if } j = k+1, \\ -1, & \text{if } j = k, \\ 0, & \text{otherwise.} \end{cases}$$

Furthermore, in analogy to the 3D material matrices as defined in Section 3.3.2, let

$$\overline{\mathbf{M}}_\alpha^i := \mathrm{diag}\big(\overline{\alpha}_1^i, \dots, \overline{\alpha}_{N^{1D,i}-1}^i\big) \tag{5.11}$$

represent the electrical (thermal) 1D wire mass matrix, where $\overline{\alpha}_j^i = \alpha^{\mathrm{w}} |\overline{A}| / |\Lambda_j^i|$. Then, the FIT discretization of the 1D currents and thermal flow reads

$$\overline{\mathbf{I}}_\alpha^i = -\overline{\mathbf{M}}_\sigma^i \overline{\mathbf{P}}_s^i \overline{u}_\alpha^i. \tag{5.12}$$

$$
\begin{array}{ll}
\begin{matrix}
5\,\bullet \\[2pt]
\qquad \bullet\,4 \\[2pt]
1\,\bullet \diagup 3 \quad \bullet\,2
\end{matrix}
&
\mathbf{R}_{\mathrm{N}} = 
\begin{bmatrix}
1 & 0 & 0 & 0 & 0 \\
0 & 0 & 1 & 0 & 0 \\
0 & 0 & 0 & 1 & 0
\end{bmatrix}
\qquad
\mathbf{X} = 
\begin{bmatrix}
-1 & 0 & 1 & 0 & 0 \\
0 & 0 & -1 & 1 & 0
\end{bmatrix}
\end{array}
$$

Figure 5.4: An exemplary wire located among five arbitrary grid points of which points 1, 3 and 4 coincide with 1D grid points. The corresponding coupling matrices $\mathbf{R}_{\mathrm{N}}$ and $\mathbf{X}$ are shown. This figure is taken from [48].

We proceed by discretizing (5.4) as

$$
\begin{aligned}
\boldsymbol{div}\mathcal{I}^i_\alpha(\mathscr{N}_k) &= -\sum_{j=1}^{N^{1\mathrm{D},i}-1} \overline{I}^i_{\alpha,j} \int_{s^i_j}^{s^i_{j+1}} \left(\frac{\mathrm{d}}{\mathrm{d}s}\vec{x}^i_\Lambda\right)\cdot(\nabla\mathscr{N}_k \circ \vec{x}^i_\Lambda)\,\mathrm{d}s \\
&= -\sum_{j=1}^{N^{1\mathrm{D},i}-1} \overline{I}^i_{\alpha,j}\big(\mathscr{N}_k(\vec{x}^i_\Lambda(s^i_{j+1})) - \mathscr{N}_k(\vec{x}^i_\Lambda(s^i_j))\big) \\
&= -\sum_{j=1}^{N^{1\mathrm{D},i}-1} \overline{I}^i_{\alpha,j}\big((\mathbf{R}^i_{\mathrm{N}})_{j+1,k} - (\mathbf{R}^i_{\mathrm{N}})_{j,k}\big) = -((\overline{\mathbf{P}}^i_s \mathbf{R}^i_{\mathrm{N}})^\top \overline{\mathbf{I}}^i_\alpha)_k,
\end{aligned}
\tag{5.13}
$$

where we have introduced the coupling matrix $\mathbf{R}^i_{\mathrm{N}} \in \mathbb{R}^{N^{1\mathrm{D},i}\times N_{\mathrm{P}}}$ by $(\mathbf{R}^i_{\mathrm{N}})_{j,k} := \mathscr{N}_k(\vec{x}^i_\Lambda(s^i_j))$. Note that, in view of (5.13), no approximation of the possibly bent wire geometry by the underlying 3D grid is required. This constitutes as the main advantage of the proposed 1D–3D coupling approach. To simplify notation, we further introduce $\mathbf{X}^i \in \mathbb{R}^{(N^{1\mathrm{D},i}-1)\times N_{\mathrm{P}}}$ as $\mathbf{X}^i := \overline{\mathbf{P}}^i_s \mathbf{R}^i_{\mathrm{N}}$, see Figure 5.4, and infer the vector representation for $\boldsymbol{div}\mathcal{I}^i_\sigma$ by combining (5.12) and (5.13) as

$$
\big(\boldsymbol{div}\mathcal{I}^i_\alpha(\mathscr{N}_1),\ldots,\boldsymbol{div}\mathcal{I}^i_\alpha(\mathscr{N}_{N_{\mathrm{P}}})\big)^\top = (\mathbf{X}^i)^\top \overline{\mathbf{M}}^i_\alpha \overline{\mathbf{P}}^i_s \overline{\boldsymbol{\varphi}}^i.
$$

We remark that the coupling matrix $\mathbf{R}^i_{\mathrm{N}}$ can be understood as the discrete counterpart of the pullback $(\vec{x}^i_\Lambda)^*$. For the simple case when the 1D points are directly obtained by pulling back the 3D grid points, $\mathbf{R}^i_{\mathrm{N}} \in \{0,1\}^{N^{1\mathrm{D},i}\times N_{\mathrm{P}}}$ becomes an operator that restricts to those points of the grid which are connected to wire $i$ and it contains only one non-zero entry in each row. In the general case of a rectilinear grid, each 1D point is allocated in a grid element defined by 8 points, this operator becomes $\mathbf{R}^i_{\mathrm{N}} \in \mathbb{R}^{N^{1\mathrm{D},i}\times N_{\mathrm{P}}}$, and contains 8 non-zero real-valued entries in each row, obtained by Whitney interpolation. In any case, the sum of all entries in each row is always equal to one.

To account for the 1D Joule losses, we introduce the vector $\overline{\mathbf{Q}}^{\mathrm{w},i}$, allocated at 1D edges, with $N^{1\mathrm{D},i}-1$ entries each given by

$$
\overline{Q}^{\mathrm{w},i}_j = -\overline{I}^i_{\sigma,j}(\overline{\mathbf{P}}^i_s \overline{\boldsymbol{\varphi}}^i)_j,
$$

representing the discretized heat power of wire $i$ with $\overline{I}^i_{\sigma,j}$ being the current at the 1D element $\overline{L}_j$. Starting from (5.5), the Joule losses of the wire part are discretized as

$$
\begin{aligned}
\mathcal{Q}^{\mathrm{w}}(\mathscr{N}_k) &= \sum_{i=1}^{\overline{N}} \sum_{j=1}^{N^{1\mathrm{D},i}-1} \frac{1}{2}\overline{Q}^{\mathrm{w},i}_j\big(\mathscr{N}_k(\vec{x}^i_\Lambda(s^i_{j+1})) + \mathscr{N}_k(\vec{x}^i_\Lambda(s^i_j))\big) \\
&= \sum_{i=1}^{\overline{N}} \sum_{j=1}^{N^{1\mathrm{D},i}-1} \frac{1}{2}\big(\mathbf{X}^i_{\mathrm{abs}}\big)_{j,k}\overline{Q}^{\mathrm{w},i}_j =: (\mathbf{Q}^{\mathrm{w}})_k,
\end{aligned}
\tag{5.14}
$$

where the entries of $\mathbf{X}^i_{\text{abs}}$ are given by the absolute values of the entries of $\mathbf{X}^i$. Let $\overline{\mathbf{T}}^i_{\text{avg}} := \frac{1}{2}\mathbf{X}^i_{\text{abs}}\mathbf{T}$ contain the averaged temperatures for each element of wire $i$. We account for nonlinearities in the wire material parameters as $\alpha^i_j((\overline{\mathbf{T}}^i_{\text{avg}})_j)$.

The last ingredient for the discretization is the discretized version $\mathbf{\Pi} \in \mathbb{R}^{N^{1D} \times N_{\text{P}}}$ of the coupling operator $\Pi$ as introduced in Section 5.1.2. It is obtained by interpolating $\vec{x}^*_\Lambda \Pi \mathbf{u}_\alpha$ to the points of the 1D grid to yield the relation

$$\overline{\mathbf{u}}^i_\alpha = \mathbf{\Pi}^i \mathbf{u}_\alpha, \tag{5.15}$$

for wire $i$. Finally, by introducing the lumped wire stiffness matrix $\mathbf{K}^{\text{w}}_\alpha$ as

$$\mathbf{K}^{\text{w}}_\alpha := \sum_{i=1}^{\overline{N}} \mathbf{K}^{\text{w},i}_\alpha = \sum_{i=1}^{\overline{N}} (\mathbf{X}^i)^\top \overline{\mathbf{M}}^i_\alpha \overline{\mathbf{P}}^i_s \mathbf{\Pi}^i,$$

we conclude

$$\boldsymbol{div}\mathcal{I}_\alpha(\mathscr{N}_k) = (\mathbf{K}^{\text{w}}_\alpha \mathbf{u}_\alpha)_k. \tag{5.16}$$

We recall the stiffness matrix $\mathbf{K}_\alpha = \mathbf{G}^\top \mathbf{M}_\alpha \mathbf{G}$, see Section 3.3.3, and collect the 1D potentials (temperatures) of all wires in a matrix denoted by $\overline{\boldsymbol{\varphi}} \in \mathbb{R}^{\overline{N} \times N^{1D}}$ ($\overline{\mathbf{T}} \in \mathbb{R}^{\overline{N} \times N^{1D}}$). Then, the discrete algebraic 1D–3D ET coupled problem is obtained by extending (3.8) with the wire contributions given by (5.14) and (5.16) and reads

$$\mathbf{K}_\sigma(\mathbf{T})\boldsymbol{\varphi} + \mathbf{K}^{\text{w}}_\sigma(\overline{\mathbf{T}})\boldsymbol{\varphi} = \mathbf{0}, \tag{5.17a}$$

$$\mathbf{M}_{\rho c}\dot{\mathbf{T}} + \mathbf{K}_\lambda \mathbf{T} + \mathbf{K}^{\text{w}}_\lambda \mathbf{T} = \mathbf{Q}^{\text{w}}(\overline{\boldsymbol{\varphi}}, \overline{\mathbf{T}}), \tag{5.17b}$$

where impressed sources have been neglected. With $\widehat{\mathbf{K}}_\alpha(\mathbf{T}) := \mathbf{K}_\alpha(\mathbf{T}) + \mathbf{K}^{\text{w}}_\alpha(\overline{\mathbf{T}})$ and $\widehat{\mathbf{Q}}(\boldsymbol{\varphi}, \mathbf{T}) := \mathbf{Q}^{\text{w}}(\overline{\boldsymbol{\varphi}}, \overline{\mathbf{T}})$, we can write (5.17) in a more compact form given by

$$\widehat{\mathbf{K}}_\sigma(\mathbf{T})\boldsymbol{\varphi} = \mathbf{0}, \tag{5.18a}$$

$$\mathbf{M}_{\rho c}\dot{\mathbf{T}} + \widehat{\mathbf{K}}_\lambda \mathbf{T} = \widehat{\mathbf{Q}}(\boldsymbol{\varphi}, \mathbf{T}). \tag{5.18b}$$

After applying BCs to (5.18) as discussed in Section 3.3.5, we obtain

$$\widehat{\mathbf{K}}^{\text{a}}_\sigma(\mathbf{T})\boldsymbol{\varphi}^{\text{a}} = -\widehat{\mathbf{K}}^{\text{Dir}}_\sigma(\mathbf{T})\boldsymbol{\varphi}^{\text{Dir}}, \tag{5.19a}$$

$$\mathbf{M}^{\text{a}}_{\rho c}\dot{\mathbf{T}}^{\text{a}} + \widehat{\mathbf{K}}^{\Gamma,\text{a}}_\lambda \mathbf{T}^{\text{a}} = \mathbf{R}^{\text{a}}_{\text{P}}\widehat{\mathbf{Q}}_{\text{J}} + \mathbf{R}^{\text{a}}_{\text{P}}\mathbf{M}^\Gamma \mathbf{T}_\infty - \mathbf{M}^{\text{Dir}}_{\rho c}\dot{\mathbf{T}}^{\text{Dir}} - \widehat{\mathbf{K}}^{\Gamma,\text{Dir}}_\lambda \mathbf{T}^{\text{Dir}}, \tag{5.19b}$$

where $\widehat{\mathbf{K}}^{\text{Dir}}_\sigma := \mathbf{R}^{\text{a}}_{\text{P}}\widehat{\mathbf{K}}^{\text{Dir}}_\alpha (\mathbf{R}^{\text{Dir}}_{\text{P}})^\top$, $\mathbf{K}^{\Gamma,\text{a}}_\lambda := \mathbf{R}^{\text{a}}_{\text{P}}(\widehat{\mathbf{K}}_\lambda + \mathbf{M}^\Gamma)(\mathbf{R}^{\text{a}}_{\text{P}})^\top$, and $\mathbf{K}^{\Gamma,\text{Dir}}_\lambda := \mathbf{R}^{\text{a}}_{\text{P}}(\widehat{\mathbf{K}}_\lambda + \mathbf{M}^\Gamma)(\mathbf{R}^{\text{Dir}}_{\text{P}})^\top$. System (5.19) is a DAE and can be integrated in time by using a suitable integration scheme, see Section 3.4. In particular, we use the implicit Euler method together with a fractional step method [236].

## 5.3 Relation to Flow Problems with Fissures

Let us further analyze the 1D–3D coupling and consider a simplified elliptic model problem, which represents, for instance, the electrical subproblem given by (5.1a), (5.1b), and (5.1g). We show that the discretization of this model is closely related to a finite element approach to a 1D–3D coupled problem of

blood flow through tissues with thin tubular structures for the vessels as analyzed in [70–72]. More precisely, we show that the simplified elliptic wire problem is obtained in the limit of infinite permeability of the vessel-tissue interface. We thereby rely on the well-known similarities between the FE method and the FIT approach, see Section 3.3.7. Several papers consider a singular Dirac right-hand side for elliptic problems in an FE context [6, 9]. It should be emphasized that in the present approach, as well as in [53, 70–72], the singular 1D contribution depends on the solution itself, which further complicates the problem.

In a first step, we introduce a weak formulation together with the associated solution spaces for the model problem, where, for simplicity, we assume a linear conductivity. Furthermore, we consider only one wire parameterized by $\Lambda = \{\vec{x}_\Lambda(s), s \in \overline{\Lambda} = (0,1)\}$, such that its index can be omitted. We denote with $u_\alpha$ and $\overline{u}_\alpha$ the 3D and 1D component of

$$-\nabla \cdot (\alpha \nabla u_\alpha) = q_\alpha(\overline{u}_\alpha)\delta_\Lambda + f, \tag{5.20a}$$

$$-\frac{\mathrm{d}}{\mathrm{d}s}\left(\overline{\alpha}\frac{\mathrm{d}}{\mathrm{d}s}\overline{u}_\alpha\right) = \overline{q}_\alpha(u_\alpha), \tag{5.20b}$$

where, in comparison to (5.1a)–(5.1d), an arbitrary function $f$ has been added to act as a non-singular source term. A major difficulty in the analysis is the singularity of $u_\alpha$ at $\Lambda$. In particular, $u_\alpha$ exhibits a logarithmic singularity, see Section 5.1.2, and does not belong to the standard space $H^1(\mathcal{D})$. Instead, the solution space can be identified with the weighted Sobolev space $V_\delta := H^1_\delta(\mathcal{D})$, see [70, Section 2], where the weight is given by the distance to $\Lambda$ to the power of $2\delta$ with $\delta \in (0,1)$. On the other hand, the 1D variables belong to the space $\overline{V} := H^1(\overline{\Lambda})$. We consider homogeneous Dirichlet BCs on $\mathcal{D}$ for simplicity and incorporate possible inhomogeneous Dirichlet BCs directly into the solution spaces. The weak form of (5.20a) reads, find $u_\alpha \in V_\delta$, such that

$$\langle \alpha \nabla u_\alpha, \nabla v\rangle_{\mathcal{D}} = (q_\alpha, \mathrm{tr}_\Lambda v)_\Lambda + (f, v)_{\mathcal{D}}, \quad \forall v \in V_{-\delta}, \tag{5.21}$$

where $\langle \cdot, \cdot\rangle_{\mathcal{D}}$ refers to the duality product of $V_\delta$ and $V_{-\delta}$, whereas $(\cdot, \cdot)_{\{\Lambda, \mathcal{D}\}}$ refers to the $L^2$-inner product on $\{\Lambda, \mathcal{D}\}$. Additionally, $\mathrm{tr}_\Lambda$ denotes the trace operator that maps from $V_{-\delta}$ to $L^2(\Lambda)$. In the ET setting of this thesis, the left-hand side of (5.21) represents the divergence of the 3D electric current (thermal flow), whereas the first term on the right-hand side represents the electric current (thermal flow) transport density from the 1D subdomain into the 3D surrounding. The weak form of (5.20b) reads, find $\overline{u}_\alpha \in \overline{V}$, subject to

$$\left(\overline{\alpha}\frac{\mathrm{d}}{\mathrm{d}s}\overline{u}_\alpha, \frac{\mathrm{d}}{\mathrm{d}s}\overline{v}\right)_{\overline{\Lambda}} = (\overline{q}_\alpha, \overline{v})_{\overline{\Lambda}}, \quad \forall \overline{v} \in \overline{V}, \tag{5.22}$$

see [70] for details. In [72], the law for $\overline{q}_\alpha$ is chosen as $\overline{q}_\alpha = \overline{\beta}((\Pi u) \circ \vec{x}_\Lambda - \overline{u}_\alpha)$, where $\overline{\beta} = |\frac{\mathrm{d}}{\mathrm{d}s}\vec{x}_\Lambda|\beta \circ \vec{x}_\Lambda$, and $\beta$ refers to the permeability coefficient for the vessel-tissue blood transfer. Note that the densities $q_\alpha$ and $\overline{q}_\alpha$ in (5.21) and (5.22) are related through $\overline{q}_\alpha = |\frac{\mathrm{d}}{\mathrm{d}s}\vec{x}_\Lambda|q_\alpha \circ \vec{x}_\Lambda$.

The coupled formulation reads, find $(u_\alpha, \overline{u}_\alpha) \in V_\delta \times \overline{V}$ subject to

$$\langle \alpha \nabla u_\alpha, \nabla v\rangle_{\mathcal{D}} + \left(\overline{\alpha}\frac{\mathrm{d}}{\mathrm{d}s}\overline{u}_\alpha, \frac{\mathrm{d}}{\mathrm{d}s}\overline{v}\right)_{\overline{\Lambda}} = \left(\overline{\beta}(\vec{x}_\Lambda^* \Pi u_\alpha - \overline{u}_\alpha), \vec{x}_\Lambda^* v - \overline{v}\right)_{\overline{\Lambda}} + (f, v)_{\mathcal{D}}, \tag{5.23}$$

for all $(v, \overline{v}) \in V_{-\delta} \times \overline{V}$. The corresponding FE formulation reads, find $(u_{\alpha,h}^{\mathrm{FE}}, \overline{u}_{\alpha,h}^{\mathrm{FE}}) \in V_h \times \overline{V}_h$, subject to

$$\langle \alpha \nabla u_{\alpha,h}^{\mathrm{FE}}, \nabla v_h\rangle_{\mathcal{D}} + \left(\overline{\alpha}\frac{\mathrm{d}}{\mathrm{d}s}\overline{u}_{\alpha,h}^{\mathrm{FE}}, \frac{\mathrm{d}}{\mathrm{d}s}\overline{v}_h\right)_{\overline{\Lambda}} = \left(\overline{\beta}(\vec{x}_\Lambda^* \Pi u_{\alpha,h}^{\mathrm{FE}} - \overline{u}_{\alpha,h}^{\mathrm{FE}}), \vec{x}_\Lambda^* v_h - \overline{v}_h\right)_{\overline{\Lambda}} + (f, v_h)_{\mathcal{D}}, \tag{5.24}$$

for all $(v_h, \overline{v}_h) \in V_h \times \overline{V}_h$, representing standard piecewise linear, globally continuous polynomial basis functions. The 3D polynomials coincide with the nodal Whitney basis functions of Section 5.2. The connection from FE to FIT is established by introducing grid-dependent inner products as follows

$$\left\langle \alpha u_{\alpha,h}^{\mathrm{FIT}}, v_h \right\rangle_{\mathcal{D},h} := \mathbf{v}^\top \mathbf{M}_\alpha \mathbf{u}_\alpha, \tag{5.25a}$$

$$(\overline{\alpha}\, \overline{u}_{\alpha,h}^{\mathrm{FIT}}, \overline{v}_h)_{\overline{\Lambda},h} := \overline{\mathbf{v}}^\top \overline{\mathbf{M}}_\alpha \overline{\mathbf{u}}_\alpha = \overline{\mathbf{v}}^\top \mathrm{diag}\big(\overline{\alpha}_1, \ldots, \overline{\alpha}_{N^{1\mathrm{D}}-1}\big) \overline{\mathbf{u}}_\alpha, \tag{5.25b}$$

$$(\overline{\beta}\, \overline{u}_{\alpha,h}^{\mathrm{FIT}}, \overline{v}_h)_{\overline{\Lambda},h} := \overline{\mathbf{v}}^\top \overline{\mathbf{M}}_\beta \overline{\mathbf{u}}_\alpha := \overline{\mathbf{v}}^\top \mathrm{diag}\big(\overline{\beta}_1, \ldots, \overline{\beta}_{N^{1\mathrm{D}}}\big) \overline{\mathbf{u}}_\alpha. \tag{5.25c}$$

Here, $\overline{\mathbf{M}}_\beta$ is implicitly defined and $\overline{\beta}_j = \beta_j |\widetilde{\Lambda}_j|$, where $|\widetilde{\Lambda}_j| = (|\Lambda_{j-1}| + |\Lambda_j|)/2$ is the length of a 1D dual element. Then, we seek $(u_{\alpha,h}^{\mathrm{FIT}}, \overline{u}_{\alpha,h}^{\mathrm{FIT}}) \in V_h \times \overline{V}_h$, subject to

$$\left\langle \alpha \nabla u_{\alpha,h}^{\mathrm{FIT}}, \nabla v_h \right\rangle_{\mathcal{D},h} + \left( \overline{\alpha} \frac{\mathrm{d}}{\mathrm{d}s} \overline{u}_{\alpha,h}^{\mathrm{FIT}}, \frac{\mathrm{d}}{\mathrm{d}s} \overline{v}_h \right)_{\overline{\Lambda},h} = \big(\overline{\beta}(\vec{x}_\Lambda^* \Pi u_{\alpha,h}^{\mathrm{FIT}} - \overline{u}_{\alpha,h}^{\mathrm{FIT}}), \vec{x}_\Lambda^* v_h - \overline{v}_h\big)_{\overline{\Lambda},h} + (f, v_h)_{\mathcal{D},h}. \tag{5.26}$$

Problem (5.26) is equivalent to the matrix system of equations given by

$$\mathbf{G}^\top \mathbf{M}_\alpha \mathbf{G} \mathbf{u}_\alpha = \mathbf{R}_{\mathrm{N}}^\top \overline{\mathbf{M}}_\beta (\mathbf{\Pi} \mathbf{u}_\alpha - \overline{\mathbf{u}}_\alpha) + \mathbf{f}, \tag{5.27a}$$

$$\overline{\mathbf{P}}_s^\top \overline{\mathbf{M}}_\alpha \overline{\mathbf{P}}_s \overline{\mathbf{u}}_\alpha = -\overline{\mathbf{M}}_\beta (\mathbf{\Pi} \mathbf{u}_\alpha - \overline{\mathbf{u}}_\alpha). \tag{5.27b}$$

Multiplying (5.27b) with $\mathbf{R}_{\mathrm{N}}^\top$ and adding it to (5.27a) we obtain

$$\mathbf{G}^\top \mathbf{M}_\alpha \mathbf{G} \mathbf{u}_\alpha + \mathbf{R}_{\mathrm{N}}^\top \overline{\mathbf{P}}_s^\top \overline{\mathbf{M}}_\alpha \overline{\mathbf{P}}_s \overline{\mathbf{u}}_\alpha = \mathbf{f}, \tag{5.28}$$

which is the same as (5.17) without the thermal transient part and the source term $\mathbf{f}$. We note that our coupling does not require the implementation of the complicated boundary term on the right-hand side of (5.24). In contrary to (5.17), the coupling condition (5.15) is not directly contained in (5.27), but recovered in the limit $\beta \to \infty$. In our setting, $\beta$ represents a contact conductivity and hence, we consider the limit of perfect conduction between 1D and 3D part. Indeed, (5.27b) is equivalent to

$$-\big(\overline{\mathbf{M}}_\beta\big)^{-1} \overline{\mathbf{P}}_s^\top \overline{\mathbf{M}}_\alpha \overline{\mathbf{P}}_s \overline{\mathbf{u}}_\alpha = (\mathbf{\Pi} \mathbf{u}_\alpha - \overline{\mathbf{u}}_\alpha), \tag{5.29}$$

and passing to the limit $\beta \to \infty$ yields $\mathbf{\Pi} \mathbf{u}_\alpha - \overline{\mathbf{u}}_\alpha = \mathbf{0}$.

A strategy to bound the total error of the numerical scheme could consist in using the relation to the FE method, established above, and the triangle inequality as

$$\|u_\alpha - u_{\alpha,h}^{\mathrm{FIT}}\| \leq \|u_\alpha - u_{\alpha,h}^{\mathrm{FE}}\| + \|u_{\alpha,h}^{\mathrm{FE}} - u_{\alpha,h}^{\mathrm{FIT}}\|. \tag{5.30}$$

D'Angelo [70] has shown that the FE error of the 3D variable is bounded by

$$\|u_\alpha - u_{\alpha,h}^{\mathrm{FE}}\| \leq C_1 h \|u_\alpha\|_{V_{1+\varepsilon}^2} + C_2 h \|\overline{u}_\alpha\|_{H^1(\Lambda)}, \tag{5.31}$$

with $\varepsilon \in (0, \delta)$, provided that the solution is sufficiently regular, $\beta$ small enough and the mesh grading strong enough. The same estimate was established for the 1D variable in a suitable norm. The norm $\| \cdot \|$ appearing in (5.31) is defined as

$$\| \cdot \| := \|\alpha^{1/2} \nabla \cdot \|_{L_\delta^2(D)},$$

where in $L_\delta^2(D)$ the weight is again given by the distance to $\Lambda$ to the power of $2\delta$. Moreover, $V_{1+\varepsilon}^2$ refers to a Kondratiev-type weighted space, see [70] for details. The second term on the right-hand side of (5.30) represents the difference between the FE method and FIT. It is equivalent to a mass lumping error in an FE context, see [179, 220]. Standard techniques for estimating this error rely on increased smoothness assumptions on the solution and yield an $\mathcal{O}(h)$ bound. In our case, due to the wire singularity, this analysis would be fairly non-standard. Furthermore, the well-posedness of the system (5.28)–(5.29) and the limit $\beta \to \infty$ for the continuous problem (5.23) and its FE approximation (5.24) are not included in [70] and have to be analyzed separately. These analysis steps are beyond the scope of this thesis.

| Parameter | Description | Value |
|-----------|-------------|-------|
| $\Delta$ | Side length of $\mathcal{D}$ | $1\,\mathrm{m}$ |
| $\sigma$ | Conductivity of $\mathcal{D}$ | $1\,\mathrm{S/m}$ |
| $\overline{r}$ | Radius of wire | $1\,\mu\mathrm{m}$ |
| $\overline{A}$ | Cross-sectional area of wire | $\pi\overline{r}^2$ |
| $\sigma^{\mathrm{w}}$ | Conductivity of wire | $10^{15}\sigma$ |
| $r_0$ | Reference radius | $\sqrt{\Delta^2/\pi}$ |
| $\Omega$ | Evaluation domain | $[0, 0.45\Delta] \times [0, \Delta] \times [0, \Delta]$ |

Table 5.1: Descriptions and values of the parameters as used for the numerical thin wire examples [48].

## 5.4 Numerical Examples

In this section, the proposed 1D–3D coupling is verified using elliptic model problems. For all implementations, the temperature dependence of all materials is neglected and thus, linear problems are considered. For all examples presented here, either an analytical or a solution on a very fine mesh was used as the reference. The MATLAB code to generate the presented results is freely available [49]. Additionally, Appendix B presents a verification using a proprietary software as the reference.

The model problems consist of one wire embedded in a homogeneous cube such that an exact representation of the domain $\mathcal{D}$ using a rectilinear grid is possible. These problems are closely related to the point and line source cases as investigated in Figure 3.13. However, the present 1D–3D coupling involves *solution-dependent* singular sources, which further complicates problem. In particular, we consider three different models in this section. First, the coupling is realized point-wise using an external circuitry resulting in a 0D–2D coupling approach. Secondly, a straight wire embedded in the cube is simulated in a 1D–3D coupling approach. Thirdly, the general case of a bent wire is considered. For the first two models, an analytical reference solution is available whereas a fine reference is used to study the convergence of the third model. For these model problems, the electrical problem given by (5.19a) is solved.

The grids $\mathcal{G}$ and $\overline{\mathcal{G}}$ for the 1D and the 3D parts, respectively, and the grading of $\mathcal{G}$ were introduced in Section 3.3.6. For all wires considered in this section, an equidistant 1D grid $\overline{\mathcal{G}}$ is employed and the corresponding step size is denoted by $\overline{h}$. Note that for the numerical implementation, the 1D grid points of $\overline{\mathcal{G}}$ coincide with 3D grid points of $\mathcal{G}$. Therefore, for straight wires and equidistant 3D grids, the 1D step size $\overline{h}$ is always a multiple of the 3D step size $h$.

The considered cubical domain $\mathcal{D}$ is of side length $\Delta = 1\,\mathrm{m}$ and of homogeneous conductivity $\sigma = 1\,\mathrm{S/m}$. In all examples, the wire's radius is $\overline{r} = 1\,\mu\mathrm{m}$ and its cross-sectional area is $\overline{A} = \pi\overline{r}^2$. The conductivity of the wire is given by $\sigma^{\mathrm{w}} = 10^{15}\sigma$ manifesting an electrical example opposing thermal examples for which $\sigma^{\mathrm{w}} \approx 10^2\sigma$. In Appendix B, the verification is also carried out for a thermal example using $\sigma^{\mathrm{w}} = 10^2\sigma$. As discussed in Section 5.1.2, the coupling coefficient $\gamma = \log(\overline{r}/r_0)/\log(r_{\mathrm{cpl}}/r_0)$ is used with a reference radius $r_0$ that we choose as the radius of an equivalent cylindrical, or circular in the 2D case, geometry such that $r_0 = \sqrt{\Delta^2/\pi}$. With *equivalent*, we refer to a geometry of equal cross-sectional area as the cube. All error definitions used in this section are defined in Section 3.6 and the errors are evaluated in the evaluation domain $\Omega = [0, 0.45\Delta] \times [0, \Delta] \times [0, \Delta]$. To resolve $\Omega$, additional grid points are inserted if required. As a reference, Table 5.1 summarizes the description and values of the parameters that were used for all numerical examples in this section.
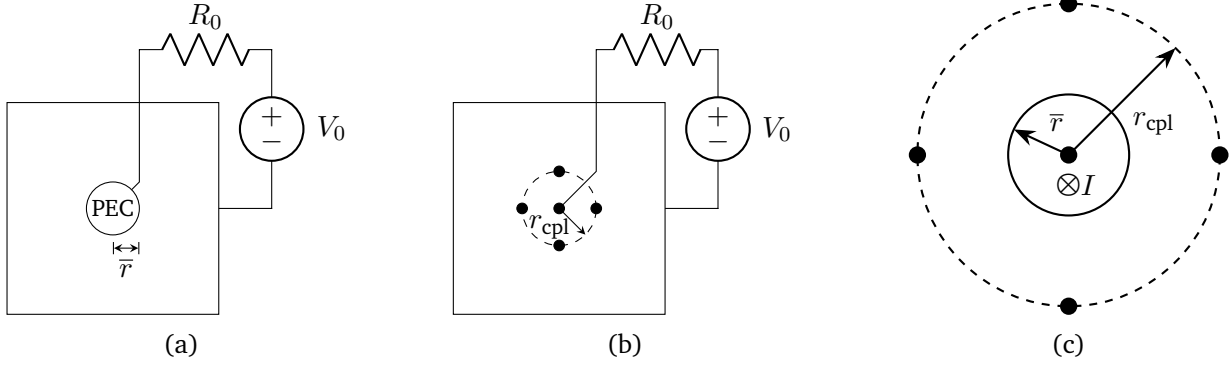
Figure 5.5: (a) 2D cross-section of a brick-shaped resistor with wire-shaped inner PEC electrode connected to an external circuit. (b) Inner electrode is replaced by a 0D representation and the coupling circle is shown as a dashed curve. (c) Magnification of the coupling circle while also depicting the actual wire radius $\bar{r}$ and the wire's current $I$. These figures are taken from [48].

### 5.4.1 0D–2D Coupling

In this section, we consider a brick-shaped resistor with parameters as given in Table 5.1. The PEC wire of radius $\bar{r}$ and the surrounding boundary serve as the resistor's inner and outer electrodes, respectively. We consider the 2D cross-section of the brick-shaped resistor and establish the coupling by connecting the inner and outer electrodes using a series connection of lumped resistor and voltage source, see Figure 5.5a. Applying the parameters as shown in Table 5.1, we use the thin wire assumption for the inner electrode and model it by a single point as shown in Figure 5.5b. Under these conditions, the coupling is identified as a 0D–2D coupling. The dashed circle depicts the coupling circle of radius $r_{\mathrm{cpl}}$ as required by the coupling condition (5.7), shown in a magnified view in Figure 5.5c. To avoid resolving the inner electrode, this coupling radius is chosen to $r_{\mathrm{cpl}} = \max_l\left(L_l^{xy}\right) \gg \bar{r}$, where $L_l^{xy}$ iterates over the lengths of all edges in the 2D domain, i.e., perpendicular to the wire.

Let the resistance per unit length of the resistor be given by

$$R'_{\mathrm{int}} = \frac{\log(r_0/\bar{r})}{2\pi\sigma},$$

let the resistance of the external resistor be $R'_0 = 1\,\Omega\mathrm{m}$, and let the applied voltage be $V_0 = 1\,\mathrm{V}$. Then, the potential $\overline{\varphi}$ at the inner electrode is of interest. For the current per unit length $I'_0 = V_0/(R'_0 + R'_{\mathrm{int}})$ and a homogeneous conductivity $\sigma$, the analytical 2D solution of Laplace's equation reads

$$\varphi(r) = -\frac{I'_0}{2\pi\sigma}\log\left(\frac{r}{r_0}\right), \tag{5.32}$$

in accordance with Section 5.1.2. Here, $r_0 = \sqrt{\Delta^2/\pi}$ is the distance from the origin to the reference potential. After applying the coupling condition (5.7) to (5.32), the 0D potential $\overline{\varphi} = \Pi\varphi$ is obtained.

Adjusting (5.17a) to the here considered 0D–2D coupling, it simplifies to

$$\mathbf{G}^\top \mathbf{M}_\sigma \mathbf{G}\boldsymbol{\varphi} + \mathbf{R}_{\mathrm{N}}^\top G'_0\overline{\varphi} = \mathbf{0}, \tag{5.33}$$

where, by abuse of notation, the matrices are 2D modifications of the usual 3D matrices and $G'_0 = (R'_0)^{-1}$. We exploit the method of manufactured solutions [171, 188] by imposing the reference solution $\varphi$ on the
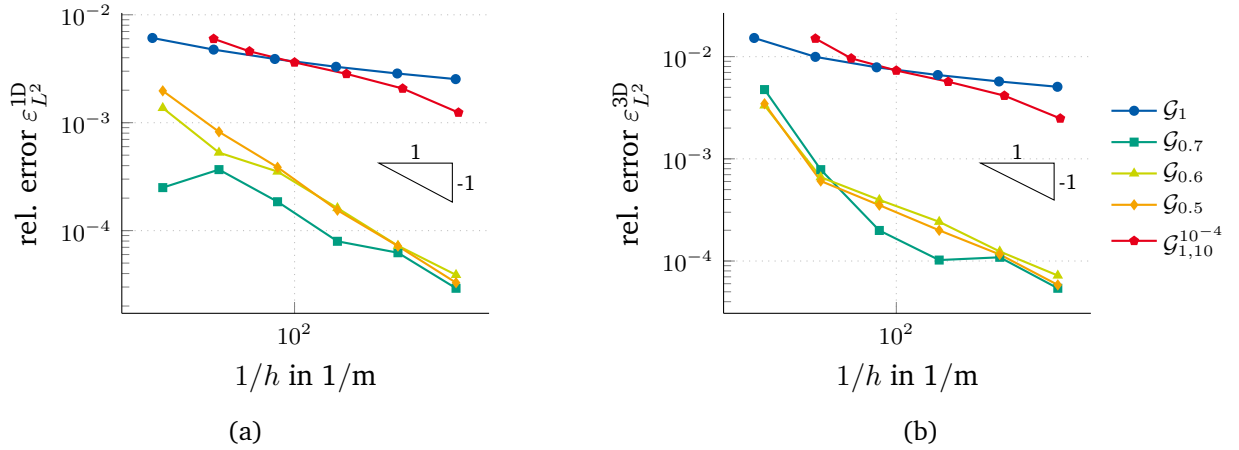
Figure 5.6: Convergence of (a) $\varepsilon_{L^2}^{\text{1D}}$ and (b) $\varepsilon_{L^2}^{\text{3D}}$ with respect to $h$ and different grid choices for the 0D–2D coupling. For the grid notations as used in the legend, see Section 3.3.6. These figures are taken from [48].

boundary $\Gamma$, apply the BCs to (5.33) as described in Section 3.3.5, and solve the resulting system to obtain the FIT solution $\overline{\varphi}_h$. Note that the implementation of FIT in 2D was carried out by using one edge of constant length in $z$-direction together with a symmetric excitation. Thus, the solution behaves two-dimensionally and we denote by $h$ the average edge length of all edges in $x$- and $y$-direction. Using the analytical solution of (5.32) as the reference, the convergence of the relative errors $\varepsilon_{L^2}^{\text{3D}}$ and $\varepsilon_{L^2}^{\text{1D}}$, see Section 3.6, for different grids with respect to $h$ is shown in Figure 5.6. First, we observe for $\varepsilon_{L^2}^{\text{1D}}$ that an equidistant grid $\mathcal{G}_1$ gives a convergence rate far lower than one. Secondly, using a globally graded grid, the convergence order can be improved to a value around one. Thirdly, a locally graded grid $\mathcal{G}_{1,10}^{10^{-4}}$ gives only a slightly higher convergence rate than $\mathcal{G}_1$. The convergence rates for the 2D error $\varepsilon_{L^2}^{\text{3D}}$ behave similarly.

### 5.4.2 1D−3D Straight Wire Coupling

In this section, we consider the 1D–3D coupling of a straight wire to the surrounding 3D domain. The wire is oriented in $z$-direction and located in the $xy$-center of a cube of side length $\Delta$ that we refer to as the computational domain $\mathcal{D}$, see Figure 5.7a. We again use the parameters as summarized in Table 5.1. Additionally, for the locally refined grids $\mathcal{G}_{1,10}^b$ and $\mathcal{G}_{0.5,10}^b$, we use $b = \frac{1}{3} \min_l (L_l^{xy})$. For this setting, according to Section 5.1.2, admissible 3D and 1D solutions are given by

$$\varphi(r, z) = -\frac{I'(z)}{2\pi\sigma} \log\left(\frac{r}{r_0}\right) \quad \text{and} \quad \overline{\varphi}(z) = -\frac{I'(z)}{2\pi\sigma} \log\left(\frac{\overline{r}}{r_0}\right), \tag{5.34}$$

where we choose $I'(z) = I_0' z/\Delta$ and $I_0' = 1\,\text{A/m}$.

The analytical solution (5.34) is impressed on the boundary $\Gamma$. Then, (5.19a) is solved for the 3D solution $\varphi_h$ and the 1D solution $\overline{\varphi}_h$. In Figure 5.8, $\overline{\varphi}_h$ is plotted on $\Lambda$ while $\varphi_h$ is plotted on $\mathcal{D} \setminus \Lambda$ for $\mathcal{G}_{0.5}$, $h \approx 1.822 \times 10^{-2}\,\text{m}$, and $\overline{h} = 3.125 \times 10^{-2}$ to compare $r_{\text{cpl}} = 0\,\text{m}$ and $r_{\text{cpl}} = \max_l(L_l^{xy})$. Although only a small difference is observed, the latter solution is more accurate, see below. In Figures 5.9 and 5.10, the convergence of the errors $\varepsilon_{L^2}^{\text{3D}}$ and $\delta_{L^2}^{\text{1D}}$, respectively, is shown. In Figure 5.9a, the convergence of $\varepsilon_{L^2}^{\text{3D}}$ with respect to $h$ is shown for $\overline{h} = 3.125 \times 10^{-2}$, $r_{\text{cpl}} = \max_l(L_l^{xy})$ and different choices of the 3D grid. For the local
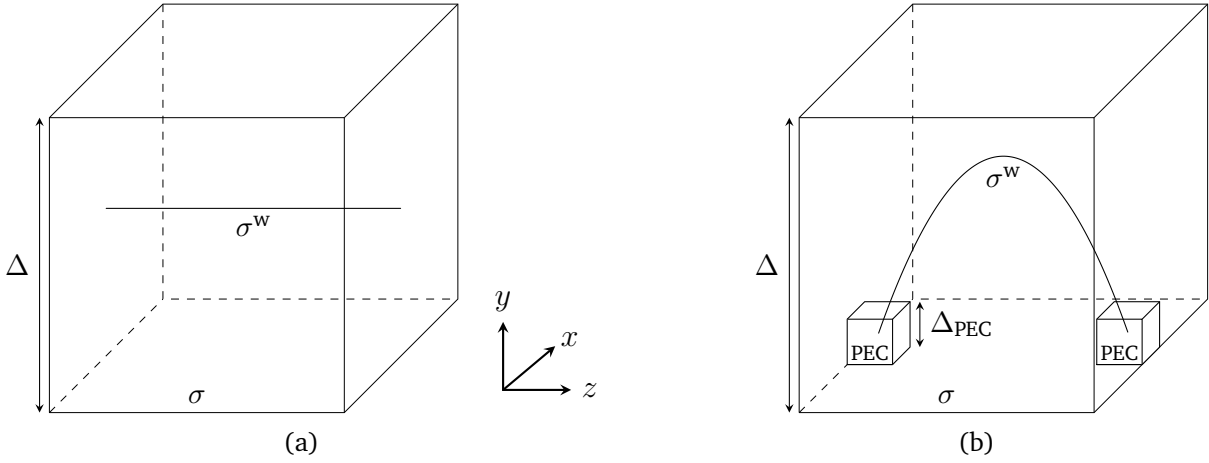
Figure 5.7: (a) Straight and (b) bent wire embedded in a cube of side length $\Delta$. In both cases, the conductivities of cube and wire are annotated and in (b), additional PEC cubes are used. These figures are taken from [48].

gradings $\mathcal{G}_{1,10}^b$ and $\mathcal{G}_{0.5,10}^b$, the asymptotic convergence order is around one, independent of $\mu$ and similar to the order for an equidistant grid $\mathcal{G}_1$. For a globally graded grid $\mathcal{G}_{0.5}$, we observe a significantly higher convergence order than for the grid $\mathcal{G}_1$. In Figure 5.9b, the influence of the coupling radius $r_{\mathrm{cpl}}$ on the error and on the convergence order is investigated. For a zero coupling radius, the 1D solution is taken directly from the 3D solution in the coupling points where the 3D solution is singular. Therefore, as expected, the error is large and the convergence is very slow. For $r_{\mathrm{cpl}} > 0\,\mathrm{m}$, a convergence order of around three is observed while the solution and the order is independent of the exact choice of $r_{\mathrm{cpl}}$. In Figure 5.10, the convergence of $\delta_{L^2}^{\mathrm{1D}}$ is shown with respect to $\overline{h}$ for a fixed but different $h$ for each 3D grid choice. For large $\overline{h}$, a wire is modeled rather by point sources along $\Lambda$ than by a line source. For the limit case of $\overline{h} \to 0$ however, the line source case is recovered and the error with respect to the line source reference solution becomes smaller. The convergence is of almost second order and independent of the 3D grid and/or grading choice. This indicates that the 1D discretization error is dominating for the considered error measure and the considered grids. On the other hand, for the here considered grids, the errors $\varepsilon_{L^2}^{\mathrm{1D}}$, $\varepsilon_{H^1}^{\mathrm{1D}}$, and $\delta_{H^1}^{\mathrm{1D}}$ are smaller than $1 \times 10^{-4}$ and do not show further improvements for a refinement of the 1D grid. This behavior is attributed to a dominance of the 3D discretization error for this setting.

### 5.4.3 1D−3D Bent Wire Coupling

In the general case, thin wires follow arbitrary curves. Therefore, in this section, we investigate the case of a single bent wire. Again, we use the parameters of Table 5.1 on a cube $\mathcal{D}$ as the computational domain. To set up a model of a bent wire with path $\Lambda$, we apply a parameterization using a Bézier curve given by

$$\vec{x}_\Lambda(s) = \begin{pmatrix} d/2 \\ y_0(1-s)^2 + (2y_0 + 4\overline{H})s(1-s) + y_0 s^2 \\ z_0(1-s)^2 + (z_0 + z_1)s(1-s) + z_1 s^2 \end{pmatrix}, \tag{5.35}$$

where we introduced the start coordinate $\vec{x}_0 := (x_0, y_0, z_0)^\top = \vec{x}_\Lambda(0) = (0.5, 0.02, 0.02)^\top\,\mathrm{m}$ and the end coordinate $\vec{x}_1 := (x_1, y_1, z_1)^\top = \vec{x}_\Lambda(1) = (0.5, 0.02, 0.98)^\top\,\mathrm{m}$, as well as the bending height $\overline{H} = 0.7\Delta$. The points

<div align="center">(a)            (b)</div>
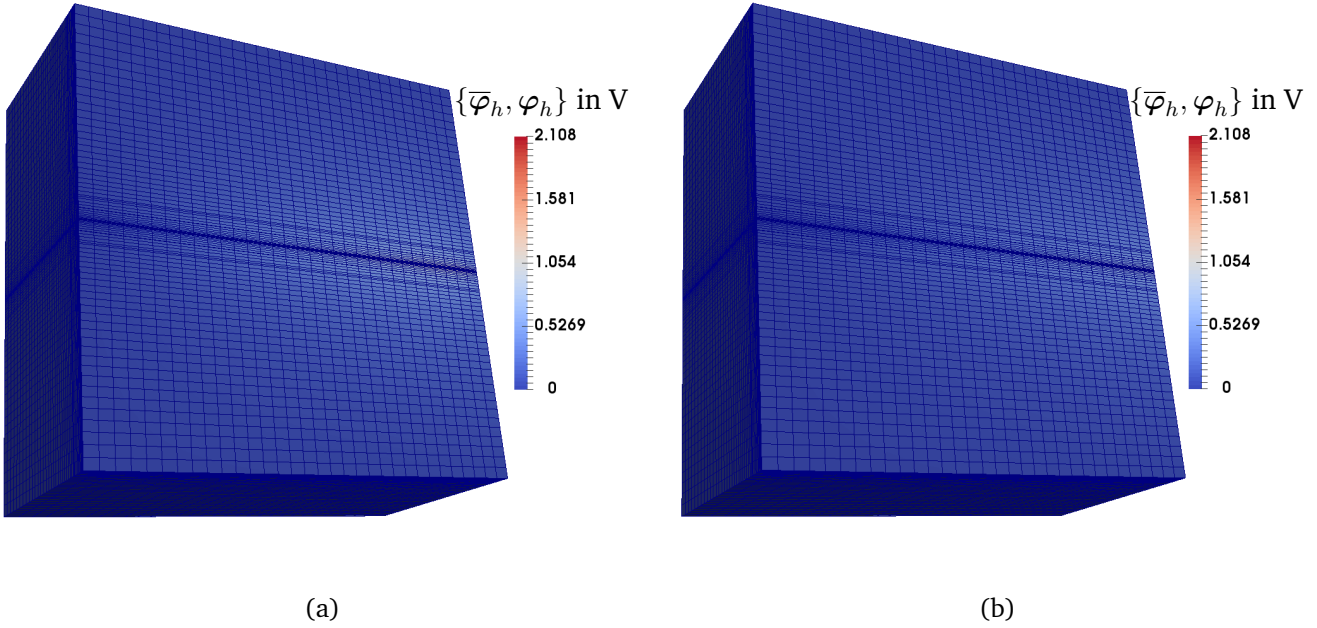
Figure 5.8: Values of $\overline{\varphi}_h$ on $\Lambda$ and $\varphi_h$ on $\mathcal{D} \setminus \Lambda$ for $\mathcal{G}_{0.5}$, $h \approx 1.822 \times 10^{-2}$ m and $\overline{h} = 3.125 \times 10^{-2}$ for the straight wire 1D–3D coupling. The results are shown for (a) $r_{\mathrm{cpl}} = 0\,\mathrm{m}$ and (b) $r_{\mathrm{cpl}} = \max_l(L_l^{xy})$. These figures are taken from [48].



<div align="center">(a)            (b)</div>
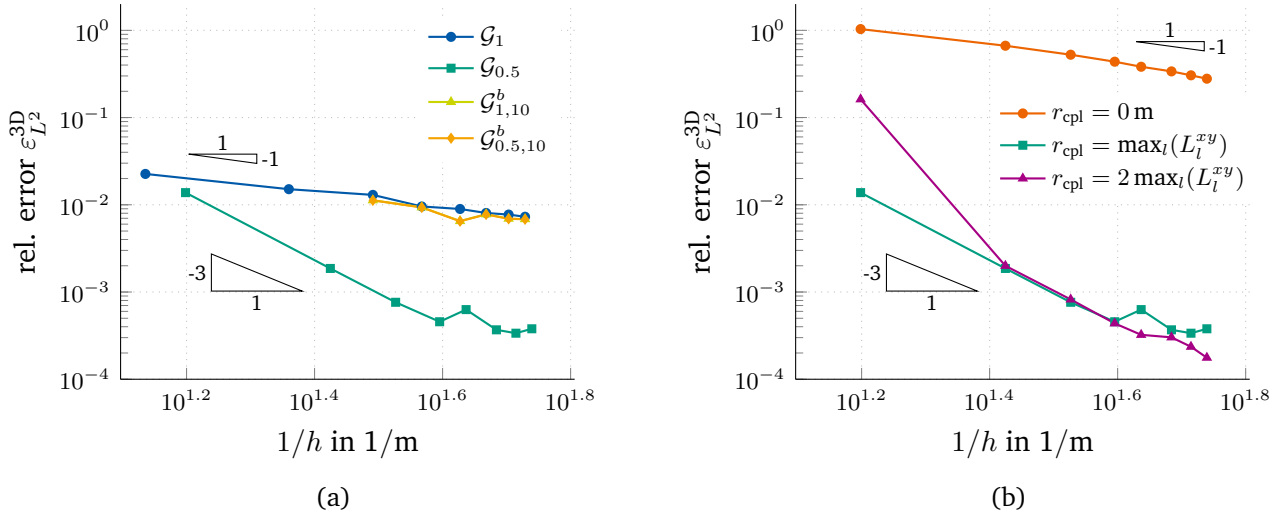
Figure 5.9: Convergence of $\varepsilon_{L^2}^{\mathrm{3D}}$ with respect to $h$ for the straight wire 1D–3D coupling and $\overline{h} = 3.125 \times 10^{-2}$. The results are shown for (a) different grid choices and (b) for $\mathcal{G}_{0.5}$ and different choices of $r_{\mathrm{cpl}}$. For the grid notations as used in the legend, see Section 3.3.6. These figures are taken from [48].
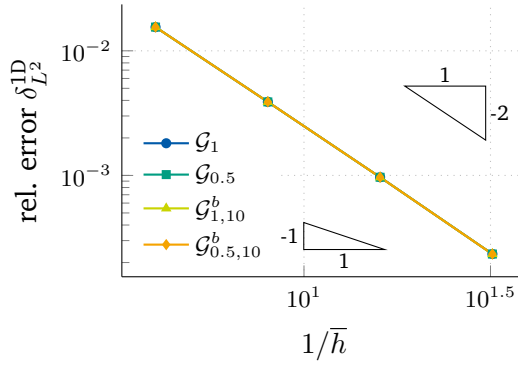
Figure 5.10: Convergence of $\varepsilon_{L^2}^{1D}$ with respect to $\overline{h}$ for a fixed (but different) $h$ for each 3D grid and for the straight wire 1D–3D coupling. For the grid notation as used in the legend, see Section 3.3.6. This figure is taken from [48].

$\vec{x}_0$ and $\vec{x}_1$ of the wire are embedded in PEC cubes of side length $\Delta_{\text{PEC}} = 40\,\text{mm}$, see Figure 5.7b. This setup is in analogy to the typical case that a wire connects two PEC contact pads.

The grids are constructed by starting with an equidistant 1D grid for the parameter $s$ giving a characteristic 1D step size $\overline{h}$. Then, the 3D wire points are determined by (5.35) and, together with the boundary points in each direction, form the basis of the 3D grid. Additional grid lines are inserted due to the error evaluation domain $\Omega$, because of the PEC cubes and between the wire and the boundary $y = \Delta$. The number of grid lines used for the latter is given by $\lfloor N^{1D}/4 \rfloor$, denoting the floor value of the division.

We apply $0\,\text{V}$ at the PEC electrode at $\vec{x}_0$, $1\,\text{V}$ at the PEC electrode at $\vec{x}_1$, solve (5.19a) and consider the 1D solution as quantity of interest (QoI). We use a coupling radius of $r_{\text{cpl}} = 1 \times 10^{-2}/\overline{\kappa}$, where $\overline{\kappa} \approx 6.08\,\text{m}^{-1}$ is the maximum Frenet-Serret curvature [90, 202] along the curve. In the following, we refer to the 1D and 3D reference solutions $\overline{\varphi}$ and $\varphi$ as the solutions computed on a fine grid using $h \approx 1.884 \times 10^{-2}\,\text{m}$ and $\overline{h} = 1.563 \times 10^{-2}$. In Figure 5.11a, $\overline{\varphi}_h$ is shown with respect to the wire parameterization $s$ and Figure 5.11b shows the solution $\overline{\varphi}_h$ on $\Lambda$ and $\varphi_h$ on $\mathcal{D} \setminus \Lambda$ using a 3D visualization. Investigating the convergence of the error, we plot $\Delta_{L^2}^{1D}$ and $\Delta_{L^2}^{3D}$ with respect to $h$ in Figure 5.12 using $\overline{\varphi}$ and $\varphi$ as the reference. For both $\Delta_{L^2}^{1D}$ and $\Delta_{L^2}^{3D}$, we observe a convergence order close to two.

## 5.5 Summary

This chapter introduced the 1D–3D coupling approach as required for an efficient inclusion of thin wires into 3D electrothermal (ET) field simulation. The continuous formulation required de Rham currents and a suitable coupling operator to obtain a consistent bi-directional coupling scheme. Then, the discretization could be carried out by introducing discrete de Rham currents together with nodal Whitney functions. The 1D discretization of the wires is carried out via piecewise constant basis functions. By this 1D–3D coupling, resolving the thin wires in the 3D grid is circumvented, yielding to substantial computational savings. For the underlying theory, we could show that our approach coincides with the problem of fluid flow in porous 3D media with 1D fractures. In particular, the thin wire coupling follows in the limit case of an infinite permeability between the 3D medium and the 1D fracture. Finally, we verified the proposed approach using suitable numerical examples. These examples showed that the deteriorated convergence rates can be alleviated when a graded grid and a non-zero coupling radius are applied.
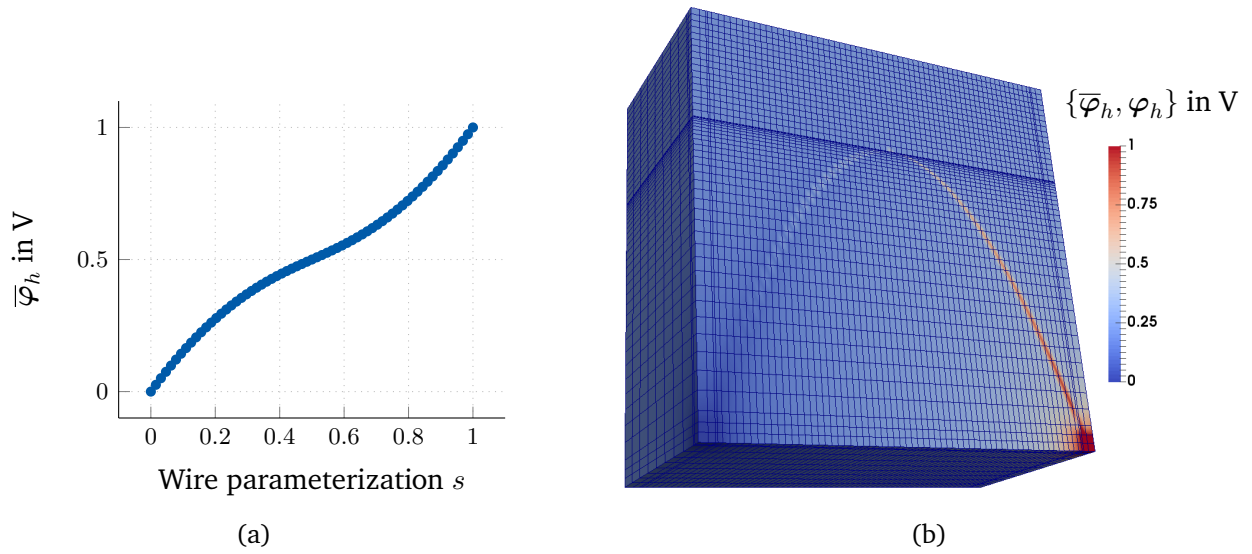
Figure 5.11: Results for the bent wire 1D–3D coupling for $r_{\mathrm{cpl}} = 1 \times 10^{-2}/\overline{\kappa}$. (a) 1D solution $\varphi_h$ with respect to the wire parameterization $s$. (b) Values of $\overline{\varphi}_h$ on $\Lambda$ and $\varphi_h$ on $\mathcal{D} \setminus \Lambda$ for the grid sizes of $h \approx 1.884 \times 10^{-2}\,\mathrm{m}$ and $\overline{h} \approx 1.563 \times 10^{-2}$. These figures are taken from [48].
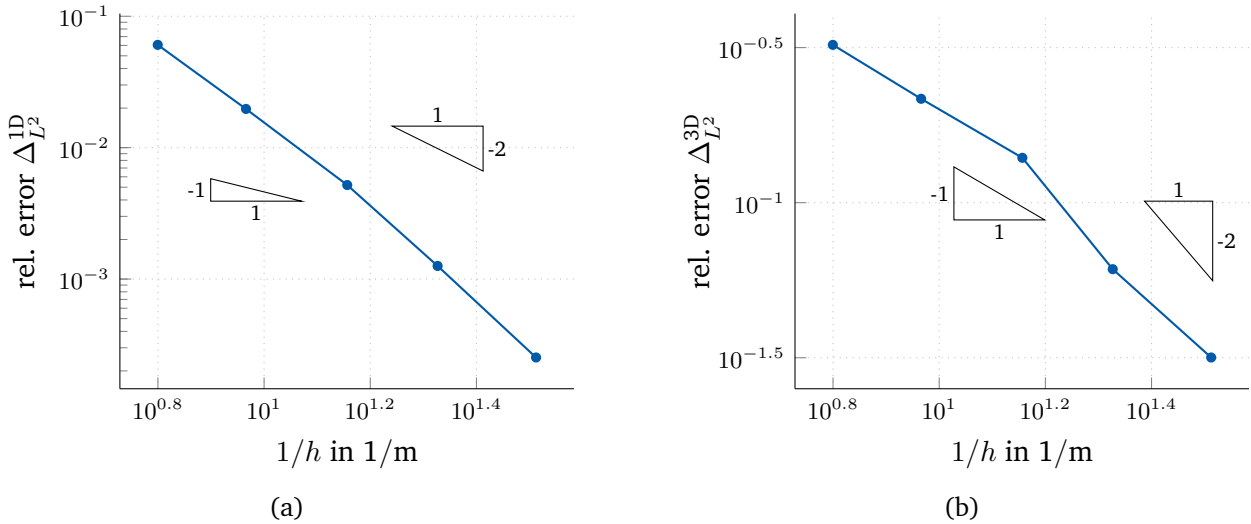


Figure 5.12: Convergence of (a) $\Delta_{L^2}^{\mathrm{1D}}$ and (b) $\Delta_{L^2}^{\mathrm{3D}}$ with respect to $h$ for the bent wire 1D–3D coupling and $r_{\mathrm{cpl}} = 1 \times 10^{e-2}/\overline{\kappa}$. The results were calculated for $\overline{h} = \{0.5, 0.25, 0.125, 0.0625, 0.03125\}$ using a fine reference solution at $\overline{h} = 1.5625 \times 10^{-2}$. These figures are taken from [48].

# 6 Circuit Extraction from 3D Field Problems

In order to analyze complex electromagnetic (EM) problems, three main routes can be identified. First, a numerical approach for solving the full set of Maxwell's field equations offers the advantage of capturing all relevant effects but can be very demanding in terms of computational resources. Secondly, *behavioral models* can be set up by fitting parameters according to obtained measurements. Thirdly, one may use *compact models* to obtain a reduced representation of a complex system. These compact models may contain simple and linear elements such as resistors, capacitors, and inductors; but they may also contain complicated and nonlinear models such as diodes and transistors. Moreover, a generic way to create these models is needed. Section 6.1 provides a survey of currently available techniques. We extend this toolbox by a method that extracts circuit models in an automated procedure. Since the description of circuits is organized in netlists, algorithms to generate the corresponding netlists are provided. Originally, this approach was motivated by problems related to the EU FP-7 project *nanoCOPS* [149].

We closely follow [46, 47] and describe the *automated* generation of a circuit description for 3D electrothermal (ET) and EM field problems. Based on a finite integration technique (FIT) discretization, see Section 3.3, a one-to-one correspondence between grid objects and circuit elements is obtained. In contrast to Yee's finite



(a)                        (b)

Figure 6.1: (a) One grid element is represented by a circuit node. Connections to neighboring cells are carried out via lumped elements. (b) The left branch of the diagram shows the standard solution approach by using a field solver. The right branch illustrates the approach described herein to generate a netlist that is then fed to a circuit simulator. These figures are taken from [47].

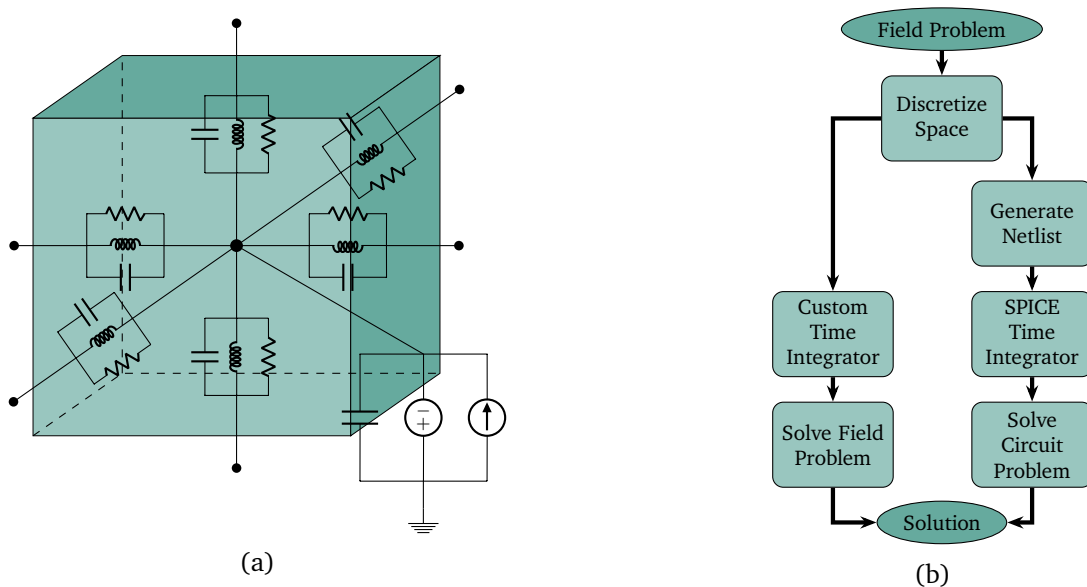difference (FD) scheme employed by Ramachandran et al. [180], FIT is a structure-preserving discretization strategy and its integral quantities translate naturally into the framework of circuit descriptions, see Section 3.3. Alternatively, equivalent approaches such as the cell method (CM) or the finite element (FE) method can be used if an orthogonal dual grid pair is available, see Section 3.3.7. In the present approach, neighboring elements in the primal grid interact via circuit elements as illustrated in Figure 6.1a. Thus, the size of the resulting circuit depends on the geometrical size of the problem and on the resolution of the computational grid. In this manner, we obtain an *exact* grid representation of the field equations that we map transparently into circuit stamps. The values of the lumped elements making up a stamp are directly taken from the entries of the material matrices. The resulting circuit can then be solved with state-of-the-art circuit simulators, circumventing the need for a dedicated field solver including its handling of nonlinearities and time integration. Moreover, existing interfaces between circuit simulators and other useful software packages can be exploited. One example is given by the interface between XYCE and DAKOTA to allow for uncertainty quantification (UQ) methods [1, 128]. Figure 6.1b summarizes this approach. Furthermore, the present methodology allows for straightforward field-circuit coupling by inserting the stamps of the additional lumped devices. Therefore, the circuit extraction is especially useful for an accurate representation of small devices in a larger circuit.

The outline of this chapter is as follows. Section 6.1 presents the currently available techniques to generate and to simulate compact circuit models. Then, the circuit representation of ET field problems is the content of Section 6.2. How to extract circuit stamps for EM field problems is presented in Section 6.3. Finally, we show numerical examples in Section 6.4 to verify the proposed approach.

## 6.1 Available Techniques for Circuit Generation and Simulation

For many years, electrical engineers employ circuits models to describe the behavior of complex devices. One of the first works concerned with equivalent circuits was presented by Kron [134]. Nevertheless, the generation of such compact models can be a tedious task often requiring empirical knowledge. To generate a circuit model, different techniques are available and an overview is provided, e.g., in [161]. For instance, mathematical analysis and physical insight allow to construct circuits representing the problem at hand as presented by Choi et al. [56]. A circuit's topology and the required component values can also be obtained from experimental results as done by Moumouni and Baker [159] and other groups. Another approach followed for instance by Codecasa et al. [63], Eller [83], Wittig et al. [246], and Yang [253], is to apply model order reduction (MOR) techniques directly to the field formulation of the problem from which a circuit description can be found more easily [63]. The resulting elements may have non-physical values, but the system description remains valid. Now, if one is able to represent an EM problem by means of an electric circuit, one can use any circuit simulator to obtain the solution. The most popular representatives are *SPICE programs* that were introduced in the 1970s [164] and are still used as a synonym for circuit solvers. In the beginning, the thermal part was simply treated by an extra node of constant temperature [111, 153]. Later, extensions to deal with thermal problems using circuits were developed *within* the SPICE framework [111, 237]. The mathematical tool employed by most SPICE-like programs is still the modified nodal analysis (MNA) presented by Ho et al. [117] in the 1970s, see Section 2.6.

First approaches to combine numerical field simulation with circuit elements were proposed in the 1990s. These were based on the finite difference time domain (FDTD) scheme [178, 211, 219, 227] because of the topological similarities between the FD scheme and circuits. Later, the insertion of lumped elements

into FE schemes in time or frequency domain was developed by Guillouard et al. [101, 102]. These approaches became known as *field-circuit coupling* and result in hybrid systems that may be difficult to solve. The corresponding mathematical structure of these problems is known as differential algebraic equations (DAEs) [37]. Due to these reasons, the topic of field-circuit coupling has evolved into an important research field [19, 129, 193, 195]. For example, a possible field-circuit coupling method consists of the direct insertion of lumped circuit elements into the field model by applying these to edges of the discretization grid [247].

To *extract compact EM circuits* from a given 3D field problem in a *generic* way, numerous approaches are found in the literature. In the partial element equivalent circuit (PEEC) method presented by Ruehli [184, 185], equivalent circuits are derived from integral equations, allowing for a combined EM circuit solution both in frequency and time domains. However, PEEC requires empirical approximations in addition to the applied discretization. Based on the boundary element method, which is another integral method, Milsom presented the automated circuit generation for quasistatic approximations [156]. The method presented therein yields circuits whose size depends on the electrical dimensions of the problem. Many methods for application-specific circuit extraction based on the device or system response are also available [5, 55, 186]. A methodology for the generation of equivalent circuits based on the semi-discrete Maxwell's field equations was also proposed by Ramachadran et al. [180]. Therein, Yee's discretisation scheme is employed to cast Maxwell's curl equations as the concatenation of interacting fundamental circuits in which voltages and currents model the sought electric and magnetic fields. In this manner, circuit stamps are required for both primal and dual edges and their interaction is organized by voltage-controlled voltage sources (VCVSs) and current-controlled current sources (CCCSs), respectively.

To handle the ET coupling in a circuit simulation framework, two general approaches are mainly available: the *relaxation method* which consists of the iterative coupling of an electric circuit with an external thermal-only field simulator [15, 57, 177, 249], and the *monolithic* approach which consists of the direct coupling of the electric circuit with a thermal circuit [68, 204], see Figure 6.2. The latter approach allows to run the simulation directly on the full ET circuit without any additional software package and thereby avoids the weak coupling between solvers. To *extract compact ET circuits* from a given 3D field problem in a *generic* way, various methods have been proposed. Some of them are based on existing EM simulation methods and have been extended in functionality to also cover the ET case, as for instance done by Lombardi et al. [144] for the PEEC. Generating compact models from the calculated or measured response function is another popular approach and has been followed by Evans et al. and Bernardoni et al. [21, 86]. For thermal problems, methods that derive an equivalent circuit directly from the mesh can also be found [69, 245], but none of them accounts for the ET coupling. Karagol and Bikdash [127] presented an approximate representation obtained from a graph-partitioning algorithm of an FE mesh resulting in a medium-sized ET circuit. Another approach for ET simulations consists of a lumped-element representation of every element in the mesh and has been proposed by Hsu and Vu-Quoc [120].

## 6.2  Circuit Representation of Electrothermal Field Problems

In this section, we neglect inductive effects and derive the circuit representation of transient ET field problems as given by (2.15). Note that the electric part of the problem requires a regularization which is typically done by choosing a reference (*ground*) node with the electric potential $\varphi_{\mathrm{gnd}} = 0$. The ground potential $\varphi_{\mathrm{gnd}}$ is one of the entries of the discrete potential vector $\varphi$ as used in the discretized ET problem given by (3.8). To generate the netlist corresponding to (3.8), the electric and thermal subproblems are considered separately. The
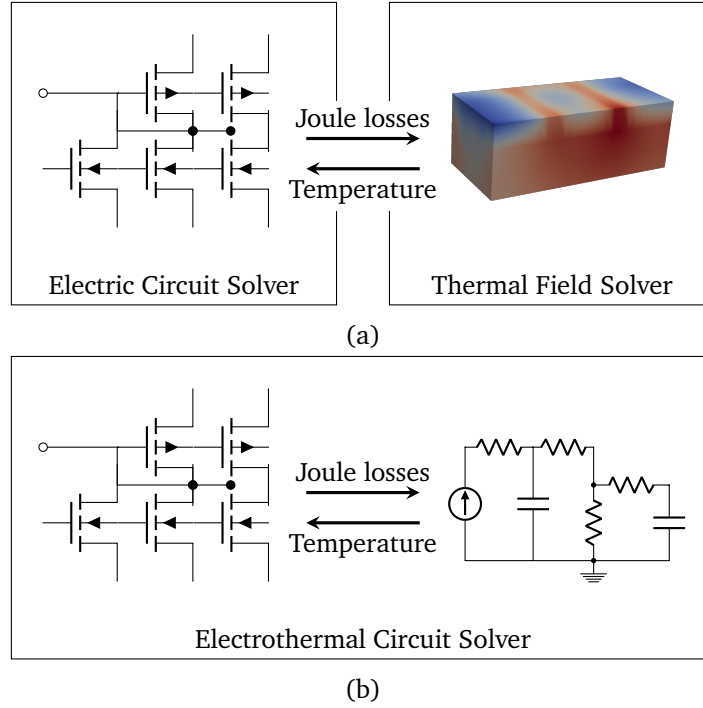
Figure 6.2: Methods for electrothermal simulation using circuit simulators. (a) Relaxation method that couples an electric circuit solver to a thermal field solver. (b) Monolithic coupling which establishes the thermal coupling to electric circuits directly by the introduction of thermal circuits.

connection is subsequently established by the Joule losses and the temperature-dependent electric conductivity. In Sections 6.2.1 and 6.2.2, the netlist generation for the electroquasistatic (EQS) case and the thermal case is presented, respectively. The procedure of including temperature-dependent materials in the circuit description is discussed in Section 6.2.3. As the last step, the implementation of initial and boundary conditions (BCs) is described in Section 6.2.4. With all these ingredients, we are able to formulate an algorithm for the automated ET netlist generation as presented in Section 6.2.5.

## 6.2.1 Electroquasistatic Circuit Representation

We concentrate on the EQS subproblem given by (2.15a). As a reference, let us here repeat its FIT discretization (3.8a), reading

$$\widetilde{\mathbf{S}}\mathbf{M}_\varepsilon\mathbf{G}\dot{\boldsymbol{\varphi}} + \widetilde{\mathbf{S}}\mathbf{M}_\sigma\mathbf{G}\boldsymbol{\varphi} = -\widetilde{\mathbf{S}}\widehat{\widehat{\mathbf{j}}}_{\mathrm{i}}, \tag{6.1}$$

with BCs yet to be applied. Since inductances are neglected in the EQS case, the MNA formulation (2.22) simplifies to

$$\mathbf{A}_\mathrm{C}\mathbf{C}\mathbf{A}_\mathrm{C}^\top\dot{\mathbf{v}} + \mathbf{A}_\mathrm{G}\mathbf{G}\mathbf{A}_\mathrm{G}^\top\mathbf{v} = -\mathbf{A}_\mathrm{I}\mathbf{I}_\mathrm{s} - \mathbf{A}_\mathrm{V}\mathbf{I}_\mathrm{V}, \tag{6.2a}$$

$$\mathbf{A}_\mathrm{V}^\top\mathbf{v} = \mathbf{V}_\mathrm{s}. \tag{6.2b}$$

Then, by inspection of (6.1) and (6.2), we are led to the following equivalences:

- The incidence matrices $\mathbf{A}_\mathrm{C}$ and $\mathbf{A}_\mathrm{G}$ can be identified with the FIT divergence matrix $\widetilde{\mathbf{S}}$.

Figure 6.3: Equivalent electroquasistatic circuit stamp for the exemplary grid point $P_i$ and the grid edge $L_m$ connecting $P_i$ to another grid point $P_j$. This figure is taken from [47].

- The capacitance matrix $\mathbf{C}$ can be identified with the FIT capacitance matrix $\mathbf{M}_\varepsilon$.

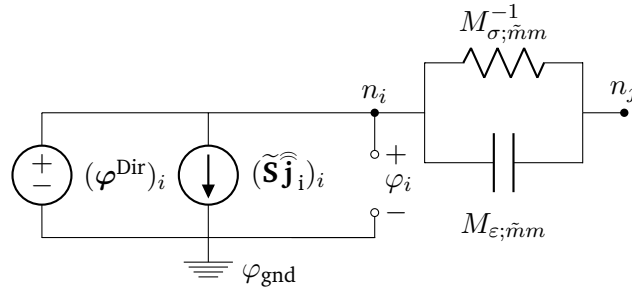- The conductance matrix $\mathbf{G}$ can be identified with the FIT conductance matrix $\mathbf{M}_\sigma$.

- The incidence matrices $\mathbf{A}_V$ and $\mathbf{A}_I$ can be identified with the identity matrix.

- The nodal voltages $\mathbf{v}$ correspond to the FIT degrees of freedom $\boldsymbol{\varphi}$.

- The source currents $\mathbf{A}_I \mathbf{I}_s$ are given by the divergence of the impressed currents $\widetilde{\mathbf{S}}\widehat{\widehat{\mathbf{j}}}_{\mathrm{i}}$.

- The source voltages $\mathbf{V}_s$ correspond to the Dirichlet potentials $\boldsymbol{\varphi}^{\mathrm{Dir}}$, which are defined with the ground node $\varphi_{\mathrm{gnd}}$ as their reference node.

- These equivalences also prevail themselves in the physical units.

In summary, the field-circuit relations for EQS read

$$\mathbf{A}_G \mathrel{\hat{=}} \mathbf{A}_C \mathrel{\hat{=}} \widetilde{\mathbf{S}}, \tag{6.3a}$$

$$\mathbf{G} \mathrel{\hat{=}} \mathbf{M}_\sigma, \quad \mathbf{C} \mathrel{\hat{=}} \mathbf{M}_\varepsilon, \tag{6.3b}$$

$$\mathbf{A}_V \mathrel{\hat{=}} \mathbf{A}_I \mathrel{\hat{=}} \mathbb{I}, \tag{6.3c}$$

$$\mathbf{v} \mathrel{\hat{=}} \boldsymbol{\varphi}, \tag{6.3d}$$

$$\mathbf{I}_s \mathrel{\hat{=}} \widehat{\widehat{\mathbf{j}}}_{\mathrm{i}}, \tag{6.3e}$$

$$\mathbf{V}_s \mathrel{\hat{=}} \boldsymbol{\varphi}^{\mathrm{Dir}}, \tag{6.3f}$$

where $\mathbb{I}$ is the identity matrix of corresponding size. To find the circuit stamp of each edge in the grid upon which (3.8a) holds, we employ the equivalences of (6.3) from which the circuit topology is derived. From (6.3a), conductors and capacitors are placed along the branches of the circuit. According to (6.3b), the values of the conductors and capacitors are directly taken from the corresponding FIT material matrices. To this end, the temperature dependence of the materials is neglected and will be discussed in Section 6.2.3. Current and voltage sources are connected between a circuit node and ground as indicated by (6.3c). Furthermore, (6.3d) shows that the circuit's nodal potentials are equal to the potentials at the grid points. According to (6.3e), the current sources in the circuit represent the divergence of the FIT impressed currents. Finally, if Dirichlet BCs are imposed, voltage sources in the circuit represent FIT Dirichlet potentials as given by (6.3f). More details about the circuit implementation of BCs are given in Section 6.2.4. To summarize, if we consider an exemplary grid point $P_i$ and the grid edge $L_m$ connecting $P_i$ to another grid point $P_j$ (or in other words, one of the 1-cofaces of the 0-cell $P_i$, see Section 3.1), we obtain a representative EQS circuit stamp as shown in Figure 6.3.
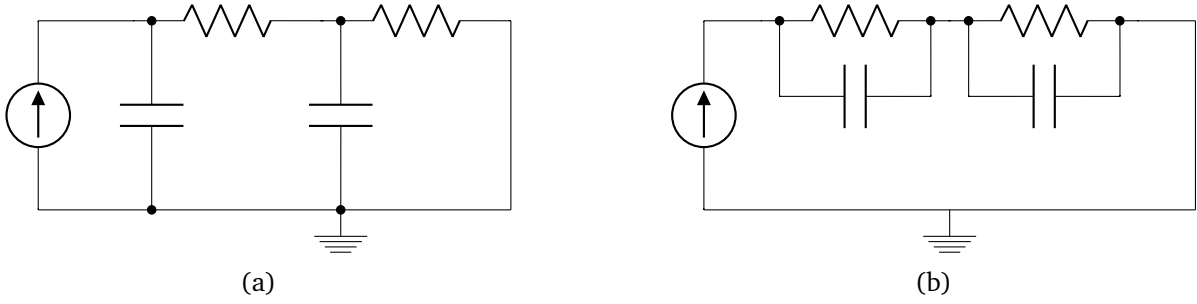
Figure 6.4: Topology of thermal circuit models involving thermal resistors and thermal capacitors. The most prominent examples are known as (a) Cauer models and (b) Foster models.

## 6.2.2 Thermal Circuit Representation

In this section, we describe the circuit representation of the subproblem described by (2.15b). As a reference, let us here repeat its FIT discretization (3.8b), reading

$$\mathbf{M}_{\rho c}\dot{\mathbf{T}} + \mathbf{K}_{\lambda}\mathbf{T} = \mathbf{Q}_{\mathrm{J}} - \widetilde{\mathbf{S}}\widehat{\widehat{\mathbf{q}}}_{\mathrm{i}}. \tag{6.4}$$

By comparing the thermal subproblem (6.4) to the electric subproblem (6.1), the equation structure is very similar. Nevertheless, thermal capacities are not subject to spatial differences and thus do not link to neighboring nodes. Instead, they influence the change rate of the absolute temperature of a node. Thus, thermal capacitors are placed along branches connecting each node to a reference node at zero temperature. This reference node is an additional non-physical node that is introduced to obtain a consistent circuit representation. In the literature, this approach is also referred to as the Cauer model representing a discretized image of the heat flow [16]. An equivalent approach is the Foster model, in which the capacitances are placed between the circuit nodes and the parameters are adjusted accordingly. In the Foster model, the heat propagation is instantaneous and does not account for the fact that an object requires some delay before changing its temperature. Therefore, it represents a valid behavioral model, but does not describe all physical phenomena correctly. Figure 6.4 shows the topology of Cauer and Foster models, while algorithms to transform them into each other are available in the literature [95].

The MNA formulation of (6.2) must be extended by the additional thermal reference ground node such that it reads

$$\widehat{\mathbf{A}}_{\mathrm{C}}\mathbf{C}\widehat{\mathbf{A}}_{\mathrm{C}}^{\top}\dot{\widehat{\mathbf{v}}} + \widehat{\mathbf{A}}_{\mathrm{G}}\mathbf{G}\widehat{\mathbf{A}}_{\mathrm{G}}^{\top}\widehat{\mathbf{v}} = -\widehat{\mathbf{A}}_{\mathrm{I}}\mathbf{I}_{\mathrm{s}} - \widehat{\mathbf{A}}_{\mathrm{V}}\mathbf{I}_{\mathrm{V}}, \tag{6.5a}$$

$$\widehat{\mathbf{A}}_{\mathrm{V}}^{\top}\widehat{\mathbf{v}} = \mathbf{V}_{\mathrm{s}}, \tag{6.5b}$$

with

$$\widehat{\mathbf{A}}_{\mathrm{C}} := \begin{bmatrix} \mathbb{I} & -\mathbf{1} \end{bmatrix}, \qquad \widehat{\mathbf{A}}_{\mathrm{G}} := \begin{bmatrix} \mathbf{A}_{\mathrm{G}} & \mathbf{0} \end{bmatrix}, \qquad \widehat{\mathbf{A}}_{\mathrm{I}} := \begin{bmatrix} \mathbb{I} & -\mathbf{1} \end{bmatrix}, \qquad \widehat{\mathbf{v}}^{\top} := \begin{bmatrix} \mathbf{v}^{\top} & v_{\mathrm{gnd}} \end{bmatrix},$$

where $\mathbf{1}$ is a column vector of ones of appropriate size and $v_{\mathrm{gnd}} = T_{\mathrm{gnd}} = 0$. With these definitions, the equivalences between the thermal formulation of (6.4) and the MNA formulation of (6.5) are readily obtained
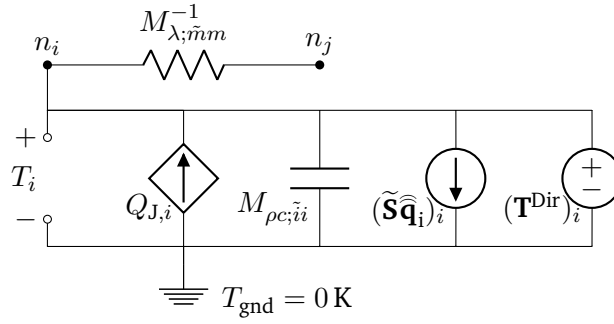
Figure 6.5: Equivalent thermal circuit stamp for the exemplary grid point $P_i$ and the grid edge $L_m$ connecting $P_i$ to another grid point $P_j$. This figure is taken from [47].

as

$$\mathbf{A}_{\mathrm{C}} \cong \mathbf{A}_{\mathrm{V}} \cong \mathbf{A}_{\mathrm{I}} \cong \mathbb{I}, \tag{6.6a}$$

$$\mathbf{A}_{\mathrm{G}} \cong \widetilde{\mathbf{S}}, \tag{6.6b}$$

$$\mathbf{G} \cong \mathbf{M}_\lambda, \quad \mathbf{C} \cong \mathbf{M}_{\rho c}, \tag{6.6c}$$

$$\mathbf{v} \cong \mathbf{T}, \tag{6.6d}$$

$$\mathbf{I}_{\mathrm{s}} \cong \widetilde{\mathbf{S}}\widehat{\mathbf{q}}_{\mathrm{i}} - \mathbf{Q}_{\mathrm{J}} \tag{6.6e}$$

$$\mathbf{V}_{\mathrm{s}} \cong \mathbf{T}^{\mathrm{Dir}}, \tag{6.6f}$$

where $\mathbf{T}^{\mathrm{Dir}}$ represents the temperatures at Dirichlet boundary points, see Section 3.3.5. To derive the circuit stamps upon which (6.4) holds, we employ the equivalences in (6.6) from which the circuit topology is derived. From (6.6a), we infer that capacitances as well as voltage and current sources are directly connected between a circuit node and the thermal ground. As in the EQS case, conductors connect two neighboring nodes in the circuit as seen from (6.6b). According to (6.6c), the values of the conductors and the capacitors are taken directly from the FIT material matrices. To this end, the temperature dependence of the materials is neglected and will be discussed in Section 6.2.3. As seen from (6.6d), the nodal potentials represent the sought temperatures. The current source is the sum of the divergence of impressed heat fluxes and the negative Joule losses, see (6.6e), where the latter are represented by current-controlled current sources (CCCSs). Finally, if Dirichlet BCs are given, these are modeled by voltage sources in the circuit as stated in (6.6f). More details about the circuit implementation of BCs are given in Section 6.2.4. To summarize, if we consider an exemplary grid point $P_i$ and the grid edge $L_m$ connecting $P_i$ to another grid point $P_j$ (or in other words, one of the 1-cofaces of the 0-cell $P_i$, see Section 3.1), we obtain a representative thermal circuit stamp as shown in Figure 6.5.

To further highlight the equivalences between electric and thermal circuits, let us briefly comment on these relationships. Many quantities in electrical circuits can find their equivalent in thermal circuits. For example, electric potentials are equivalent to temperatures while electric currents are equivalent to heat fluxes. Table 6.1 summarizes some of these equivalences.

## 6.2.3 Temperature-Dependent Circuit Components

Most materials exhibit a temperature-dependent behavior. For the problems considered in this thesis, the dominant temperature dependence is attributed to the electric conductivity of the involved materials, see

| Electrical circuit | Thermal circuit |
| :---: | :---: |
| Electric potential (V) | Temperature (K) |
| Electric voltage (V) | Temperature difference (K) |
| Electric current (A) | Thermal heat flux (W) |
| Electric charge (C) | Thermal energy (J) |
| Electric conductance (S) | Thermal conductance (W/K) |
| Electric capacitance (F) | Thermal capacitance (J/K) |

Table 6.1: Equivalences between electric and thermal quantities in circuit representations. This table is taken from [47].

Section 2.3. In this section, we describe how to account for its temperature-dependent when generating the corresponding SPICE netlist. Nevertheless, for the temperature dependence of other materials such as the thermal conductivity or the volumetric mass density, the presented approach can be applied accordingly.

Since the SPICE elements that represent the electric conductivities are conductors allocated to circuit branches, see Section 6.2.1, we first need to define the temperature of a branch $b_m$. To this end, we take the average temperature $T_m^{\mathrm{avg}}$ of the nodes interconnected by the branch $b_m$. In other words, it is the temperature of the 0-faces of the 1-cell $b_m$, see Section 3.1. Assuming that the temperature dependence of the electric conductivity is known, the temperature-dependent electric conductance of branch $b_m$ is given by

$$G_m(T_m^{\mathrm{avg}}) = \sigma_m^{\mathrm{avg}}(T_m^{\mathrm{avg}}) \frac{|\widetilde{A}_m|}{|L_m|}, \tag{6.7}$$

where $\sigma_m^{\mathrm{avg}}$ is the averaged conductivity of the branch $b_m$, in analogy to the one defined for a dual grid facet in Section 3.3.2. As described in Section 6.2.5, we implement (6.7) by means of behavioral sources in the SPICE language.

## 6.2.4  Circuit Implementation of Initial and Boundary Conditions

When a coupled problem of more than one transient differential equation is considered, each subproblem requires its own initial conditions and BCs. Therefore, we impose these conditions on the EQS and thermal subproblems separately. However, certain equivalences allow us to follow the same procedure for both subproblems. For a general overview of initial conditions and BCs for ET problems, see Sections 2.5 and 3.3.5 for the continuous and discrete case, respectively.

Since every SPICE dialect supports directives to specify initial conditions, we impose these conditions directly in the netlist. Dirichlet BCs are represented in the circuit by voltage sources between the Dirichlet nodes and the ground node. Homogeneous Neumann conditions are automatically fulfilled by construction since no edge or branch leaves the domain. For simplicity but without loss of generality, we do not consider inhomogeneous Neumann conditions for the present approach of automated circuit extraction. A Robin BC can be understood as the thermal conduction between a boundary node and an external node $n_\infty$ at the fixed ambient temperature $T_\infty$. Therefore, Robin BCs are represented in the circuit by conductors connected between the boundary nodes and $n_\infty$ as shown in Figure 6.6. We collect the relevant BCs and their circuit implementation in Table 6.2.
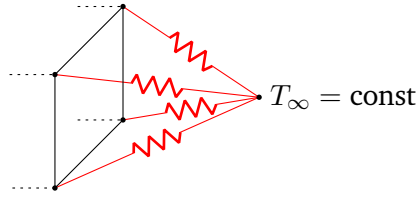
Figure 6.6: Circuit view of Robin BCs. This figure is taken from [47].

| Boundary condition | Implementation |
| --- | --- |
| Dirichlet | Lumped voltage sources |
| Homogeneous Neumann | No edges leaving the circuit |
| Robin | Additional non-physical ground |

Table 6.2: Considered BCs and their circuit implementation. This table is taken from [47].

### 6.2.5 Electrothermal Netlist Generation

Now, we possess all the required ingredients to formulate Algorithm 2 for the automated generation of ET SPICE netlists from field problems discretized by FIT. For every grid edge $L_m$ that connects the grid points $P_i$ and $P_j$ (in other words, $L_m$ is the common 1-coface of the 0-cells $P_i$ and $P_j$), where $i < j$, the temperature-dependent electric conductance, the electric capacitance, and the thermal conductance are written to the netlist to connect the nodes $n_i$ and $n_j$ of the circuit (lines 2–4). Due to the possible nonlinearity of the electric conductivity, see Section 6.2.3, a behavioral source is used, where $V_{ij}$ is the voltage between node $n_i$ and $n_j$. Initial conditions for the electric part can be included using a pre-charging of the electric capacitors, denoted by the directive ic in the netlist. Here, we use zero initial conditions as an example. Additionally, for every grid point $P_i$, the thermal capacitance and the CCCS representing the Joule losses are added to the netlist to connect node $n_i$ and the ground node gnd of the circuit (lines 7 and 8). Initial conditions for the thermal part are stated by specifying the initial temperature $T_0$ as the pre-charging of the thermal capacitors. If $P_i$ is specified as an electric (thermal) Dirichlet node, an additional voltage source connecting node $n_i$ and the ground node of the circuit is inserted (lines 9–14). Furthermore, if an impressed current (heat flux) flows out of the dual element surrounding the point $P_i$, an additional current source is added to the netlist connecting node $n_i$ and the ground node of the circuit (lines 15–20).

## 6.3 Circuit Representation of Electromagnetic Field Problems

In this section, we neglect thermal effects and derive the circuit representation of general 3D EM field problems as given by (2.1). However, the thermo-EM coupling can be established analogously. First, we introduce an auxiliary set notion to collect specific edges and facets of the grid. Then, the Maxwell grid equations (MGEs) given by (3.6) are transparently mapped into an electric circuit that fully describes the problem at hand. For the generation of a circuit description corresponding to the magnetic vector potential formulation, see [47]. Therein, specific circuit stamps that realize absorbing boundary conditions (ABCs) are introduced as well [84, 162].

In the following, we will take sums over specific edges or facets of the grid. Since the edges and facets in the neighborhood of a specific edge $L_m$ are of interest, we introduce sets containing collections of these edges

**Algorithm 2** ET SPICE netlist generation. This listing is taken from [47].

```
 1: for each edge $L_m \in \mathcal{G}$ between primal grid points $P_i$ and $P_j$ do
 2:     write BGel$m$    n$i$    n$j$    I=$V_{ij}G_m(T_m^{\mathrm{avg}})$
 3:     write Cel$m$    n$i$    n$j$    $M_{\varepsilon;\tilde{m}m}$    ic = 0
 4:     write Rth$m$    n$i$T    n$j$T    $M_{\lambda;\tilde{m}m}^{-1}$
 5: end for
 6: for each node $P_i \in \mathcal{G}$ do
 7:     write Cth$i$    n$i$T    gnd    $M_{\rho c;\tilde{i}i}$    ic = $T_0$
 8:     write BLoss$i$    gnd    n$i$T    I=$Q_{\mathrm{J},i}(t)$
 9:     if $P_i$ is electric Dirichlet node then
10:         write VDirEl$i$    n$i$    gnd    $\varphi_i^{\mathrm{Dir}}(t)$
11:     end if
12:     if $P_i$ is thermal Dirichlet node then
13:         write VDirTh$i$    n$i$T    gnd    $T_i^{\mathrm{Dir}}(t)$
14:     end if
15:     if an impressed current flows out of $P_i$ then
16:         write IimpEl$i$    n$i$    gnd    $(\widetilde{\mathbf{S}}\widehat{\widehat{\mathbf{j}}}_{\mathrm{i}}(t))_i$
17:     end if
18:     if an impressed heat flux flows out of $P_i$ then
19:         write IimpTh$i$    n$i$T    gnd    $(\widetilde{\mathbf{S}}\widehat{\widehat{\mathbf{q}}}_{\mathrm{i}}(t))_i$
20:     end if
21: end for
```

and facets and label them with the superscript $^m$. Let us remark here that the concepts of algebraic topology, as introduced in Section 3.1, are very useful for a precise definition of the relation between different grid entities. Let $\mathcal{A}^m$ be the set of all facets in which $L_m$ is embedded, or in other words, let $\mathcal{A}^m$ be the set of 2-cofaces of the 1-cell $L_m$, see Section 3.1. For a rectilinear grid, these facets are shown in Figure 6.7. All edges that are embedded in the facets contained in $\mathcal{A}^m$ are collected in the set $\mathcal{L}^m$, where this definition also implies $L_m \in \mathcal{L}^m$. We denote by $\mathcal{L}^{m,0}$ the resulting set after extracting the very edge $L_m$ from $\mathcal{L}^m$, that is $\mathcal{L}^{m,0} := \mathcal{L}^m \setminus \{L_m\}$. In other words, $\mathcal{L}^{m,0}$ contains the 1-cells that belong to the boundary of the chain given by the linear combination of all 2-cells in $\mathcal{A}^m$. Additionally, we denote the sets of edges that form the boundary of a facet $A_k \in \mathcal{A}^m$ by $\mathcal{L}_k^m$ and $\mathcal{L}_k^{m,0}$, where again, $\mathcal{L}_k^{m,0}$ does not contain the edge $L_m$. The definitions of the sets $\mathcal{L}^m$, $\mathcal{L}^{m,0}$, $\mathcal{L}_k^m$ and $\mathcal{L}_k^{m,0}$ are visualized in Figure 6.7 for the case of a rectilinear grid. For such a grid, $\mathcal{L}^m$, $\mathcal{L}^{m,0}$, $\mathcal{L}_k^m$ and $\mathcal{L}_k^{m,0}$ contain 13, 12, 4 and 3 edges, respectively. Lastly, the dual edges that form the boundary of the dual facet $\widetilde{A}_m$ are collected in the set $\widetilde{\mathcal{L}}_{\tilde{m}}^m$.

We now derive the circuit description that represents the MGEs given by (3.6). The goal is to find an expression for the electric voltage on one primal edge such that a circuit stamp for each edge is obtained. Let $L_m$ be the edge of interest with its corresponding dual facet $\widetilde{A}_m$. To find the voltage $\widehat{e}_m$ on $L_m$, let us consider the pair of interlocked oriented facets $A_k$ and $\widetilde{A}_m$ as illustrated in Figure 6.8. For this part of the grid, it suffices to consider only the $k$-th row of (3.6a) and the $\tilde{m}$-th row of (3.6b) giving

$$-\sum_{n \in \mathcal{L}_k^m} C_{kn} \widehat{e}_{k;n} = M_{\nu;\tilde{k}k}^{-1} \frac{\mathrm{d}\widehat{h}_{\tilde{k}}}{\mathrm{d}t}, \tag{6.8a}$$

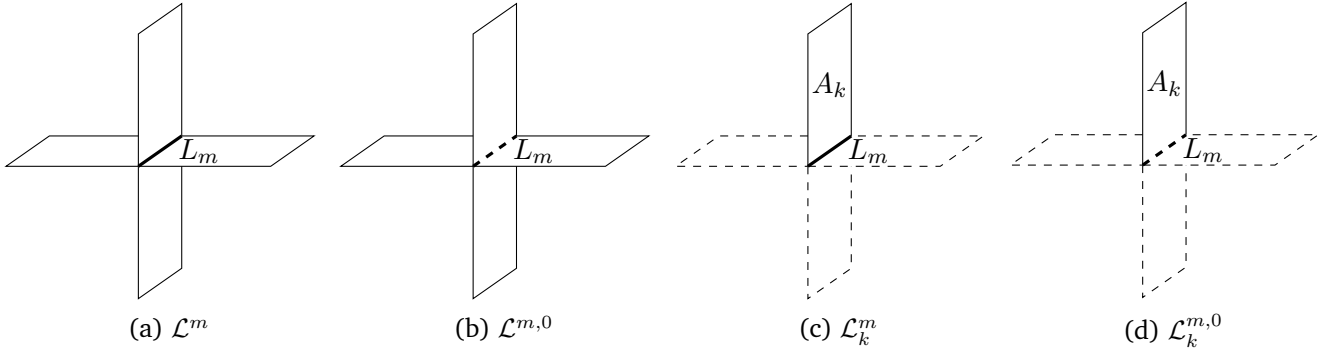(a) $\mathcal{L}^m$      (b) $\mathcal{L}^{m,0}$      (c) $\mathcal{L}_k^m$      (d) $\mathcal{L}_k^{m,0}$

Figure 6.7: Edge $L_m$ and the four facets collected in $\mathcal{A}^m = \{A_1, \ldots, A_4\}$ for a 3D rectilinear grid. The highlighted edges illustrate the sets (a) $\mathcal{L}^m$, (b) $\mathcal{L}^{m,0}$, (c) $\mathcal{L}_k^m$, and (d) $\mathcal{L}_k^{m,0}$. These figures are taken from [47].
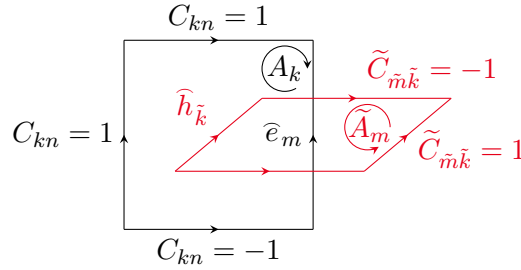


Figure 6.8: A pair of interlocked oriented primal and dual facets $A_k$ and $\widetilde{A}_m$ for the case of a rectilinear grid, respectively. The values of $C_{kn}$ and $\widetilde{C}_{\tilde{m}\tilde{k}}$ for the edges $L_n$ of $A_k$ and the edges $\widetilde{L}_k$ of $\widetilde{A}_m$ are annotated. This figure is taken from [47].

and

$$\sum_{\tilde{k} \in \widetilde{\mathcal{L}}_{\tilde{m}}^m} \widetilde{C}_{\tilde{m}\tilde{k}} \widehat{h}_{\tilde{m};\tilde{k}} = M_{\varepsilon;\tilde{m}m} \frac{\mathrm{d}\widehat{e}_m}{\mathrm{d}t} + M_{\sigma;\tilde{m}m} \widehat{e}_m + \widehat{\widetilde{j}}_{\mathrm{i};\tilde{m}}, \tag{6.8b}$$

where convective currents have been neglected. Note that $m = \tilde{m}$ and $k = \tilde{k}$, and the difference in the notation is used solely to underline whether the object is allocated to the primal or to the dual grid. From (6.8a), the magnetic grid voltage $\widehat{h}_{\tilde{k}}$ allocated to edge $\widetilde{L}_{\tilde{k}}$ reads

$$\widehat{h}_{\tilde{k}} = -M_{\nu;\tilde{k}k} \sum_{n \in \mathcal{L}_k^m} C_{kn} \int \widehat{e}_{k;n} \, \mathrm{d}t. \tag{6.9}$$

By inserting (6.9) in (6.8b) for all $\widehat{h}_{\tilde{m};\tilde{k}}$, the voltage $\widehat{e}_m$ on edge $L_m$ is implicitly given by

$$- \sum_{\tilde{k} \in \widetilde{\mathcal{L}}_{\tilde{m}}^m} \sum_{n \in \mathcal{L}_k^m} \widetilde{C}_{\tilde{m}\tilde{k}} M_{\nu;\tilde{k}k} C_{kn} \int \widehat{e}_{k;n} \, \mathrm{d}t = M_{\varepsilon;\tilde{m}m} \frac{\mathrm{d}\widehat{e}_m}{\mathrm{d}t} + M_{\sigma;\tilde{m}m} \widehat{e}_m + \widehat{\widetilde{j}}_{\mathrm{i};\tilde{m}}.$$

Since $L_m$ is contained in $\mathcal{L}_k^m$, we can extract the contribution of $L_m$ from the sum on the left-hand side such that

$$M_{\nu;\tilde{m}m}^\Sigma \int \widehat{e}_m \, \mathrm{d}t + \sum_{\tilde{k} \in \widetilde{\mathcal{L}}_{\tilde{m}}^m} \sum_{n \in \mathcal{L}_k^{m,0}} \widehat{\widetilde{j}}_{\mathrm{c};\tilde{m}kn} + M_{\varepsilon;\tilde{m}m} \frac{\mathrm{d}\widehat{e}_m}{\mathrm{d}t} + M_{\sigma;\tilde{m}m} \widehat{e}_m + \widehat{\widetilde{j}}_{\mathrm{i};\tilde{m}} = 0, \tag{6.10}$$
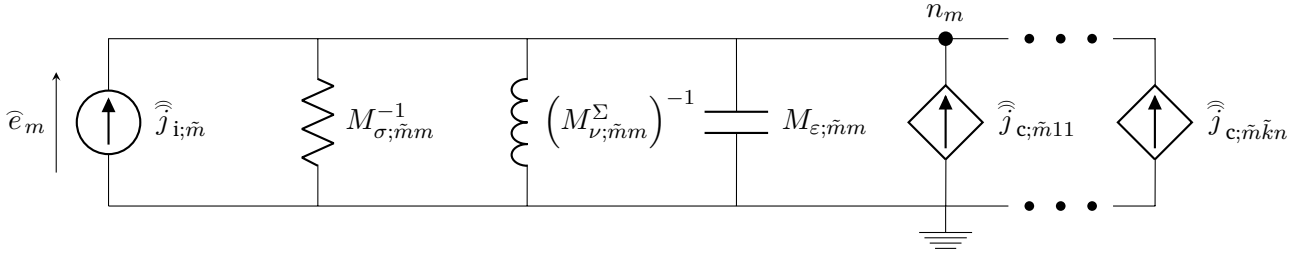
Figure 6.9: Circuit stamp of a primal edge $L_m$ with material matrices mapped into RLC lumped elements as stated by (6.10). VCCSs account for the interaction with neighboring edges. This figure is taken from [47].

where

$$M^{\Sigma}_{\nu;\tilde{m}m} := \sum_{\tilde{k} \in \widetilde{\mathcal{L}}^m_{\tilde{m}}} \widetilde{C}_{\tilde{m}\tilde{k}} M_{\nu;\tilde{k}k} C_{km} = \sum_{\tilde{k} \in \widetilde{\mathcal{L}}^m_{\tilde{m}}} M_{\nu;\tilde{k}k}, \tag{6.11a}$$

$$\widehat{\widehat{j}}_{\mathrm{c};\tilde{m}\tilde{k}n} := \widetilde{C}_{\tilde{m}\tilde{k}} M_{\nu;\tilde{k}k} C_{kn} \int \widehat{e}_{k;n} \, \mathrm{d}t. \tag{6.11b}$$

Still considering the edge $L_m$, $m = \tilde{m}$, $k = \tilde{k}$, and $\tilde{k} \in \widetilde{\mathcal{L}}^m_{\tilde{m}}$, the properties $\mathbf{C} = \widetilde{\mathbf{C}}^\top$, $\widetilde{C}_{\tilde{m}\tilde{k}} \in \{-1, 1\}$ and $C_{km} \in \{-1, 1\}$ result in $\widetilde{C}_{\tilde{m}\tilde{k}} = C_{km}$ and thus, their product equals to unity. However, the product $\widetilde{C}_{\tilde{m}\tilde{k}} C_{kn}$ can be either $-1$ or $1$ as illustrated in Figure 6.8. Equation (6.10) is the Kirchhoff's current law (KCL) associated with the primal edge $L_m$ with $\widehat{e}_m$ representing the voltage drop along the edge. In fact, according to the definitions of the field quantities in (6.10), it is easy to realize that

- $\widehat{e}_m$ has unit of voltage (V),

- $\widehat{\widehat{j}}_{\mathrm{i};\tilde{m}}$ has unit of current (A),

- $M_{\varepsilon;\tilde{m}m}$ is positive and has unit of capacitance (F),

- $M_{\sigma;\tilde{m}m}$ is positive and has unit of conductance (S),

- $M^{\Sigma}_{\nu;\tilde{m}m}$ is positive and has unit of reluctance (H$^{-1}$),

- $\widehat{\widehat{j}}_{\mathrm{c};\tilde{m}\tilde{k}n}$ has unit of current (A).

Thus, by using voltage-controlled current sources (VCCSs) to model $\widehat{\widehat{j}}_{\mathrm{c};\tilde{m}\tilde{k}n}$ accounting for the contributions from neighboring edges, we can directly represent (6.10) with the circuit stamp depicted in Figure 6.9, which preserves the voltage drop between the terminals of $L_m$. There are as many of these stamps as primal edges in the 3D grid $\mathcal{G}$, and all of them interact via VCCSs. The concatenation of these elementary stamps constitutes the electric circuit representing the EM problem at hand.

In Algorithm 3, the steps to generate the netlist corresponding to the EM circuit representation for the entire grid are listed. A circuit stamp, as shown in Figure 6.9, needs to be created for every edge $L_m$ in the grid, being realized by a loop in the algorithm. In each iteration, a resistor, an inductor, and a capacitor with the values taken from the material matrices is added (lines 2–4). If an impressed current source shall be placed along $L_m$, an independent current source is used (lines 5–7). Finally, an inner double loop is required to insert the controlled current sources that model the influence of the edges in the neighborhood. For this

**Algorithm 3** EM SPICE netlist generation. This listing is taken from [47].

1: **for** edge $L_m \in G$ **do**
2:      write R$m$    n$m$    gnd    $M_{\sigma;\tilde{m}m}^{-1}$
3:      write L$m$    n$m$    gnd    $(M_{\nu;\tilde{m}m}^{\Sigma})^{-1}$
4:      write C$m$    n$m$    gnd    $M_{\varepsilon;\tilde{m}m}$
5:      **if** an impressed current is placed on $L_m$ **then**
6:          write I$m$    gnd    n$m$    $\widehat{\widetilde{j}}_{\mathrm{i};\tilde{m}}$
7:      **end if**
8:      **for** edge $\widetilde{L}_k \in \widetilde{\mathcal{L}}_{\tilde{m}}^{m}$ **do**
9:          **for** edge $L_n \in \mathcal{L}_k^{m,0}$ **do**
10:             write F$mn$    gnd    n$m$    $\widehat{e}_{k;n}$    $g_{\tilde{m}\tilde{k}n}^{\mathrm{I}}$
11:          **end for**
12:      **end for**
13: **end for**

purpose, we choose to insert CCCSs being controlled by the current $M_{\nu;\tilde{n}n}^{\Sigma} \int \widehat{e}_{k;n} \, \mathrm{d}t$ with a gain of (lines 8–12)

$$g_{\tilde{m}\tilde{k}n}^{\mathrm{I}} := \widetilde{C}_{\tilde{m}\tilde{k}} M_{\nu;\tilde{k}k} C_{kn} (M_{\nu;\tilde{n}n}^{\Sigma})^{-1}.$$

By abuse of notation, we denote the controlling device by $\widehat{e}_{k;n}$.

## 6.4 Numerical Examples

In this section, the presented methodology to generate circuit stamps representing 3D field problems is applied to several representative numerical examples. In Section 6.4.1, we use the netlist extraction method as described in Section 6.2 on an ET model problem consisting of a 3D field problem corresponding to the series connection of a capacitor and a resistor. Applying an external voltage, the transient heating due to the resulting current is simulated using SPICE, and then compared to a reference solution obtained by a field solver. To quantify the scalability of state-of-the-art circuit simulators, a convergence study with up to 1 000 028 circuit elements and 400 024 unknowns is presented. In Section 6.4.3, we apply the method of circuit extraction for EM field problems as described in Section 6.3 to compute the resonant frequencies of a rectangular cavity with perfect electric conducting (PEC) boundaries. For this example, the availability of an analytic formula for the resonant frequencies permits a direct error assessment. For all presented examples, the MATLAB code to generate the corresponding netlists from the discretized 3D field problem is freely available [51]. All circuit simulations in this section were carried out using the freely available LTSPICE in its version 4.22x with default settings. Thus, LTSPICE uses the modified trapezoidal rule together with an adaptive time integration scheme, and a sparse LU decomposition to solve the linear systems of equations. On the other hand, the field solver is based on FIT, see Section 3.3, uses the fractional step method as described in Section 3.4, and applies MATLAB's backslash operator to solve the resulting linear systems.

### 6.4.1 Electrothermal RC Block

To verify the netlist extraction method for an ET problem, we consider the Joule heating in a 3D field model represented by a series connection of a resistor and a capacitor. The temperature dependence of the electric
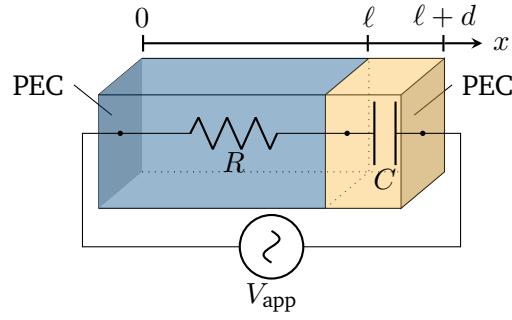
Figure 6.10: Geometry of the ET test case. The series connection of a resistive part and a capacitive part is excited with a voltage source $V_{\text{app}}$ imposed as a Dirichlet condition. This figure is taken from [47].

| Symbol | Description | $0 < x < \ell$ | $\ell < x < \ell + d$ |
|---|---|---|---|
| $\sigma$ (S/m) | Electric conductivity | $1 \times 10^{-4}$ | 0 |
| $\varepsilon_{\text{r}}$ | Relative permittivity | 1 | 3.9 |
| $\lambda$ (W/K/m) | Thermal conductivity | 401 | 1400 |
| $\rho c$ (J/K/cm$^3$) | Volumetric heat capacity | 3.48 | 2.10 |
| $\alpha$ (1/K) | Temperature coefficient | $3.9 \times 10^{-3}$ | – |

Table 6.3: Material properties at the reference temperature $T_0 = 293\,\text{K}$ for the ET test case. This figure is taken from [47].

conductivity is manifested via the temperature coefficient $\alpha = 3.9 \times 10^{-3}\,1/\text{K}$. The relevant configuration is realized by a brick of two different materials as shown in Figure 6.10. The brick is of dimension $0.4 \times 0.1 \times 0.1\,\mu\text{m}^3$, with the resistive part having a length of $\ell = 0.3\,\mu\text{m}$, and the capacitive part having a length of $d = 0.1\,\mu\text{m}$. At $x = 0$ and $x = \ell + d$, PEC electrodes are used. Table 6.3 summarizes all material properties at a reference temperature of $T_0 = 293\,\text{K}$.

An equidistant spatial grid with $9 \times 9 \times 9$ cells is employed and the simulation time amounts to $t_1 = 13\,\mu\text{s}$. We use Algorithm 2 to generate the corresponding netlist, where we use behavioral sources instead of CCCSs for a straightforward incorporation of the Joule losses. For the adaptive time stepping as applied by LTSPICE, we choose initial time step of $\Delta t_{\text{init}} = 0.13\,\mu\text{s}$. To counteract the lower order time stepping scheme of the field solver, the non-equidistant time axis obtained by LTSPICE is refined by a factor of three before it is used for the fractional stepping. A voltage $V_{\text{app}} = 1\,\text{kV}(1 - \exp(-t/\tau))$ with $\tau = 0.1t_1$ is applied at the electrodes as shown in Figure 6.10. Using this setting, two simulations are run. The first run neglects the temperature dependence of the conductivities and thus a linear setting ensues. The second run accounts for the temperature dependence of the electric conductivity via the temperature coefficient $\alpha$ entailing a nonlinear setting. To observe the transient behavior, we select the resistor–capacitor interface point $\vec{x}_0 = (\ell, 0, 0)$ as observation point and plot the potential and temperature in Figure 6.11.

For a quantitative error assessment of the solution, we define the measures

$$\Delta_{\varphi} = \frac{\max_i \|\boldsymbol{\varphi}^{\text{Cir}}(t_i) - \boldsymbol{\varphi}^{\text{FIT}}(t_i)\|_2}{\max_i \|\boldsymbol{\varphi}^{\text{FIT}}(t_i)\|_2}, \qquad \Delta_{\mathbf{T}} = \frac{\max_i \|\mathbf{T}^{\text{Cir}}(t_i) - \mathbf{T}^{\text{FIT}}(t_i)\|_2}{\max_i \|\mathbf{T}^{\text{FIT}}(t_i)\|_2}, \qquad (6.12)$$
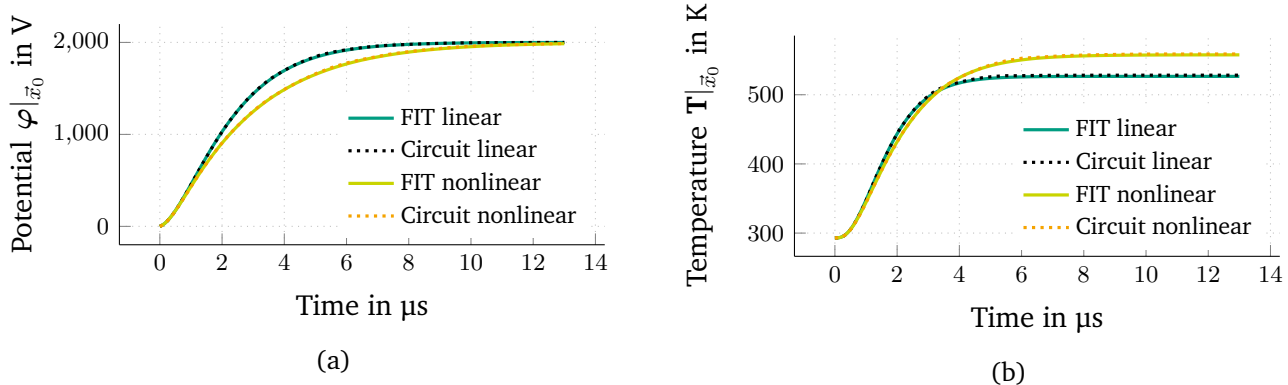
Figure 6.11: Results of the ET test case at $\vec{x} = \vec{x}_0$ for (a) the electric potential $\varphi$ and (b) the temperature **T**. A comparison between the FIT and circuit simulation results is shown for the linear and nonlinear cases. These figures are taken from [47].

where $\varphi^{\mathrm{Cir}}$, $\varphi^{\mathrm{FIT}}$, $\mathbf{T}^{\mathrm{Cir}}$ and $\mathbf{T}^{\mathrm{FIT}}$ are the potential and temperature solution vectors obtained via circuit and FIT simulation, respectively. To calculate these errors, the circuit solution is interpolated to the time axis employed by the FIT solution using cubic spline interpolation. Let us remark that the quantities in (6.12) are not errors in the classical sense since none of the solutions is exact. The computed differences amount to $\Delta_{\varphi}^{\mathrm{lin}} \approx 0.36\,\%$ and $\Delta_{\mathbf{T}}^{\mathrm{lin}} \approx 0.48\,\%$ for the linear case and $\Delta_{\varphi}^{\mathrm{nlin}} \approx 0.42\,\%$ and $\Delta_{\mathbf{T}}^{\mathrm{nlin}} \approx 0.44\,\%$ for the nonlinear case. The remaining error is assumed to be attributed to the different time integrators.

## 6.4.2 Convergence of Circuit Simulation

To analyze the convergence of the solution obtained by circuit simulation, we consider a 1D stationary ET example with an available analytical solution. We use the example from Figure 6.10, which exhibits 1D behavior for a symmetric excitation. In particular, we neglect the transient and impressed terms in (3.8), generate the corresponding netlist using Algorithm 2, and solve the problem using LTSPICE. While using only one element in $y$- and $z$-direction, the number of elements in $x$-direction is varied. Figure 6.12 shows the convergence of the relative error $\varepsilon_{L^2}^{\mathrm{3D}}(\mathbf{T})$ with respect to the analytical solution, giving the expected second order convergence. For the finest resolution of 80 024 unknowns, a relative error of $\varepsilon_{L^2}^{\mathrm{3D}} \approx 5.652 \times 10^{-9}$ is achieved and it stagnates for further refinements. This error is obtained by an LTSPICE simulation which requires about 410 s on an Intel Core i7-3820 with 16 GB of memory. However, more optimized circuit simulators for large circuits are available. Using XYCE [128] to solve the problem on the same machine demonstrates this benefit by requiring only about 40 seconds. Pushing the capabilities of XYCE to a limit, the simulation of a refinement with 1 000 028 circuit elements and 400 024 unknowns finished after about 14 minutes.

## 6.4.3 TE and TM Modes in a Cubic Resonant Cavity

In this section, we verify the method presented in Section 6.3 for the circuit representation of EM field problems. To this end, a lossless rectangular resonant cavity with PEC boundaries and outer dimensions of $a \times b \times d = 0.1 \times 0.2 \times 0.2\,\mathrm{m}^3$ is considered and its resonant frequencies are computed. In such a resonant cavity, depending on the excitation and the BCs, *transverse electric (TE)* and *transverse magnetic (TM)* modes are established at the cavity's *resonant frequencies* [122]. This cavity example is quite illustrative and easy
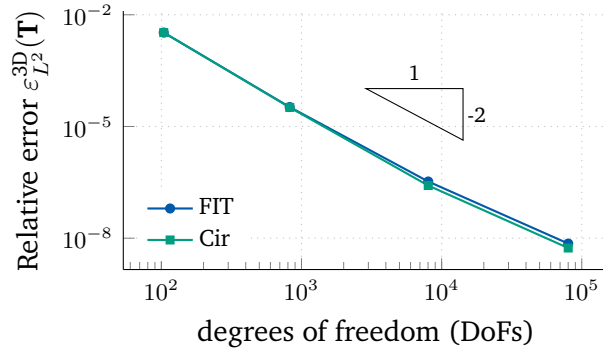
Figure 6.12: Second order convergence in space of the relative temperature error $\varepsilon_{L^2}^{3D}(\mathbf{T})$ obtained by field and circuit simulation with respect to the analytical solution of the stationary ET problem. The result for the circuit simulation is taken from [47].

to implement because it suffices to not print the circuit stamp associated with tangential edges on the wall, meaning that the associated stamps are short-circuited. The homogeneous material within the cavity is specified by the relative permittivity $\varepsilon_{\mathrm{r}} = 2$ and the relative permeability $\mu_{\mathrm{r}} = 1$. The resonant frequencies can be calculated by means of the formula [99]

$$f_{\mathrm{r}}^{mnp} = \frac{c_0}{2\sqrt{\mu_{\mathrm{r}}\varepsilon_{\mathrm{r}}}}\sqrt{\left(\frac{m}{a}\right)^2 + \left(\frac{n}{b}\right)^2 + \left(\frac{p}{d}\right)^2},$$

where $c_0$ is the speed of light and $\{m, n, p\}$ are the indices of the resonant modes, given by the natural numbers including zero. For these resonant frequencies, the TE and TM field components are given by

$$H_z^{mnp} = H_0^{mnp}\cos\left(\frac{m\pi}{a}x\right)\cos\left(\frac{n\pi}{b}y\right)\sin\left(\frac{p\pi}{d}z\right), \tag{6.13a}$$

$$E_z^{mnp} = E_0^{mnp}\sin\left(\frac{m\pi}{a}x\right)\sin\left(\frac{n\pi}{b}y\right)\cos\left(\frac{p\pi}{d}z\right), \tag{6.13b}$$

respectively, where $H_0^{mnp}$ and $E_0^{mnp}$ are the corresponding field amplitudes. For a TE (TM) mode $mnp$ to *exist*, $H_z^{mnp}$ ($E_z^{mnp}$) must not become zero.

To simulate the excitation of modes within the cavity, we discretize the interior of the cavity using a rectilinear grid of 10 elements in each direction and apply PECs upon all cavity walls. Then, we obtain the resonant frequencies by solving the generalized eigenvalue problem given by

$$\widetilde{\mathbf{C}}\mathbf{M}_\nu\mathbf{C}\widehat{\mathbf{e}} = \left(2\pi f_{\mathrm{r;E}}^{\mathrm{FIT}}\right)^2\mathbf{M}_\varepsilon\widehat{\mathbf{e}},$$

where a resonant frequency is denoted by $f_{\mathrm{r;E}}^{\mathrm{FIT}}$. Alternatively, we can use appropriate excitations to analyze the resulting field at a set of given frequencies. For example, TM modes are excited by using an electric current source allocated at a primal edge that is oriented along the positive $z$-direction and attached to the central grid point. In a similar manner, TE modes are excited by means of a looping electric current source located in the cavity center. We then solve the discretized problem given by

$$(\widetilde{\mathbf{C}}\mathbf{M}_\nu\mathbf{C} - \omega^2\mathbf{M}_\varepsilon)\widehat{\mathbf{e}} = -j\omega\widehat{\widehat{\mathbf{j}}}_{\mathrm{i}}$$

for a set of angular frequencies $\omega$, where $\widehat{\widehat{\mathbf{j}}}_{\mathrm{i}}$ is the current source vector whose entries are all zero except at the corresponding source edges. The frequency axis from 0.5 to 3 GHz is discretized using 2000 points for the TM
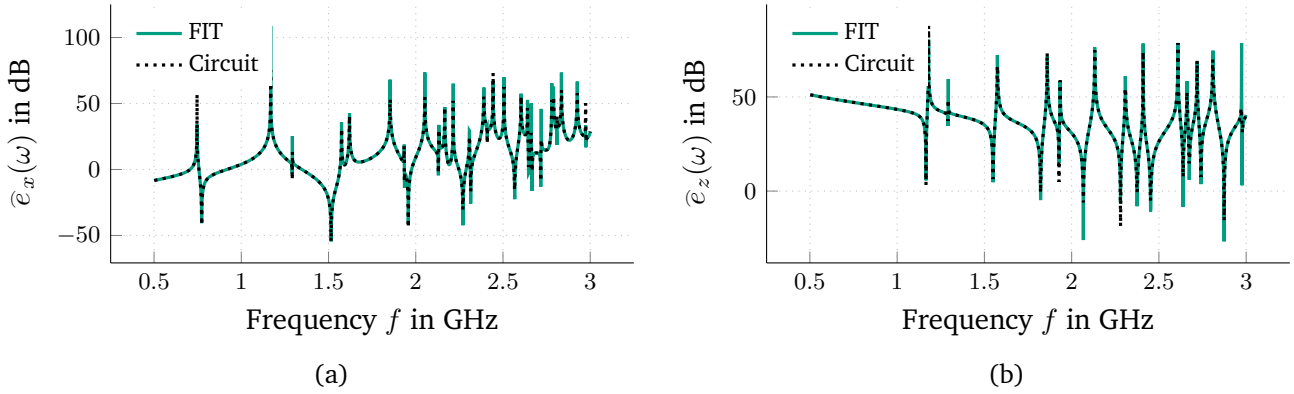
Figure 6.13: Integrated fields with respect to frequency for the (a) TE and (b) TM modes by using FIT and by using circuit simulation. These figures are taken from [47].

| Mode $mnp$ | $f_{\text{r;E}}^{\text{FIT}}$ | $f_{\text{r;TE}}^{\text{Cir}}$ | $f_{\text{r;TE}}^{\text{FIT}}$ | $f_{\text{r;TM}}^{\text{Cir}}$ | $f_{\text{r;TM}}^{\text{FIT}}$ | $f_{\text{r}}^{mnp}$ | $\epsilon_{\text{r;TE}}$ (%) | $\epsilon_{\text{r;TM}}$ (%) |
|---|---|---|---|---|---|---|---|---|
| 011 | 0.746 | 0.746 | 0.747 | — | — | 0.749 | 0.0471 | — |
| 110/101/012/021 | 1.180 | 1.169 | 1.169 | 1.180 | 1.180 | 1.185 | 0.0030 | 0.0086 |
| 111 | 1.293 | 1.293 | 1.293 | 1.293 | 1.293 | 1.298 | 0.0270 | 0.0216 |
| 121 | 1.575 | 1.575 | 1.575 | 1.574 | 1.574 | 1.590 | 0.0354 | 0.0262 |
| 013 | 1.620 | 1.621 | 1.620 | — | — | 1.676 | 0.0050 | — |
| 122 | 1.853 | 1.853 | 1.853 | 1.860 | 1.861 | 1.836 | 0.0244 | 0.0465 |

Table 6.4: Analytical and simulated resonant frequencies in GHz for several resonant modes and the corresponding relative errors. Due to the modes in the cavity being degenerated, an exact identification of the mode indices from the plots in Figure 6.13 is not possible. This table is taken from [47].

excitation and 3000 points for the TE excitation. The results are evaluated on one edge for each excitation type. For the TM case, an edge in positive $z$-direction connected to the central grid point is used while for the TE case, an edge in positive $x$-direction connected to the point (5,6,10) cm is used. In Figure 6.13, the integrated fields $\widehat{e}_x(\omega)$ and $\widehat{e}_z(\omega)$ along these edges are plotted with respect to frequency. From the peaks in the plots, the corresponding resonant frequencies $f_{\text{r;TE}}^{\text{FIT}}$ and $f_{\text{r;TM}}^{\text{FIT}}$ are identified. Note that we have used the function `findpeaks` of MATLAB R2017a to identify the peaks in the plot.

To verify our circuit extraction method for EM problems, we generate the netlist of the resonant cavity according to Algorithm 3 and simulate the resulting circuit in LTSPICE by performing an AC analysis in the same frequency range as before. Due to the integral term in the expression for $\widehat{\widehat{j}}_{\text{c};\tilde{m}\tilde{k}n}$ in lines 8–12 in Algorithm 3, a direct translation into VCCSs is not possible. Instead, behavioral sources or CCCSs can be used. We then identify the circuit voltages corresponding to $\widehat{e}_x(\omega)$ and $\widehat{e}_z(\omega)$ and plot them directly in Figure 6.13 for a comparison. The circuit resonant frequencies $f_{\text{r;TE}}^{\text{Cir}}$ and $f_{\text{r;TM}}^{\text{Cir}}$ are again identified by means of the peaks and we collect the computed resonant frequencies for the first few modes in Table 6.4. Note that, according to (6.13), the TM-mode does not exist for $m = 0$. Additionally, the errors

$$\epsilon_{\text{r;TE}} := \frac{\left| f_{\text{r;TE}}^{\text{FIT}} - f_{\text{r;TE}}^{\text{Cir}} \right|}{f_{\text{r;TE}}^{\text{FIT}}}, \qquad \epsilon_{\text{r;TM}} := \frac{\left| f_{\text{r;TM}}^{\text{FIT}} - f_{\text{r;TM}}^{\text{Cir}} \right|}{f_{\text{r;TM}}^{\text{FIT}}}$$

are presented. For all modes, these errors are smaller than $0.1\,\%$.

## 6.5 Summary

Circuit simulation is still a very important method used by electric engineers to design electronic devices. First, we recalled currently available methods for the construction of these circuits. In the main part of this chapter, we proposed a novel method for the generic automated netlist generation corresponding to 3D electrothermal (ET) field problems. We introduced the individual circuit stamps as required for the electroquasistatic (EQS) and the thermal subproblems. Then, we discussed temperature-dependent materials and the specification of initial and boundary conditions (BCs). With all required information at hand, we were able to provide an algorithm for the automated ET netlist generation such that an exact representation of the discretized field problem is obtained. Moreover, we applied a similar procedure to obtain a circuit representation for general electromagnetic (EM) field problems. To close this chapter, some numerical examples showed the convergence of the circuit simulation when using the netlists as generated by the proposed algorithms.

# 7 Application to Problems in Micro- and Nanoelectronics

In the scope of the nanoCOPS project [149], methods applicable to problems in micro- and nanoelectronics were developed. Particular focus lay on the fields of power electronics and nanoelectronic devices. For the design of nanoelectronic devices, electrothermally coupled field simulation is indispensable [192]. Thanks to the dominating rectangular geometries in these applications, see Figure 1.1a, a finite integration technique (FIT) discretization is very practical; thus, it is also used by Magwel, one of the industrial members of the nanoCOPS-consortium. Moreover, micro- and nanoelectronic chip designs may be decomposed into 2D layers to allow for efficient simulations. This chapter presents two examples of application from the field of micro- and nanoelectronics. However, the area of possible applications is vast and may even originate from other disciplines, such as blood flow in thin tubular structures in a human body [53, 70, 71]. First, electrothermal (ET) simulation for thermal-aware placement in digital circuit designs is discussed in Section 7.1. Secondly, in Section 7.2, we compute failure probabilities of bond wires in a microelectronic chip package using a coupled 1D–3D ET simulation.

## 7.1 Thermal-Aware Placement in Digital Circuit Design

One field of applications in which ET considerations are of high importance is the design of integrated circuits. Such a design process typically consists of the steps known as circuit design, physical design, verification, and fabrication. First, during the circuit design, the desired functionality is built and verified using a circuit simulator. Secondly, a layout of the resulting circuit is generated during the physical design step, which includes the placement and routing of the different standard cells. Thirdly, before the final fabrication, the
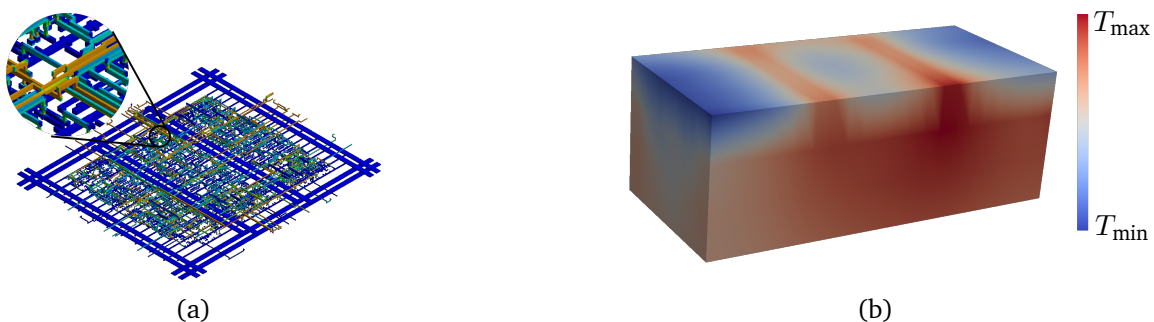


<center>(a)          (b)</center>

Figure 7.1: (a) Current density distribution within the interconnects of a circuit design. (b) Three-dimensional heat map as the result of the in-house FIT solver.

verification step may include different simulation runs to ensure that a robust and functional chip is obtained. It is important that an estimation of a layout's robustness is carried out as early as possible, such that enough time and options for corresponding countermeasures remain available. Especially during the physical design step, thermal considerations are of major importance such that they enter the algorithms for the placement of the standard cells. This requirement becomes increasingly pronounced due to the continuous shrinking of the size of the components in the field of electronics.

One of the most important failure mechanisms in integrated circuits is electromigration, which itself is highly dependent on the temperature. Thus, high temperature locations would be inconvenient for standard cells which are critical to electromigration. Most placement algorithms calculate standard cell locations iteratively; hence, numerical simulations may be executed between these iterations to gain additional information. In the classical approach, numerical simulations are carried out outside the physical design step without a direct feedback for the placement algorithms. However, for an efficient thermal-aware placement, ideally, the numerical simulations must be carried out directly within the placement software to enable a direct feedback for an iterative improvement of the design. One step in this direction was proposed by [22] with the introduction of a layout-driven discretization which reduces discretization time and hence enables an efficient numerical simulation in between the iterations of the placement algorithm.

As an example, Figure 7.1a shows the interconnects of an integrated circuit design. The color indicates the current density of the different connections which results in heat sources due to Joule losses. Computing these losses, the resulting temperature distribution can be obtained as the solution to the heat equation. Using FIT to solve this equation, such an exemplary temperature distribution is shown in Figure 7.1b. One advantage of using FIT for this problem is that the regular placement grid as typically used in electronic designs may be used directly as the rectilinear computational grid for the field solver.

## 7.2 Microelectronic Chip Package

In this section, an industry-relevant microelectronic chip package model is modeled for ET field and circuit simulation. The material for this section was partly taken from [47, 48, 50]. Figures 7.2a and 7.2b show X-ray pictures of the package, where Figure 7.2a shows a top view of the package and Figure 7.2b shows a perspective view. The chip itself resides at the center of the package and is connected via bond wires to the contact pads at the boundary of the package. Since package designers are interested in the reliability of these bond wires, we compute failure probabilities using suitable algorithms, see Chapter 4. An example of failing bond wires is shown in Figure 7.2b, in which the bond wires have suffered from a high stress level that resulted in a breakage of the wires.

For the simulation, the computational domain $\mathcal{D}$ represents the chip package modeled as shown in Figure 7.2c, with a computational grid generated by CST DESIGN STUDIO. For simplicity, we assume all material characteristics to be linear and refer to Appendix A for more details about the chip geometry and its parameters. Section 7.2.1 demonstrates the computation of the bond wire temperatures that are efficiently modeled and discretized by the 1D–3D coupling method as presented in Chapter 5. Then, an ET circuit is extracted using the automated ET netlist generation algorithm from Chapter 6 to demonstrate the agreement of circuit and field simulation. With the computation of wire temperatures available, the probability of system failure is defined in Section 7.2.3. Next, the hybrid iterative algorithm from Chapter 4 is used to compute the system failure probability in Section 7.2.4. Finally, Section 7.2.5 assesses the computational efficiency of a surrogate model for the determination of failure probabilities when using the hybrid iterative algorithm.
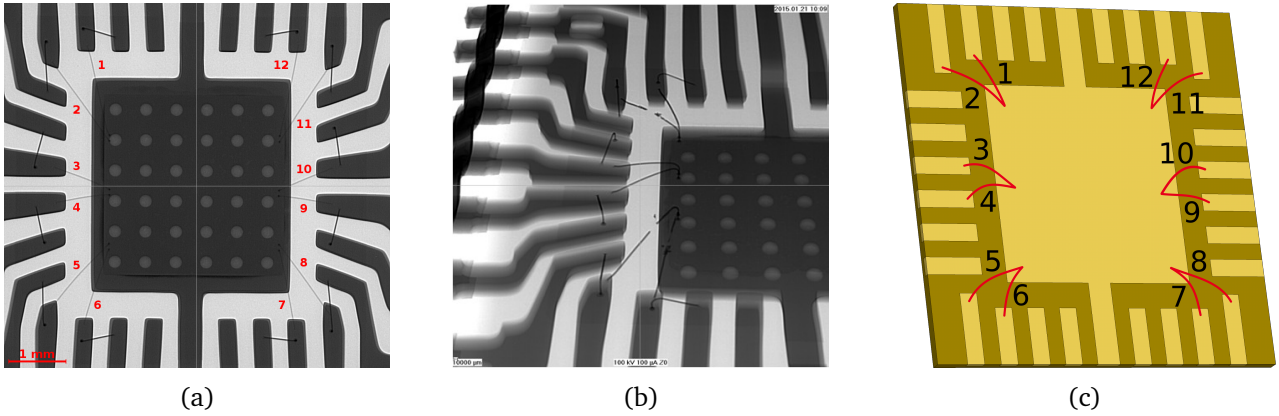
Figure 7.2: (a) Top view and (b) perspective view of X-ray pictures of a microelectronic chip package [150]. In (b), some wires have broken due to thermal stress. (c) Model of the chip package with applied bond wires [48].

### 7.2.1 Temperature of Bond Wires

The bond wire failure model used in this chapter is solely based on a wire's temperature. Therefore, we compute the temperature distribution for the different wires using the ET model given by (5.1). For each wire, the 1D–3D coupling as presented in Chapter 5 is carried out using a coupling radius $r_{\text{cpl}} = \overline{H}^2 \overline{\kappa}$ and $N^{1\text{D}} = 4$ 1D points, where $\overline{H}$ is the height of the bond wires, $\overline{\kappa}$ is their maximal Frenet-Serret curvature [90, 202]. In addition to the initial 3D grid as generated by a proprietary meshing tool, the grid lines are inserted at the 1D wire discretization points and at the 1D–3D coupling points, yielding $297\,648$ 3D nodes and an average step size of $h \approx 4.05 \times 10^{-5}$ m. The time discretization is given by $N_t = 10$ time steps with $t_1 = 1\,\text{s}$ and we apply a voltage of $V_{\text{app}} = 0.1\,\text{V}$ along each wire. For $\overline{h} = 1/3$, we solve (5.19) using the fractional step method as discussed in Section 3.4 and obtain the results for $\boldsymbol{\varphi}_h(t_1)$, $\overline{\boldsymbol{\varphi}}_h(t_1)$, $\mathbf{T}_h(t_1)$, and $\overline{\mathbf{T}}_h(t_1)$ as shown in Figures 7.3 and 7.4. The presented results demonstrate the capability to predict the temperature distribution in a chip package *including* the temperature profile of the bond wires.

### 7.2.2 Circuit Model

Now, let us apply the circuit extraction method as described in Chapter 6 to the 3D microelectronic chip package as shown in Figure 7.2c. For this example, only wire 9 is included in the model. The field problem is discretized as described in Chapter 3 and Algorithm 2 is used to generate the corresponding ET netlist. The resulting netlist contains $101\,147$ circuit elements to describe a field problem that has been discretized on a 3D grid with $9660$ nodes. Running a transient analysis of this netlist, a relative error of $\Delta_\varphi \approx 0.23\,\%$ and $\Delta_{\mathbf{T}} \approx 0.17\,\%$ compared to the field simulation is achieved. For the definition of these error measures, see Chapter 6. Figure 7.5a compares the temperature of the hottest point in the chip package obtained by FIT and circuit simulation. The 3D temperature distribution in the chip package resulting from circuit simulation is shown in Figure 7.5b. In summary, for a 3D ET problem, we achieve a good agreement of the circuit simulation results compared to those obtained by the corresponding field solver and we assume the remaining error to be attributed to the different time integrators. We recall that the possibility to replace a field model by a netlist without any loss of accuracy opens many perspectives in the simulation of electronic devices, e.g., it allows to embed complicated field behavior in traditional circuit models.

Figure 7.3: Resulting electric solution for the ET chip package simulation using grids with $h \approx 8.51 \times 10^{-5}$ m and $\bar{h} = 1/3$. (a) 1D solution $\overline{\varphi}_h(t_1)$ for the 12 wires attached to the 3D chip package. For the wire numbering, see Figure 7.2c. (b) 3D solution $\varphi_h(t_1)$ at $z = 150\,\mu$m in the $xy$-plane. These figures are taken from [48].
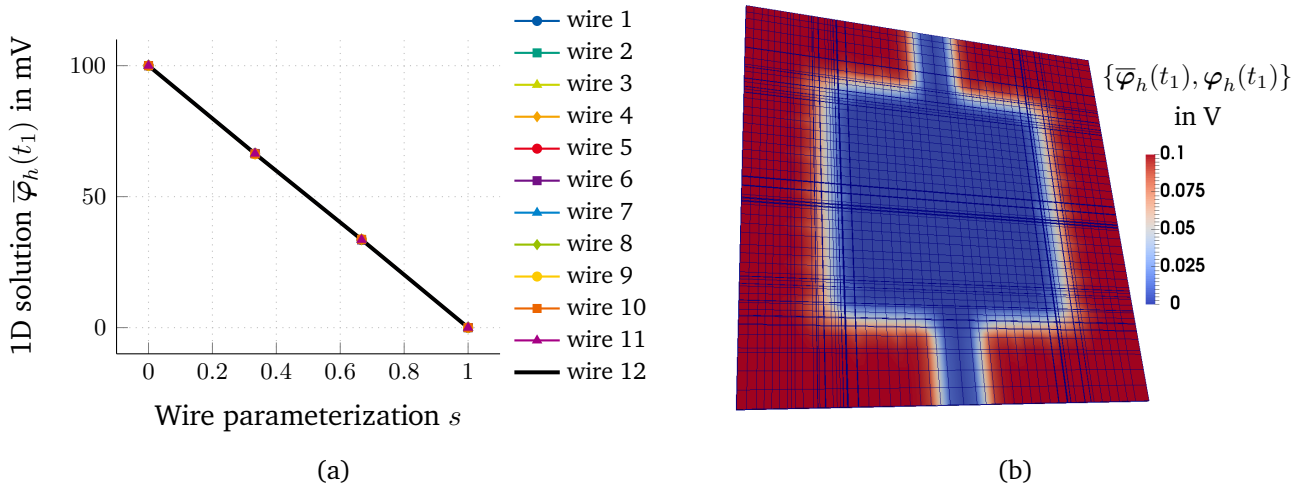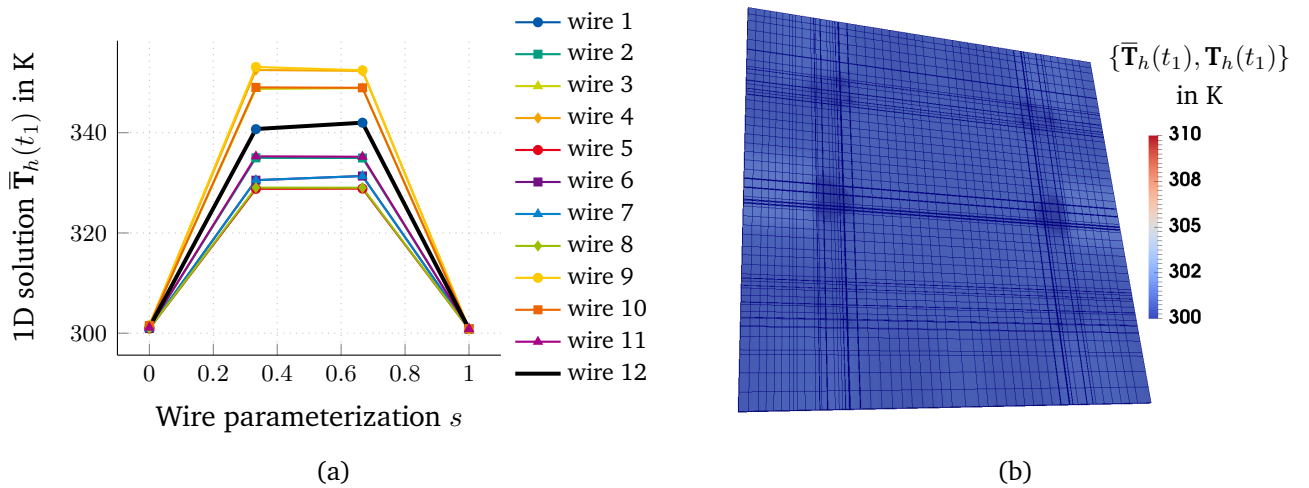


Figure 7.4: Resulting thermal solution for the ET chip package simulation using grids with $h \approx 8.51 \times 10^{-5}$ m and $\bar{h} = 1/3$. (a) 1D solution $\overline{\mathbf{T}}_h(t_1)$ for the 12 wires attached to the 3D chip package. For the wire numbering, see Figure 7.2c. (b) 3D solution $\mathbf{T}_h(t_1)$ at $z = 150\,\mu$m in the $xy$-plane. These figures are taken from [48].
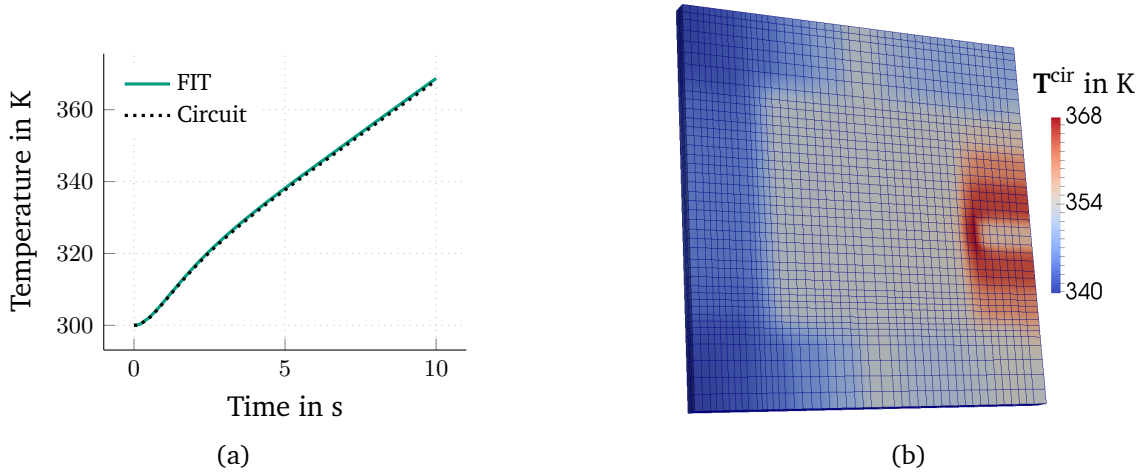
Figure 7.5: (a) Temperature at the hottest point of the chip package obtained by FIT and circuit simulation. (b) Temperature distribution in the chip package obtained by circuit simulation. These figures are taken from [47].

### 7.2.3 System Failure Probability

One reason why bond wires are subject to failure is given by Joule heating effects that stem from the currents in the wires. We define a system failure as the breakage of at least one of the bond wires in the chip package. We thereby assume that a system's failure originates predominantly from the bond wires themselves and hence neglect any other possible source of failure. Due to manufacturing tolerances, the geometry of the bond wires is subject to uncertainty, which we model by the realization $\mathbf{y}$ of a random variable, see Chapter 4. To avoid resolving this uncertainty in the grid, we model the geometrical uncertainty by the electric and thermal conductances of the wires such that they become dependent on $\mathbf{y}$. Then, based on the discrete problem (5.18), the ET solution becomes dependent on $\mathbf{y}$ and we obtain the stochastic setting as

$$\widehat{\mathbf{K}}_\sigma(\mathbf{T}, \mathbf{y})\boldsymbol{\varphi}(t, \mathbf{y}) = \mathbf{0}, \tag{7.1a}$$

$$\mathbf{M}_{\rho c}\dot{\mathbf{T}}(t, \mathbf{y}) + \widehat{\mathbf{K}}_\lambda(\mathbf{y})\mathbf{T}(t, \mathbf{y}) = \widehat{\mathbf{Q}}(\boldsymbol{\varphi}, \mathbf{T}, \mathbf{y}), \tag{7.1b}$$

where the wire contribution is included in $\widehat{\mathbf{K}}_\sigma$ and $\widehat{\mathbf{K}}_\lambda$. In contrast to (5.18), we explicitly denote the time dependence. To evaluate the ET problem for failure, we use the performance function $g(\mathbf{y}) = g(\boldsymbol{\varphi}(\mathbf{y}), \mathbf{T}(\mathbf{y}))$, see Chapter 4.

Let us first define the failure condition for a single wire and come to the precise definition of system failure afterwards. The breakage of a single bond wire may be induced by stress, electromigration, or other reasons, and is modeled by a critical temperature $T_{cr}$ that we assume to be equal for all wires considered here. Then, a failure occurs when the wire's maximal temperature $T^w := \max_{j=1...N^{1D}} \overline{\mathbf{T}}$ exceeds the critical temperature $T_{cr}$ at any instant in time, where $\overline{\mathbf{T}} = \boldsymbol{\Pi}\mathbf{T}$ as defined in (5.15). The corresponding condition is given by

$$\max_{t \in I} T^w(t, \mathbf{y}) > T_{cr}, \tag{7.2}$$

and the performance function $g$ reads

$$g(\mathbf{y}) = -\max_{t \in I} T^w(t, \mathbf{y}) + T_{cr}. \tag{7.3}$$

| Symbol | Description | Value |
|--------|-------------|-------|
| $T_{\mathrm{cr}}$ | Critical temperature | $523\,\mathrm{K}$ |
| $N$ | No. of uncertain wires | 2 |
| $M$ | No. of samples | $1 \times 10^5$ |
| $p$ | Polynomial degree of surrogate | 1 |
| $\eta$ | Tolerance for hybrid algorithm | $1 \times 10^{-10}$ |

Table 7.1: Settings for the computation of the hybrid failure probability.

For a system of $\overline{N}$ bond wires, we define a system failure to occur if any of these wires fails, resulting in the corresponding condition given by

$$\max_{i=1,\ldots,\overline{N}} \max_{t \in I} T^{\mathrm{w},i}(t,\mathbf{y}) > T_{\mathrm{cr}}.$$

It has been observed that the maximum over all bond wires gives rise to a non-smooth performance function [145]; hence, it is difficult to approximate with polynomials. Therefore, for an efficient surrogate approximation, we use (7.3) to compute the failure probability $P_{\mathrm{F},i}^{\mathrm{hyb}}$ for every wire independently, see Chapter 4 for the general definition of failure probabilities. This also requires the repetitive application of Algorithm 1 to every wire, as the $\{\mathbf{y}^j\}_{j=1}^M$ are reordered for each wire. In general, the event of a failure of a single wire is not independent from the event of a failure of another wire. Hence, we deduce from the basic axioms of probability theory, that the system failure probability can be estimated as

$$P_{\mathrm{F},s}^{\mathrm{hyb}} \leq \sum_{i=1}^{\overline{N}} P_{\mathrm{F},i}^{\mathrm{hyb}}. \tag{7.4}$$

### 7.2.4 Hybrid Failure Probability

Now, we apply Algorithm 1 to compute the hybrid system failure probability of the chip package with bond wires of uncertain geometry. The goal of a bond wire designer is to dimension the bond wires such that a small failure probability at minimal cost is obtained. For simplicity, we assume the lengths of the wires to be predetermined by the package, leaving the wires' diameter as the design parameter. The uncertain quantities $\mathbf{y}$ are modeled as the relative change of the bond wire lengths. Therefore, we assume that the diameter of a wire is precisely controlled by the manufacturing process and that wire $i$ is solely subject to an uncertain length $l^i = l_0^i/(1-y^i)$, with a deterministic length $l_0^i$.

For simplicity, we choose bond wires 1 and 2 to be subject to an uncertain length, while the parameters of all other wires are assumed to be known exactly. Thus, $\overline{N} = 12$ wires are included in the problem, but only $N = 2$ uncertain parameters are involved, simplifying the setup of the surrogate model. For the high-dimensional case of $N = 12$, we refer to [145]. For both wires, we choose $y^j$ to be uniformly distributed in the interval $[\mathbb{E}[Y] - \sigma_Y^2, \mathbb{E}[Y] + \sigma_Y^2]$, with $\mathbb{E}[Y] = 0.17$ and $\sigma_Y^2 = 0.048$. In this section, a first order surrogate ($p = 1$) with $M = 1 \times 10^5$ samples is used. The tolerance to determine the termination of the hybrid iterative algorithm is chosen to $\eta = 1 \times 10^{-10}$. We further assume that a designer has specified the radius of all wires and we compute the corresponding failure probability using Algorithm 1. The settings as used for the hybrid iterative algorithm are summarized in Table 7.1.

We apply a constant voltage $V_{\mathrm{app}} = 40\,\mathrm{mV}$ over the bond wires and convective thermal boundary conditions (BCs) at all boundaries with the heat transfer coefficient $h_{\mathrm{cv}} = 25\,\mathrm{W/(m^2K)}$, resulting in a stationary thermal
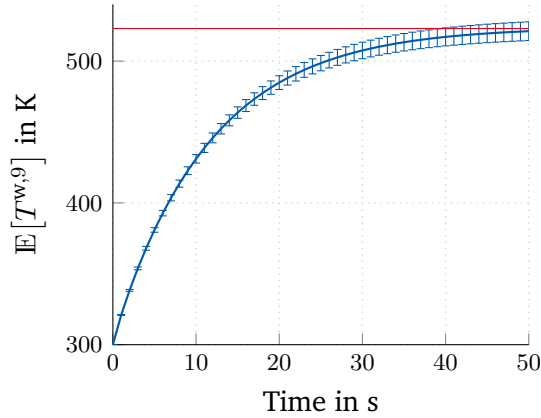
Figure 7.6: Expected value of the temperature of bond wire 9 over time with $6\sigma_T$ variation in blue evaluated using the hybrid iterative algorithm with $\delta M = 10$. The horizontal red line shows the critical temperature $T_{\mathrm{cr}}$ as a reference for the failure condition. This figure is taken from [50].

state. Figure 7.6 depicts the expected value of the temperature of bond wire 9 as a result of the hybrid iterative Algorithm 1 with $\delta M = 10$. The red horizontal line shows the critical temperature $T_{\mathrm{cr}}$ as a reference for the failure condition. Furthermore, error bars showing the $6\sigma_T$-deviation are plotted, where $\sigma_T$ is the standard deviation of the temperature. As such, $\sigma_T$ is a statistical moment measured at the output, see Section 4.1 for the difference between input and output variables. At the end time $t_1 = 50\,\mathrm{s}$, this standard deviation is given by $\sigma_T = 1.10\,\mathrm{K}$.

From Figure 7.6, we see that a small but nonzero failure probability is expected since the $6\sigma_T$ deviation crosses the reference line for a wire failure. Note that in proper six sigma design, the upper limit of the six sigma interval would be expected to be entirely below the red line. However, the present setting was chosen such that an exemplary nonzero hybrid failure probability may be computed.

We recall that the quantification of failure probabilities based on even very accurate surrogate models may be inaccurate [141]. Hence, we use Algorithm 1 to compute the failure probability of each wire separately with different values for $\delta M$. Since wires 9 and 10 are the shortest wires in the model, they exhibit a higher conductance than all other wires. Together with the voltage-driven excitation, the highest temperatures are observed for these two wires. Due to this setting, the used number of samples does not resolve the very rare failure probabilities of the other wires and they compute to zero.

The resulting evolutions of the hybrid failure probabilities of wire 9 and 10 are shown in Figure 7.7. The computed failure probability for wire 9 reads $P_{\mathrm{F},9}^{\mathrm{hyb}} \approx 0.013$ and the one for wire 10 reads $P_{\mathrm{F},10}^{\mathrm{hyb}} \approx 0.0071$. It can be observed that the computed value of the failure probability changes only slightly during the execution of the algorithm. The reason for the small variation is that a change in the failure probability only occurs if a sample falls within the very small threshold region, see Figure 4.2. Additionally, we note that the number of required iterations until convergence depends highly on the value of $\delta M$. Moreover, the algorithm might not converge if $\delta M$ is too small. This is, e.g., observed for $\delta M = \{2, 4\}$ in the case of wire 9 and for $\delta M = \{2, 4, 6, 8\}$ in the case of wire 10, see Figure 7.7. Hence, to ensure the accuracy of the final probability estimate, repetitive runs of Algorithm 1 with different choices of $\delta M$ are recommended.

Apart from the failure probability of a single wire, an estimate for the system failure probability was given in Section 7.2.3. With (7.4) and for the different values of $\delta M$, the results range from 0.0191 to 0.0200, see Table 7.2. However, we recall that the results for $\delta M = \{2, 4, 6, 8\}$ have not converged as observed from
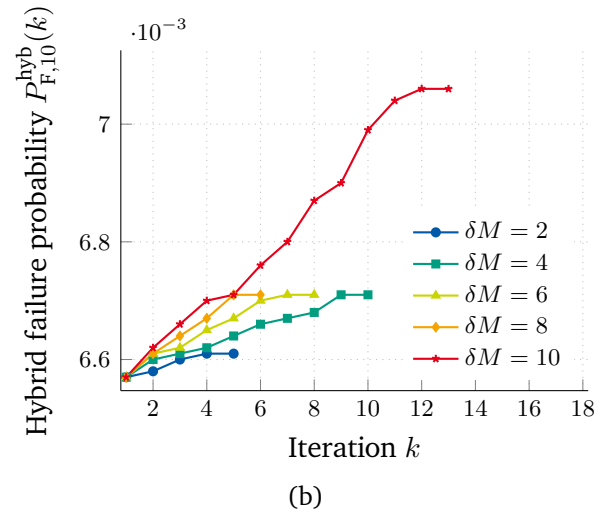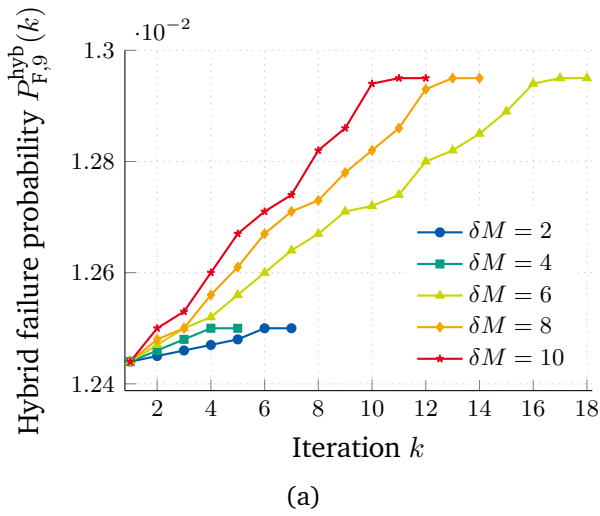
Figure 7.7: Hybrid failure probability (a) $P_{\mathrm{F},9}^{\mathrm{hyb}}$ and (b) $P_{\mathrm{F},10}^{\mathrm{hyb}}$ over iteration $k$ for bond wires 9 and 10, respectively, and different choices of $\delta M$. These results are based on [50].

| $\delta M$ | 2 | 4 | 6 | 8 | 10 |
|---|---|---|---|---|---|
| $P_{\mathrm{F,s}}^{\mathrm{hyb}}$ | 0.0191 | 0.0192 | 0.0197 | 0.0197 | 0.0200 |

Table 7.2: Hybrid system failure probability $P_{\mathrm{F,s}}^{\mathrm{hyb}}$ for different $\delta M$. These results are based on [50].

Figure 7.7. As already mentioned, the failure probability of all other wires was computed to zero since none of the Monte Carlo (MC) samples falls neither in the failure region nor in the threshold region defined by $\delta$. Thus, the algorithm for these wires converges directly after the first iteration.

## 7.2.5 Efficiency of Surrogate Model

For the results as presented in Section 7.2.4, the surrogate model is constructed using a tensor grid with $(p+1)^N$ collocation points for which the full model needs to be evaluated. Therefore, the effort to construct the surrogate model depends on the number of uncertain parameters and on its polynomial degree. Furthermore, the number of required iterations to execute Algorithm 1 depends on the choice of $\delta M$ as it is visible from Figure 7.7. In Table 7.3, the total number of full model calls to calculate the hybrid failure probability of wires 9 and 10 is given as a function of the polynomial degree $p$ and the iteration parameter $\delta M$. Comparing surrogate degree 1 and 2 under the condition that convergence was observed for the chosen $\delta M$, it is seen that the accuracy of the higher order surrogate leads to less iterations and therefore less full model calls. Furthermore, for degree 3, it is observed that the algorithm terminates directly after only one iteration.

The cost of using a surrogate with $p = 3$ is comparable to the case $p = 2$. However, the hybrid iterative algorithm with surrogates of degree $p > 3$ requires a more expensive setup without giving more accurate results. In the best case of $p = 2$ and $\delta M = 2$, the system failure probability for this example is obtained by using only 22 instead of $M = 1 \times 10^5$ full model evaluations in the case of pure MC sampling.

| Wire | $p$ | $\delta M$ | | | | |
|------|-----|----|----|-----|-----|-----|
|      |     | 2  | 4  | 6   | 8   | 10  |
|      | 1   | 16 | 20 | 106 | 108 | 114 |
| 9    | 2   | 11 | 13 | 15  | 17  | 19  |
|      | 3   | 18 | 20 | 22  | 24  | 26  |
|      | 1   | 12 | 40 | 46  | 44  | 124 |
| 10   | 2   | 11 | 13 | 15  | 17  | 19  |
|      | 3   | 18 | 20 | 22  | 24  | 26  |

Table 7.3: Number of full model calls to compute the hybrid failure probabilities for wires 9 and 10 in dependence of the surrogate polynomial level $p$ and the iteration parameter $\delta M$. The number of model calls to set up the surrogate model is included in the data. These results are based on [50].

## 7.3 Summary

In this final chapter, possible applications of the presented methods have been pointed out. First, the important field of thermal-aware placement of electronic components in digital circuit design was discussed. Considering the predicted temperature distribution already in the placement and routing steps, hot spots in the final design can be avoided. By this approach, a more homogeneous temperature distribution is obtained, which may yield a longer lifetime of the individual components and thus, of the entire device. Secondly, the electrothermal (ET) simulation of a microelectronic chip package including bond wires was presented. To determine the temperatures of the different wires, the thin wire approach from Chapter 5 was applied. Furthermore, using Algorithm 2 from Chapter 6 to extract an ET circuit from the 3D field problem with the wires inserted as lumped elements, a good agreement of field and circuit simulation was achieved. After establishing a way of computing the temperature of the bond wires, we were able to compute failure probabilities for the individual wires, yielding a system failure probability for the considered microelectronic chip package. To evaluate this system failure probability efficiently, we used a hybrid iterative algorithm together with a polynomial surrogate model, see Chapter 4 for details. The efficiency of the considered surrogate model was assessed by collecting the number of full model calls for different polynomial levels of the surrogate, and for different values of the empirical parameter $\delta M$ as used by the hybrid iterative algorithm.

# 8  Conclusions and Prospects

Driven by the impressive developments in micro- and nanoelectronics during the last decades, this thesis dealt with the evaluation of failure probabilities of thin wires in chip packages. Due to the steadily shrinking feature sizes in electronics, power densities increase and thermal problems arise. These thermal issues motivate the application of electrothermal (ET) field and circuit simulation, which was used to determine failure probabilities of bond wires in chip packages.

One particular challenge for the simulation of problems involving thin wires is the discrepancy between the typically small diameter of the wires compared to the size of the surrounding package. As an alternative to resolving the wires in the 3D grid, it has been shown that a 1D–3D coupling can lead to substantial computational savings. The main challenge of this problem was identified to be the solution-dependent line source term in the 3D domain. Using the theory of de Rham currents to describe the arising singularities, a consistent continuous and discrete formulation of the 1D–3D ET coupling has been derived. To put this work into context, it has been shown that the considered problem is closely related to fluid flow in porous 3D media with 1D fractures as, e.g., investigated by [53, 70, 72]. In particular, the thin wire formulation follows from the limit case of an infinite permeability between the 3D medium and the 1D fracture. The coupling condition follows the work in [53, 70, 72] to average the 3D solution at a coupling radius around a wire to define the 1D solution. In this thesis, it became evident that an additional scaling factor is required to yield a physical solution. It was shown numerically that a grid grading towards the 1D wire alleviates the deteriorated convergence rate and that the solution is independent of the coupling radius. However, the latter is only true for straight wires, or in a sufficiently small neighborhood of a bent wire. Moreover, a direct coupling when using a zero coupling radius reduces the order of convergence. Apart from the implementation for the purposes of this thesis, the proposed approach was also implemented by an industry partner in the nanoCOPS project using a coarse 1D grid and a zero coupling radius.

To provide a generic method for the construction of equivalent circuit models, a method for the loss-free automated generation of netlist descriptions for general 3D ET and electromagnetic (EM) problems has been presented. The topology of each circuit stamp associated with primal grid edges has been derived using the finite integration technique (FIT) for the spatial discretization. However, there is no general restriction to apply the present approach also to other discretization schemes, such as the finite element (FE) method. Exploiting the similarities of the topological FIT matrices and the non-reduced circuit incidence matrix as used in the modified nodal analysis (MNA), the FIT-discretized ET formulation was mapped into a circuit that can be solved by any SPICE-like program. When temperature-dependent materials are involved, the corresponding nonlinear circuit elements can be described by behavioral sources. To include thin wires in the circuit model, the 1D–3D coupling approach was used together with a coarse 1D discretization and a zero coupling radius such that additional circuit elements represent the wires. For the generation of EM circuits, the full set of Maxwell's equations was used as the starting point and transformed into a set of circuit stamps, each representing a primal grid edge. Thanks to the straightforward mapping from the 3D field discretization into a circuit, no further approximations are introduced, i.e., the circuit is an *exact* representation of the

discretized field problem. Thus, state-of-the-art circuit solvers can be exploited to deal with the coupling, the nonlinearities, and the time integration. With this generic and accurate method at hand, many perspectives for the simulation of electronic devices open up, e.g., it allows to embed complicated field behavior in traditional circuit models.

To investigate numerical errors and convergence rates of the proposed methods, well-chosen model problems were investigated. Moreover, the ET simulation of a chip package including bond wires was presented. Being interested in the failure probability of the entire system, it was assumed that failure originates from the overheating of a bond wire. Therefore, the failure probability of a single wire was considered, where failure was defined by its temperature exceeding a certain critical value. Due to the typically small failure probabilities for bond wire designs, classical Monte Carlo (MC) sampling would require a very large number of samples; thus, a hybrid iterative approach was used. This hybrid approach is understood as a compromise between running an expensive 3D field solver and the cheap evaluation of a polynomial surrogate model as an alternative. As a result, the hybrid system failure probability could be computed with a substantial saving of full model evaluations. Furthermore, it was shown that a more accurate surrogate model leads to a faster convergence of the iterative algorithm. When choosing the surrogate model, one has to consider the trade-off of its setup cost against the gain in computational efficiency. Nevertheless, compared to pure MC sampling, even the simplest surrogate models showed a significant speedup. The drawback of the presented algorithm lies in the parameters $\delta M$ and $\eta$ that need to be determined empirically.

With the results from this thesis, further research perspectives opened up. An extension of the proposed 1D–3D coupling to the full Maxwell case including nonlinearities is part of future research. This extension would also allow to compute mutual capacitances of the wires, as it is often requested by engineers. Furthermore, an error bound for the coupling radius as a function of the wire's curvature requires further analysis. Depending on the application, the 3D losses may become relevant and must be included despite the fact that the 3D energy tends to infinity. From the theoretical point of view, existence and uniqueness of the wire coupling needs to be established for the case of an infinite permeability, which is not included in the FE analysis presented in [70]. Additionally, the error analysis for the special case of the FIT discretization is still open. Concerning the circuit extraction, a combination of the methods for the ET and EM problems would result in fully coupled thermo-EM circuit stamps. Until now, the EM circuit extraction was only outlined for linear materials, leaving nonlinear material characteristics for future research. However, one can follow similar ideas to those presented in the ET case. To incorporate wires into the obtained circuit description, a coupling radius greater than zero or a finer 1D discretization would lead to more accurate results. For the efficient simulation of the resulting large circuits, dedicated model order reduction (MOR) techniques for circuits can be applied [87, 113, 172]. For the computation of failure probabilities, an error estimator used in conjunction with the hybrid scheme could provide guidance to assess which samples require a full model evaluation in order to guarantee full control of the corresponding results [43].

# A Geometry of the Chip Model and Simulation Settings

The microelectronic chip model with numbered wires is shown in Figure A.1. The subdomain modeled by conducting parts, such as the chip in the middle of the domain, and the contact pads, is denoted by $\mathcal{D}_{\mathrm{con}}$, whereas $\mathcal{D}_{\mathrm{ins}}$ denotes the insulating subdomain. Furthermore, the wires are denoted by $\Lambda$ with wire radius $\bar{r}$. Electrical signals are imposed on contact electrodes $\Gamma_{\mathrm{Dir},l} \subset \partial\mathcal{D}$ and transferred to the chip by the bond wires. The chip itself is used as the ground electrode. The contact pads are centered in $z$-direction with a height of $100\,\mu\mathrm{m}$. The curvature of the wires is given by (5.35) and a wire height $\overline{H}$, where $\vec{x}_0$ and $\vec{x}_1$ differ for the different wires. We model each bond wire with a uniform cross-section $\overline{A}$. We assume linear materials, which are given by copper for all conducting parts and by a specific epoxy resin for the insulating parts. The parameters, their descriptions and values are listed in Table A.1.
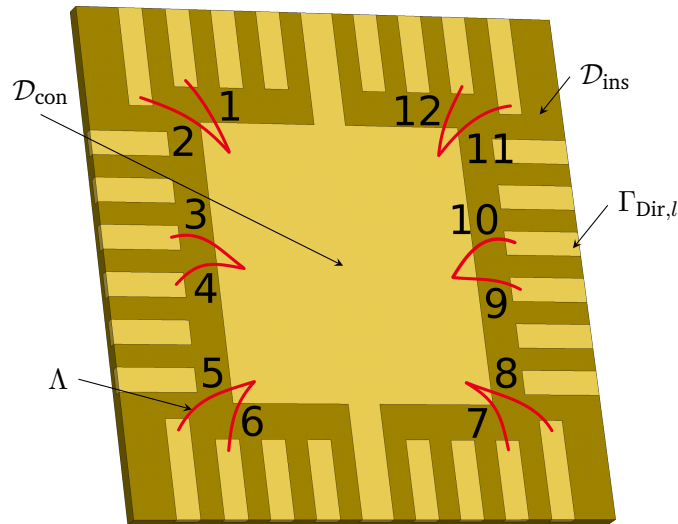


Figure A.1: Computational domain $\mathcal{D}$ with boundary $\partial\mathcal{D}$ consisting of a microelectronic chip package with bond wires. The package is modeled with a homogeneous conducting domain $\mathcal{D}_{\mathrm{con}}$ (chip in the center and contact pads located around the chip) and an insulating background domain $\mathcal{D}_{\mathrm{ins}}$. The boundary part of a contact pad with index $l$ is denoted by $\Gamma_{\mathrm{Dir},l} \subset \partial\mathcal{D}$. Furthermore, the wires are denoted by $\Lambda$. This figure is taken from [48].

| Parameter | Description | Value |
|---|---|---|
| $\overline{A}$ | cross-sectional area of wire | $\pi \bar{r}^2$ |
| $\sigma_{\text{con}}$ | electric conductivity of $\mathcal{D}_{\text{con}}$ | $5.96 \times 10^7$ S/m |
| $\sigma_{\text{ins}}$ | electric conductivity of $\mathcal{D}_{\text{ins}}$ | 1 S/m |
| $\lambda_{\text{con}}$ | thermal conductivity of $\mathcal{D}_{\text{con}}$ | 401 W/(Km) |
| $\lambda_{\text{ins}}$ | thermal conductivity of $\mathcal{D}_{\text{ins}}$ | 0.87 W/(Km) |
| $\rho_{\text{con}}$ | volumetric mass density of $\mathcal{D}_{\text{con}}$ | 8930 kg/m$^3$ |
| $\rho_{\text{ins}}$ | volumetric mass density of $\mathcal{D}_{\text{ins}}$ | 1500 kg/m$^3$ |
| $c_{\text{con}}$ | specific heat density of $\mathcal{D}_{\text{con}}$ | 390 J/(Kkg) |
| $c_{\text{ins}}$ | specific heat density of $\mathcal{D}_{\text{ins}}$ | 882 J/(Kkg) |
| $\sigma^{\text{w}}$ | electric conductivity of $\Lambda$ | $\sigma_{\text{con}}$ |
| $\lambda^{\text{w}}$ | thermal conductivity of $\Lambda$ | $\lambda_{\text{con}}$ |
| $\varphi_{\text{init}}$ | initial potential | 0 V |
| $T_{\text{init}}$ | initial temperature | 300 K |
| $T_{\infty}$ | ambient temperature | 300 K |

Table A.1: Parameters for the microelectronic chip package simulation.

# B Verification of 1D–3D Coupling Using COMSOL

In addition to the verification of the 1D–3D coupling approach as presented in Chapter 5, let us consider the comparison to a proprietary tool in which a thin wire is represented by the mesh as a three-dimensional object. Here, we use COMSOL MULTIPHYSICS for the comparison of the straight and bent wire couplings for an electric and a thermal example. We define an electric example by $\sigma^{\mathrm{w}} = 1 \times 10^{15}\sigma$ and a thermal example by $\sigma^{\mathrm{w}} = 1 \times 10^{2}\sigma$. Those model parameters that are not mentioned here are chosen according to the numerical examples in Chapter 5. For the straight wire coupling as presented in Section 5.4.2, Figure B.1 and Figure B.2 show the solution for $\bar{r} = 1 \times 10^{-3}$ m with respect to $y$ at $z = 0.5$ m (perpendicular to the wire) and with respect to the 1D coordinate $s$ (along the wire) for an electric and a thermal example, respectively. For the bent wire coupling as presented in Section 5.4.3, Figure B.3 and Figure B.4 show the solution for $\bar{r} = 1 \times 10^{-2}$ m and $r_{\mathrm{cpl}} = 1 \times 10^{-1}/\bar{\kappa}$ with respect to $z$ at $y = 0.3$ m (intersecting the wire at two points) and with respect to the 1D coordinate $s$ (along the wire) for an electric and a thermal example, respectively. In all cases, the solutions agree up to a certain error, which consists of the discretization error due to the different discretizations and the modeling error of the thin wire approach. The smaller error for the electric examples can be explained by $\sigma^{\mathrm{w}}/\sigma$ to be very large, yielding a very weak 1D–3D coupling.
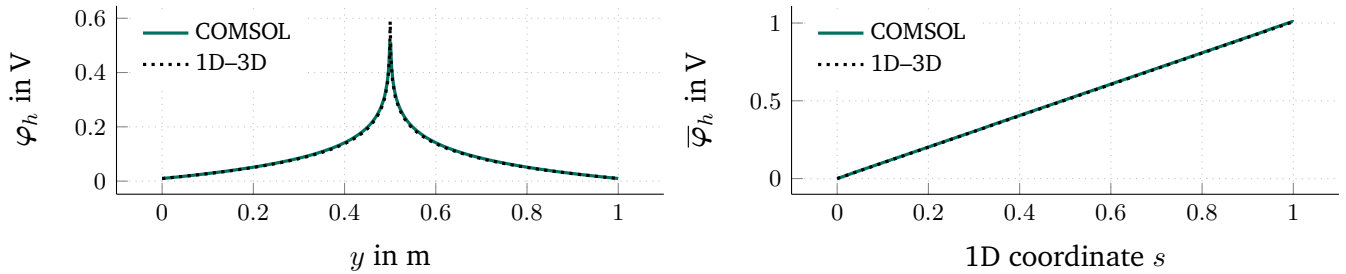


Figure B.1: Comparison of the straight wire 1D–3D coupling with COMSOL MULTIPHYSICS for an electric example and $\bar{r} = 1 \times 10^{-3}$ m.



Figure B.2: Comparison of the straight wire 1D–3D coupling with COMSOL MULTIPHYSICS for a thermal example and $\bar{r} = 1 \times 10^{-3}$ m.

Figure B.3: Comparison of the bent wire 1D–3D coupling approach with COMSOL Multiphysics for an electric example and $\overline{r} = 1 \times 10^{-2}$ m.
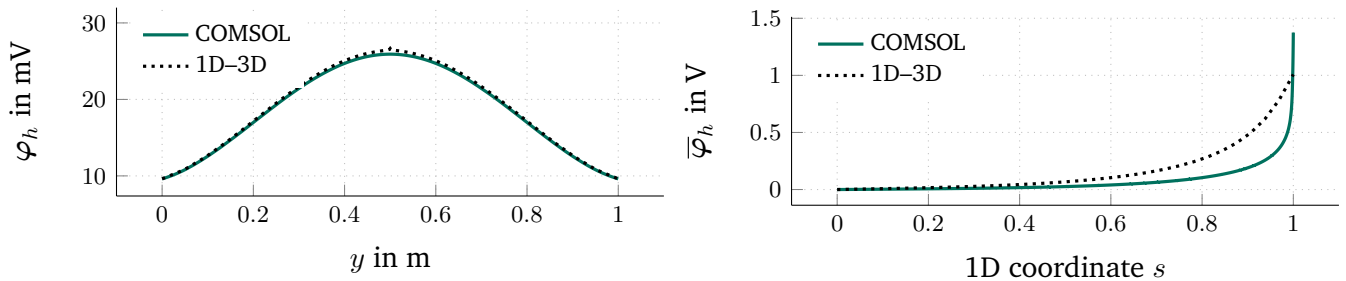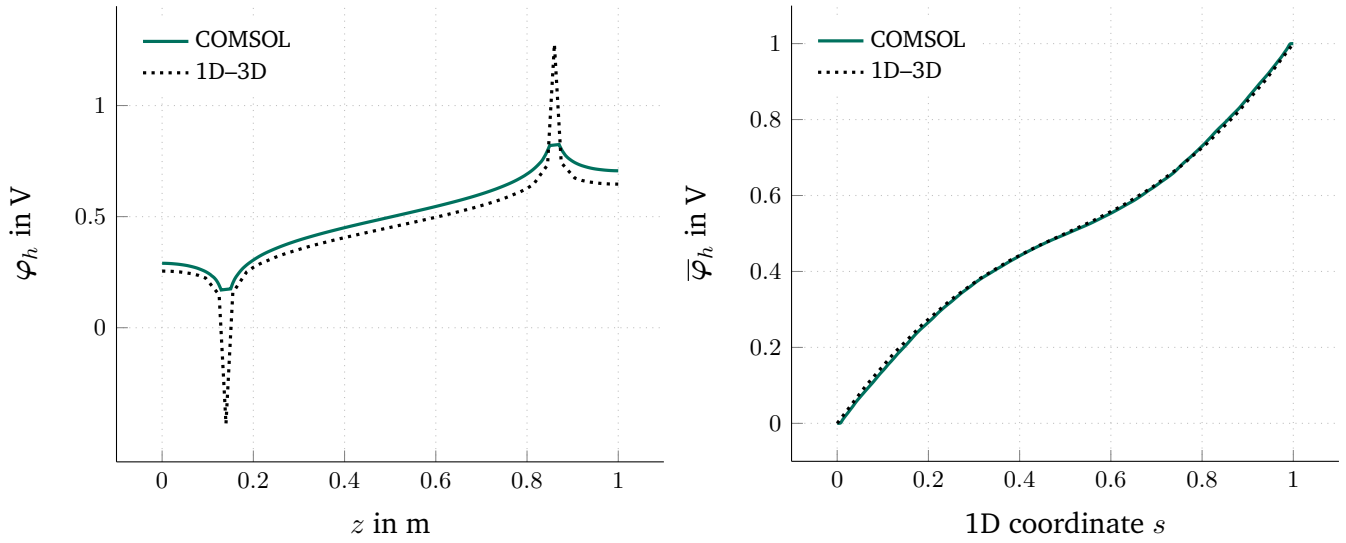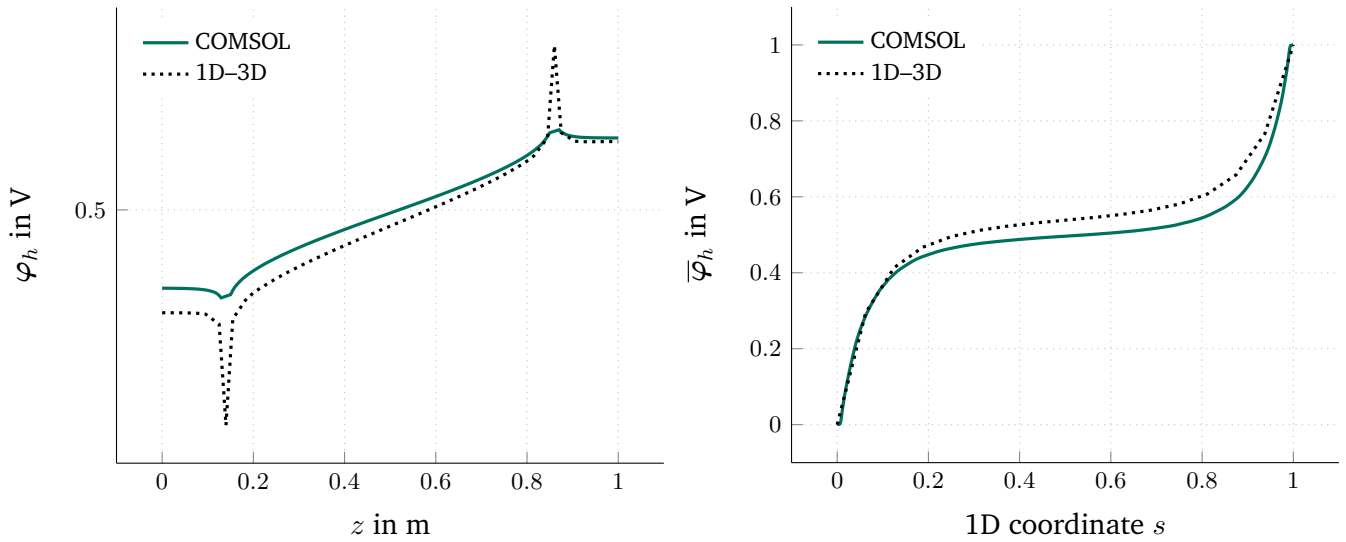


Figure B.4: Comparison of the bent wire 1D–3D coupling approach with COMSOL Multiphysics for a thermal example and $\overline{r} = 1 \times 10^{-2}$ m.

# Bibliography

[1] B. M. Adams *et al.*, *Dakota, a multilevel parallel object-oriented framework for design optimization, parameter estimation, uncertainty quantification, and sensitivity analysis*, 6.1, SAND2014-4633, User's Manual, Sandia National Laboratories, 2014.

[2] P. Alotto, A. De Cian, and G. Molinari, "A time-domain 3-D full-Maxwell solver based on the cell method", *IEEE Transactions on Magnetics*, vol. 42, no. 4, pp. 799–802, 2006, ISSN: 0018-9464. DOI: `10.1109/tmag.2006.871381`.

[3] P. Alotto, F. Freschi, and M. Repetto, "Multiphysics problems via the cell method: The role of Tonti diagrams", *IEEE Transactions on Magnetics*, vol. 46, no. 8, pp. 2959–2962, 2010, ISSN: 0018-9464. DOI: `10.1109/TMAG.2010.2044487`.

[4] ANSYS, *HFSS: High frequency electromagnetic field simulation*, User's Manual, 2018.

[5] G. Antonini, "SPICE equivalent circuits of frequency-domain responses", *IEEE Transactions on Electromagnetic Compatibility*, vol. 45, no. 3, pp. 502–512, 2003, ISSN: 0018-9375. DOI: `10.1109/TEMC.2003.815528`.

[6] T. Apel, O. Benedix, D. Sirch, and B. Vexler, "A priori mesh grading for an elliptic problem with Dirac right-hand side", *SIAM Journal on Numerical Analysis*, vol. 49, no. 3, pp. 992–1005, 2011, ISSN: 0036-1429. DOI: `10.1137/090778018`.

[7] T. Apel, A.-M. Sändig, and J. R. Whiteman, "Graded mesh refinement and error estimates for finite element solutions of elliptic boundary value problems in non-smooth domains", *Mathematical Methods in the Applied Sciences*, vol. 19, no. 1, pp. 63–85, 1996, ISSN: 1099-1476. DOI: `10.1002/(SICI)1099-1476(19960110)19:1<63::AID-MMA764>3.0.CO;2-S`.

[8] B. Auchmann and S. Kurz, "De Rham currents in discrete electromagnetism", *COMPEL: The International Journal for Computation and Mathematics in Electrical and Electronic Engineering*, vol. 26, no. 3, pp. 743–757, 2007, ISSN: 0332-1649. DOI: `10.1108/03321640710751190`.

[9] I. Babuška, "Error-bounds for finite element method", *Journal of Numerical Mathematics*, vol. 16, no. 4, pp. 322–333, 1969, ISSN: 0945-3245. DOI: `10.1007/BF02165003`.

[10] I. Babuška, F. Nobile, and R. Tempone, "A stochastic collocation method for elliptic partial differential equations with random input data", *SIAM Journal on Numerical Analysis*, vol. 45, no. 3, pp. 1005–1034, 2007, ISSN: 0036-1445. DOI: `10.1137/100786356`.

[11] I. Babuška, R. Tempone, and G. Zouraris, "Galerkin finite element approximations of stochastic elliptic partial differential equations", *SIAM Journal on Numerical Analysis*, vol. 42, no. 2, pp. 800–825, 2004, ISSN: 0036-1429. DOI: `10.1137/S0036142902418680`.

[12] N. Banagaaya, L. Feng, and P. Benner, "Sparse (P)MOR for electro-thermal coupled problems with many inputs", in *Nanoelectronic Coupled Problems Solutions*, E. J. W. ter Maten, H.-G. Brachtendorf, R. Pulch, W. Schoenmaker, and H. De Gersem, Eds., ser. Mathematics in Industry. Cham, Switzerland: Springer, 2019, ch. 15, ISBN: 978-3-030-30725-7. DOI: `10.1007/978-3-030-30726-4`.

[13]  A. Barchanski, M. Clemens, H. De Gersem, T. Steiner, and T. Weiland, "Using domain decomposition techniques for the calculation of low-frequency electric current densities in high-resolution 3D human anatomy models", *COMPEL: The International Journal for Computation and Mathematics in Electrical and Electronic Engineering*, vol. 24, no. 2, pp. 458–467, 2005, ISSN: 0332-1649. DOI: `10.1108/03321640510586097`.

[14]  R. Barrett *et al.*, *Templates for the Solution of Linear Systems: Building Blocks for Iterative Methods*, 2nd ed. Philadelphia, PA, USA: Society for Industrial and Applied Mathematics, 1994, ISBN: 978-0-89871-328-2. DOI: `10.1137/1.9781611971538`.

[15]  A. Bartel, M. Brunk, M. Günther, and S. Schöps, "Dynamic iteration for coupled problems of electric circuits and distributed devices", *SIAM Journal on Scientific Computing*, vol. 35, no. 2, B315–B335, 2013, ISSN: 1095-7197. DOI: `10.1137/120867111`.

[16]  T. Bechtold, E. B. Rudnyi, and J. G. Korvink, *Fast Simulation of Electro-Thermal MEMS: Efficient Dynamic Compact Models*, H. Fujita and D. Liepmann, Eds., ser. Microtechnology and MEMS. Heidelberg, Germany: Springer, 2006, ISBN: 978-3-540-34612-8. DOI: `10.1007/978-3-540-34613-5`.

[17]  R. E. Bellman, *Dynamic Programming*. Princeton University Press, 1957.

[18]  G. Benderskaya, "Numerical methods for transient field-circuit coupled simulations based on the finite integration technique and a mixed circuit formulation", PhD thesis, Technische Universität Darmstadt, Darmstadt, 2006.

[19]  G. Benderskaya, H. De Gersem, T. Weiland, and M. Clemens, "Transient field-circuit coupled formulation based on the finite integration technique and a mixed circuit formulation", *COMPEL: The International Journal for Computation and Mathematics in Electrical and Electronic Engineering*, vol. 23, no. 4, pp. 968–976, 2004, ISSN: 0332-1649. DOI: `10.1108/03321640410553391`.

[20]  T. L. Bergman, A. S. Lavine, F. P. Incropera, and D. P. DeWitt, *Introduction to Heat Transfer*, 6th ed. John Wiley & Sons, Ltd., 2011, ISBN: 978-0-470-50196-2.

[21]  M. Bernardoni, N. Delmonte, D. Chiozzi, and P. Cova, "Non-linear thermal simulation at system level: Compact modelling and experimental validation", *Microelectronics Reliability*, vol. 80, pp. 223–229, 2018, ISSN: 0026-2714. DOI: `10.1016/j.microrel.2017.12.005`.

[22]  S. Bigalke, J. Lienig, T. Casper, and S. Schöps, "Increasing EM robustness of placement and routing solutions based on layout-driven discretization", in *14th Conference on Ph.D. Research in Microelectronics and Electronics (PRIME 2018)*, A. Gola, Ed., Prague, Czech Republic: IEEE, 2018, ISBN: 978-1-5386-5386-9. DOI: `10.1109/PRIME.2018.8430323`.

[23]  P. T. Boggs *et al.*, "DART system analysis", Sandia National Laboratories, Tech. Rep., 2005. DOI: `10.2172/876325`.

[24]  K. Böhmer and H. J. Stetter, Eds., *Defect Correction Methods*. Vienna, Austria: Springer, 1984, ISBN: 978-3-211-81832-9. DOI: `10.1007/978-3-7091-7023-6`.

[25]  A. Bondeson, T. Rylander, and P. Ingelström, *Computational Electromagnetics*, ser. Texts in Applied Mathematics. New York, NY, USA: Springer, 2005, ISBN: 978-0-387-26158-4. DOI: `10.1007/b136922`.

[26]  A. Bossavit, "A rationale for "edge-elements" in 3-D fields computations", *IEEE Transactions on Magnetics*, vol. 24, no. 1, pp. 74–79, 1988, ISSN: 0018-9464. DOI: `10.1109/20.43860`.

[27]  ——, "Computational electromagnetism and geometry (2): Network constitutive laws", *The Japan Society of Applied Electromagnetics and Mechanics*, vol. 7, no. 3, pp. 294–301, 1999.

[28] ——, "Computational electromagnetism and geometry: Building a finite-dimensional 'Maxwell's house'. (1): Network equations", *The Japan Society of Applied Electromagnetics and Mechanics*, vol. 7, no. 2, pp. 150–159, 1999.

[29] ——, *Computational Electromagnetism: Variational Formulations, Complementarity, Edge Elements.* San Diego, CA, USA: Academic Press, 1998, ISBN: 978-0-12-118710-1. DOI: `10.1016/B978-0-12-118710-1.X5000-4`.

[30] ——, "On the geometry of electromagnetism. (4): 'Maxwell's house'", *The Japan Society of Applied Electromagnetics and Mechanics*, vol. 6, no. 4, pp. 318–326, 1999.

[31] ——, "Whitney forms: A class of finite elements for three-dimensional computations in electromagnetism", *IEE Proceedings*, vol. 135, no. 8, pp. 493–500, 1988, ISSN: 0143-702X. DOI: `10.1049/ip-a-1:19880077`.

[32] A. Bossavit and L. Kettunen, "Yee-like schemes on a tetrahedral mesh, with diagonal lumping", *International Journal of Numerical Modelling: Electronic Networks, Devices and Fields*, vol. 12, no. 1-2, pp. 129–142, 1999, ISSN: 0894-3370. DOI: `10.1002/(SICI)1099-1204(199901/04)12:1/2<129::AID-JNM327>3.0.CO;2-G`.

[33] ——, "Yee-like schemes on staggered cellular grids: A synthesis between FIT and FEM approaches", *IEEE Transactions on Magnetics*, vol. 36, no. 4, pp. 861–867, 2000, ISSN: 0018-9464. DOI: `10.1109/20.877580`.

[34] R. Bracewell, *The Fourier Transform and Its Applications*. Singapore: McGraw-Hill, 2000, ISBN: 978-0-07-116043-8.

[35] A. Brandt, "Multi-level adaptive solutions to boundary-value problems", *Mathematics of Computation*, vol. 31, no. 138, pp. 333–390, 1977, ISSN: 0025-5718. DOI: `10.1090/S0025-5718-1977-0431719-X`.

[36] F. H. Branin, "The algebraic-topological basis for network analogies and the vector calculus", in *Proceedings of the Symposium on Generalized Networks*, ser. Microwave Research Institute Symposia Series, vol. 16, Polytechnic Press of the Polytechnic Institute of Brooklyn, 1966, pp. 453–491.

[37] K. E. Brenan, S. L. Campbell, and L. R. Petzold, *Numerical Solution of Initial-Value Problems in Differential-Algebraic Equations*. Philadelphia, PA, USA: Society for Industrial and Applied Mathematics, 1995, ISBN: 978-0-89871-353-4. DOI: `10.1137/1.9781611971224`.

[38] F. Brezzi, K. Lipnikov, and M. Shashkov, "Convergence of mimetic finite difference method for diffusion problems on polyhedral meshes with curved faces", *Mathematical Models and Methods in Applied Sciences*, vol. 16, no. 02, pp. 275–297, 2006, ISSN: 0218-2025. DOI: `10.1142/S0218202506001157`.

[39] W. L. Briggs, V. E. Henson, and S. F. McCormick, *A Multigrid Tutorial*, 2nd ed. Philadelphia, PA, USA: Society for Industrial and Applied Mathematics, 2000, ISBN: 978-0-89871-462-3. DOI: `10.1137/1.9780898719505`.

[40] H.-J. Bungartz and M. Griebel, "Sparse grids", *Acta Numerica*, vol. 13, pp. 147–269, 2004, ISSN: 0962-4929. DOI: `10.1017/s0962492904000182`.

[41] W. L. Burke, *Applied Differential Geometry*. Cambridge, UK: Cambridge University Press, 1985, ISBN: 978-0-521-26929-2.

[42] J. C. Butcher, *Numerical Methods for Ordinary Differential Equations*. Chichester, UK: Wiley, 2016, ISBN: 978-1-119-12150-3. DOI: `10.1002/9781119121534`.

[43] T. Butler and T. Wildey, "Utilizing adjoint-based error estimates for surrogate models to accurately predict probabilities of events", *International Journal for Uncertainty Quantification*, vol. 8, no. 2, pp. 143–159, 2018, ISSN: 2152-5080. DOI: `10.1615/int.j.uncertaintyquantification.2018020911`.

[44] Cadence, *Spectre circuit simulator*, User's Manual, 2018.

[45] R. E. Caflisch, "Monte Carlo and quasi-Monte Carlo methods", *Acta Numerica*, vol. 7, pp. 1–49, 1998, ISSN: 1474-0508. DOI: `10.1017/S0962492900002804`.

[46] T. Casper, H. De Gersem, and S. Schöps, "Automatic generation of equivalent electrothermal SPICE netlists from 3D electrothermal field models", in *17th International Conference on Thermal, Mechanical and Multi-Physics Simulation and Experiments in Microelectronics and Microsystems (EuroSimE 2016)*, W. van Driel and P. Rodgers, Eds., Montpellier, France: IEEE, 2016, ISBN: 9781509021079. DOI: `10.1109/EuroSimE.2016.7463329`. arXiv: `1610.04304`.

[47] T. Casper, D. Duque, S. Schöps, and H. De Gersem, "Automated netlist generation for 3D electrothermal and electromagnetic field problems", *Journal of Computational Electronics*, 2019, ISSN: 1569-8025. DOI: `10.1007/s10825-019-01368-6`. arXiv: `1809.08588`.

[48] T. Casper, U. Römer, H. De Gersem, and S. Schöps, "Coupled simulation of transient heat flow and electric currents in thin wires: Application to bond wires in microelectronic chip packaging", *Computers and Mathematics with Applications*, 2019, ISSN: 0898-1221. DOI: `10.1016/j.camwa.2019.10.009`. arXiv: `1809.09034`.

[49] ——, (2018). ETwireSim - Efficient Thin wire Simulator for 3D electrothermal problems, [Online]. Available: `https://github.com/tc88/ETwireSim`.

[50] T. Casper, U. Römer, and S. Schöps, "Determination of bond wire failure probabilities in microelectronic packages", in *22nd International Workshop on Thermal Investigations of ICs and Systems (THERMINIC 2016)*, C. Bailey, S. Volz, A. Poppe, and J. Parry, Eds., Budapest, Hungary: IEEE, 2016, pp. 39–44, ISBN: 978-1-5090-5450-3. DOI: `10.1109/THERMINIC.2016.7748645`. arXiv: `1609.06187`.

[51] T. Casper *et al.* (2018). ANTHEM - Automatic Netlist generator for THermo-EM field problems, [Online]. Available: `https://github.com/tc88/ANTHEM`.

[52] T. Casper *et al.*, "Electrothermal simulation of bonding wire degradation under uncertain geometries", in *Proceedings of the 2016 Design, Automation & Test in Europe Conference & Exhibition (DATE)*, L. Fanucci and J. Teich, Eds., Dresden, Germany: IEEE, 2016, pp. 1297–1302, ISBN: 978-3-9815370-6-2. arXiv: `1610.04303`.

[53] L. Cattaneo and P. Zunino, "Numerical investigation of convergence rates for the FEM approximation of 3D-1D coupled problems", in *Numerical Mathematics and Advanced Applications – ENUMATH 2013*, A. Abdulle, S. Deparis, D. Kressner, F. Nobile, and M. Picasso, Eds., Cham, Switzerland: Springer, 2014, pp. 727–734, ISBN: 978-3-319-10704-2. DOI: `10.1007/978-3-319-10705-9_72`.

[54] A. Chkifa, A. Cohen, and C. Schwab, "Breaking the curse of dimensionality in sparse polynomial approximation of parametric PDEs", *Journal de Mathématiques Pures et Appliquées*, vol. 103, no. 2, pp. 400–428, 2015, ISSN: 0021-7824. DOI: `10.1016/j.matpur.2014.04.009`.

[55] M. J. Choi and A. C. Cangellaris, "A quasi three-dimensional distributed electromagnetic model for complex power distribution networks", *IEEE Transactions on Advanced Packaging*, vol. 25, no. 1, pp. 28–34, 2002, ISSN: 1521-3323. DOI: `10.1109/TADVP.2002.1017681`.

[56]   M. J. Choi, K.-P. Hwang, and N. Cangellaris, "Direct generation of SPICE compatible passive reduced order models of ground/power planes", T. G. Reynolds, P. Slota, M. McShane, and W. J. Howell, Eds., Las Vegas, NV, USA: IEEE, 2000, pp. 775–780, ISBN: 978-0-7803-5908-6. DOI: `10.1109/ECTC.2000.853247`.

[57]   A. Chvala *et al.*, "Fast 3-D electrothermal device/circuit simulation of power superjunction MOSFET based on SDevice and HSPICE interaction", *IEEE Transactions on Electron Devices*, vol. 61, no. 4, pp. 1116–1122, 2014, ISSN: 0018-9383. DOI: `10.1109/TED.2014.2305848`.

[58]   M. Clemens, E. Gjonaj, P. Pinder, and T. Weiland, "Self-consistent simulations of transient heating effects in electrical devices using the finite integration technique", *IEEE Transactions on Magnetics*, vol. 37, no. 5, pp. 3375–3379, 2001, ISSN: 0018-9464. DOI: `10.1109/20.952617`.

[59]   M. Clemens and T. Weiland, "Discrete electromagnetism with the finite integration technique", *Progress In Electromagnetics Research (PIER)*, vol. 32, pp. 65–87, 2001, ISSN: 1070-4698. DOI: `10.2528/PIER00080103`.

[60]   ——, "Magnetic field simulation using conformal FIT formulations", *IEEE Transactions on Magnetics*, vol. 38, no. 2, pp. 389–392, 2002, ISSN: 0018-9464. DOI: `10.1109/20.996104`.

[61]   M. Clemens *et al.*, "Aspects of coupled problems in computational electromagnetics formulations", *ICS Newsletter (International Compumag Society)*, vol. 19, no. 2, pp. 3–12, 2012, ISSN: 1026-0854.

[62]   R. W. Clough, "Early history of the finite element method from the view point of a pioneer", *International Journal for Numerical Methods in Engineering*, vol. 60, no. 1, pp. 283–287, 2004, ISSN: 1097-0207. DOI: `10.1002/nme.962`.

[63]   L. Codecasa, V. d'Alessandro, A. Magnani, and A. Irace, "Circuit-based electrothermal simulation of power devices by an ultrafast nonlinear MOR approach", *IEEE Transactions on Power Electronics*, vol. 31, no. 8, pp. 5906–5916, 2016, ISSN: 0885-8993. DOI: `10.1109/TPEL.2015.2494500`.

[64]   L. Codecasa, R. Specogna, and F. Trevisan, "Symmetric positive-definite constitutive matrices for discrete eddy-current problems", *IEEE Transactions on Magnetics*, vol. 43, no. 2, pp. 510–515, 2007, ISSN: 0018-9464. DOI: `10.1109/TMAG.2006.887065`.

[65]   Council on Competitiveness, "HPC case study – Boeing catches a lift with high performance computing", Department of Energy, Tech. Rep., 2009.

[66]   M. J. Crowe, *A History of Vector Analysis: The Evolution of the Idea of a Vectorial System*. Dover Publications, 2011, ISBN: 978-0-486-67910-5.

[67]   CST AG, *CST STUDIO SUITE 2016*, Darmstadt, Germany, 2016.

[68]   M. Culpo, "Numerical algorithms for system level electro-thermal simulation", Dissertation, Bergische Universität Wuppertal, Wuppertal, 2009.

[69]   M. Culpo, C. de Falco, G. Denk, and S. Voigtmann, "Automatic thermal network extraction and multiscale electro-thermal simulation", in *Scientific Computing in Electrical Engineering SCEE 2008*, J. Roos and L. R. J. Costa, Eds., ser. Mathematics in Industry, vol. 14, Berlin, Germany: Springer, 2010, pp. 281–288, ISBN: 978-3-642-12293-4. DOI: `10.1007/978-3-642-12294-1\_36`.

[70]   C. D'Angelo, "Finite element approximation of elliptic problems with Dirac measure terms in weighted spaces: Applications to one- and three-dimensional coupled problems", *SIAM Journal on Numerical Analysis*, vol. 50, no. 1, pp. 194–215, 2012, ISSN: 0036-1429. DOI: `10.1137/100813853`.

[71]   ——, "Multiscale modelling of metabolism and transport phenomena in living tissues", PhD thesis, École Polytechnique Fédérale de Lausanne, 2007. DOI: `10.5075/epfl-thesis-3803`.

[72] C. D'Angelo and A. Quarteroni, "On the coupling of 1D and 3D diffusion-reaction equations. Application to tissue perfusion problems", *Mathematical Models and Methods in Applied Sciences*, vol. 18, no. 8, pp. 1481–1504, 2008, ISSN: 0218-2025. DOI: `10.1142/S0218202508003108`.

[73] H. De Gersem, M. Clemens, and T. Weiland, "Coupled finite-element, spectral-element discretisation for models with circular inclusions and far-field domains", *IET Science, Measurement & Technology*, vol. 149, no. 5, pp. 237–241, 2002. DOI: `10.1049/ip-smt:20020620`.

[74] H. De Gersem, R. Mertens, U. Pahner, R. J. M. Belmans, and K. Hameyer, "A topological method used for field-circuit coupling", *IEEE Transactions on Magnetics*, vol. 34, no. 5, pp. 3190–3193, 1998, ISSN: 0018-9464. DOI: `10.1109/20.717748`.

[75] G. De Rham, *Differentiable Manifolds*. Berlin, Germany: Springer, 1984, ISBN: 978-3-642-61754-6. DOI: `10.1007/978-3-642-61752-2`.

[76] B. Delaunay, "Sur la sphère vide", *Bulletin de l'Académie des Sciences de l'URSS. Classe des sciences mathématiques et na*, vol. 1934, no. 6, pp. 793–800, 1934.

[77] G. A. Deschamps, "Electromagnetics and differential forms", *Proceedings of the IEEE*, vol. 69, no. 6, pp. 676–696, 1981, ISSN: 0018-9219. DOI: `10.1109/PROC.1981.12048`.

[78] J. Dick, F. Y. Kuo, and I. H. Sloan, "High-dimensional integration: The quasi-Monte Carlo way", *Acta Numerica*, vol. 22, pp. 133–288, 2013, ISSN: 0962-4929. DOI: `10.1017/S0962492913000044`.

[79] H. K. Dirks, "Quasi-stationary fields for microelectronic applications", *Electrical Engineering (Archiv für Elektrotechnik)*, vol. 79, no. 2, pp. 145–155, 1996, ISSN: 0948-7921. DOI: `10.1007/BF01232924`.

[80] C. C. Douglas, "Multigrid methods in science and engineering", *IEEE Computational Science and Engineering*, vol. 3, no. 4, pp. 55–68, 1996, ISSN: 1070-9924. DOI: `10.1109/99.556513`.

[81] S. Drobny and T. Weiland, "Numerical calculation of nonlinear transient field problems with the Newton-Raphson method", *IEEE Transactions on Magnetics*, vol. 36, no. 4, pp. 809–812, 2000, ISSN: 0018-9464. DOI: `10.1109/20.877568`.

[82] D. J. Duque, T. Götthans, R. Guillon, and S. Schöps, "An extended analytic model for the heating of bondwires", Technische Universität Darmstadt, Tech. Rep., 2017. arXiv: `1709.10069`.

[83] M. Eller, "A low-frequency stable Maxwell formulation in frequency domain and industrial applications", Dissertation, Technische Universität Darmstadt, Darmstadt, 2017.

[84] B. Engquist and A. Majda, "Absorbing boundary conditions for the numerical simulation of waves", *Mathematics of Computation*, vol. 31, no. 139, pp. 629–651, 1977, ISSN: 0025-5718. DOI: `10.2307/2005997`.

[85] K. Eriksson, D. Estep, P. Hansbo, and C. Johnson, "Introduction to adaptive methods for differential equations", *Acta Numerica*, vol. 4, p. 105, 1995, ISSN: 0962-4929. DOI: `10.1017/s096249290000 02531`.

[86] P. L. Evans, A. Castellazzi, and C. M. Johnson, "Automated fast extraction of compact thermal models for power electronic modules", *IEEE Transactions on Power Electronics*, vol. 28, no. 10, pp. 4791–4802, 2013, ISSN: 0885-8993. DOI: `10.1109/TPEL.2012.2236687`.

[87] P. Feldmann and R. W. Freund, "Reduced-order modeling of large linear subcircuits via a block Lanczos algorithm", B. T. Preas, T. P. Pennino, and E. J. Yoffa, Eds., San Francisco, CA, USA: ACM, 1995, ISBN: 978-0-89791-725-4. DOI: `10.1145/217474.217573`.

[88] L. Feng and P. Benner, "Parametric model order reduction for electro-thermal coupled problems", in *Nanoelectronic Coupled Problems Solutions*, E. J. W. ter Maten, H.-G. Brachtendorf, R. Pulch, W. Schoenmaker, and H. De Gersem, Eds., ser. Mathematics in Industry. Cham, Switzerland: Springer, 2019, ch. 14, ISBN: 978-3-030-30725-7. DOI: `10.1007/978-3-030-30726-4`.

[89] H. Flanders, *Differential Forms with Applications to the Physical Sciences*. New York, NY, USA: Dover Publications, 1989, ISBN: 978-0-486-66169-8.

[90] J. F. Frenet, "Sur les courbes à double courbure.", *Journal de Mathématiques Pures et Appliquées*, vol. 17, pp. 437–447, 1852, ISSN: 0021-7874.

[91] F. Freschi and M. Repetto, "Tonti diagrams and algebraic methods for the solution of coupled problems", in *Scientific Computing in Electrical Engineering SCEE 2010*, B. Michielsen and J.-R. Poirier, Eds., ser. Mathematics in Industry, vol. 16, Berlin, Germany: Springer, 2012, pp. 195–203, ISBN: 978-3-540-71979-3. DOI: `10.1007/978-3-642-22453-9_21`.

[92] A. Galetzka, Z. Bontinck, U. Römer, and S. Schöps, "Multilevel Monte Carlo simulation of the eddy current problem with random parameters", in *2017 International Applied Computational Electromagnetics Society (ACES) Symposium*, Florence, Italy: IEEE, 2017, ISBN: 978-1-5090-5335-3. DOI: `10.23919/ROPACES.2017.7916062`. arXiv: `1705.08173`.

[93] B. Ganapathysubramanian and N. Zabaras, "Sparse grid collocation schemes for stochastic natural convection problems", *Journal of Computational Physics*, vol. 225, no. 1, pp. 652–685, 2007, ISSN: 0021-9991. DOI: `https://doi.org/10.1016/j.jcp.2006.12.014`.

[94] C. W. Gear and D. R. Wells, "Multirate linear multistep methods", *BIT Numerical Mathematics*, vol. 24, no. 4, pp. 484–502, 1984, ISSN: 0006-3835. DOI: `10.1007/BF01934907`.

[95] Y. C. Gerstenmaier, W. Kiffe, and G. Wachutka, "Combination of thermal subsystems modeled by rapid circuit transformation", in *13th International Workshop on Thermal Investigations of ICs and Systems (THERMINIC 2007)*, B. Courtois, M. Rencz, C. Lasance, and V. Székely, Eds., Budapest, Hungary: IEEE, 2007, ISBN: 978-2-355-00002-7. DOI: `10.1109/therminic.2007.4451758`.

[96] M. B. Giles, "Multilevel Monte Carlo methods", *Acta Numerica*, vol. 24, pp. 259–328, 2015, ISSN: 0962-4929. DOI: `10.1017/S09624929`.

[97] G. H. Golub and C. F. van Loan, *Matrix Computations*, 3rd ed. Baltimore, MD, USA: The Johns Hopkins University Press, 1996, ISBN: 978-0-8018-5413-2.

[98] D. Griffiths and D. J. Higham, *Numerical Methods for Ordinary Differential Equations: Initial Value Problems*, ser. Springer Undergraduate Mathematics Series. London, UK: Springer, 2010, ISBN: 978-0-85729-147-9. DOI: `10.1007/978-0-85729-148-6`.

[99] D. F. Griffiths, *Introduction to Electrodynamics*. Upper Saddle River, NJ, USA: Prentice-Hall, 1999, ISBN: 978-0-13-805326-0.

[100] P. W. Gross and P. R. Kotiuga, *Electromagnetic Theory and Computation: A Topological Approach*. Cambridge, UK: Cambridge University Press, 2004, ISBN: 978-0-521-80160-7.

[101] K. Guillouard, M.-F. Wong, V. F. Hanna, and J. Citerne, "A new global finite element analysis of microwave circuits including lumped elements", *IEEE Transactions on Microwave Theory and Techniques*, vol. 44, no. 12, pp. 2587–2594, 1996, ISSN: 0018-9480. DOI: `10.1109/22.554608`.

[102] ——, "A new global time-domain electromagnetic simulator of microwave circuits including lumped elements based on finite-element method", *IEEE Transactions on Microwave Theory and Techniques*, vol. 47, no. 10, pp. 2045–2049, 1999, ISSN: 0018-9480. DOI: `10.1109/22.795085`.

[103] M. Günther, Ed., *Coupled Multiscale Simulation and Optimization in Nanoelectronics*, ser. Mathematics in Industry. Berlin, Germany: Springer, 2015, vol. 21, ISBN: 978-3-662-46672-8. DOI: `10.1007/978-3-662-46672-8`.

[104] M. Günther, U. Feldmann, and E. J. W. ter Maten, "Modelling and discretization of circuit problems", in *Numerical Methods in Electromagnetics*, W. H. A. Schilders and E. J. W. ter Maten, Eds., ser. Handbook of Numerical Analysis. Amsterdam, Netherlands: Elsevier BV, 2005, vol. 13, pp. 523–659, ISBN: 978-0-444-51375-5. DOI: `10.1016/s1570-8659(04)13006-8`.

[105] S. Gutschling, H. Krüger, and T. Weiland, "Time-domain simulation of dispersive media with the finite integration technique", *International Journal of Numerical Modelling: Electronic Networks, Devices and Fields*, vol. 13, no. 4, pp. 329–348, 2000, ISSN: 0894-3370. DOI: `10.1002/1099-1204(200007/08)13:4<329::aid-jnm383>3.0.co;2-c`.

[106] E. Hairer, S. P. Nørsett, and G. Wanner, *Solving Ordinary Differential Equations I: Nonstiff Problems*, 2nd ed., ser. Springer Series in Computational Mathematics. Berlin, Germany: Springer, 2000, ISBN: 978-3-540-56670-0.

[107] ——, *Solving Ordinary Differential Equations II: Stiff and Differential-Algebraic Problems*, 2nd ed., ser. Springer Series in Computational Mathematics. Berlin, Germany: Springer, 2002, ISBN: 978-3-642-05220-0.

[108] K. Hameyer, J. Driesen, H. De Gersem, and R. J. M. Belmans, "The classification of coupled field problems", *IEEE Transactions on Magnetics*, vol. 35, no. 3, pp. 1618–1621, 1999, ISSN: 0018-9464. DOI: `10.1109/20.767304`.

[109] H. A. Haus and J. R. Melcher, *Electromagnetic Fields and Energy*. Prentice-Hall, 1989, ISBN: 978-0-13-249020-7.

[110] M. T. Heath, *Scientific Computing: An Introductory Survey*. New York, NY, USA: McGraw-Hill, 2002, ISBN: 978-1-259-00228-1.

[111] A. R. Hefner and D. L. Blackburn, "Simulating the dynamic electrothermal behavior of power electronic circuits and systems", *IEEE Transactions on Power Electronics*, vol. 8, no. 4, pp. 376–385, 1993, ISSN: 0885-8993. DOI: `10.1109/63.261007`.

[112] L. Heltai and A. Caiazzo, "Multiscale modeling of vascularized tissues via non-matching immersed methods", *Numerical Methods for in Biomedical Engineering*, 2018, ISSN: 2198-5855. DOI: `10.1002/cnm.3264`.

[113] M. Hinze, M. Kunkel, and U. Matthes, "POD model order reduction of electrical networks with semiconductors modeled by the transient drift-diffusion equations", in *Progress in Industrial Mathematics at ECMI 2010*, M. Günther, A. Bartel, M. Brunk, S. Schöps, and M. Striebel, Eds., ser. Mathematics in Industry, vol. 17, Berlin, Germany: Springer, 2012, ISBN: 978-3-642-25099-6. DOI: `10.1007/978-3-642-25100-9`.

[114] R. Hiptmair, "Discrete Hodge operators", *Numerische Mathematik*, vol. 90, no. 2, pp. 265–289, 2001, ISSN: 0945-3245. DOI: `10.1007/s002110100295`.

[115] ——, "Finite elements in computational electromagnetism", *Acta Numerica*, vol. 11, pp. 237–339, 2002, ISSN: 0962-4929. DOI: `10.1017/S0962492902000041`.

[116] ——, "Multigrid method for Maxwell's equations", *SIAM Journal on Numerical Analysis*, vol. 36, no. 1, pp. 204–225, 1998, ISSN: 0036-1429. DOI: `10.1137/S0036142997326203`.

[117]  C.-W. Ho, A. E. Ruehli, and P. A. Brennan, "The modified nodal approach to network analysis", *IEEE Transactions on Circuits and Systems*, vol. 22, no. 6, pp. 504–509, 1975, ISSN: 0098-4094. DOI: `10.1109/TCS.1975.1084079`.

[118]  R. Holland, "Finite-difference solution of Maxwell's equations in generalized nonorthogonal coordinates", *IEEE Transactions on Nuclear Sciences*, vol. 30, no. 6, pp. 4589–4591, 1983, ISSN: 0018-9499. DOI: `10.1109/TNS.1983.4333176`.

[119]  ——, "Pitfalls of staircase meshing", *IEEE Transactions on Electromagnetic Compatibility*, vol. 35, no. 4, pp. 434–439, 1993, ISSN: 0018-9375. DOI: `10.1109/15.247856`.

[120]  J. T. Hsu and L. Vu-Quoc, "A rational formulation of thermal circuit models for electrothermal simulation – part I: Finite element method", *IEEE Transactions on Circuits and Systems Part I: Fundamental Theory and Applications*, vol. 43, no. 9, pp. 721–732, 1996, ISSN: 1057-7122. DOI: `10.1109/81.536742`.

[121]  T. J. R. Hughes, J. A. Cottrell, and Y. Bazilevs, "Isogeometric analysis: CAD, finite elements, NURBS, exact geometry and mesh refinement", *Computer Methods in Applied Mechanics and Engineering*, vol. 194, pp. 4135–4195, 2005, ISSN: 0045-7825. DOI: `10.1016/j.cma.2004.10.008`.

[122]  J. D. Jackson, *Classical Electrodynamics*, 3rd. New York, NY, USA: Wiley & Sons, 1998, ISBN: 978-0-471-30932-1. DOI: `10.1017/CBO9780511760396`.

[123]  K. Jänich, *Vektoranalysis*, 5th ed. Berlin, Germany: Springer, 2005, ISBN: 978-3-540-27338-7. DOI: `10.1007/b138936`.

[124]  B.-N. Jiang, J. Wu, and L. Povinelli, "The origin of spurious solutions in computational electromagnetics", *Journal of Computational Physics*, vol. 125, no. 1, pp. 104–123, 1996, ISSN: 0021-9991. DOI: `10.1006/jcph.1996.0082`.

[125]  E. F. Kaasschieter, "Preconditioned conjugate gradients for solving singular systems", *Journal of Computational and Applied Mathematics*, vol. 24, no. 1-2, pp. 265–275, 1988, ISSN: 0377-0427. DOI: `10.1016/0377-0427(88)90358-5`.

[126]  C. Kanzow, *Numerik linearer Gleichungssysteme*. Berlin, Germany: Springer, 2005, ISBN: 978-3-540-20654-5.

[127]  S. Karagol and M. Bikdash, "Generation of equivalent-circuit models from simulation data of a thermal system", *IEEE Transactions on Power Electronics*, vol. 25, no. 4, pp. 820–828, 2010, ISSN: 0885-8993. DOI: `10.1109/TPEL.2009.2035317`.

[128]  E. R. Keiter *et al.*, *Xyce parallel electronic simulation: User's guide, version 6.10*, SAND2018-12373, User's Manual, Albuquerque, NM, USA, 2018.

[129]  L. Kettunen, "Fields and circuits in computational electromagnetism", *IEEE Transactions on Magnetics*, vol. 37, no. 5, pp. 3393–3396, 2001, ISSN: 0018-9464. DOI: `10.1109/20.952621`.

[130]  Keysight Technologies, *EMPro 3D EM simulation software*, User's Manual, 2018.

[131]  V. Košel, R. Illing, M. Glavanovics, and A. Šatka, "Non-linear thermal modeling of DMOS transistor and validation using electrical measurements and FEM simulations", *Microelectronics Journal*, vol. 41, no. 12, pp. 889–896, 2010, ISSN: 0026-2692. DOI: `10.1016/j.mejo.2010.07.016`.

[132]  B. Krietenstein, R. Schuhmann, P. Thoma, and T. Weiland, "The perfect boundary approximation technique facing the big challenge of high precision field computation", in *Proceedings of the XIX International Linear Accelerator Conference*, Argonne, IL, USA, 1998, pp. 860–862.

[133] A. Krimm, T. Casper, S. Schöps, H. De Gersem, and L. Chamoin, "Proper generalized decomposition of parameterized electrothermal problems discretized by the finite integration technique", *IEEE Transactions on Magnetics*, vol. 55, no. 6, p. 7 204 404, 2019, ISSN: 0018-9464. DOI: `10.1109/TMAG.2019.2907223`. arXiv: `1812.06867`.

[134] G. Kron, "Numerical solution of ordinary and partial differential equations by means of equivalent circuits", *Journal of Applied Physics*, vol. 16, no. 3, pp. 172–186, 1945, ISSN: 0021-8979. DOI: `10.1063/1.1707568`.

[135] H. Krüger, H. Spachmann, and T. Weiland, "Time domain modeling of gyromagnetic materials using the finite integration technique", *IEEE Transactions on Magnetics*, vol. 37, no. 5, pp. 3269–3272, 2001, ISSN: 0018-9464. DOI: `10.1109/20.952592`.

[136] S. Kurz, J. Fetzer, G. Lehner, and W. M. Rucker, "A novel formulation for 3D eddy current problems with moving bodies using a lagrangian description and BEM-FEM coupling", *IEEE Transactions on Magnetics*, vol. 34, no. 5, pp. 3068–3073, 1998, ISSN: 0018-9464. DOI: `10.1109/20.717718`.

[137] J. Larsson, "Electromagnetics from a quasistatic perspective", *American Journal of Physics*, vol. 75, no. 3, pp. 230–239, 2007, ISSN: 0002-9505. DOI: `10.1119/1.2397095`.

[138] G. Lehner, *Elektromagnetische Feldtheorie: für Ingenieure und Physiker*. Berlin, Germany: Springer, 2010, ISBN: 978-3-642-13042-7. DOI: `10.1007/978-3-642-13042-7`.

[139] E. Lelarasmee, A. E. Ruehli, and A. L. Sangiovanni-Vincentelli, "The waveform relaxation method for time-domain analysis of large scale integrated circuits", *IEEE Transactions on Computer-Aided Design of Integrated Circuits and Systems*, vol. 1, no. 3, pp. 131–145, 1982, ISSN: 0278-0070. DOI: `10.1109/TCAD.1982.1270004`.

[140] J. Li, J. Li, and D. Xiu, "An efficient surrogate-based method for computing rare failure probability", *Journal of Computational Physics*, vol. 230, no. 24, pp. 8683–8697, 2011, ISSN: 0021-9991. DOI: `10.1016/j.jcp.2011.08.008`.

[141] J. Li and D. Xiu, "Evaluation of failure probability via surrogate models", *Journal of Computational Physics*, vol. 229, no. 23, pp. 8966–8980, 2010, ISSN: 0021-9991. DOI: `10.1016/j.jcp.2010.08.022`.

[142] J. H. Lienhard IV and J. H. Lienhard V, *A Heat Transfer Textbook*, 4th ed., ser. Dover Books on Engineering. Cambridge, MA, USA: Phlogiston Press, 2011, ISBN: 978-0-486-47931-6.

[143] J. S. Liu, *Monte Carlo Strategies In Scientific Computing*. New York, NY, USA: Springer, 2004, ISBN: 978-0-387-76371-2. DOI: `10.1007/978-0-387-76371-2`.

[144] L. Lombardi, R. Raimondo, and G. Antonini, "Electrothermal formulation of the partial element equivalent circuit method", *International Journal of Numerical Modelling: Electronic Networks, Devices and Fields*, vol. 31, no. 4, e2253, 2018, ISSN: 0894-3370. DOI: `10.1002/jnm.2253`.

[145] D. Loukrezis, U. Römer, T. Casper, S. Schöps, and H. De Gersem, "High dimensional uncertainty quantification for an electrothermal field problem using stochastic collocation on sparse grids and tensor train decomposition", *International Journal of Numerical Modelling: Electronic Networks, Devices and Fields*, vol. 31, no. 2, 2018, ISSN: 0894-3370. DOI: `10.1002/jnm.2222`. arXiv: `1610.03863`.

[146] X. Ma and N. Zabaras, "An adaptive hierarchical sparse grid collocation algorithm for the solution of stochastic differential equations", *Journal of Computational Physics*, vol. 228, no. 8, pp. 3084–3113, 2009, ISSN: 0021-9991. DOI: `10.1016/j.jcp.2009.01.006`.

[147] G. Marchuk, "Splitting and alternating direction methods", in *Handbook of Numerical Analysis Volume 1*, vol. 1, Amsterdam, The Netherlands: Elsevier, 1990, pp. 197–462, ISBN: 978-0-444-70366-8. DOI: `10.1016/s1570-8659(05)80035-3`.

[148] M. März and P. Nance, "Thermal modeling of power-electronic systems", Fraunhofer IIS, Tech. Rep., 2000, pp. 1–8.

[149] E. J. W. ter Maten, H.-G. Brachtendorf, R. Pulch, W. Schoenmaker, and H. De Gersem, Eds., *Nanoelectronic Coupled Problems Solutions*, ser. Mathematics in Industry. Cham, Switzerland: Springer, 2019, ISBN: 978-3-030-30725-7. DOI: `10.1007/978-3-030-30726-4`.

[150] E. J. W. ter Maten *et al.*, "nanoCOPS: Nanoelectronic COupled Problem Solutions", *ECMI Newsletter Mathematics & Industry*, no. 56, E. J. W. ter Maten and P. Putek, Eds., pp. 62–67, 2014, ISSN: 1013-9338.

[151] E. J. W. ter Maten *et al.*, "Nanoelectronic COupled Problems Solutions - nanoCOPS: Modelling, multi-rate, model order reduction, uncertainty quantification, fast fault simulation", *Journal of Mathematics in Industry*, vol. 7, no. 2, 2016, ISSN: 2190-5983. DOI: `10.1186/s13362-016-0025-5`.

[152] C. Mattiussi, "An analysis of finite volume, finite element, and finite difference methods using some concepts from algebraic topology", *Journal of Computational Physics*, vol. 133, no. 2, pp. 289–309, 1997, ISSN: 0021-9991. DOI: `10.1006/jcph.1997.5656`.

[153] P. Mawby, P. Igic, and M. Towers, "New physics-based compact electro-thermal model of power diode dedicated to circuit simulation", in *Proceedings IEEE Circuits and Systems ISCAS*, Sydney, NSW, Australia: IEEE, 2001, pp. 401–404, ISBN: 978-0-7803-6685-5. DOI: `10.1109/ISCAS.2001.921332`.

[154] R. Mertens *et al.*, "An algebraic multigrid method for solving very large electromagnetic systems", *IEEE Transactions on Magnetics*, vol. 34, no. 5, pp. 3327–3330, 1998, ISSN: 0018-9464. DOI: `10.1109/20.717782`.

[155] A. Mertol, "Estimation of aluminum and gold bond wire fusing current and fusing time", *IEEE Transactions on Components, Packaging, and Manufacturing Technology – Part B*, vol. 18, no. 1, pp. 210–214, 1995, ISSN: 1070-9894. DOI: `10.1109/96.365510`.

[156] R. F. Milsom, "Efficient SPICE-compatible electromagnetic model of arbitrarily shaped integrated passive structure", *IEEE Transactions on Microwave Theory and Techniques*, vol. 47, no. 7, pp. 1033–1044, 1999, ISSN: 0018-9480. DOI: `10.1109/22.775435`.

[157] P. Monk and E. Süli, "A convergence analysis of Yee's scheme on nonuniform grids", *SIAM Journal on Numerical Analysis*, vol. 31, no. 2, pp. 393–412, 1994, ISSN: 0036-1429. DOI: `10.1137/0731021`.

[158] G. E. Moore, "Cramming more components onto integrated circuits", *Electronics*, vol. 38, no. 8, 114ff. 1965, ISSN: 1098-4232. DOI: `10.1109/N-SSC.2006.4785860`.

[159] Y. Moumouni and R. J. Baker, "Concise thermal to electrical parameters extraction of thermoelectric generator for SPICE modeling", T. Chen and R. J. Baker, Eds., Fort Collins, CO, USA: IEEE, 2015, ISBN: 978-1-4673-6557-4. DOI: `10.1109/MWSCAS.2015.7282014`.

[160] W. Müller *et al.*, "Numerical solution of 2- and 3-dimensional nonlinear field problems by means of the computer program PROFI", *Electrical Engineering (Archiv für Elektrotechnik)*, vol. 65, no. 4–5, pp. 299–307, 1982, ISSN: 0003-9039. DOI: `10.1007/BF01452154`.

[161]  I. Munteanu and D. Ioan, "A survey on parameter extraction techniques for coupling electromagnetic devices to electric circuits", in *Scientific Computing in Electrical Engineering*, U. van Rienen, M. Günther, and D. Hecht, Eds., ser. Lecture Notes in Computational Science and Engineering, vol. 18, Berlin, Germany: Springer, 2001, pp. 337–357, ISBN: 978-3-540-42173-3. DOI: 10.1007/978-3-642-56470-3_35.

[162]  G. Mur, "Absorbing boundary conditions for the finite-difference approximation of the time-domain electromagnetic-field equations", *IEEE Transactions on Electromagnetic Compatibility*, vol. EMC-23, no. 4, pp. 377–382, 1981, ISSN: 0018-9375. DOI: 10.1109/TEMC.1981.303970.

[163]  ——, "The modeling of singularities in the finite-difference approximation of the time-domain electromagnetic-field equations", *IEEE Transactions on Microwave Theory and Techniques*, vol. 29, no. 10, pp. 1073–1077, 1981, ISSN: 0018-9480. DOI: 10.1109/TMTT.1981.1130501.

[164]  L. W. Nagel and D. O. Pederson, "Simulation program with integrated circuit emphasis", EECS Department, University of California, Berkeley, Tech. Rep. UCB/ERL M382, 1973.

[165]  A. Narayan, C. Gittelson, and D. Xiu, "A stochastic collocation algorithm with multifidelity models", *SIAM Journal on Scientific Computing*, vol. 36, no. 2, A495–A521, 2014, ISSN: 1064-8275. DOI: 10.1137/130929461.

[166]  J. C. Nédélec, "Mixed finite elements in $r^3$", *Numerische Mathematik*, vol. 35, no. 3, pp. 315–341, 1980, ISSN: 0945-3245. DOI: 10.1007/BF01396415.

[167]  G. T. Nöbauer and H. Moser, "Analytical approach to temperature evaluation in bonding wires and calculation of allowable current", *IEEE Transactions on Advanced Packaging*, vol. 23, no. 3, pp. 426–435, 2000, ISSN: 1521-3323. DOI: 10.1109/6040.861557.

[168]  F. Nobile, R. Tempone, and C. G. Webster, "A sparse grid stochastic collocation method for partial differential equations with random input data", *SIAM Journal on Numerical Analysis*, vol. 46, no. 5, pp. 2309–2345, 2008, ISSN: 0036-1429. DOI: 10.1137/060663660.

[169]  T. Noda and S. Yokoyama, "Thin wire representation in finite difference time domain surge simulation", *IEEE Transactions on Power Delivery*, vol. 17, no. 3, pp. 840–847, 2002, ISSN: 0272-1724. DOI: 10.1109/MPER.2002.4312236.

[170]  T. Noda, R. Yonezawa, S. Yokoyama, and Y. Takahashi, "Error in propagation velocity due to staircase approximation of an inclined thin wire in FDTD surge simulation", *IEEE Transactions on Power Delivery*, vol. 19, no. 4, pp. 1913–1918, 2004, ISSN: 0885-8977. DOI: 10.1109/TPWRD.2004.835396.

[171]  W. L. Oberkampf and C. J. Roy, *Verification and Validation in Scientific Computing*. New York, NY, USA: Cambridge University Press, 2010, ISBN: 978-0-521-11360-1.

[172]  A. Odabasioglu, M. Celik, and L. T. Pileggi, "PRIMA: Passive reduced-order interconnect macromodeling algorithm", *IEEE Transactions on Computer-Aided Design of Integrated Circuits and Systems*, vol. 17, no. 8, pp. 645–654, 1998, ISSN: 0278-0070. DOI: 10.1109/43.712097.

[173]  OrCAD, *PSpice user's guide*, 17.2, User's Manual, 2016.

[174]  I. V. Oseledets, "Tensor-train decomposition", *SIAM Journal on Scientific Computing*, vol. 33, no. 5, pp. 2295–2317, 2011, ISSN: 1064-8275. DOI: 10.1137/090752286.

[175]  B. Peherstorfer, K. Willcox, and M. Gunzburger, "Survey of multifidelity methods in uncertainty propagation, inference, and optimization", ACDL, Tech. Rep. TR16-1, 2016.

[176] A. Pels, J. Gyselinck, R. V. Sabariego, and S. Schöps, "Efficient simulation of DC-DC switch-mode power converters by multirate partial differential equations", *IEEE Journal on Multiscale and Multiphysics Computational Techniques*, vol. 4, no. 1, pp. 64–75, 2019, ISSN: 2379-8793. DOI: `10.1109/JMMCT.2018.2888900`. arXiv: `1707.01947`.

[177] W. van Petegem, B. Geeraerts, W. Sansen, and B. Graindourze, "Electrothermal simulation and design of integrated circuits", *IEEE Journal of Solid-State Circuits*, vol. 29, no. 2, pp. 143–146, 1994, ISSN: 0018–9200. DOI: `10.1109/4.272120`.

[178] M. Piket-May, A. Taflove, and J. Baron, "FD-TD modeling of digital signal propagation in 3-D circuits with passive and active loads", *IEEE Transactions on Microwave Theory and Techniques*, vol. 42, no. 8, pp. 1514–1523, 1994, ISSN: 0018-9480. DOI: `10.1109/22.297814`.

[179] A. Quarteroni and A. Valli, *Numerical Approximation of Partial Differential Equations*, ser. Springer Series in Computational Mathematics. Berlin, Germany: Springer, 2008, vol. 23, ISBN: 978-3-540-85267-4. DOI: `10.1007/978-3-540-85268-1`.

[180] A. Ramachandran, A. Ramachandran, and A. C. Cangellaris, "SPICE-compatible stamps for semi-discrete approximations of Maxwell's equations", *International Journal of Numerical Modelling: Electronic Networks, Devices and Fields*, vol. 21, no. 4, pp. 265–277, 2008, ISSN: 0894-3370. DOI: `10.1002/jnm.669`.

[181] D. A. Reed, "Computational science: Ensuring america's competitiveness", NCO NITRD, Tech. Rep., 2005.

[182] U. van Rienen and T. Weiland, "Triangular discretization method for the evaluation of RF-fields in cylindrically symmetric cavities", *IEEE Transactions on Magnetics*, vol. 21, no. 6, pp. 2317–2320, 1985, ISSN: 0018-9464. DOI: `10.1109/TMAG.1985.1064183`.

[183] J. Roychowdhury, "Analyzing circuits with widely separated time scales using numerical PDE methods", *IEEE Transactions on Circuits and Systems Part I: Fundamental Theory and Applications*, vol. 48, no. 5, pp. 578–594, 2001, ISSN: 1057-7122. DOI: `10.1109/81.922460`.

[184] A. E. Ruehli, "Equivalent circuit models for three-dimensional multiconductor systems", *IEEE Transactions on Microwave Theory and Techniques*, vol. 22, no. 3, pp. 216–221, 1974, ISSN: 0018-9480. DOI: `10.1109/TMTT.1974.1128204`.

[185] A. E. Ruehli, G. Antonini, and L. Jiang, *Circuit Oriented Electromagnetic Modeling Using the PEEC Techniques*, 1st ed. Hoboken, NJ, USA: John Wiley & Sons, 2017, ISBN: 978-1-118-43664-6.

[186] P. Russer, M. Righi, C. Eswarappa, and W. J. R. Hoefer, "Lumped element equivalent circuit parameter extraction of distributed microwave circuits via TLM simulation", H. Kuno and C. Wen, Eds., San Diego, CA, USA: IEEE Press, 1994, pp. 887–890, ISBN: 978-0-7803-1778-9. DOI: `10.1109/MWSYM.1994.335215`.

[187] Y. Saad, *Iterative Methods for Sparse Linear Systems*, 2nd ed. Boston, MA, USA: Society for Industrial and Applied Mathematics, 2003, ISBN: 978-0-89871-534-7.

[188] K. Salari and P. Knupp, "Code verification by the method of manufactured solutions", Sandia National Laboratories, Tech. Rep. SAND2000-1444, 2000. DOI: `10.2172/759450`.

[189] M. Schauer, P. Hammes, P. Thoma, and T. Weiland, "Nonlinear update scheme for partially filled cells", *IEEE Transactions on Magnetics*, vol. 39, no. 3, pp. 1421–1423, 2003, ISSN: 0018-9464. DOI: `10.1109/TMAG.2003.810415`.

[190] W. H. A. Schilders and E. J. W. ter Maten, Eds., *Numerical Methods in Electromagnetics*, ser. Handbook of Numerical Analysis. Amsterdam, Netherlands: Elsevier, 2005, vol. 13, ISBN: 978-0-444-51375-5.

[191]  W. Schoenmaker, H.-G. Brachtendorf, K. Bittner, C. Tischendorf, and C. Strohm, "EM-equations, coupling to heat and to circuits", in *Nanoelectronic Coupled Problems Solutions*, E. J. W. ter Maten, H.-G. Brachtendorf, R. Pulch, W. Schoenmaker, and H. De Gersem, Eds., ser. Mathematics in Industry. Cham, Switzerland: Springer, 2019, ch. 2, ISBN: 978-3-030-30725-7. DOI: `10.1007/978-3-030-30726-4`.

[192]  W. Schoenmaker *et al.*, "Fully-coupled 3D electro-thermal field simulator for chip-level analysis of power devices", in *19th International Workshop on Thermal Investigations of ICs and Systems (THERMINIC 2013)*, Berlin, Germany: IEEE, 2013, pp. 210–215, ISBN: 978-1-4799-2271-0. DOI: `10.1109/THERMINIC.2013.6675199`.

[193]  S. Schöps, "Multiscale modeling and multirate time-integration of field/circuit coupled problems", VDI Verlag. Fortschritt-Berichte VDI, Reihe 21, Dissertation, Bergische Universität Wuppertal & Katholieke Universiteit Leuven, Düsseldorf, Germany, 2011, ISBN: 978-3-18-339821-8.

[194]  S. Schöps, H. De Gersem, and A. Bartel, "A cosimulation framework for multirate time-integration of field/circuit coupled problems", *IEEE Transactions on Magnetics*, vol. 46, no. 8, pp. 3233–3236, 2010, ISSN: 0018-9464. DOI: `10.1109/TMAG.2010.2045156`.

[195]  S. Schöps, H. De Gersem, and T. Weiland, "Winding functions in transient magnetoquasistatic field-circuit coupled simulations", *COMPEL: The International Journal for Computation and Mathematics in Electrical and Electronic Engineering*, vol. 32, no. 6, pp. 2063–2083, 2013, ISSN: 0332-1649. DOI: `10.1108/COMPEL-01-2013-0004`.

[196]  S. Schöps, I. Niyonzima, and M. Clemens, "Parallel-in-time simulation of eddy current problems using parareal", *IEEE Transactions on Magnetics*, vol. 54, no. 3, pp. 1–4, 2018, ISSN: 0018-9464. DOI: `10.1109/TMAG.2017.2763090`. arXiv: `1706.05750`.

[197]  R. Schuhmann and T. Weiland, "A stable interpolation technique for FDTD on non-orthogonal grids", *International Journal of Numerical Modelling: Electronic Networks, Devices and Fields*, vol. 11, no. 6, pp. 299–306, 1998, ISSN: 0894-3370. DOI: `10.1002/(SICI)1099-1204(199811/12)11:6<299::AID-JNM314>3.0.CO;2-A`.

[198]  ——, "Conservation of discrete energy and related laws in the finite integration technique", *Progress In Electromagnetics Research (PIER)*, vol. 32, pp. 301–316, 2001, ISSN: 1070-4698. DOI: `10.2528/PIER00080112`.

[199]  ——, "FDTD on nonorthogonal grids with triangular fillings", *IEEE Transactions on Magnetics*, vol. 35, no. 3, pp. 1470–1473, 1999, ISSN: 0018-9464. DOI: `10.1109/20.767244`.

[200]  L. Schwartz, *Théorie des Distributions*. Paris, France: Hermann, 1957, ISBN: 978-2-7056-5551-8.

[201]  R. Scott, "Finite element convergence for singular data", *Numerische Mathematik*, vol. 21, no. 4, pp. 317–327, 1973, ISSN: 0029-599X. DOI: `10.1007/bf01436386`.

[202]  J. A. Serret, "Sur quelques formules relatives à la théorie des courbes à double courbure.", *Journal de Mathématiques Pures et Appliquées*, vol. 16, pp. 193–207, 1851, ISSN: 0021-7874.

[203]  P. P. Silvester and R. L. Ferrari, *Finite Elements for Electrical Engineers*, 2nd ed. Cambridge, UK: Cambridge University Press, 1996, ISBN: 978-0-521-44505-4.

[204]  N. Simpson, R. Wrobel, and P. Mellor, "An accurate mesh-based equivalent circuit approach to thermal modeling", *IEEE Transactions on Magnetics*, vol. 50, no. 2, pp. 269–272, 2014, ISSN: 0018-9464. DOI: `10.1109/TMAG.2013.2282047`.

[205] B. F. Smith, P. E. Bjørstad, and W. D. Gropp, *Domain Decomposition: Parallel Multilevel Methods for Elliptic Partial Differential Equations*. Cambridge, UK: Cambridge University Press, 1996, ISBN: 978-0-521-49589-9.

[206] G. Söderlind, "Automatic control and adaptive time-stepping", *Numerical Algorithms*, vol. 31, no. 1, pp. 281–310, 2002, ISSN: 1572-9265. DOI: `10.1023/A:1021160023092`.

[207] H. Spachmann, S. Gutschling, H. Krüger, and T. Weiland, "FIT-formulation for non-linear dispersive media", *International Journal of Numerical Modelling: Electronic Networks, Devices and Fields*, vol. 12, no. 1-2, pp. 81–92, 1999, ISSN: 0894-3370. DOI: `10.1002/(sici)1099-1204(199901/04)12:1/2<81::aid-jnm324>3.0.co;2-l`.

[208] T. Steinmetz *et al.*, "Efficient symmetric FEM-BEM coupled simulations of electro-quasistatic fields", *IEEE Transactions on Magnetics*, vol. 44, no. 6, pp. 1346–1349, 2008, ISSN: 0018-9464. DOI: `10.1109/TMAG.2008.915785`.

[209] R. J. Stephenson, "Development of vector analysis from quaternions", *American Journal of Physics*, vol. 34, no. 3, pp. 194–201, 1966, ISSN: 0002-9505. DOI: `10.1119/1.1972885`.

[210] P. Su and R. L. S. Drysdale, "A comparison of sequential delaunay triangulation algorithms", *Computational Geometry*, vol. 7, no. 5-6, pp. 361–385, 1997, ISSN: 0925-7721. DOI: `10.1016/s0925-7721(96)00025-9`.

[211] W. Sui, D. A. Christensen, and C. H. Durney, "Extending the two-dimensional FDTD method to hybrid electromagnetic systems with active and passive lumped elements", *IEEE Transactions on Microwave Theory and Techniques*, vol. 40, no. 4, pp. 724–730, 1992, ISSN: 0018-9480. DOI: `10.1109/22.127522`.

[212] D. Sun, J. Manges, X. Yuan, and Z. Cendes, "Spurious modes in finite-element methods", *IEEE Antennas and Propagation Magazine*, vol. 37, no. 5, pp. 12–24, 1995, ISSN: 1045-9243. DOI: `10.1109/74.475860`.

[213] A. Taflove, *Advances in Computational Electrodynamics: The Finite-Difference Time-Domain-Method*, A. Taflove, Ed. Dedham, MA, USA: Artech House, 1998, ISBN: 978-0-89006-834-2.

[214] ——, "Application of the finite-difference time-domain method to sinusoidal steady-state electromagnetic-penetration problems", *IEEE Transactions on Electromagnetic Compatibility*, vol. EMC-22, no. 3, pp. 191–202, 1980, ISSN: 0018-9375. DOI: `10.1109/temc.1980.303879`.

[215] ——, *Computational Electrodynamics: The Finite-Difference Time-Domain-Method*. Norwood, MA, USA: Artech House, 1995, ISBN: 978-1-58053-832-9.

[216] T. Tarhasaari, L. Kettunen, and A. Bossavit, "Some realizations of a discrete Hodge operator: A reinterpretation of finite element techniques", *IEEE Transactions on Magnetics*, vol. 35, no. 3, pp. 1494–1497, 1999, ISSN: 0018-9464. DOI: `10.1109/20.767250`.

[217] The MAFIA Collaboration, *User's guide MAFIA*, 1987.

[218] P. Thoma and T. Weiland, "A consistent subgridding scheme for the finite difference time domain method", *International Journal of Numerical Modelling: Electronic Networks, Devices and Fields*, vol. 9, no. 5, pp. 359–374, 1996, ISSN: 0894-3370. DOI: `10.1002/(SICI)1099-1204(199609)9:5<359::AID-JNM245>3.0.CO;2-A`.

[219] V. A. Thomas, M. E. Jones, M. Piket-May, A. Taflove, and E. Harrigan, "The use of SPICE lumped circuits as sub-grid models for FDTD analysis", *IEEE Microwave and Guided Wave Letters*, vol. 4, no. 5, pp. 141–143, 1994, ISSN: 1051-8207. DOI: `10.1109/75.289516`.

[220] V. Thomée, *Galerkin Finite Element Methods for Parabolic Problems*, 2nd ed., ser. Series in Computational Mathematics. Berlin, Germany: Springer, 2006, vol. 25, ISBN: 978-3-540-33121-6.

[221] E. Tonti, "A direct discrete formulation of field laws: The cell method", *Computer Modeling in Engineering & Sciences*, vol. 2, no. 2, pp. 237–258, 2001, ISSN: 1526-1492. DOI: `10.3970/cmes.2001.002.237`.

[222] ——, "Finite formulation of electromagnetic field", *IEEE Transactions on Magnetics*, vol. 38, no. 2, pp. 333–336, 2002, ISSN: 0018-9464. DOI: `10.1109/20.996090`.

[223] ——, "Finite formulation of the electromagnetic field", *Progress In Electromagnetics Research (PIER)*, vol. 32, pp. 1–44, 2001, ISSN: 1070-4698. DOI: `10.2528/PIER00080101`.

[224] ——, "On the geometrical structure of electromagnetism", in *Gravitation, Electromagnetism and Geometrical Structures*, G. Ferrarese, Ed. Bologna, Italy: Pitagora Editrice, 1995, pp. 281–308.

[225] F. Traub, J. Hansen, W. Ackermann, and T. Weiland, "Generation of physical equivalent circuits using 3D simulations", in *2012 IEEE International Symposium on Electromagnetic Compatibility (EMC)*, Pittsburgh, PA, USA: IEEE, 2012, pp. 486–491, ISBN: 978-1-4673-2061-0. DOI: `10.1109/ISEMC.2012.6351683`.

[226] L. N. Trefethen and D. Bau, *Numerical Linear Algebra*. Philadelphia, PA, USA: Society for Industrial and Applied Mathematics, 1997, ISBN: 978-0-89871-361-9. DOI: `10.1137/1.9780898719574`.

[227] Y.-S. Tsuei, A. C. Cangellaris, and J. L. Prince, "Rigorous electromagnetic modeling of chip-to-package (first-level) interconnections", *IEEE Transactions on Components, Hybrids, and Manufacturing Technology*, vol. 16, no. 8, pp. 876–883, 1993, ISSN: 0148-6411. DOI: `10.1109/33.273688`.

[228] I. A. Tsukerman, A. Konrad, G. Meunier, and J. C. Sabonnadière, "Coupled field-circuit problems: Trends and accomplishments", *IEEE Transactions on Magnetics*, vol. 29, no. 2, pp. 1701–1704, 1993, ISSN: 0018-9464. DOI: `10.1109/20.250733`.

[229] R. Tucker, "Differential form valued forms and distributional electromagnetic sources", *Journal of Mathematical Physics*, vol. 50, no. 3, p. 033 506, 2009, ISSN: 0022-2488. DOI: `10.1063/1.3085761`.

[230] M. J. Turner, R. W. Clough, H. C. Martin, and L. J. Topp, "Stiffness and deflection analysis of complex structures", *Journal of the Aeronautical Sciences*, vol. 23, no. 9, pp. 805–823, 1956, ISSN: 0095-9812. DOI: `10.2514/8.3664`.

[231] K. R. Umashankar, A. Taflove, and B. Beker, "Calculation and experimental validation of induced currents on coupled wires in an arbitrary shaped cavity", *IEEE Transactions on Antennas and Propagation*, vol. 35, no. 11, pp. 1248–1257, 1987, ISSN: 0018-926X. DOI: `10.1109/TAP.1987.1144000`.

[232] J. G. Van Bladel, *Singular Electromagnetic Fields and Sources*. Piscataway, NJ, USA: IEEE Press, 1991, ISBN: 978-0-19-856200-9.

[233] S. Vandekerckhove, B. Vandewoestyne, H. De Gersem, K. Van Den Abeele, and S. Vandewalle, "Mimetic discretisation and higher order time integration for acoustic, electromagnetic and elastodynamic wave propagation", *Journal of Computational and Applied Mathematics*, vol. 259, pp. 65–76, 2014, ISSN: 0377-0427. DOI: `10.1016/j.cam.2013.02.027`.

[234] VDI, Ed., *VDI Heat Atlas*, 2nd ed. Berlin, Germany: Springer, 2010, ISBN: 978-3-540-77876-9. DOI: `10.1007/978-3-540-77877-6`.

[235] O. Veblen and J. H. C. Whitehead, *The Foundations of Differential Geometry*. Cambridge, UK: Cambridge University Press, 1932, ISBN: 978-0-521-06674-7.

[236]  P. K. Vijalapura, J. Strain, and S. Govindjee, "Fractional step methods for index-1 differential-algebraic equations", *Journal of Computational Physics*, vol. 203, no. 1, pp. 305–320, 2005, ISSN: 0021-9991. DOI: `10.1016/j.jcp.2004.08.015`.

[237]  R. Vogelsong and C. Brzezinski, "Extending SPICE for electro-thermal simulation", in *Proceedings of the IEEE 1989 Custom Integrated Circuits Conference*, R. Milano, M. Hartranft, and D. Brown, Eds., San Diego, CA, USA: IEEE, 1989, pp. 21.4/1–21.4/4. DOI: `10.1109/CICC.1989.56803`.

[238]  G. Voronoi, "Nouvelles applications des paramètres continus à la théorie des formes quadratiques. deuxième mémoire. recherches sur les parallélloèdres primitifs.", *Journal für die reine und angewandte Mathematik*, vol. 1908, no. 134, 1908, ISSN: 0075-4102. DOI: `10.1515/crll.1908.134.198`.

[239]  ——, "Nouvelles applications des paramètres continus à la théorie des formes quadratiques. premier mémoire. sur quelques propriétés des formes quadratiques positives parfaites.", *Journal für die reine und angewandte Mathematik*, vol. 1908, no. 133, 1908, ISSN: 0075-4102. DOI: `10.1515/crll.1908.133.97`.

[240]  T. Weiland, "A discretization method for the solution of Maxwell's equations for six-component fields", *International Journal of Electronics and Communications*, vol. 31, pp. 116–120, 1977.

[241]  ——, "On the unique numerical solution of Maxwellian eigenvalue problems in three dimensions", *Particle Accelerators*, vol. 17, no. 227–242, 1985, ISSN: 0031-2460.

[242]  ——, "Time domain electromagnetic field computation with finite difference methods", *International Journal of Numerical Modelling: Electronic Networks, Devices and Fields*, vol. 9, no. 4, pp. 295–319, 1996, ISSN: 0894-3370. DOI: `10.1002/(SICI)1099-1204(199607)9:4<295::AID-JNM240>3.0.CO;2-8`.

[243]  P. Wesseling, *An Introduction to Multigrid Methods*. Chichester, UK: John Wiley & Sons Inc, 1992, ISBN: 978-0-471-93083-9.

[244]  H. Whitney, *Geometric Integration Theory*. Princeton, NJ, USA: Princeton University Press, 1957.

[245]  P. Wilkerson, A. Raman, and M. Turowski, "Fast, automated thermal simulation of three-dimensional integrated circuits", in *The Ninth Intersociety Conference on Thermal and Thermomechanical Phenomena in Electronic Systems, ITHERM'04*, K. Ramakrishna, Ed., IEEE, vol. 1, 2004, pp. 706–713, ISBN: 978-0-7803-8357-9. DOI: `10.1109/ITHERM.2004.1319245`.

[246]  T. Wittig, I. Munteanu, R. Schuhmann, and T. Weiland, "Model order reduction and equivalent circuit extraction for FIT discretized electromagnetic systems", *International Journal of Numerical Modelling: Electronic Networks, Devices and Fields*, vol. 15, no. 5-6, pp. 517–533, 2002, ISSN: 0894-3370. DOI: `10.1002/jnm.471`.

[247]  M. Witting and T. Pröpper, "Cosimulation of electromagnetic fields and electrical networks in the time domain", *Surveys on Mathematics for Industry*, vol. 9, no. 2, pp. 101–115, 1999, ISSN: 0938-1953.

[248]  H. Wu and A. C. Cangellaris, "Efficient finite element electromagnetic modeling of thin wires", *Microwave and Optical Technology Letters*, vol. 50, no. 2, pp. 350–354, 2008, ISSN: 0895-2477. DOI: `10.1002/mop.23060`.

[249]  S. Wünsche, C. Clauss, P. Schwarz, and F. Winkler, "Electro-thermal circuit simulation using simulator coupling", *IEEE Transactions on Very Large Scale Integration (VLSI) Systems*, vol. 5, no. 3, pp. 277–282, 1997, ISSN: 1063-8210. DOI: `10.1109/92.609870`.

[250]  D. Xiu, *Numerical Methods for Stochastic Computations: A Spectral Method Approach*. Princeton, NJ, USA: Princeton University Press, 2010, ISBN: 978-0-691-14212-8.

[251] D. Xiu and J. S. Hesthaven, "High-order collocation methods for differential equations with random inputs", *SIAM Journal on Scientific Computing*, vol. 27, no. 3, pp. 1118–1139, 2005, ISSN: 1064-8275. DOI: 10.1137/040615201.

[252] N. N. Yanenko, *The method of fractional steps: the solution of problems of mathematical physics in several variables*, ser. Lecture Notes in Mathematics. Berlin, Germany: Springer, 1971, vol. 91, ISBN: 978-3-642-65110-6. DOI: 10.1007/978-3-642-65108-3.

[253] F. Yang, X. Zeng, Y. Su, and D. Zhou, "RLCSYN: RLC equivalent circuit synthesis for structure-preserved reduced-order model of interconnect", in *IEEE International Symposium on Circuits and Systems, 2007. ISCAS 2007*, New Orleans, LA, USA, 2007, pp. 2710–2713, ISBN: 978-1-4244-0920-4. DOI: 10.1109/ISCAS.2007.378521.

[254] K. S. Yee, "Numerical solution of initial boundary value problems involving Maxwell's equations in isotropic media", *IEEE Transactions on Antennas and Propagation*, vol. 14, no. 3, pp. 302–307, 1966, ISSN: 0018-926X. DOI: 10.1109/TAP.1966.1138693.

# Acknowledgments

This brings me to the final thoughts for this manuscript, and I gratefully use this page to thank all the people who were involved in its compilation.

First of all, I would like to thank Prof. Herbert De Gersem and Prof. Sebastian Schöps for the invaluable scientific and personal support during the last years. They provided advice when it was needed, inspiring discussions when there was time, and the required challenges to remain productive. Moreover, I greatly appreciated the professional atmosphere and their open-door policy.

There has been a great number of collaborators who provided guidance, inspiring ideas, and helped with the sometimes nasty implementation of clever algorithms. In alphabetical order, I thank Steve Bigalke, Prof. Ludovic Chamoin, David Duque, Victoria Heinz, Katrin Hirmer, Alexander Krimm, Dimitrios Loukrezis, Abdul Moiz, Prof. Ulrich Römer, and all the colleagues from the nanoCOPS project.

I would also like to thank Prof. Stefan Kurz and Mehdi Elasmi for reviewing my writings on differential forms, algebraic topology, de Rham currents, and Hodge operators. They provided valuable advice for a substantial improvement of the corresponding sections.

During the time at the graduate school and the TEMF institute, many people provided company such that the hard work became much more enjoyable. I really enjoyed our joint activities such as the "Kickerabende", summer events, board game sessions, cinema nights, and cake meetings. Moreover, I will always remember our annual retreats, namely the excursions to Seeheim and the workshops in Kleinwalsertal. I always enjoyed the scientific discussions, the long nights in the beer cellar, and the "kamikaze" hiking trips.

On a special note, I thank the administrative staff working in the background of the graduate school and the institute. Without these people, our lives as PhD students would be much more painful.

Apart from the academic world, I thank my parents for giving me the opportunity to carry out my studies all over these years. They have always been patient and (almost) never asked the nasty questions. Finally, I thank Sabrina, who always supported me, shared my sufferings, and never gave up on me.